Numerical modelling of pulse wave propagation in the cardiovascular system: development, validation and clinical applications

by

Jordi Alastruey Arimon

Departments of Aeronautics and Bioengineering

Imperial College London

This thesis is submitted for the degree of Doctor of Philosophy of the University of London

2006

Abstract

The purpose of this thesis is to develop a non-linear, one-dimensional (1-D) model of pulse wave propagation in arterial networks in the cardiovascular system. Arteries are simulated as thin, homogeneous and elastic tubes and the blood as a homogeneous, incompressible, and Newtonian fluid. The governing equations are analysed by means of the method of characteristics and are solved using a discontinuous Galerkin scheme, with a 1-D spectral/hp element spatial discretisation and a second-order Adams-Bashforth time-integration scheme. A linearised model is also studied to obtain analytical solutions that are very useful in providing insight into the interpretation of the results.

The modelling capabilities of the existing 1-D code are enhanced by including viscous dissipation and more realistic models of the inflow and outflow boundary conditions. The new code is validated against a well-defined experimental model and against *in-vivo* data when available. It is applied to study pulse propagation along the human aorta to understand the pulse waveforms measured *in-vivo*, and to study the effect of anastomoses in two arterial networks: the arm and the cerebral circulation. In the arm, the reliability of the modified Allen's test to determine the presence of sufficient collateral flow through the palmar arch artery is assessed. In the cerebral circulation, the ability of the circle of Willis to compensate for partial or total occlusions of arteries is examined.

The main contribution of this thesis has been the development and validation of a reliable 1-D model that produces clinically relevant results with a reasonable computational cost. This model offers an important insight into the performance of the arterial system, in healthy conditions and after total or partial occlusions of arteries, and it has the potential to assist in the diagnosis and treatment of cardiovascular diseases if applied with patient-specific data.

To Mara and my parents

Acknowledgements

First, I would like to deeply thank Mara for her patience, encouragement and support throughout my PhD. I would also like to express my gratitude to my parents, my grandmother and my family in Italy for their constant moral support.

I would like to thank Prof. Kim H. Parker, Dr. Joaquim Peiró and Prof. Spencer J. Sherwin for their excellent supervision, full of advices, knowledge and patience, since the very beginning of this work. I am also very grateful to them for providing me with plenty of opportunities to attend conferences and schools to complement my research training, and for thouroughly proof-reading this thesis.

I also wish to express my gratitude to Prof. Patrick Segers and Prof. Pascal Verdonck (University of Ghent, Belgium) for sharing with me their experimental data, Dr. Peter D. Weinberg (Department of Bioengineering, Imperial College) for his inspiring observations on my model of the human aorta, Jazmin Aguado (Department of Bioengineering, Imperial College) and Sheila M. Raynor (Faculty of Medicine, Imperial College) for measuring pressure and velocity waves on my neck, Oliver Krause (Department of Bioengineering, Imperial College) for his excellent IT assistance throughout my PhD, and all the people from Aeronautics, Bioengineering and the Haemodel project with whom I had very productive discussions throughout the course of this work.

I also want to acknowledge the financial support given by the European Union Research Training Network *Mathematical Modelling for Haemodynamics*, HaeMO$\partial\varepsilon$l project (contract HPRN-CT-2002-00270).

London, September 2006.

Preface

This research work has been accomplished at the Departments of Aeronautics and Bioengineering, Imperial College London, under the supervision of Prof. Kim H. Parker, Dr. Joaquim Peiró and Prof. Spencer J. Sherwin, and the financial support of the European Union Research Training Network *Mathematical Modelling for Haemodynamics*, HaeMO$\partial\varepsilon$l project (contract HPRN-CT-2002-00270).

The results presented in Section 3.1 are published in the proceedings of the 2005 Summer Bioengineering Conference organised by the American Society of Mechanical Engineers [1]. The study carried out in Section 4.3 has been accepted by the journal *Computer Methods in Biomechanics and Biomedical Engineering* [2], and the study presented in Chapter 5 has been accepted by the *Journal of Biomechanics* [3].

Contents

Abstract 2

Acknowledgements 4

Table of contents 6

List of tables 10

1 Introduction 12

1.1 Cardiovascular anatomy and physiology 14

1.1.1 The heart 15

1.1.2 The systemic blood vessels 16

1.1.3 The blood 19

1.2 Propagation of pressure and flow waves 20

1.3 Brief historical review 25

1.4 Motivation and objectives 27

1.5 Organisation of the thesis 27

2 Mathematical formulation 29

2.1 Assumptions and justification of the 1-D formulation 30

2.2 Governing equations 31

2.3 Characteristic analysis 34

2.4 Wave separation 37

2.5 Linearisation of the governing equations 38

2.6 Numerical solution: the discontinuous Galerkin formulation 39

2.6.1 The Riemann problem 42

2.6.2 Application to the linear formulation 43

2.7 Boundary conditions 44
2.7.1 Inflow boundary conditions 45
2.7.2 Junction boundary conditions 46
2.7.2.1 Connection of two arteries 46
2.7.2.2 Linear analysis of a connection of two arteries 46
2.7.2.3 Junctions 48
2.7.2.4 Linear analysis of junctions 50
2.7.3 Terminal boundary conditions 52
2.7.3.1 Zero-dimensional equations 53
2.7.3.2 The windkessel model 54
2.7.3.3 Terminal reflection coefficient 56
2.7.3.4 Terminal resistance 57
2.7.3.5 Two-element (CR) windkessel model 58
2.7.3.6 Three-element (RCR) windkessel model 59
2.7.3.7 Four-element (RCLR) windkessel model 60
2.8 Estimation of the peripheral resistance, inertia and compliance 61
2.8.1 Resistance 63
2.8.2 Inertia 64
2.8.3 Compliance 65
2.8.4 Which values of φ and λ? 66
2.9 Final remarks 67

3 Validation **68**

3.1 Validation versus a well-defined experimental arterial system 69
3.1.1 Description of the experimental model 70
3.1.2 1-D simulation 76
3.1.3 Results and discussion 77
3.2 Implementation of the technique to estimate the peripheral RLC parameters 83
3.3 Pulse wave propagation along the aorta 86
3.4 Sensitivity analysis 94
3.4.1 Numerical convergence 94

3.4.2 The effect of non-linearities 95
3.4.3 Sensitivity to changes in the geometry 97
3.4.4 Sensitivity to changes in the elasticity 100
3.4.5 Sensitivity to the density and viscosity 100
3.4.6 Sensitivity to the peripheral resistance, compliance and venous pressure 101
3.4.7 Summary 103
3.4.8 Role of the terminal lumped parameter models 104
3.4.8.1 Terminal resistance 104
3.4.8.2 Three-element (RCR) windkessel model 105
3.4.8.3 Four-element (RCLR) windkessel model 106
3.5 Final remarks 107

4 Pulse wave propagation in the palmar arch 109
4.1 Models studied 110
4.2 Study of pulse wave propagation 114
4.2.1 Impulse wave 114
4.2.2 Physiological conditions 119
4.3 Assessment of the modified Allen's test (MAT) 121
4.3.1 Simulation of the test 122
4.3.2 Effect of reducing the calibre of the SPA 126
4.3.3 Effect of insufficient compression of the RA 128
4.4 Final remarks 129

5 Pulse wave propagation in the cerebral circulation 131
5.1 Previous models of the circle of Willis 133
5.2 The model of the circle of Willis 134
5.3 Pulse wave propagation along the aorta and in the arteries supplying the circle of Willis 138
5.4 Flow in the cerebral arteries 140
5.4.1 Normal conditions 140
5.4.2 The effects of occlusions in the afferent arteries 144
5.4.3 The effect of partial occlusions in the communicating arteries . 146

5.5 Final remarks 147

6 Conclusions **150**

6.1 Summary of the thesis achievements 150

6.2 Future Work 153

6.2.1 Further applications of the model 154

6.2.2 Further developments of the methodology 154

Bibliography **157**

List of Tables

1.1 Approximate number of each type of systemic vessel along with the approximate lumen calibre (D), wall thickness (h), total cross-sectional area (A_T), and percentage of the total blood volume (V) contained in each type of systemic vessel. The rest of the volume is contained in the heart (12%) and in the pulmonary circulation (18%). (From Gregg [30].) 17

1.2 Estimated blood flow distribution among body parts in normal conditions. (From Burton [12].) 25

3.1 Geometrical and elastic properties of the 55 arterial segments in the hydrodynamic model shown in Figures 3.1 to 3.3. Cross-sectional diameters and wall thicknesses decrease approximately linearly and elastic moduli increase approximately linearly. $D_{in} \rightarrow D_{out}$: diastolic cross-sectional diameters at the inlet and at the outlet of each vessel, $h_{in} \rightarrow h_{out}$: wall thicknesses at the inlet and at the outlet of each vessel, $E_{in} \rightarrow E_{out}$: elastic moduli at the inlet and at the outlet of each vessel. Continued on Table 3.2. (Data from Prof. Segers' PhD thesis [77].) . 72

3.2 Continued from Table 3.1. 73

3.3 Comparison between the experimental (bold numbers) and numerical (normal numbers) systolic (p_s) and diastolic (p_d) pressures, pulse pressures (pp), mean pressures ($\overline{p}$), maximum (Q_{max}) and minimum (Q_{min}) flow rates, maximum minus minimum flow rates ($Q_{max} - Q_{min}$) and mean flow rates ($\overline{Q}$) at the six measuring locations along the aorta indicated in Figure 3.2 (bottom right). Pressures in kPa and flow rates in ml/s. 80

3.4 Comparison of the peripheral resistance (R_{T_N}) and compliance (C_T) calculated by the algorithm proposed in Section 2.8 (normal numbers) against the corresponding values used by Stergiopulos *et al* [88] (bold numbers). The first columns indicate the name of each terminal artery, its length (l), radius (R), and wave speed (c_0), the number of generations of bifurcations to reach the capillaries (N) and the value of λ. 83

3.5 Comparison between the haemodynamic parameters measured by Simon *et al* [83] at a brachial artery of normal patients and the corresponding parameters simulated using the 1-D aorta at $x = 0.0$, $x = 0.2$ m, and $x = 0.4$ m. 90

3.6 Effect on the mean, systolic and diastolic pressures, the mean flow and the peak velocity obtained with the 1-D model of the human aorta at $x = 0.2$ m, of the linear formulation, the non-linear inviscid formulation and changes by $\pm 10\%$ in the length, diameter, wall thickness, elastic modulus, peripheral resistance and venous pressure of the control case. Numbers express the percentage of change relative to the values of the control case. 103

4.1 Physiological data used in Model 0. The fifth column indicates the time it takes a wave to travel the artery at a speed c_0. 112

4.2 Physiological data used in Model 1. The fifth column indicates the time it takes a wave to travel the artery at a speed c_0. 112

4.3 Physiological data used in Model 2. The fifth column indicates the time it takes a wave to travel the artery at a speed c_0. 113

4.4 Linear reflection coefficients at the splitting flow junctions of the models shown in Figure 4.1 (right) for a wave coming from the parent vessel (R_{f_1}), the daughter vessel I (R_{f_2}), or the daughter vessel II (R_{f_3}). 113

5.1 Physiological data used in the model shown in Figure 5.1 (right) based upon the data collected by Stergiopulos *et al* [88], Fahrig *et al* [22] and Moore *et al* [53]. . . 137

5.2 Mean outflow rates (in ml/s) at the outlet of the efferent arteries and in the middle of the communicating arteries for different study cases. The last row shows an average of published *in-vivo* measurements at the efferent arteries calculated by Fahrig *et al* [22]. Positive values of flow in the communicating arteries follow the direction of the arrows in Figure 5.1 (right). R stands for right and L for left. . . 141

Chapter 1

Introduction

Numerical models are playing an increasingly significant role in improving the diagnosis and treatment of cardiovascular diseases, which are the major cause of death in developed countries. In the United Kingdom, for instance, cardiovascular diseases claimed about 40% of all the deaths in 2002, according to the British Heart Foundation [69].

This research focuses on the development of a numerical model to understand the physical phenomenon of blood pressure and flow pulse wave propagation occurring within the human systemic arterial tree. It studies the relation of this phenomenon to the geometry and distensibility of the arteries, and to other physical parameters that characterise the cardiovascular system, such as heart rate, cardiac output and peripheral impedances.

Several cardiovascular pathologies introduce variations in the physical properties of the system that significantly change pulse waveforms. For instance, atherosclerosis, which is a common and life-threatening disease consisting in the formation of fat deposits inside the vessels, decreases the diameter of the vessels and hinders, or even stops, the flow of blood. Anatomical variations (changes in the topology of the arterial network) also affect the pattern of pressure and velocity pulse waves. These variations are common in the arteries supplying the hand and the brain, where they provide collateral pathways to flow in some cases. Detection of these anatomical variations is of paramount importance in several clinical procedures, as will be explained in this thesis. Implanted vascular prosthesis also affect pulse wave propagation because of the changes they introduce in the elasticity of the arterial wall.

These are some of the problems that can be assessed using the model developed in this thesis.

The systemic arterial tree is simulated as a network of flexible tubes through which pressure and flow waves propagate. Only the axial direction of arteries is simulated, since a three-dimensional (3-D) simulation is not feasible because of its computational cost. A one-dimensional (1-D) simulation is fast and allows to carry out a sensitivity analysis. Although the 1-D model used is simpler and cheaper than a 3-D model, it still provides clinically relevant information, because pulse wave propagation occurs mainly in the axial direction of arteries. At any time and any point in the system, the model provides the average pressure and axial velocity of blood, and the cross-sectional area of the lumen. Total or partial occlusions of arteries are easily simulated, along with changes in the geometry, elasticity and connectivity of each arterial segment. Only the large arteries are simulated, since the rest of arteries and the arterioles and capillary beds are too large in number, it is difficult to measure their geometric and elastic properties required by the algorithm, and the assumptions of the model are only valid for blood flow in arteries. The effect of the flow resistance, compliance and inertia of the smaller vessels on pulse wave propagation in the large arteries is simulated by lumped parameter models or zero-dimensional models (0-D) coupled to the terminal branches of the 1-D model. The blood flow at the proximal end of the system is generally specified as the input boundary condition. Usually, the input to the system is the upper ascending aorta, and so the outflow from the left ventricle is enforced as the input boundary condition.

All the simulations presented in this work are implemented with parameters estimated from *in-vivo* or *postmortem* published data. Consequently, the objective of the model is to produce quantitatively physiological results.

This chapter starts with an anatomical and physiological description of the cardiovascular system (Section 1.1), focusing on the haemodynamic quantities and mechanisms simulated by the 1-D model, such as the cardiac output generated by the heart (Section 1.1.1), the geometric and elastic properties of the systemic blood vessels (Section 1.1.2), and the physical properties of the blood (Section 1.1.3). Section 1.2 outlines the main physiological features of pressure and velocity pulse wave propagation that the 1-D model should be able to capture. Section 1.3 presents a

historical review of the main contributions to the understanding of the functioning of the system and its mathematical and numerical simulation. The chapter concludes by identifying the goals pursued by this thesis (Section 1.4) and outlining the strategy followed to achieve them (Section 1.5).

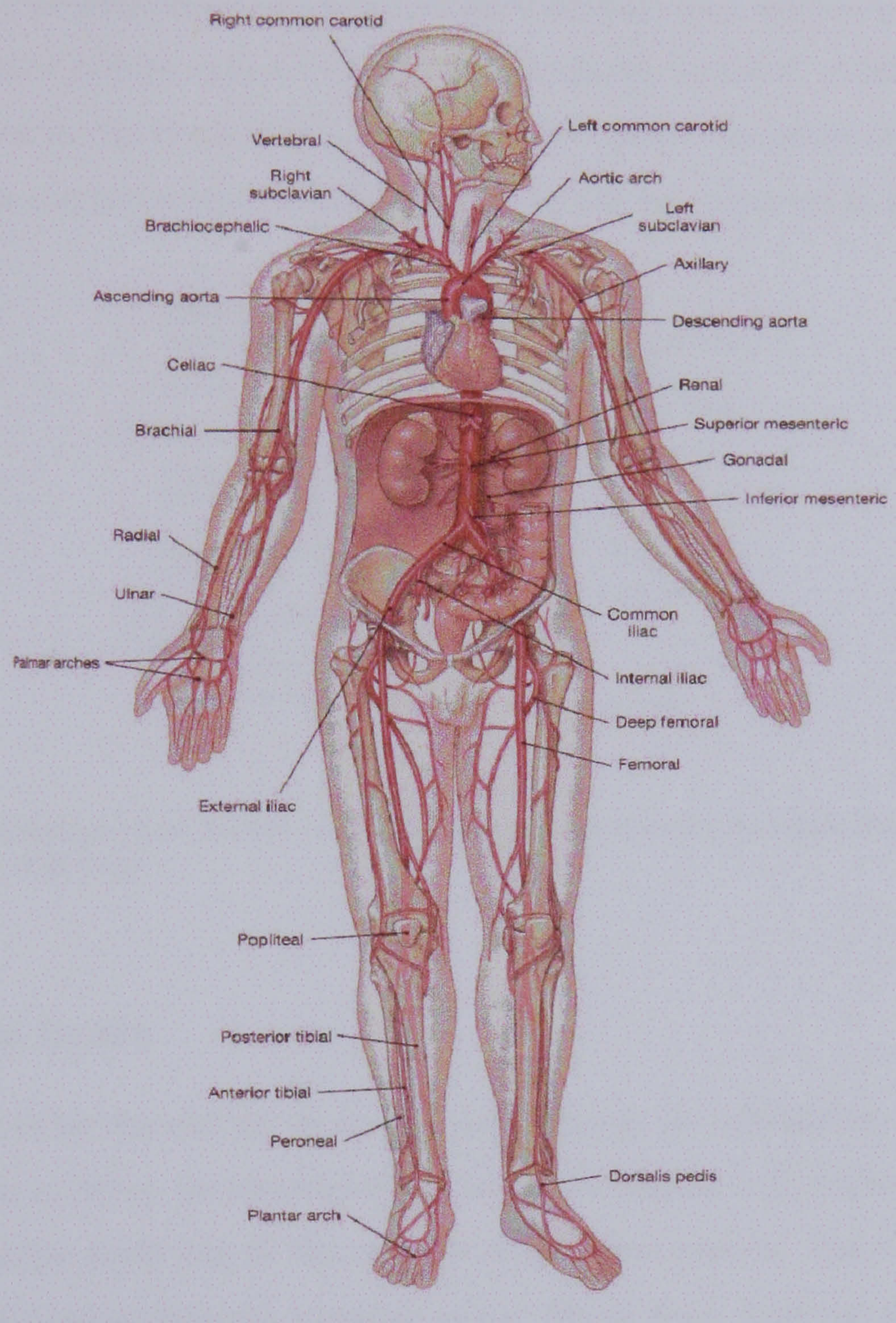


Figure 1.1: The heart and the main conduit arteries of the systemic circulation. (Image from Purves *et al* [71].)

1.1 Cardiovascular anatomy and physiology

The cardiovascular, or circulatory, system transports oxygen and nutrients to all the tissues of the body, from where it removes carbon dioxide and other harmful waste

products of cell metabolism. Although it performs several other functions, this work only simulates its transport by convection. From a physical point of view, the system consists of two synchronised pumps in parallel (the right and the left hearts) that propel a viscous liquid (the blood) through a network of flexible tubes (the arterial tree). The right heart pumps deoxygenated blood through the *pulmonary circulation* and the left heart pumps oxygen-rich blood through the *systemic circulation*. The model described in this thesis only accounts for the system formed by the left heart and the largest conduit arteries of the systemic circulation (depicted in Figure 1.1).

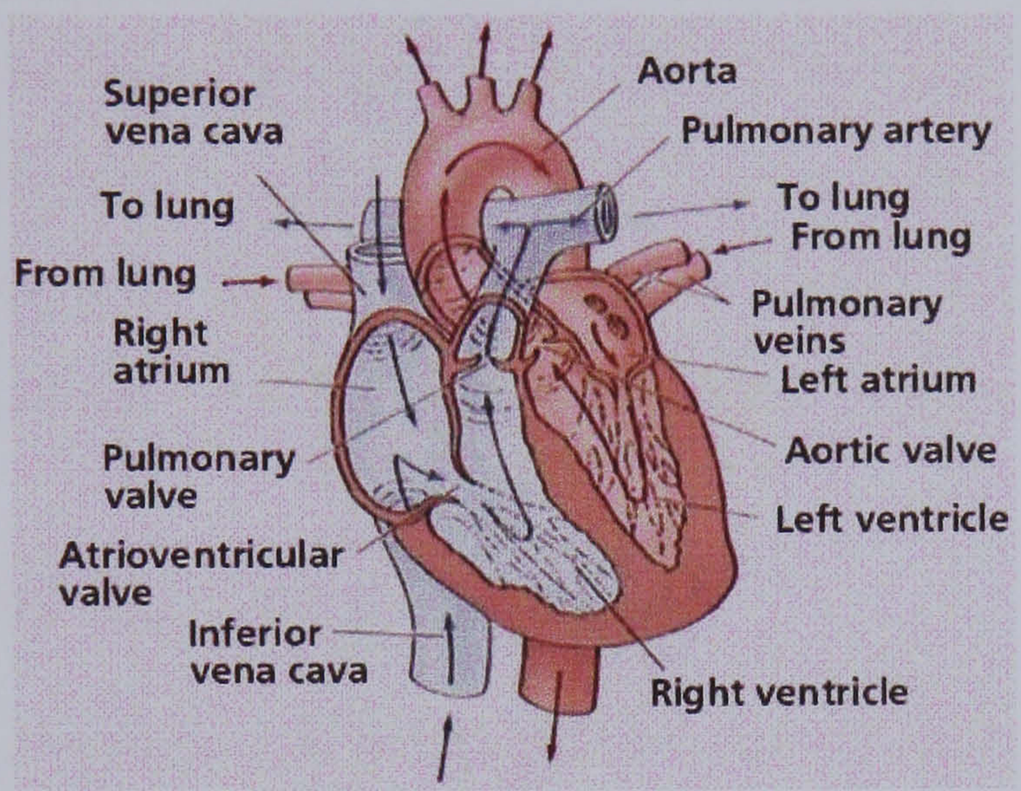


Figure 1.2: Structure of the human heart with the path described by the blood flow. (Image from Purves *et al* [71].)

1.1.1 The heart

The heart provides the energy to move blood through the circulatory system. It consists of four cavities: two ventricles and two atria (Figure 1.2), whose size varies during the cardiac cycle due to the activity of the heart muscle. The right atrium receives blood coming from the systemic veins. Blood flows from the right atrium to the right ventricle and out to the lungs through the pulmonary vessels. From the lungs it flows to the left atrium through the pulmonary veins, down into the left ventricle, and out to the aorta and the rest of the body through the systemic circulation. Four valves, one at the exit of each heart cavity, regulate blood flow in the heart and ensure bulk unidirectional motion through both pulmonary and systemic circulations. However, only the aortic valve at the exit of the left ventricle is part of the domain of the model presented in this thesis. The coronary arteries,

which originate from the aorta just above the aortic valve, are also neglected because pulse wave propagation in these arteries is considerably affected by the movement of the heart, which is not simulated in this work.

Each cardiac cycle consists of a systolic and a diastolic phase, with the latter lasting about twice the time of the former under resting conditions. During systole (contraction of the heart muscle) blood is pumped into the ascending aorta and during diastole (relaxation of the heart muscle) the aortic valve shuts and blood flows into the ventricular cavity from the atrium. In a healthy adult at rest, the duration of the cardiac cycle is about 0.85 s (approximately 70 beats/min) and each ventricle ejects about 70 ml of blood per stroke [92], which yields a *cardiac output* (amount of blood ejected from the left ventricle to the ascending aorta per unit of time) of about 5 l/min. The model described in this thesis considers the outflow from the heart at the ascending aorta as an input boundary condition.

1.1.2 The systemic blood vessels

The systemic circulation consists of a network of curved and branching vessels whose size decreases in the arteries, arterioles, and capillaries, and increases in the venules and veins. Arteries distribute blood throughout the body and maintain blood pressure between heartbeats, arterioles transport blood to capillary beds, capillaries diffuse oxygen and nutrients to cells, and venules collect deoxygenated blood from capillaries and return it to the heart through veins. Orders of magnitude of the number of each systemic vessel and the lumen calibre, wall thickness, total cross-sectional area, and percentage of the total blood volume contained in each type of systemic vessel are given in Table 1.1, according to data published by Gregg [30]. We observe that capillaries have the thinest wall and the largest total cross-sectional area to facilitate the diffusion of oxygen and nutrients to the surrounding tissues, and that about half of the total blood volume is contained in venules and veins.

As it can be observed in Figure 1.1, the topological pattern of the large systemic arteries is mainly a binary tree structure, with the exception of some arterial anastomoses (merging flow arterial bifurcations), such as the palmar arch in the hand. the plantar arch in the foot, and the circle of Willis in the cerebral circulation, and some arteriovenous anastomoses (union of an artery and a vein) in the skin and in the gut.

Table 1.1: Approximate number of each type of systemic vessel along with the approximate lumen calibre (D), wall thickness (h), total cross-sectional area (A_T), and percentage of the total blood volume (V) contained in each type of systemic vessel. The rest of the volume is contained in the heart (12%) and in the pulmonary circulation (18%). (From Gregg [30].)

Vessel	Aorta	Arteries	Arterioles	Capillaries	Venules	Veins	Vena cava
Number	1	10^2	10^7	10^{10}	10^9	10^2	1
D (mm)	25	4	0.03	0.008	0.02	5	30
h (mm)	2	1	0.02	0.001	0.002	0.5	1.5
A_T (cm^2)	5	20	400	4500	4000	40	18
V (%)	2	8	1	5	†	†	†

(†) Venules and veins contain 54% of the total blood volume.

Anastomoses are more frequent in smaller vessels. Arterioles, capillaries and venules are arranged in a dense network with many interconnections (Figure 1.3). According to Olufsen [62], the small systemic vessels are distributed in a structured way such that they cover the tissue evenly by minimising their volume and maximising their surface, to facilitate the diffusion of oxygen and nutrients to cells.

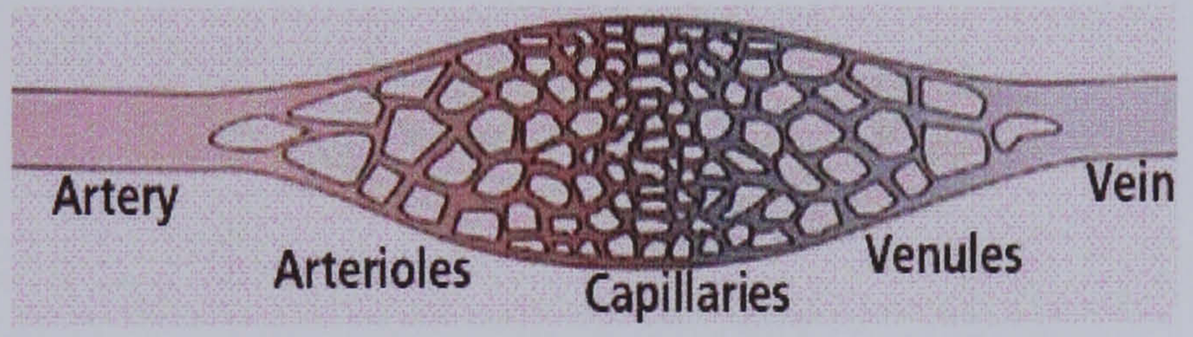


Figure 1.3: Typical arrangement of the arterioles, capillaries and venules linking an artery and a vein. (Image from Purves *et al* [71].)

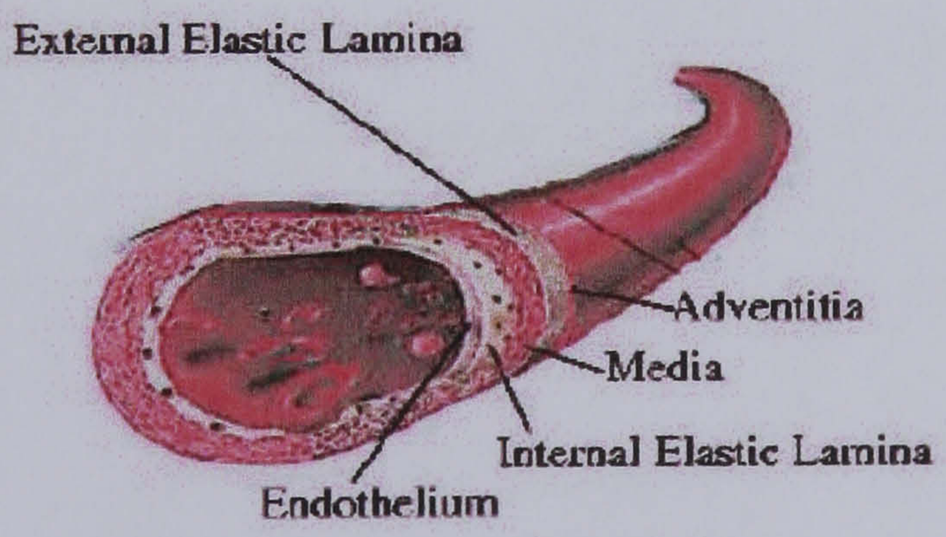


Figure 1.4: Main layers present in the wall of any blood vessel (except for capillaries). The endothelium is part of the intima. (Taken from the notes published by Formaggia and Veneziani [26].)

Every kind of blood vessel (except for the capillaries) contains the same structural components shown in Figure 1.4, though the proportions vary between vessel

types [13]. The inner part is called *intima* and consists of a monolayer of cells called *endothelium*. Next, we find the *internal elastic lamina* separating the intima from the *media*, which is usually the thickest layer and the one which shows the greatest variation in structure and properties between different regions of the circulation. The *external elastic lamina* is located between the media and the outer part or *adventitia*. Smooth muscle cells are present in the media and the external elastic lamina.

Arteries are able to expand and contract because they contain two elastic layers made up of two fibrous proteins: *elastin* and *collagen*. Elastin forms highly extensible elastic fibres and sheets, whereas collagen only forms fibres that are about 1000 times stiffer than elastin fibres. In the unstretched configuration of an artery, collagen fibres are normally kinked and bent. As pressure rises, an increasing number of collagen fibres reach their normal resting lengths, the smooth muscle contracts, and the arterial wall gets stiffer (Figure 1.5). Therefore, the elastic properties of arterial walls are non-linear. According to Tardy *et al* [90], viscoelastic effects are small within the physiological ranges of pressures.

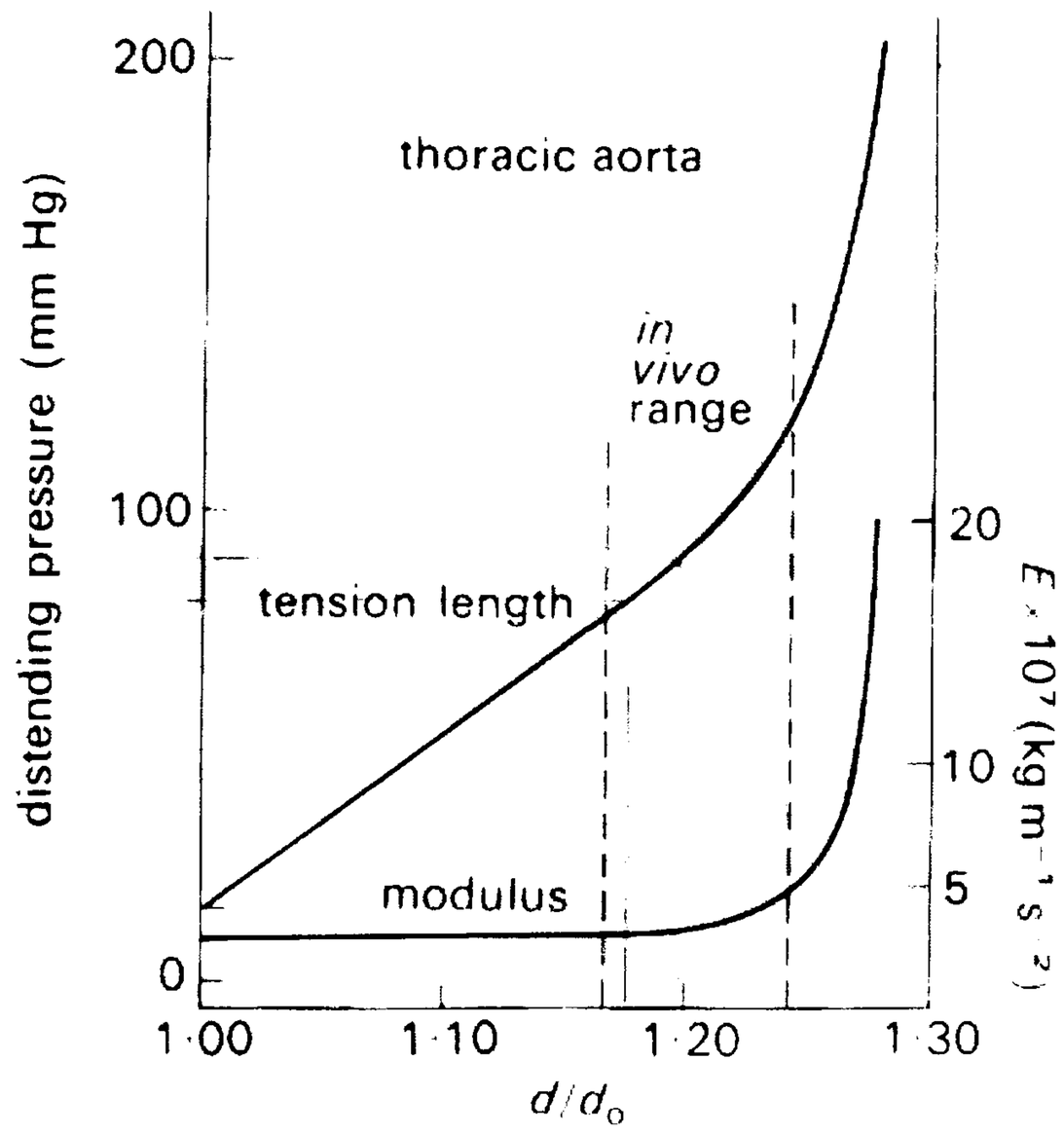


Figure 1.5: Pressure versus diameter (d) for a piece of artery of fixed length (d_o is the unstretched diameter). This is the typical non-linear behaviour of a systemic artery. The normal *in-vivo* range is highlighted by the two vertical dashed lines. The figure also shows the Young's modulus (E) relating circumferential stress to circumferential strain, which increases dramatically for distending pressures greater than their normal physiological range. (From McDonald [50].)

Large arteries have a thick media with a large proportion of elastic tissue, which make these vessels elastic and able to facilitate the windkessel effect described in Section 1.2. As we move away from the heart, arteries present a media with less elastic tissues and more layers of smooth muscle cells, so arteries become stiffer with the distance from the heart (their Young's modulus progressively increases). Recent experiments by Ioannou *et al* [39] with Yucatan miniature swine showed that about half of the total arterial compliance (ability of the arterial system to distend) is located in the proximal thoracic aorta. Arterioles have a smaller amount of elastic tissue than arteries, but more smooth muscle, which enables them to regulate the flow by constriction or dilatation of their lumen, producing important adjustments in the flow pattern of arteries.

In the long term, the systemic vessels can undergo chronic adaptations, such as wall remodelling and formation of functional collateral pathways. This is of paramount importance to maintain blood supply in case of lumen narrowing (*stenosis*), as will be shown in the studies of the palmar circulation (Chapter 4) and the cerebral circulation (Chapter 5).

1.1.3 The blood

Blood consists of an aqueous solution (*plasma*) which carries cells of varying sorts and sizes in suspension, as well as dissolved gases, salts, hormones, droplets of fat, energy-yielding molecules such as glucose, waste materials such as urea, and a wide variety of proteins involved in such functions as clotting and inflammatory responses [92]. These materials enter and leave the blood as it passes through the capillaries of the various organs. According to Caro *et al* [13], whole blood may be regarded, from a mechanical point of view, as consisting of flexible red cells suspended in a Newtonian fluid (the plasma). Therefore, red blood cells make blood non-Newtonian; i.e, its viscosity depends on shear rate.

Based on several experimental studies with human blood, Whitmore [97] showed that when the shear rate is about $1\,000\ s^{-1}$ (a typical value for many blood vessels *in-vivo*, according to Caro *et al* [13]), the non-Newtonian behaviour becomes insignificant and the apparent viscosity (the viscosity of blood as a whole) approaches an asymptotic value in the range $3 - 4$ mPa s. However, the apparent viscosity

increases slowly as the shear rate decreases and at a shear rate less than 1 s^{-1} it rises extremely steeply. Therefore, blood can be approximated as a Newtonian fluid (constant viscosity at all shear rates) when it flows within the large systemic arteries, but not in the small systemic vessels. Since more than 90% of the plasma is water [13] and the materials in suspension are several orders of magnitude smaller than the diameter of the systemic arteries, blood is also approximated as a homogeneous and incompressible fluid by the 1-D model, with, according to Pedley [68], a density of 1 050 Kg/m^3 and a viscosity of 4.0 mPa s (at 37°C).

We notice that blood has a similar density to water but its viscosity is more than twice the viscosity of water. Moreover, the previous assumptions are not valid to simulate blood flow in vessels beyond the systemic arteries, since the volume of blood cells becomes increasingly significant. In the capillaries, blood cells make up nearly half of the volume of the flowing blood (Figure 1.6).



Figure 1.6: Cross-sectional area of a capillary with a red blood cell inside (TEMx32,830). In the microcirculation, blood cells make up nearly half of the volume of the flowing blood. Hence, blood can not be simulated as a Newtonian fluid. (This image is copyright Dennis Kunkel at *www.DennisKunkel.com.*)

1.2 Propagation of pressure and flow waves

Pressure and flow (or velocity) waves are generated by the ventricular ejection and its interaction with the distensible arterial walls. In Section 1.1.3 we saw that arterial blood can be approximated as an incompressible fluid. Consequently, the aorta and the rest of the elastic arteries must distend to accommodate the sudden

increase in arterial blood volume caused by the contraction of the left ventricle during systole. Arterial distension starts at the ascending aorta and propagates down the arterial system producing continuous changes in the intralumenal pressures and blood velocities through all the arteries. When the elastic energy absorbed during distension is released, arteries contract, starting from the inlet of the ascending aorta and continuing in the same turn as they were expanded. Again, they produce continuous changes in their intralumenal pressures and blood velocities. Therefore, arteries present a regular beating, called the *pulse*, that follows the heartbeat and yields propagation of pressure and velocity changes, which can be studied as pressure and velocity waves running forth and back. Backward waves originate in the reflection of forward waves. The propagation speed of pulse waves relative to the blood at rest is called the *pulse wave velocity*, which is about 5 m/s at the ascending aorta, increasing up to 30 m/s at the peripheral arteries, and one or two orders of magnitude higher than blood velocity. With these orders of magnitude, a pulse wave has enough time to travel from the ascending aorta to the peripheral arterioles and get reflected back to the heart several times during a heartbeat. The mathematical formulation shown in Chapter 2 indicates that pulse wave velocity depends on the elastic modulus of the arterial wall, increasing with increasing elastic modulus.

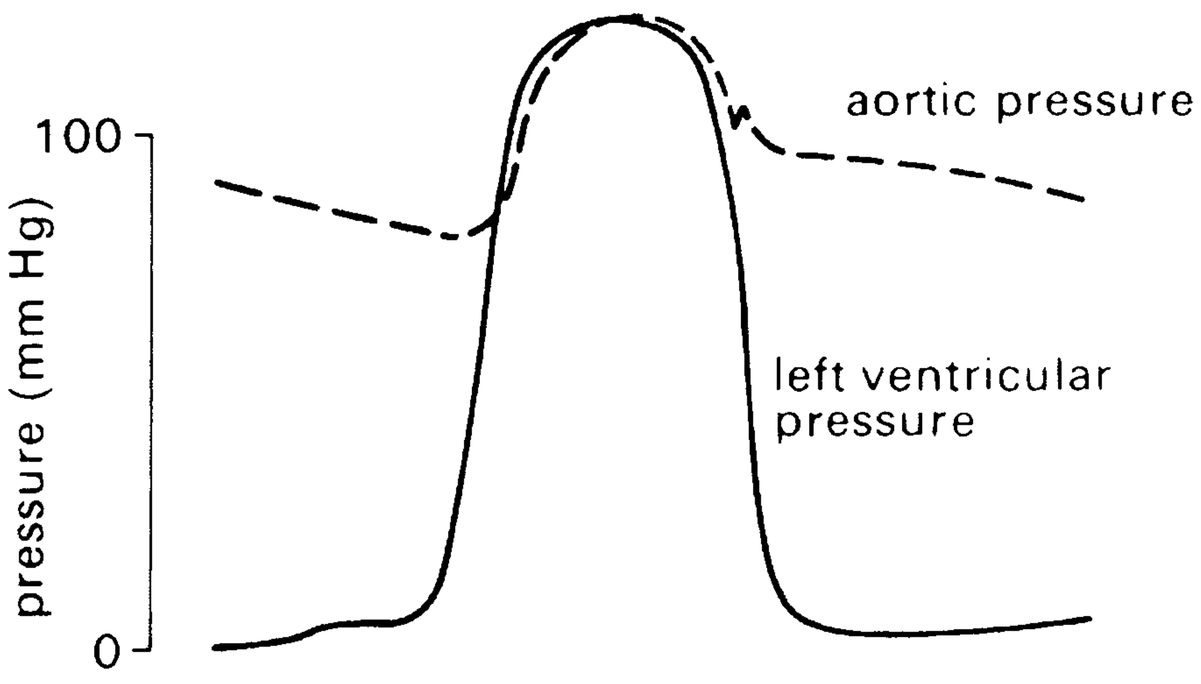


Figure 1.7: Typical pressure patterns in the aorta and the left ventricle during one cardiac cycle. The abrupt pressure pattern in the left ventricle is transformed into a smoother pattern in the aorta. (From Caro *et al* [13].)

The elasticity of the arterial walls is also responsible for transforming the discontinuous left ventricular pressure and cardiac output into a more steady and smooth pressure and flow in the aorta and the rest of the arterial system (Figures 1.7 and 1.8). We note that if arteries were rigid, pressure changes would occur

at the same time everywhere in the system, and the blood flow-rate into the system would always be equal to the blood flow-rate out. Therefore, blood flow would be zero during diastole. This smoothing mechanism is called the *windkessel effect* and was first described by Hales in 1733 with an air chamber (or windkessel in German) model (Figure 1.8). Frank put Hales' idea into mathematical form in 1899 [27], in which it is assumed that all pressure changes in the arteries occur synchronously and, hence, without accounting for pulse wave propagation.

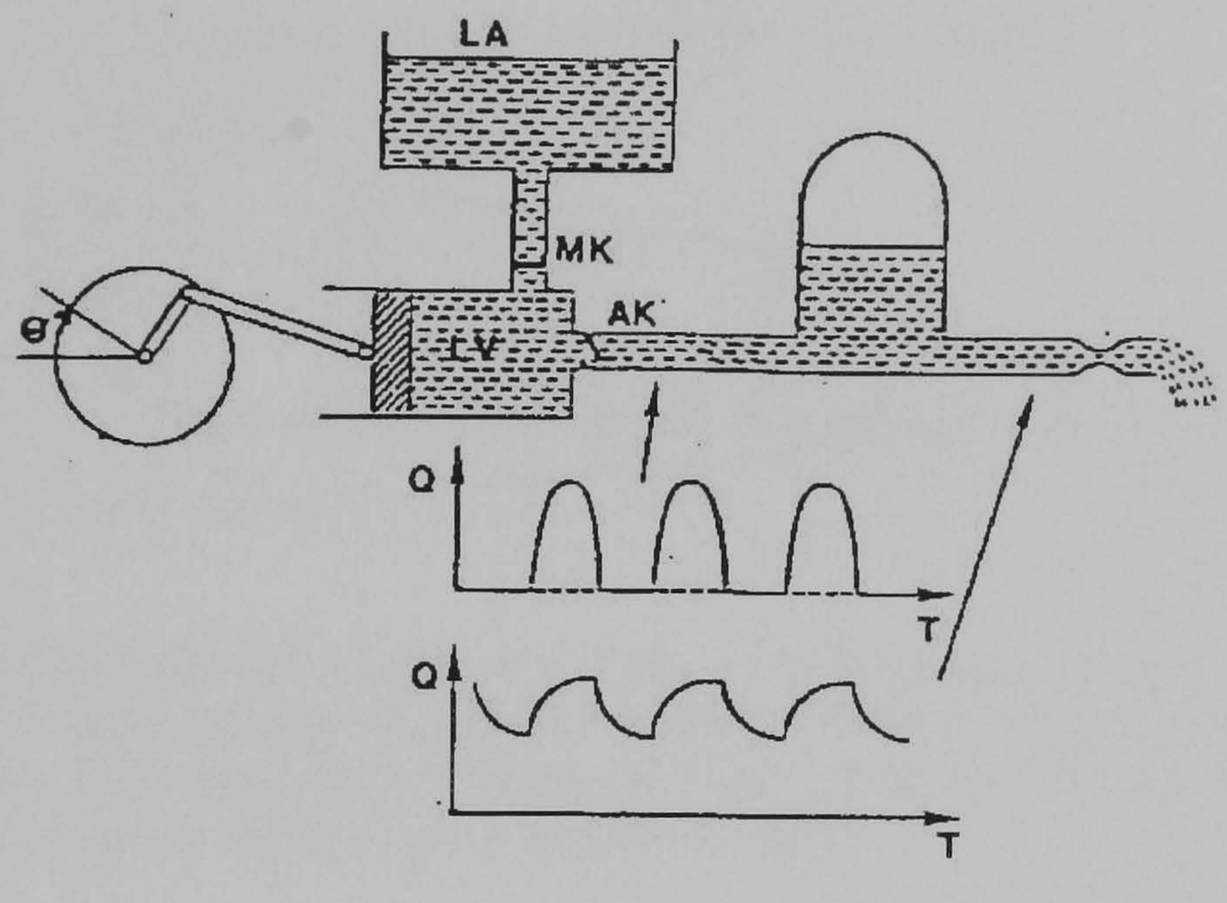


Figure 1.8: Diagram of the windkessel effect as described by Hales in 1733. The pulsatile inflow at the aortic valve (AK), caused by the contraction of the left ventricle (LV) while the mitral valve (MK) is closed, is transformed into a smoother outflow by the compliance of the arterial system represented by an air chamber. The left atrium (LA) is represented by a water reservoir. (Taken from the notes published by IBITECH [79].)

By the time blood reaches the capillary beds, its flow is relatively constant, steady and slow, which facilitates diffusive exchange of nutrients and waste products between the blood and the surrounding tissue. The windkessel effect has also the virtue of minimising the pulsatile power expenditure of the heart. Furthermore, it also facilitates the coronary flow (impeded during systole by the compression of the intramyocardial vessels) because the aortic pressure during diastole is kept at a high level.

Arterial pressure evolves between a maximum value, the *systolic pressure*, and a minimum value, the *diastolic pressure*. The *pulse pressure* is the difference between them. Pressure and velocity waveforms depend on both the performance of the heart and the characteristics of the arterial network. Their shape and amplitude vary along the systemic arteries, because of wave reflections at branch points, at

the aortic valve when shut, at sites of change in the geometric and elastic properties of the arterial wall (and, hence, in the pulse wave velocity), at arterioles, and because of viscous attenuation. Figure 1.9 shows the main features of pressure and velocity waveforms under normal conditions. At the ascending aorta, the systolic

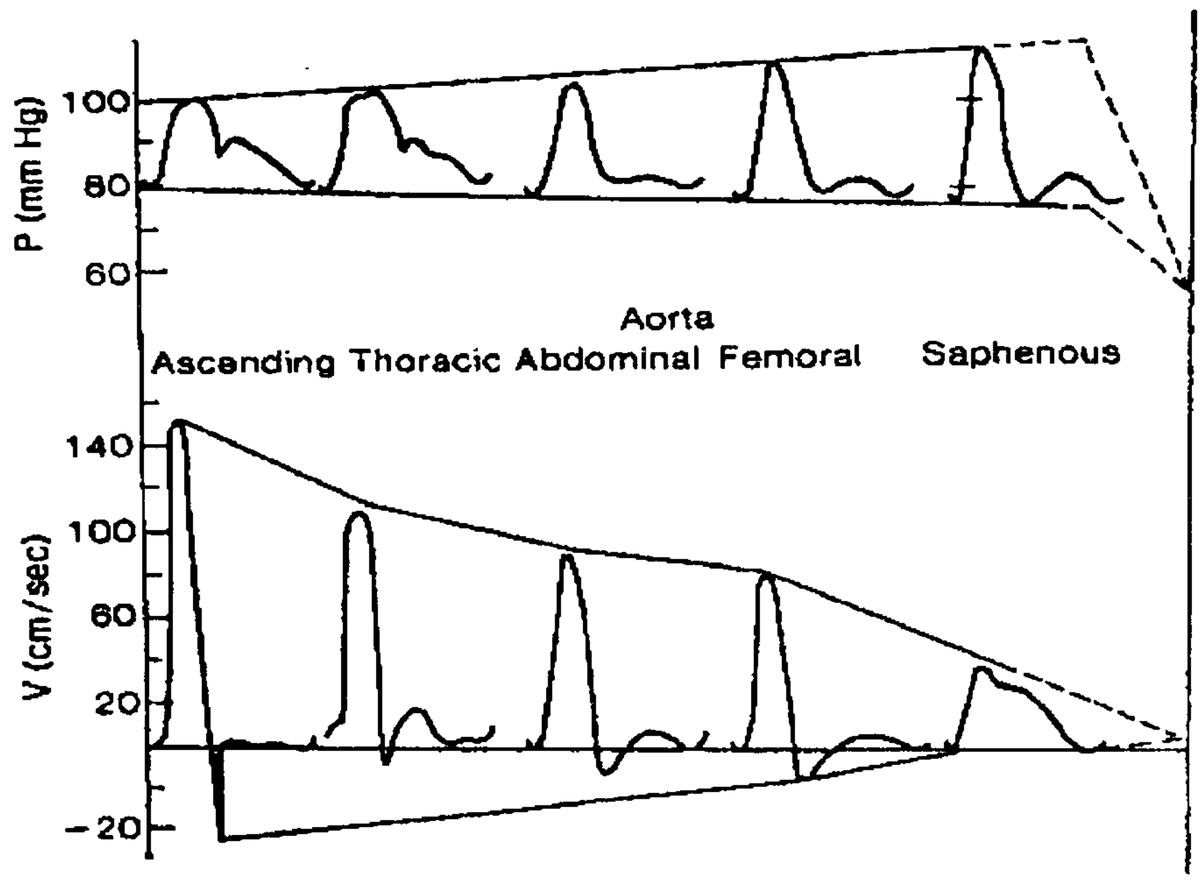


Figure 1.9: Qualitative pattern of pressure (top) and velocity (bottom) in various segments of the canine aorta and in arteries of the inferior limb. Pressure waves increase in amplitude and steepness with increasing distance from the heart, whereas velocity waves decrease in amplitude and increase in width. (After McDonald [50].)

ejection yields a sudden rise in pressure followed by a sharp drop. A second pressure peak is observed during diastole, which forms the so-called *dicrotic notch*, followed by a much smoother pressure decrease. The diastolic sharp peak disappears in the abdominal aorta and in the other systemic arteries as we move downstream the arterial network. Pulse pressure increases as we move away from the heart (*peaking phenomenon*), whereas mean pressure gradually decreases. Furthermore, the initial pressure increase is steeper and narrower in more peripheral locations (*wave steepening*). We also observe the formation of a second rear wave from the abdominal aorta to the saphenous artery. As we move away from the heart, the velocity wave is characterised by a reduction in amplitude and mean value, because of flow division at branching sites and increase in flow impedance, an increase in width and a decrease in reversal flow.

Pressure and velocity waveforms are altered by aging, vascular diseases, such as atherosclerosis, and invasive clinical procedures, some of them discussed in Chapters 4 and 5. Murgo *et al* [57] measured an increase in pulse pressure with age in human patients and Avolio *et al* [7] demonstrated that aging increases the stiffness

of the arterial wall, and, hence, decreases the ability of the windkessel effect to smooth the cardiac output.

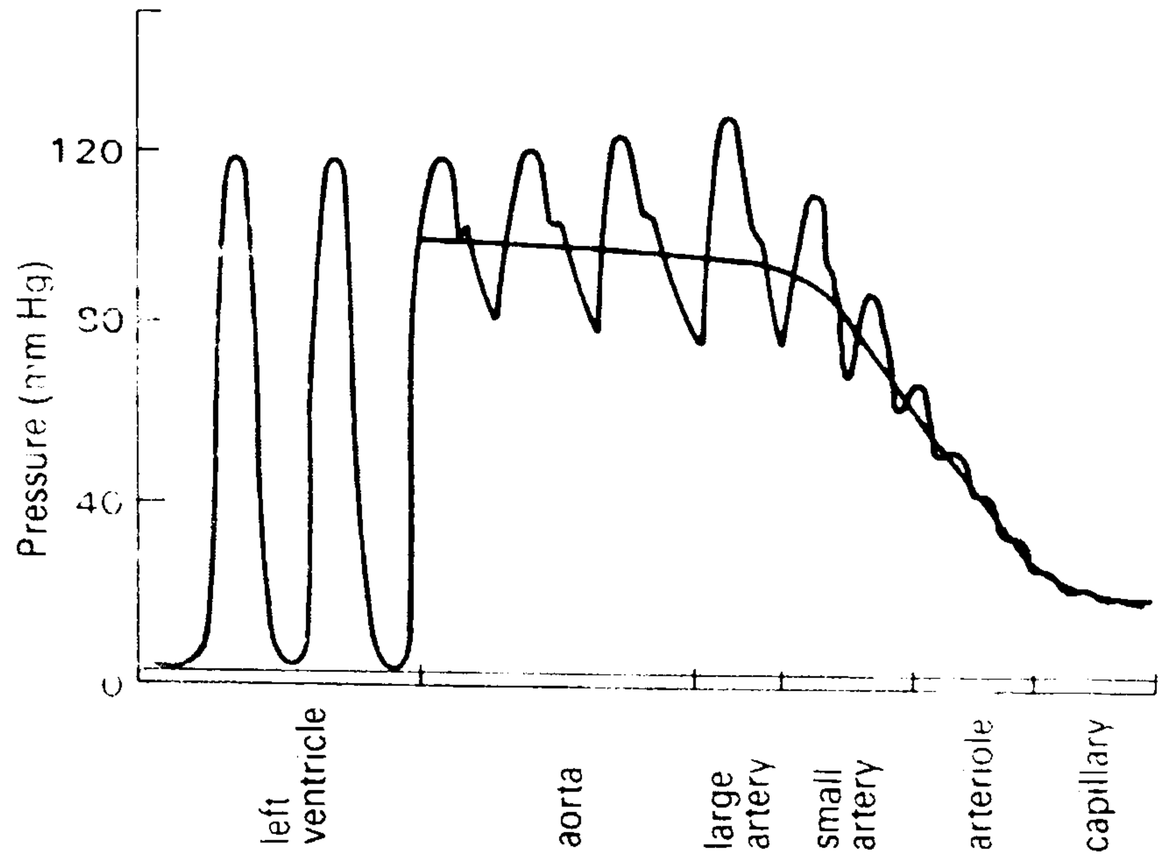


Figure 1.10: Waveforms and mean values of pressures in the systemic circulation. The greatest fall in pressure occurs across arterioles. (From Caro *et al* [13].)

Figure 1.10 shows indicative values of mean pressures in the systemic circulation. During diastole, the pressure in the left ventricle is close to zero and the aortic valve is held shut by a pressure difference of about 90 mmHg. In the ascending aorta, mean blood pressure is about 100 mmHg, with a systolic pressure of about 120 mmHg and a diastolic pressure of approximately 90 mmHg. In the arterioles, pressure drops sharply and the systolic and diastolic pressures gradually converge. By the time blood reaches the capillaries, the fluctuations are minor, and the pressure has gone down to about 35 mmHg. Pressure drops down to 20 mmHg at the venous ends of the capillaries, although it should be noted that the pressure drop per unit length of pipe is especially great in these relatively short vessels. Table 1.2 shows an estimated blood flow distribution among body parts in normal conditions, which can change significantly during exercise by constriction or dilatation of the arterioles.

Although the objective of this thesis is to simulate pulse wave propagation in the large systemic arteries, the effect of the small arteries, arterioles and capillaries have to be considered, since these vessels play an important role in the characteristics of pulse waves along the large systemic arteries. Therefore, the development of accurate terminal models to enforce appropriate outflow boundary conditions is of paramount importance to guarantee the accuracy of the 1-D model. Terminal models should account for the resistance to flow introduced mainly by the arterioles and capillaries

Table 1.2: Estimated blood flow distribution among body parts in normal conditions. (From Burton [12].)

Body part	% cardiac output
Brain	15
Heart muscle	5
Kidney	25
Muscle	20
Liver	15
Skin	10
Other viscera	10

(Figure 1.10), and the effects of blood inertia and arterial compliance of the vessels they simulate.

1.3 Brief historical review

Although Gallen (130 – 200 AD) had already studied the strength and frequency of the blood pulse, William Harvey (1578 – 1657) was the first to realise the cyclic movement of blood from the heart to the rest of the body and back to the heart through the veins. He also detected that the arterial pulse is passive and caused by the contraction of the heart, and he deduced the existence of the capillaries, which were discovered by Marcello Malpighi (1628 – 1694).

Reverend Stephen Hales (1677 – 1761) introduced the idea of the windkessel effect by comparing the heart and the arterial system to a medieval fire cart, in which the air filled chamber plays the role of the arterial compliance and the fire hose nozzle represents the peripheral resistance of the arterioles and capillaries (Figure 1.8). Otto Frank (1865 – 1944) described Hales' concept mathematically in 1899 [27]. Hales was also the first to measure arterial pressure in an animal and to show that the arterioles and capillaries contribute to the greatest flow resistance.

The first suitable mathematical model of pulse wave propagation was proposed by Leonhart Euler (1707 – 1783) in 1775 [21]. He derived the partial differential equations expressing the conversation of mass and momentum of an inviscid fluid, but, apparently, he did not recognise the wave-like nature of the blood flow and was not able to find a solution to his equations. Thomas Young (1773 – 1829)

first described scientifically the wave nature of the flow and proposed an intuitive relation between pulse wave speed and the elasticity of the arterial wall based on Newton's theory of sound in gases [100]. An equation for the wave speed in thin elastic vessels was independently derived by Moens [52] and Korteweg [44]. In 1860, Bernhard Riemann (1826 – 1866) provided the method of characteristics [74], which was crucial to solve the system of hyperbolic partial differential equations that governs wave propagation in one dimension.

Other important contributions to the field came from Newton (1642 – 1727), who provided the mathematical tools to treat fluid dynamics and introduced the concept of fluid viscosity, Daniel Bernoulli (1700 – 1782), who established the equation of potential and kinematic energy of a fluid, Fourier (1768 – 1830), who provided the tools to analyse periodic functions, and Hagen (1797 – 1884) and Poiseuille (1799 – 1869), with their experimental work relating mean flow and pressure gradient.

The equations introduced by Euler are weakly non-linear when applied to the simulation of blood flow under physiological conditions. Once linearised they are analogue to the electrical transmission line equations, which has led to several investigations of arterial flow in the frequency domain using Fourier techniques and assuming that the arterial system is in steady-state oscillation (Landes [45], Womersley [99], McDonald [50]). Noordergraaf *et al* [58, 59] constructed an analog model of the largest human systemic arteries, in which arteries were represented by interconnected segments consisting of a resistor in series with an inductor and a capacitor, the left ventricle was represented by a waveform synthesizer and the neglected vessels beyond the terminal branches were modelled by resistors. This model was improved by Westerhof *et al* in 1969 [96].

Later, computers were used to solve pulse wave propagation in the arterial system. Avolio [6] added extra vessels to Noordergraaf and Westerhof's model and solved it numerically based on the linear formulation in the frequency domain. On the other hand, we have non-linear simulations solved in the time-domain (Anliker *et al* [4], Raines *et al* [72], Schaaf and Abbrecht [75], Hughes [38], Pedley [68], Stergiopulos *et al* [88], Olufsen *et al* [63], Sherwin *et al* [82], Formaggia *et al* [25]). The key aspects of these models are the effects of non-linearities and viscous terms, the treatment of bifurcations, the inflow and outflow boundary conditions and the

validation of the results.

The pulse wave propagation phenomenon in the arterial system has also been studied by means of physical models, such as the anatomically correct 1:1 replica of the left heart and the 55 largest conduit arteries built by Segers *et al* [78] and used in this thesis to assess the accuracy of the 1-D model.

1.4 Motivation and objectives

The starting point of this research is an existing 1-D code to model pulse wave propagation within compliant vessels. The model is inviscid and with limited modelling of the neglected vessels beyond the 1-D terminal branches. To date only qualitative results of its ability have been obtained. This work aims at (i) enhancing the modelling capabilities by including viscous dissipation within an artery and more realistic models of the inflow and outflow boundary conditions, (ii) improving the interpretation of results assisted by a technique that separates forward and backward travelling waves, (iii) validating the code against experimental data, (iv) applying it to the study of blood flow in arterial networks with arterial anastomoses, including the palmar arch in the hand and the circle of Willis in the cerebral circulation, and (v) increasing the confidence in the code and its ability to be applied in a clinical environment by comparison with some clinical data. The final objective of this thesis is to develop a reliable and clinically relevant model to understand the performance of any arterial system in normal and pathological conditions, to assist in the diagnosis and therapy planning of diseases with a reasonable computational cost.

1.5 Organisation of the thesis

The anatomical and physiological description of blood flow in the systemic circulation have been described in this chapter. Chapter 2 contains a detailed explanation of the mathematical formulation used to simulate blood pressure and velocity pulse wave propagation in the large systemic arteries. In Chapter 3, the capabilities of the formulation are tested by running a simulation of a well-defined experimental 1:1 replica of the left heart and the main conduit systemic arteries, along with a model

of the human aorta. In the following chapters, the 1-D model is applied to study pulse wave propagation in parts of the systemic circulation with arterial anastomoses: the palmar arch is studied in Chapter 4 and the circle of Willis in Chapter 5. Finally, Chapter 6 summarises the thesis achievements and suggests directions for future work.

Chapter 2

Mathematical formulation

This chapter details the 1-D mathematical formulation of blood pressure and velocity pulse wave propagation in the systemic circulation. It starts by justifying the reduction of such a complex 3-D problem to a single dimension and discussing the main assumptions needed (Section 2.1). Next, the governing equations of the 1-D formulation are introduced (Section 2.2) and manipulated algebraically to obtain the pulse wave speed and the characteristic variables of the system (Section 2.3), and to separate forward and backward travelling waves (Section 2.4). The 1-D governing equations are also linearised to study the effect of non-linear terms on wave propagation (Section 2.5). Both linear and non-linear formulations are solved by means of the discontinuous Galerkin scheme (Section 2.6) with appropriate boundary conditions (Section 2.7), which are classified into inflow boundary conditions (Section 2.7.1), usually to account for the cardiac outflow, junction boundary conditions (Section 2.7.2), and terminal boundary conditions at the outlet of each 1-D terminal branch to account for the effect of the neglected arteries, arterioles and capillaries (Section 2.7.3). The linearised system of governing equations yields an analytical solution of wave reflection and transmission at junctions (Section 2.7.2), and integrated over space provides a lumped parameter description of the fluid resistance, compliance and inertia of the vessels not simulated by the 1-D formulation (Section 2.7.3). This chapter also proposes a method to determine the fluid resistance, compliance and inertia of the terminal lumped parameter models from the geometry and the elasticity of the 1-D terminal vessels (Section 2.8). The chapter concludes with some final remark (Section 2.9).

2.1 Assumptions and justification of the 1-D formulation

As we have seen in Chapter 1, the systemic circulation contains a very large number of vessels that makes a 3-D simulation of pulse wave propagation in all of them unfeasible because of the high computational cost. The complexity of the system is reduced by simulating the flow in one dimension and only in the largest conduit arteries.

Each artery is approximated by a 1-D impermeable tube of length l, centreline s, circular cross-sectional area $A(s,t)$ normal to s, and thickness $h(s)$, with uniform properties around the circumference (Figure 2.1, left). We notice that A is allowed to change in time, t, since the deformability of the arterial wall is a key characteristic of the performance of the system, as was explained in Section 1.2. Assuming that the curvature of s is everywhere small enough, the axial direction can be approximated by a Cartesian coordinate x (Figure 2.1, right) so that the problem can be described in one spatial dimension. This assumption is suitable in the large conduit arteries (except possibly for the aortic arch) because of their small curvature compared to their diameter.

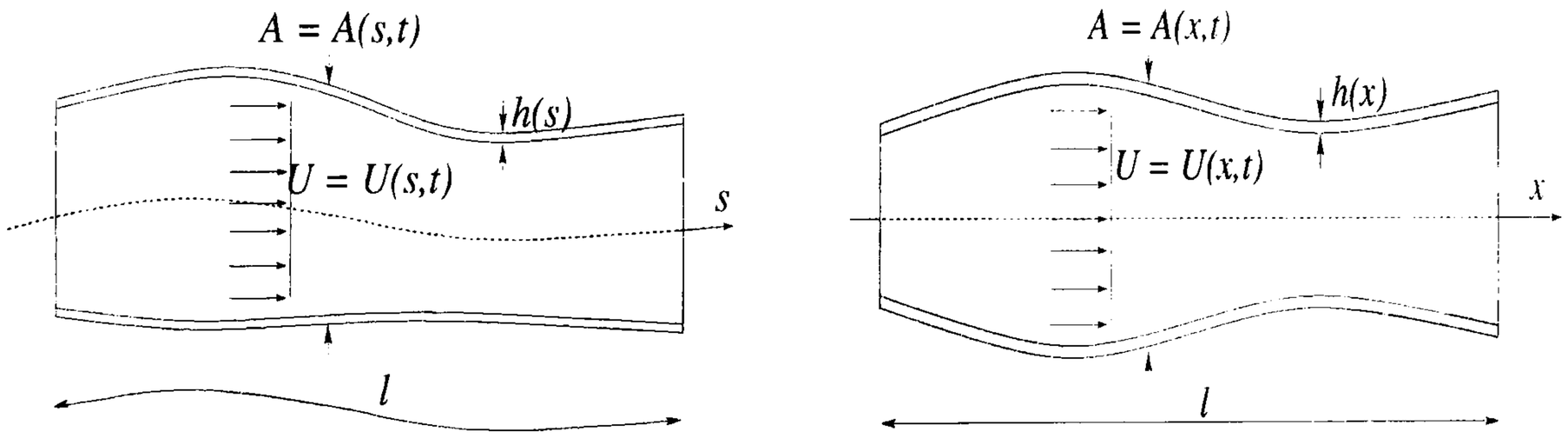


Figure 2.1: Layout of a 1-D compliant vessel. General orientation (left) and 1-D orientation (right).

The 1-D formulation permits the efficient simulation of the problem because the lengths of arterial pulse waves are large compared to arterial diameters (long wave approximation), so that wave propagation takes place mainly in the axial direction. However, it introduces some simplifications in blood flow and the mechanical description of the arterial wall that need to be discussed.

Blood flow is only described in the axial direction through $U(x,t)$, defined as the average velocity over the cross-section $A(x,t)$, $U = \frac{1}{R^2}\int_0^R 2ru\mathrm{d}r$, where r is

the radial coordinate, $R(x,t)$ is the radius of the lumen, and $u(x,r,t)$ is the axial velocity of each fluid particle (assumed to be axisymmetric) in the cross-section $A(x,t)$. *In-vivo* observations under normal conditions have shown that the velocity profile is relatively flat and uniaxial in the large arteries (Schultz *et al* [76]), even in the ascending aorta (Caro *et al* [13]), and it has a more parabolic shape in the peripheral arteries (Olufsen *et al* [63]).

During wall motion, arteries are assumed to be tethered in the longitudinal direction, with their central axis fixed, so that the arterial wall deforms only in the radial direction. The arterial wall is deformed by the action of the internal pressure, denoted by $p(x,t)$, which is considered to be constant over the cross-section of the lumen. This is consistent with the previous assumption that the radial velocity is small compared to the axial velocity, as showed by Smith *et al* [84]. The external pressure beyond the arterial wall is assumed to be constant in time and space and the action of any body force such as gravity is neglected.

The fluid resistance, compliance and inertia of the arteries, arterioles and capillaries not simulated by the 1-D model are taken into account by means of linear lumped parameter models (or 0-D models) in which pressure and flow rate are only time-dependent. They are coupled to the 1-D formulation through the boundary conditions.

In Section 1.1.3 we saw that blood can be modelled as a homogeneous, incompressible and Newtonian fluid in normal arterial flow. Hence, both blood viscosity, μ, and density, ρ, are considered to be constant and only dependent on temperature, which can be considered as a parameter without the need of a thermodynamic equation of state or an energy equation.

Finally, the blood flow is considered to be laminar, since Reynolds' numbers throughout the system are well below 2 000 in normal conditions (Zamir [101]).

2.2 Governing equations

Blood pressure and velocity pulse wave propagation within each artery is simulated as a coupling problem between blood flow and arterial wall displacement. Conservation of mass and momentum applied to a 1-D impermeable tubular and straight

control volume (Figure 2.1, right) of incompressible and Newtonian fluid yields the system of governing equations (see Sherwin *et al* [82] for a formal derivation)

$$\frac{\partial A}{\partial t} + \frac{\partial (AU)}{\partial x} = 0, \tag{2.1}$$

$$\frac{\partial U}{\partial t} + (2\alpha - 1)U\frac{\partial U}{\partial x} + (\alpha - 1)\frac{U^2}{A}\frac{\partial A}{\partial x} + \frac{1}{\rho}\frac{\partial p}{\partial x} = \frac{f}{\rho A}, \tag{2.2}$$

where $f(x,t)$ is the friction force per unit length and $\alpha(x,t)$ is a non-dimensional correction factor to account for the non-linearity of the sectional integration of the radial velocity profile across each section $A(x,t)$. In this work, α is assumed to be constant (which implies that the velocity profile is constant in shape) and is defined as

$$\alpha = \frac{1}{U^2 R^2}\int_0^R 2ru^2 \mathrm{d}r. \tag{2.3}$$

Equations (2.1) and (2.2) can also be derived by integrating the 3-D incompressible Navier-Stokes equations over a cross-section, as explained by Smith *et al* [84]. In either case, the shape of the radial velocity profile must be prescribed. This work uses a velocity profile of the form adopted by Smith *et al* [84]

$$u = U\frac{\gamma + 2}{\gamma}\left[1 - \left(\frac{r}{R}\right)^{\gamma}\right], \tag{2.4}$$

where γ is a constant. This profile satisfies the no-slip condition ($u|_{r=R} = 0$), it assumes axisymmetric flow ($\partial u/\partial r|_{r=0} = 0$), and satisfies $U = \frac{1}{R^2}\int_0^R 2ru\mathrm{d}r$. Substitution of (2.4) into (2.3) yields $\gamma = \frac{2-\alpha}{\alpha-1}$ and, hence, the velocity profile (2.4) can be expressed in terms of α as

$$u = U\frac{\alpha}{2 - \alpha}\left[1 - \left(\frac{r}{R}\right)^{\frac{2-\alpha}{\alpha-1}}\right]. \tag{2.5}$$

The value $\gamma = 9$ ($\alpha = 1.1$) is considered for the rest of this thesis, which is the value used by Smith *et al* [84] to give a compromise fit to experimental data obtained at different points in the cardiac cycle. Figure 2.2 shows the shape of this velocity profile compared to a parabolic profile ($\gamma = 2$).

Following Brook *et al* [11], the convective inertia terms $2(\alpha - 1)U\frac{\partial U}{\partial x}$ and $(\alpha - 1)\frac{U^2}{A}\frac{\partial A}{\partial x}$ of the momentum equation (2.2) are neglected. These terms account for the fact that the velocity profile is not flat and they are much smaller than the rest of the terms in the momentum equation, which is reduced to

$$\frac{\partial U}{\partial t} + U\frac{\partial U}{\partial x} + \frac{1}{\rho}\frac{\partial p}{\partial x} = \frac{f}{\rho A}. \tag{2.6}$$

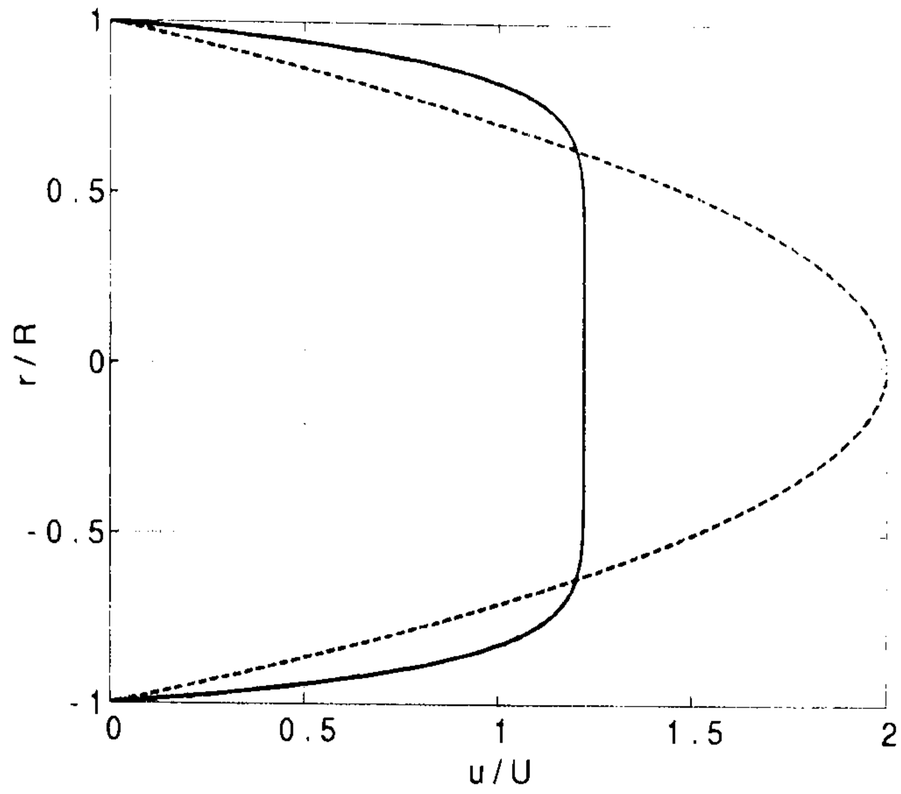


Figure 2.2: Shape of the velocity profile used by Smith *et al* [84] ($\gamma = 9$) (solid line) compared to a parabolic profile ($\gamma = 2$) (dashed line).

Integration of the incompressible 3-D Navier-Stokes equations provides the following expression for $f(x,t)$ (Smith *et al* [84])

$$f = 2\mu \frac{A}{R} \left[\frac{\partial u}{\partial r}\right]_R . \tag{2.7}$$

Substitution of (2.5) into (2.7) yields

$$f = -2\mu\pi \frac{\alpha}{\alpha - 1} U = -22\mu\pi U. \tag{2.8}$$

Equations (2.1) and (2.6) are completed with a pressure-area relationship or *tube law* $p = p(A; x, t)$. The tube law used in this work considers the lumen to be circular at any internal pressure and the arterial wall to be a linear, elastic and isotropic material with a small thickness compared to the vessel radius ($h \ll R$, as shown in Table 1.1), so that the external forces applied to the arterial wall are reduced to stresses acting in the circumferential direction. Therefore, Laplace's law applies and the circumferential tensile stress, σ, takes the form

$$\sigma = \frac{R_0 \left(p - p_0\right)}{h}, \tag{2.9}$$

with p_0 and R_0 the pressure and arterial radius at the reference state $(A, p, U) = (A_0, p_0, U_0)$. The corrresponding circumferential strain, ϵ, is [5]

$$\epsilon = \frac{1}{1 - \nu^2} \frac{R - R_0}{R_0}, \tag{2.10}$$

where ν is the Poisson's ratio, taken to be 1/2 since biological tissue is almost incompressible. Equations (2.9) and (2.10) are related through $\sigma = E\epsilon$, with $E(x)$

the Young's modulus in the circumferential direction, which leads to the tube law used in the 1-D model,

$$p = p_0 + \frac{\beta}{A_0}\left(\sqrt{A} - \sqrt{A_0}\right), \qquad \beta = \frac{\sqrt{\pi}hE}{(1-\nu^2)}, \tag{2.11}$$

where $\beta(x)$ is a space-dependent parameter related to the mechanical properties of the arterial wall. Although the arterial wall behaves as a non-linear elastic material (Section 1.1.2), linear elasticity is assumed in this work, which implies that the curves of pressure and Young's modulus in the physiological range of values (see Figure 1.5) are approximated by straight lines. It is also important to notice that $\partial p/\partial A$ decreases with increasing A in the tube law (2.11), contrary to the physiological behaviour observed in Figure 1.5, in which the arterial wall gets stiffer with increasing p. In the same figure we also note an increase in E with the increasing pressure. In this work, E is modelled constant in a given section x, but it can change along any artery to account for the increase in the stiffness of the arterial wall towards the periphery.

2.3 Characteristic analysis

With the tube law (2.11), the pressure gradient term in the momentum equation (2.6) takes the form

$$\frac{1}{\rho}\frac{\partial p}{\partial x} = \frac{1}{\rho}\left(\frac{\partial p}{\partial A}\frac{\partial A}{\partial x} + \frac{\partial p}{\partial \beta}\frac{\mathrm{d}\beta}{\mathrm{d}x} + \frac{\partial p}{\partial A_0}\frac{\mathrm{d}A_0}{\mathrm{d}x}\right),$$

and Equations (2.1) and (2.6) can be written in non-conservative form as

$$\frac{\partial \mathbf{U}}{\partial t} + \mathbf{H}\frac{\partial \mathbf{U}}{\partial x} = \mathbf{S}, \tag{2.12}$$

where

$$\mathbf{U} = \begin{bmatrix} A \\ U \end{bmatrix}, \quad \mathbf{H} = \begin{bmatrix} U & A \\ \frac{1}{\rho}\frac{\partial p}{\partial A} & U \end{bmatrix}, \quad \mathbf{S} = \begin{bmatrix} 0 \\ \frac{1}{\rho}\left(\frac{f}{A} - \frac{\partial p}{\partial \beta}\frac{\mathrm{d}\beta}{\mathrm{d}x} - \frac{\partial p}{\partial A_0}\frac{\mathrm{d}A_0}{\mathrm{d}x}\right) \end{bmatrix}.$$

Since $A > 0$ and $\frac{1}{\rho}\frac{\partial p}{\partial A} > 0$, $\mathbf{H}$ has two real eigenvalues, $\lambda_{f,b} = U \pm c$, where

$$c = \sqrt{\frac{A}{\rho}\frac{\partial p}{\partial A}} \tag{2.13}$$

is the pulse wave speed of the system. Under physiological flow conditions. c is around one order of magnitude higher than U. Therefore, $\lambda_f > 0$ and $\lambda_b < 0$. The matrix $\mathbf{H}$ can be written as

$$\mathbf{H} = \mathbf{L}^{-1}\mathbf{\Lambda}\mathbf{L}, \tag{2.14}$$

where

$$\mathbf{L} = \zeta \begin{bmatrix} \frac{c}{A} & 1 \\ -\frac{c}{A} & 1 \end{bmatrix}, \quad \mathbf{\Lambda} = \begin{bmatrix} \lambda_f & 0 \\ 0 & \lambda_b \end{bmatrix},$$

and ζ is an arbitrary scaling factor. Substitution of (2.14) into (2.12) and premultiplication of (2.12) by $\mathbf{L}$ yields

$$\mathbf{L}\frac{\partial \mathbf{U}}{\partial t} + \mathbf{\Lambda}\mathbf{L}\frac{\partial \mathbf{U}}{\partial x} = \mathbf{L}\mathbf{S}. \tag{2.15}$$

With the change of variables

$$\frac{\partial \mathbf{W}}{\partial \mathbf{U}} = \mathbf{L}, \tag{2.16}$$

where $\mathbf{W} = [W_f\,, W_b]^T$ is the vector of characteristic or Riemann variables, System (2.15) reduces to

$$\frac{\partial \mathbf{W}}{\partial t} + \mathbf{\Lambda}\frac{\partial \mathbf{W}}{\partial x} = \mathbf{L}\mathbf{S}. \tag{2.17}$$

If we define $\hat{x}(t)$ as a parametric function $\hat{x} = \hat{x}(t)$ in the (x, t) space, then the variation of $\mathbf{W}$ along the path $\hat{x}(t)$ is written as

$$\frac{\mathrm{d}\mathbf{W}(\hat{x}(t), t)}{\mathrm{d}t} = \frac{\partial \mathbf{W}}{\partial t} + \frac{\mathrm{d}\hat{x}}{\mathrm{d}t}\mathbf{I}\frac{\partial \mathbf{W}}{\partial \hat{x}}. \tag{2.18}$$

Comparison of (2.17) and (2.18) shows that if $\frac{\mathrm{d}\hat{x}}{\mathrm{d}t}\mathbf{I} = \mathbf{\Lambda}$, then

$$\frac{\mathrm{d}\mathbf{W}}{\mathrm{d}t} = \mathbf{L}\mathbf{S} \tag{2.19}$$

along the path $\hat{x}(t)$; i.e, $\mathbf{W}(\hat{x}(t), t)$ depends only on its initial value and on the integration of $\frac{\mathrm{d}\mathbf{W}}{\mathrm{d}t}$ along $\hat{x}(t)$. Therefore, $\hat{x}(t)$ defines the characteristic paths along which the information contained in $\mathbf{W}$ propagates in the (x, t) space. According to $\frac{d\hat{x}}{dt}\mathbf{I} = \mathbf{\Lambda}$, there are two characteristic paths, C_f and C_b, defined by

$$C_{f,b} \equiv \frac{\mathrm{d}\hat{x}_{f,b}}{\mathrm{d}t} = \lambda_{f,b} = U \pm c. \tag{2.20}$$

The characteristic analysis shows that the 1-D governing equations (2.1) and (2.6) combined with the tube law (2.11) form a system of non-linear hyperbolic partial differential equations. In the (x, t) space, W_f and W_b propagate along the

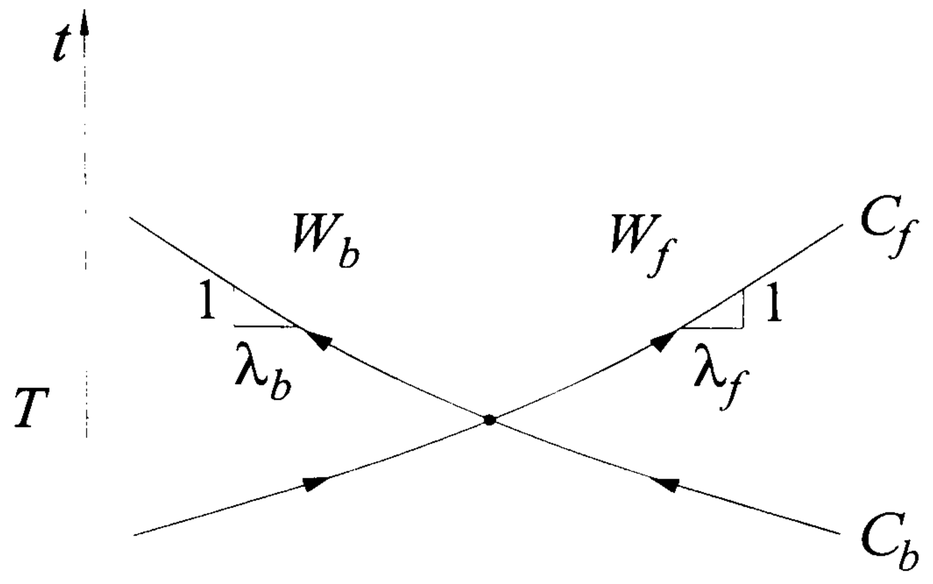


Figure 2.3: In the (x,t) space, every point (X,T) of the domain is intersected by a unique pair of characteristic curves C_f and C_b. W_f moves along C_f and carries pressure and velocity information in the positive direction of x. Similarly, W_b travels along C_b carrying the same information in the negative direction of x.

paths C_f and C_b at speeds λ_f and λ_b, respectively (Figure 2.3), changing their value because of viscous dissipation and geometric and elastic changes according to (2.19). Since $U \ll c$, W_f propagates changes in pressure and velocity from proximal to distal parts of the arterial system (i.e., the forward direction), whereas W_b carries pressure and velocity information from distal to proximal parts (i.e., the backward direction). We notice that if $f = 0$ and β and A_0 are constant along x, then $\mathbf{S} = \mathbf{0}$, which implies that System (2.17) is decoupled and that W_f and W_b are constant along C_f and C_b, respectively, according to (2.19).

To satisfy the Cauchy-Riemann condition, $\frac{\partial^2 W_{f,b}}{\partial A\,\partial U} = \frac{\partial^2 W_{f,b}}{\partial U \partial A}$, the value of ζ in $\mathbf{L}$ (2.14) must be constant. This thesis considers $\zeta = 1$. The characteristic variables W_f and W_b are determined by integration of (2.16),

$$W_{f,b} = U - U_0 \pm \int_{A_0}^{A} \frac{c}{A} \mathrm{d}A. \tag{2.21}$$

Considering the tube law (2.11) and the expression for the wave speed (2.13) we obtain

$$W_f = U - U_0 + 4\left(c - c_0\right), \tag{2.22}$$

$$W_b = U - U_0 - 4\left(c - c_0\right), \tag{2.23}$$

with

$$c = \sqrt{\frac{\beta}{2\rho A_0}} A^{1/4}, \tag{2.24}$$

and

$$c_0 = \sqrt{\frac{\beta}{2\rho}} A_0^{-1/4}. \tag{2.25}$$

2.4 Wave separation

A better interpretation of pressure and flow time histories measured at any point in the arterial system can be achieved by separating the forward and backward contributions that produced them. The separation technique described in this section is based on the work by Parker and Jones [67], which takes into account non-linear effects due to the convective acceleration and the non-linear dependence of p on A.

According to the change of variables (2.16), the variation of the Riemann functions, $\mathrm{d}\mathbf{W}$, is related to the variation of area and velocity, $\mathrm{d}\mathbf{U}$, through

$$\mathrm{d}\mathbf{W} = \mathbf{L}\mathrm{d}\mathbf{U}. \tag{2.26}$$

If β and A_0 can be considered to be constant in a neighbourhood of the measurement site, Equation (2.13) yields $c = \frac{A}{\rho c}\frac{\mathrm{d}p}{\mathrm{d}A}$, so that Equation (2.26) produces

$$\mathrm{d}W_f = \mathrm{d}U + \frac{\mathrm{d}p}{\rho c}, \tag{2.27}$$

$$\mathrm{d}W_b = \mathrm{d}U - \frac{\mathrm{d}p}{\rho c}. \tag{2.28}$$

Solving for $\mathrm{d}p$ and $\mathrm{d}U$ we obtain

$$\mathrm{d}p = \rho c \frac{\mathrm{d}W_f - \mathrm{d}W_b}{2}, \tag{2.29}$$

$$\mathrm{d}U = \frac{\mathrm{d}W_f + \mathrm{d}W_b}{2}. \tag{2.30}$$

Since in Section 2.3 we observed that W_f propagates changes in area (or pressure) and velocity forwards and W_b propagates them backwards, the forward, $\mathrm{d}p_f$, and the backward, $\mathrm{d}p_b$, contributions to $\mathrm{d}p$ are defined as

$$\mathrm{d}p_f = \rho c \frac{\mathrm{d}W_f}{2}, \tag{2.31}$$

$$\mathrm{d}p_b = -\rho c \frac{\mathrm{d}W_b}{2}, \tag{2.32}$$

and the forward, $\mathrm{d}U_f$, and the backward, $\mathrm{d}U_b$, contributions to $\mathrm{d}U$ as

$$\mathrm{d}U_f = \frac{\mathrm{d}W_f}{2}, \tag{2.33}$$

$$\mathrm{d}U_b = \frac{\mathrm{d}W_b}{2}. \tag{2.34}$$

Substitution of (2.27) and (2.28) into (2.31) to (2.34) leads to

$$\mathrm{d}p_{f,b} = \frac{1}{2}\left(\mathrm{d}p \pm \rho c \mathrm{d}U\right), \tag{2.35}$$

$$\mathrm{d}U_{f,b} = \frac{1}{2}\left(\mathrm{d}U \pm \frac{\mathrm{d}p}{\rho c}\right). \tag{2.36}$$

Finally, forward and backward pressure contributions, $p_{f,b}$, and forward and backward velocity contributions, $U_{f,b}$, at a point x can be determined by integrating in time the changes in pressure $\mathrm{d}p_{f,b}$ and velocity $\mathrm{d}U_{f,b}$

$$p_f = \int_{p_f(0)}^{p_f(t')} \mathrm{d}p_f, \quad p_b = \int_{p_b(0)}^{p_b(t')} \mathrm{d}p_b, \tag{2.37}$$

$$U_f = \int_{U_f(0)}^{U_f(t')} \mathrm{d}U_f, \quad U_b = \int_{U_b(0)}^{U_b(t')} \mathrm{d}U_b. \tag{2.38}$$

2.5 Linearisation of the governing equations

System (2.12) is not linear because of the convective term $U\frac{\partial U}{\partial x}$ in the momentum equation, the non-linear dependence of p on A through the tube law (2.11), and the non-linear viscous term $\frac{f}{\rho A}$. If we perturb a reference state $(A, p, U) = (A_0, 0, 0)$ with small amounts Δa, Δp and Δu, and ignore quadratic terms, System (2.12) reduces to

$$\frac{\partial \Delta \mathbf{U}}{\partial t} + \mathbf{H}_0 \frac{\partial \Delta \mathbf{U}}{\partial x} = \mathbf{S}_0, \tag{2.39}$$

where,

$$\Delta \mathbf{U} = \begin{bmatrix} \Delta a \\ \Delta u \end{bmatrix}, \quad \mathbf{H}_0 = \begin{bmatrix} 0 & A_0 \\ \frac{\beta}{2\rho A_0^{3/2}} & 0 \end{bmatrix}, \quad \mathbf{S}_0 = \begin{bmatrix} 0 \\ \frac{1}{\rho}\left(\frac{f_0}{A_0} - \frac{\partial \Delta p}{\partial \beta}\frac{\mathrm{d}\beta}{\mathrm{d}x} - \frac{\partial \Delta p}{\partial A_0}\frac{\mathrm{d}A_0}{\mathrm{d}x}\right) \end{bmatrix},$$

and $f_0 = -22\mu\pi\Delta u$. We notice that $\frac{\partial \Delta p}{\partial \Delta a}$ have been approximated by $\frac{\partial \Delta p}{\partial \Delta a}\big|_{\Delta a = 0} = \frac{\beta}{2A_0^{3/2}}$, which yields

$$\Delta p = \frac{\beta}{2A_0^{3/2}}\Delta a = \frac{\rho\left(c_0\right)^2}{A_0}\Delta a, \tag{2.40}$$

with c_0 defined by (2.25).

The characteristic analysis of System (2.39) provides the linear characteristic functions ΔW_f and ΔW_b,

$$\Delta W_f = \Delta u + \frac{c_0}{A_0}\Delta a, \tag{2.41}$$

$$\Delta W_b = \Delta u - \frac{c_0}{A_0}\Delta a, \tag{2.42}$$

which propagate in the (x,t) space at constant speeds $+c_0$ and $-c_0$, respectively. The characteristic paths are straight lines defined by

$$C_{f,b} \equiv \frac{\mathrm{d}\hat{x}_{f,b}}{\mathrm{d}t} = \pm c_0. \tag{2.43}$$

2.6 Numerical solution: the discontinuous Galerkin formulation

The non-linear system of 1-D governing equations (2.12) is solved by means of a discontinuous Galerkin scheme, with a high-order 1-D spectral/hp element spatial discretisation. This scheme is suitable for the 1-D formulation because it can propagate waves of different frequencies without suffering from excessive dispersion and diffusion errors [42]. Section 2.6.2 explains the adjustments needed to solve the linear system of 1-D governing equations (2.39).

To start, the domain of each artery, $\Omega = [0, l]$, is discretized into a mesh of N_{el} non-overlapping elemental regions $\Omega_e = [x_e^L, x_e^R]$, $e = 1, \ldots, N_{el}$, such that $x_e^R = x_{e+1}^L$ for $e = 1, \ldots, N_{el} - 1$, and $\bigcup_{e=1}^{N_{el}} \Omega_e = \Omega$. The superscripts L and R refer to the left and right boundaries of each elemental region Ω_e. Next, System (2.12) is written in conservative form as

$$\frac{\partial \mathbf{U}}{\partial t} + \frac{\partial \mathbf{F}}{\partial x} = \mathbf{S}, \tag{2.44}$$

where

$$\mathbf{U} = \begin{bmatrix} U_1 \\ U_2 \end{bmatrix} = \begin{bmatrix} A \\ U \end{bmatrix}, \qquad \mathbf{F}(\mathbf{U}) = \begin{bmatrix} F_1 \\ F_2 \end{bmatrix} = \begin{bmatrix} AU \\ \frac{U^2}{2} + \frac{p}{\rho} \end{bmatrix},$$

$$\mathbf{S}(\mathbf{U}) = \begin{bmatrix} S_1 \\ S_2 \end{bmatrix} = \begin{bmatrix} 0 \\ \frac{1}{\rho}\left(\frac{f}{A} - \frac{\partial p}{\partial \beta}\frac{\mathrm{d}\beta}{\mathrm{d}x} - \frac{\partial p}{\partial A_0}\frac{\mathrm{d}A_0}{\mathrm{d}x}\right) \end{bmatrix}.$$

We note that the vector $\mathbf{F}(\mathbf{U})$ contains the volume flux and the energy per unit of mass, and $\mathbf{S}(\mathbf{U})$ is a source term.

The weak form of the system is obtained by multiplying (2.44) by a vector of test functions $\mathbf{\Phi}$ and integrating over the domain Ω; i.e.,

$$\left(\frac{\partial \mathbf{U}}{\partial t}, \mathbf{\Phi}\right)_\Omega + \left(\frac{\partial \mathbf{F}}{\partial x}, \mathbf{\Phi}\right)_\Omega = (\mathbf{S}, \mathbf{\Phi})_\Omega, \tag{2.45}$$

where

$$(\mathbf{u}, \mathbf{v})_\Omega = \int_\Omega \mathbf{u}\,\mathbf{v}\,\mathrm{d}x \tag{2.46}$$

is the standard $\mathcal{L}^2(\Omega)$ inner product. The integrals of the weak form (2.45) are decomposed into the elemental regions Ω_e, $e = 1, \ldots, N_{el}$, to obtain

$$\sum_{e=1}^{N_{el}} \left[\left(\frac{\partial \mathbf{U}}{\partial t}, \mathbf{\Phi} \right)_{\Omega_e} + \left(\frac{\partial \mathbf{F}}{\partial x}, \mathbf{\Phi} \right)_{\Omega_e} \right] = \sum_{e=1}^{N_{el}} (\mathbf{S}, \mathbf{\Phi})_{\Omega_e} . \tag{2.47}$$

Integration of the second term of (2.47) by parts leads to

$$\sum_{e=1}^{N_{el}} \left[\left(\frac{\partial \mathbf{U}}{\partial t}, \mathbf{\Phi} \right)_{\Omega_e} - \left(\mathbf{F}, \frac{\mathrm{d}\mathbf{\Phi}}{\mathrm{d}x} \right)_{\Omega_e} + [\mathbf{F} \cdot \mathbf{\Phi}]_{x_e^L}^{x_e^R} \right] = \sum_{e=1}^{N_{el}} (\mathbf{S}, \mathbf{\Phi})_{\Omega_e} . \tag{2.48}$$

Next, the solution $\mathbf{U}(x,t)$ is approximated by a discretized expansion denoted by $\mathbf{U}^\delta(x,t)$. Following the traditional Galerkin approach, the test functions $\mathbf{\Phi}(x)$ are chosen to be in the same discrete space as the numerical solution $\mathbf{U}^\delta$; i.e, they are approximated by $\mathbf{\Phi}^\delta(x)$. The expansion basis are chosen to be polynomials of degree P on each elemental region Ω_e. We notice that $\mathbf{U}^\delta$ and $\mathbf{\Phi}^\delta$ are not required to be C^0 continuous at the interface of every elemental region, although they must be continuous within each elemental region, in which they are denoted as $\mathbf{U}_e^\delta$ and $\mathbf{\Phi}_e^\delta$. To obtain a global solution in the domain Ω, information must propagate between elemental regions Ω_e. This is achieved by upwinding the boundary flux in the third term of Equation (2.48), which will be explained in Section 2.6.1. Denoting the upwinded flux as $\mathbf{F}^u$, the discrete weak formulation can be written in Greens form as

$$\sum_{e=1}^{N_{el}} \left[\left(\frac{\partial \mathbf{U}_e^\delta}{\partial t}, \mathbf{\Phi}_e^\delta \right)_{\Omega_e} - \left(\mathbf{F}(\mathbf{U}_e^\delta), \frac{\mathrm{d}\mathbf{\Phi}_e^\delta}{\mathrm{d}x} \right)_{\Omega_e} + [\mathbf{F}^u \cdot \mathbf{\Phi}_e^\delta]_{x_e^L}^{x_e^R} \right] = \sum_{e=1}^{N_{el}} \left(\mathbf{S}(\mathbf{U}_e^\delta), \mathbf{\Phi}_e^\delta \right)_{\Omega_e} . \tag{2.49}$$

The second term is once again integrated by parts to have a derivative on $\mathbf{U}_e^\delta$ rather than on $\mathbf{\Phi}_e^\delta$, which leads to the divergence form

$$\sum_{e=1}^{N_{el}} \left[\left(\frac{\partial \mathbf{U}_e^\delta}{\partial t}, \mathbf{\Phi}_e^\delta \right)_{\Omega_e} + \left(\frac{\partial \mathbf{F}(\mathbf{U}_e^\delta)}{\partial x}, \mathbf{\Phi}_e^\delta \right)_{\Omega_e} + [[\mathbf{F}^u \dot{-} \mathbf{F}(\mathbf{U}_e^\delta)] \cdot \mathbf{\Phi}_e^\delta]_{x_e^L}^{x_e^R} \right] = \sum_{e=1}^{N_{el}} \left(\mathbf{S}(\mathbf{U}_e^\delta), \mathbf{\Phi}_e^\delta \right)_{\Omega_e} . \tag{2.50}$$

The implementation of the method can be simplified if each elemental region Ω_e is mapped onto the standard element $\Omega_{st} = \{-1 \leq \xi \leq 1\}$. The elemental mapping is defined as

$$\chi_e(\xi) = x_e^L \frac{(1-\xi)}{2} + x_e^R \frac{(1+\xi)}{2}, \qquad \xi \in \Omega_{st}, \tag{2.51}$$

and the inverse of the linear transformation χ_e is

$$\xi = \chi_e^{-1}(x) = 2\frac{(x_e - x_e^L)}{(x_e^R - x_e^L)} - 1, \qquad x_e \in \Omega_e. \tag{2.52}$$

The expansion basis are selected to be Legendre polynomials, denoted by $L_p(\xi)$ (with p the polynomial order), because they are orthogonal with respect to the $\mathcal{L}^2(\Omega)$ inner product (2.46). Thus, the solution is expanded on each elemental region Ω_e as

$$\mathbf{U}_e^\delta(\chi_e(\xi), t) = \sum_{p=0}^{P} L_p(\xi)\hat{\mathbf{U}}_e^p(t), \tag{2.53}$$

with $\hat{\mathbf{U}}_e^p(t)$ the time-varying coefficients of the expansion.

Since the discrete solution and test functions have been chosen to be discontinuous, the problem is decoupled on each elemental region Ω_e, the only link being the upwinded boundary fluxes $\mathbf{F}^u$, through which we are able to enforce inflow and outflow boundary conditions and to join arterial domains into junctions. Substitution of (2.53) into (2.50) and letting $\mathbf{\Phi}_e^\delta = \mathbf{U}_e^\delta$, yields $2P$ equations to be solved for each Ω_e, $e = 1, \ldots, N_{el}$,

$$\frac{\mathrm{d}\hat{U}_{i,e}^p}{\mathrm{d}t} = \mathcal{F}\left(\mathbf{U}_e^\delta\right), \quad p = 0, \ldots, P, \quad i = 1, 2, \tag{2.54}$$

where $\hat{U}_{i,e}^p$, $i = 1, 2$, are each of the two components of $\hat{\mathbf{U}}_e^p(t)$,

$$\mathcal{F}\left(\mathbf{U}_e^\delta\right) = -\left(\frac{\partial F_i}{\partial x}, L_p\right)_{\Omega_e} - \frac{1}{J_e}\left[L_p[F_i^u - F_i(\mathbf{U}_e^\delta)]\right]_{x_e^L}^{x_e^R} + \left(S_i(\mathbf{U}_e^\delta), L_p\right)_{\Omega_e},$$

and $J_e = \frac{1}{2}(x_e^R - x_e^L)$ is the Jacobian of the elemental mapping from the standard element Ω_{st}. The method is completed with a second-order Adams-Bashforth time-integration scheme, in which

$$\left(\hat{U}_{i,e}^p\right)^{n+1} = \left(\hat{U}_{i,e}^p\right)^n + \frac{3\Delta t}{2}\mathcal{F}\left(\left(\mathbf{U}_e^\delta\right)^n\right) - \frac{\Delta t}{2}\mathcal{F}\left(\left(\mathbf{U}_e^\delta\right)^{n-1}\right), \tag{2.55}$$

$$p = 0, \ldots, P, \quad i = 1, 2, \quad e = 1, \ldots, N_{el},$$

with Δt the time step and n the number of every time step. In every elemental region Ω_e, $\mathbf{U}_e^\delta(\chi_e(\xi), t)$ is projected into a Gauss quadrature of order q, which is used to solve the integrals $\left(\frac{\partial F_i}{\partial x}, L_p\right)_{\Omega_e}$ and $(S_i, L_p)_{\Omega_e}$.

Each simulation is started with an initial state $(A, p, U) = (A_0, p_0, U_0)$ in each arterial domain Ω.

2.6.1 The Riemann problem

The upwinded fluxes $\mathbf{F}^u$ required in Equation (2.55) at the interfaces of each elemental region Ω_e are calculated through the solution of a Riemann problem that takes into account the characteristic information arriving at both sides of the interfaces and neglects the characteristic information moving away. At a time t, each interface separates two constant states, (A_L, U_L) and (A_R, U_R) (Figure 2.4), with their corresponding β and A_0. These states are located at the end point of the elemental region on the left and at the initial point of the elemental region on the right. If there are discontinuities in β and A_0 across the interface, Equation (2.19) does not apply across the interface, which results in a discontinuity in the characteristic information propagating across the interface. Therefore, two upwinded states, (A_L^u, U_L^u) and (A_R^u, U_R^u), originate on each side of the interface at a time $t + \Delta t$. Two of the four equations required to determine these states relate the characteristic information arriving at the interface from the two constant states at time t. Assuming inviscid flow between the two initial states in Figure 2.4, we have $\frac{\mathrm{d}\mathbf{W}}{\mathrm{d}t} = \mathbf{0}$ between each initial constant state and its corresponding upwinded state, according to (2.19), and, hence,

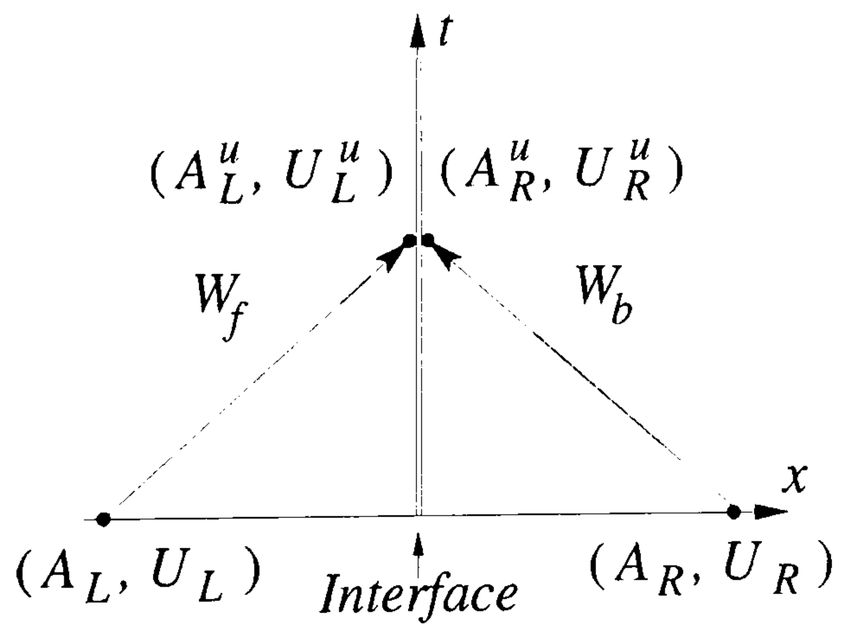


Figure 2.4: Layout of the Riemann problem that calculates the upwinded states (A_L^u, U_L^u) and (A_R^u, U_R^u) originated from the discontinuity between two initial states (A_L, U_L) and (A_R, U_R).

$$W_f(A_L, U_L) = W_f(A_L^u, U_L^u), \tag{2.56}$$

$$W_b(A_R, U_R) = W_b(A_R^u, U_R^u), \tag{2.57}$$

with W_f and W_b determined from (2.22) and (2.23). The remaining equations follow from conservation of mass and continuity of the total pressure at the interface,

$$A_L^u U_L^u = A_R^u U_R^u, \tag{2.58}$$

$$\rho\frac{(U_L^u)^2}{2} + p\,(A_L^u) = \rho\frac{(U_R^u)^2}{2} + p\,(A_R^u)\,, \tag{2.59}$$

with $p\,(A)$ expressed through the pressure-area relationship (2.11). Equations (2.56) to (2.59) are solved by means of the iterative Newton-Raphson method to obtain (A_L^u, U_L^u) and (A_R^u, U_R^u). The upwinded fluxes on each side of the interface, $\mathbf{F}_L^u$ and $\mathbf{F}_R^u$, are calculated as $\mathbf{F}_L^u = \mathbf{F}\,(A_L^u, U_L^u)$ and $\mathbf{F}_R^u = \mathbf{F}\,(A_R^u, U_R^u)$.

We notice that the characteristic information moving away from both sides of the interface does not change the solution above if this information does not have enough time to interact with the characteristic information propagating from the adjacent quadrature points. Therefore, Δt has to be limited by

$$\Delta t \max(|U \pm c|) \leq \frac{1}{2}\Delta x, \tag{2.60}$$

where Δx is the distance between two successive quadrature points.

We also notice that if β and A_0 have the same value on both sides of the interface, then $\frac{\mathrm{d}\mathbf{W}}{\mathrm{d}t} = \mathbf{0}$ applies across the interface, according to (2.19). Therefore, $W_f(A_L, U_L) = W_f(A_R^u, U_R^u)$ and $W_b(A_R, U_R) = W_b(A_L^u, U_L^u)$, which combined with (2.56) and (2.57) lead to $A_L^u = A_R^u$ and $U_L^u = U_R^u$; i.e., we have the same updated state, (A^u, U^u), on both sides of the interface. Combination of Equations (2.56) and (2.57) yields

$$A^u = \left[\frac{W_f(A_L, U_L) - W_b(A_R, U_R)}{8}\sqrt{\frac{2\rho A_0}{\beta}} + A_0^{1/4}\right]^4, \tag{2.61}$$

$$U^u = \frac{W_f(A_L, U_L) + W_b(A_R, U_R)}{2}. \tag{2.62}$$

The fluxes $\mathbf{F}^u$ of the elemental regions at the inlet (Ω_1) and the outlet $(\Omega_{N_{el}})$ of every arterial domain Ω are calculated through the solution of a Riemann problem involving suitable boundary conditions. This will be explained in more detail in Section 2.7.

2.6.2 Application to the linear formulation

The algorithm described in Section 2.6 can also be applied to solve the linear system of governing equations (2.39) if we consider

$$\mathbf{U} = \Delta\mathbf{U} = \begin{bmatrix} \Delta a \\ \Delta u \end{bmatrix}, \qquad \mathbf{F} = \mathbf{F}_0(\Delta\mathbf{U}) = \begin{bmatrix} A_0\Delta u \\ \frac{\beta}{2\rho A_0^{3/2}}\Delta a \end{bmatrix},$$

$$\mathbf{S} = \mathbf{S}_0(\mathbf{\Delta U}) = \begin{bmatrix} 0 \\ \frac{1}{\rho}\left(\frac{f_0}{A_0} - \frac{\partial \Delta p}{\partial \beta}\frac{\mathrm{d}\beta}{\mathrm{d}x} - \frac{\partial \Delta p}{\partial A_0}\frac{\mathrm{d}A_0}{\mathrm{d}x}\right) \end{bmatrix}.$$

In the linear version of the Riemann problem presented in Section 2.6.1, the state on the left elemental region is denoted as $(\Delta a_L, \Delta u_L)$, the state on the right elemental region as $(\Delta a_R, \Delta u_R)$, and the corresponding updated states as $(\delta a_L, \delta u_L)$ and $(\delta a_R, \delta u_R)$, respectively. As it has been shown for the non-linear formulation, if β and A_0 are equal on both sides of the interface and flow is inviscid between the two initial states, then $\delta a_L = \delta a_R$ and $\delta u_L = \delta u_R$; i.e., a single updated state, denoted by $(\delta a, \delta u)$, is obtained. Combining the linear characteristic information arriving at the interface as

$$\Delta W_f\left(\Delta a_L, \Delta u_L\right) = \Delta W_f\left(\delta a, \delta u\right), \tag{2.63}$$

$$\Delta W_b\left(\Delta a_R, \Delta u_R\right) = \Delta W_b\left(\delta a, \delta u\right), \tag{2.64}$$

with ΔW_f and ΔW_b determined from (2.41) and (2.42), we obtain

$$\delta a = \frac{A_0\left(\Delta W_f\left(\Delta a_L, \Delta u_L\right) - \Delta W_b\left(\Delta a_R, \Delta u_R\right)\right)}{2c_0}, \tag{2.65}$$

$$\delta u = \frac{\Delta W_f\left(\Delta a_L, \Delta u_L\right) + \Delta W_b\left(\Delta a_R, \Delta u_R\right)}{2}. \tag{2.66}$$

It will be shown in Section 2.7.2.2 how to obtain an analytical solution to the linear Riemann problem when β and A_0 are different on both sides of the interface.

2.7 Boundary conditions

The boundary conditions at the inlet and outlet of an arterial domain are classified into three types depending on the location of the domain in the arterial network. These are an inflow boundary condition (Section 2.7.1) if the artery receives an inflow exterior to the network, a junction boundary condition (Section 2.7.2) if the artery is part of a junction with other segments, and a terminal boundary condition (Section 2.7.3) if it is coupled to a lumped parameter model. Each case is explained for both the non-linear and the linear formulations.

2.7.1 Inflow boundary conditions

The 1-D model allows us to prescribe an inflow time-dependent area, $A_{bc}(t)$, velocity, $U_{bc}(t)$, or flow rate, $Q_{bc}(t)$. The other variables defining the flow are calculated in a way consistent with the Riemann problem described in Section 2.6.1. Now, one of the two states separated by the interface ((A_L, U_L) or (A_R, U_R) in Figure 2.4) belongs to the inlet (Ω_1) or the outlet ($\Omega_{N_{el}}$) of the arterial domain and the other to a virtual region outside the arterial domain. It is assumed that the virtual region has the same β and A_0 as the adjacent state in Ω_1 or $\Omega_{N_{el}}$, so that a single upwinded state (A^u, U^u) is obtained through the solution of Equations (2.61) and (2.62). To prescribe the desired inflow boundary condition, we need to determine the state in the virtual region that produces $A^u = A_{bc}$, $U^u = U_{bc}$ or $A^u U^u = Q_{bc}$ when combined with the state at the inlet or the outlet of the arterial domain.

To prescribe $A_{bc}(t)$ at the inlet of an arterial domain, $U_L = U_R$ is assumed. In that case, Equation (2.61) reduces to $2\left(A^u\right)^{1/4} = \left(A_L\right)^{1/4} + \left(A_R\right)^{1/4}$, from which the value of A_L that yields the desired $A^u = A_{bc}$ at the next time step is determined,

$$A_L = \left(2\left(A_{bc}\right)^{1/4} - \left(A_R\right)^{1/4}\right)^4. \tag{2.67}$$

To prescribe $U_{bc}(t)$ at the inlet of an arterial domain, $A_L = A_R$ is assumed, which leads to $2U^u = U_L + U_R$, according to Equation (2.62). Therefore, we need to enforce the following U_L to obtain the desired U^u at the next time step

$$U_L = 2U_{bc} - U_R. \tag{2.68}$$

To prescribe $Q_{bc}(t)$, Equation (2.68) is applied as

$$U_L = 2\frac{Q_{bc}}{A_R} - U_R. \tag{2.69}$$

Following the same procedure, we need to enforce the following A_R, U_R and Q_R to prescribe the desired inflow boundary condition at the outlet of an arterial domain

$$A_R = \left(2\left(A_{bc}\right)^{1/4} - \left(A_L\right)^{1/4}\right)^4, \tag{2.70}$$

$$U_R = 2U_{bc} - U_L, \tag{2.71}$$

$$U_R = 2\frac{Q_{bc}}{A_L} - U_L. \tag{2.72}$$

Since Equation (2.66) has the same form as Equation (2.62), Equations (2.68), (2.69), (2.71), and (2.72) are also valid for the linear formulation, with $(A_L, U_L) = (\Delta a_L + A_{0_L}, \Delta u_L)$ and $(A_R, U_R) = (\Delta a_R + A_{0_R}, \Delta u_R)$. However, to prescribe $A_{bc}(t)$ in the linear theory we need to use Equation (2.65) with $\Delta u_L = \Delta u_R$, which leads to $2\delta a = \Delta a_L + \Delta a_R$. Therefore, at the inlet of an arterial domain we need to prescribe

$$\Delta a_L = 2(A_{bc} - A_{0_R}) - \Delta a_R, \tag{2.73}$$

and at the outlet we need to prescribe

$$\Delta a_R = 2(A_{bc} - A_{0_L}) - \Delta a_L. \tag{2.74}$$

2.7.2 Junction boundary conditions

This section details how to determine the upwinded states at the boundary of an arterial domain that is connected to another arterial domain (Section 2.7.2.1) or that is part of a junction (Section 2.7.2.3). Both problems are also solved analytically for the linear formulation (Sections 2.7.2.2 and 2.7.2.4).

2.7.2.1 Connection of two arteries

To calculate the upwinded states of the two elemental regions involved in the connection of two arterial domains we need to solve the Riemann problem described in Section 2.6.1, whose layout is depicted in Figure 2.4. Now (A_L, U_L) is the initial state at the end point of the elemental region at the outlet of one arterial domain and (A_R, U_R) is the initial state at the initial point of the elemental region at the inlet of the other arterial domain. The corresponding upwinded states (A_L^u, U_L^u) and (A_R^u, U_R^u) are determined through the numerical solution of Equations (2.56) to (2.59).

2.7.2.2 Linear analysis of a connection of two arteries

This section calculates analytically for the linear formulation the upwinded states of the two elemental regions involved in the connection of two arterial domains, or two adjacent elemental regions in the same arterial domain but with different values of β and A_0. Since $\Delta u \ll c_0$ under physiological conditions, any perturbation $(\Delta a, \Delta p, \Delta u)$ on the initial state $(A, p, U) = (A_0, 0, 0)$ at the point of either

elemental region next to the connection produces an upwinded state on the left of the connection, denoted by $(A_{0_L} + \delta a_L, \delta p_L, \delta u_L)$, and an upwinded state on the right, denoted by $(A_{0_R} + \delta a_R, \delta p_R, \delta u_R)$. Following the same procedure as in the non-linear version of the problem (see Section 2.6.1), the first two equations to be satisfied relate the linear characteristic variables (2.41) and (2.42) arriving at the connection as

$$\delta u_L + \frac{c_{0_L}}{A_{0_L}} \delta a_L = \Delta u_L + \frac{c_{0_L}}{A_{0_L}} \Delta a_L, \tag{2.75}$$

$$\delta u_R - \frac{c_{0_R}}{A_{0_R}} \delta a_R = \Delta u_R - \frac{c_{0_R}}{A_{0_R}} \Delta a_R. \tag{2.76}$$

Conservation of mass and continuity of pressure yield the other two equations to be satisfied. Neglecting second order terms, they take the form

$$A_{0_L} \delta u_L = A_{0_R} \delta u_R, \tag{2.77}$$

$$\delta p_L = \delta p_R. \tag{2.78}$$

If the state on the left elemental region is perturbed with $(\Delta a_L, \Delta p_L, \Delta u_L)$ and $\Delta a_R = \Delta p_R = \Delta u_R = 0$ in the right elemental region, Expressions (2.75) and (2.76) reduce to

$$\delta u_L = \Delta u_L + \frac{c_{0_L}}{A_{0_L}} \left(\Delta a_L - \delta a_L \right), \tag{2.79}$$

$$\delta u_R = \frac{c_{0_R}}{A_{0_R}} \delta a_R. \tag{2.80}$$

Substituting (2.79) and (2.80) into (2.77) and expressing area variations in terms of pressure variations through (2.40), we obtain

$$A_{0_L} \left(\Delta u_L + \frac{1}{\rho c_{0_L}} \left(\Delta p_L - \delta p_L \right) \right) = \frac{A_{0_R}}{\rho c_{0_R}} \delta p_R. \tag{2.81}$$

Making use of (2.78) in (2.81) and rearranging terms we have

$$\delta p_L = \delta p_R \equiv \delta p = R_L \left(\Delta p_L + \rho c_{0_L} \Delta u_L \right), \tag{2.82}$$

with

$$R_L = \frac{\frac{A_{0_L}}{c_{0_L}}}{\frac{A_{0_L}}{c_{0_L}} + \frac{A_{0_R}}{c_{0_R}}}.$$

Similarly, if the state in the right elemental region is perturbed with $(\Delta a_R, \Delta p_R, \Delta u_R)$ and $\Delta a_L = \Delta p_L = \Delta u_L = 0$ in the left elemental region, we obtain

$$\delta p_L = \delta p_R \equiv \delta p = R_R \left(\Delta p_R - \rho c_{0_R} \Delta u_R \right), \tag{2.83}$$

with

$$R_R = \frac{\frac{A_{0_R}}{c_{0_R}}}{\frac{A_{0_L}}{c_{0_L}} + \frac{A_{0_R}}{c_{0_R}}}.$$

Because of the linearity of the problem, if both perturbations $(\Delta a_L, \Delta p_L, \Delta u_L)$ and $(\Delta a_R, \Delta p_R, \Delta u_R)$ take place during the same time step, the results (2.82) and (2.83) combine to produce

$$\delta p_L = \delta p_R \equiv \delta p = R_L \left(\Delta p_L + \rho c_{0_L} \Delta u_L\right) + R_R \left(\Delta p_R - \rho c_{0_R} \Delta u_R\right). \tag{2.84}$$

The final perturbed areas δa_L and δa_R are determined through (2.40) as

$$\delta a_L = \frac{A_{0_L}}{\rho \left(c_{0_L}\right)^2} \delta p, \qquad \delta a_R = \frac{A_{0_R}}{\rho \left(c_{0_R}\right)^2} \delta p, \tag{2.85}$$

and the final perturbed velocities δu_L and δu_R result from (2.75) and (2.76) once δa_L and δa_R have been determined.

From Equations (2.85) we notice that if $c_{0_L} = c_{0_R}$ and $A_{0_L} = A_{0_R}$, then $\delta a_L = \delta a_R$, and, hence, $\delta u_L = \delta u_R$ according to (2.77).

2.7.2.3 Junctions

Two types of junctions are considered: (a) splitting flow junctions (Figure 2.5, left), in which the outlet of the parent vessel is connected to the inlets of the two daughter vessels, and (b) merging flow junctions (Figure 2.5, right), in which the inlet of the parent vessel is connected to the outlets of the two daughter vessels. Splitting flow junctions are the most common arrangement in the large human systemic arteries. Merging flow junctions are rare in the large arteries but occur more frequently in peripheral systemic arteries (such as the circle of Willis and the palmar arch), arterioles and capillaries and are the most common form of junctions in the venous system (see Figure 1.3). They are also important for modelling surgical interventions such as arterial bypass grafting.

If (A_1, p_1, U_1), (A_2, p_2, U_2) and (A_3, p_3, U_3) are the initial states at the points of each elemental region adjacent to a splitting flow junction (Figure 2.5, left), then their corresponding upwinded states (A_i^u, p_i^u, U_i^u) $(i = 1, 2, 3)$ are determined by solving a non-linear system of six algebraic equations using the Newton-Raphson method. Assuming inviscid flow within the points adjacent to the junction, we have

$$W_f(A_1^u, U_1^u) = W_f(A_1, U_1), \tag{2.86}$$

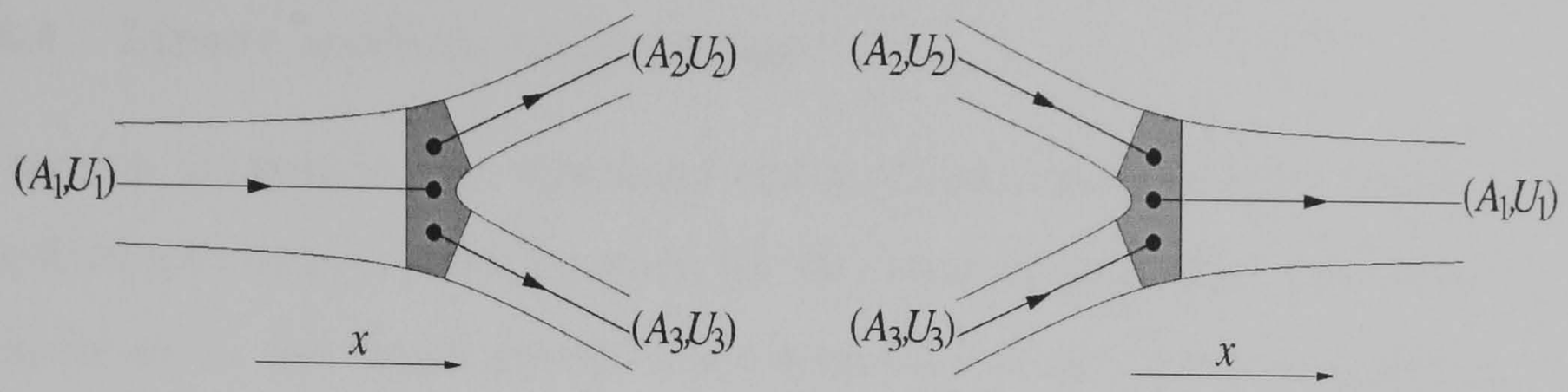


Figure 2.5: Types of junctions considered: splitting flow (left) and merging flow (right), along with the nomenclature used for each vessel. The arrows indicate the positive direction of the axial coordinate x.

$$W_b(A_2^u, U_2^u) = W_b(A_2, U_2), \tag{2.87}$$

$$W_b(A_3^u, U_3^u) = W_b(A_3, U_3), \tag{2.88}$$

with W_f and W_b determined from (2.22) and (2.23). Conservation of mass applied to the upwinded variables provides

$$A_1^u U_1^u = A_2^u U_2^u + A_3^u U_3^u. \tag{2.89}$$

Bernoulli's law provides the last two equations

$$p(A_1^u) + \frac{1}{2}\rho\,(U_1^u)^2 = p(A_2^u) + \frac{1}{2}\rho\,(U_2^u)^2\,, \tag{2.90}$$

$$p(A_1^u) + \frac{1}{2}\rho\,(U_1^u)^2 = p(A_3^u) + \frac{1}{2}\rho\,(U_3^u)^2\,, \tag{2.91}$$

with $p\,(A)$ expressed through the tube law (2.11). We note that Bernoulli's law is only an approximation to the balance of energy occurring at the junction, since flow separation and vortex formation are possible just downstream from the junction because of the discontinuous change in area across the junction.

In the case of a merging flow junction with the initial states (A_1, p_1, U_1), (A_2, p_2, U_2) and (A_3, p_3, U_3) as shown in Figure 2.5 (right), their corresponding upwinded states (A_i^u, p_i^u, U_i^u) $(i = 1, 2, 3)$ are determined by solving the following six non-linear equations. Conservation of the characteristic variables moving towards the junction in each vessel yields

$$W_b(A_1^u, U_1^u) = W_b(A_1, U_1), \tag{2.92}$$

$$W_f(A_2^u, U_2^u) = W_f(A_2, U_2), \tag{2.93}$$

$$W_f(A_3^u, U_3^u) = W_f(A_3, U_3). \tag{2.94}$$

Conservation of mass and Bernoulli's law are also enforced by means of Equations (2.89) to (2.91).

2.7.2.4 Linear analysis of junctions

This section determines the upwinded states of the three elemental regions involved in a splitting or merging flow junction for the linear formulation. Following the same procedure as in the linear study of a connection of two arteries (Section 2.7.2.2), any perturbation $(\Delta a, \Delta p, \Delta u)$ in the initial state $(A, p, U) = (A_0, 0, 0)$ at any of the three points adjacent to the junction produces three upwinded states, denoted by $(A_{0_i} + \delta a_i, \delta p_i, \delta u_i)$ $(i = 1, 2, 3)$ (the numbering for the parent and daughter vessels is indicated in Figure 2.5, left). In the case of a splitting flow junction, the following relation between the linear characteristic variables (2.41) and (2.42) moving towards the junction is satisfied

$$\delta u_1 + \frac{c_{0_1}}{A_{0_1}}\delta a_1 = \Delta u_1 + \frac{c_{0_L}}{A_{0_1}}\Delta a_1, \tag{2.95}$$

$$\delta u_2 - \frac{c_{0_2}}{A_{0_2}}\delta a_2 = \Delta u_2 - \frac{c_{0_2}}{A_{0_2}}\Delta a_2, \tag{2.96}$$

$$\delta u_3 - \frac{c_{0_3}}{A_{0_3}}\delta a_3 = \Delta u_3 - \frac{c_{0_3}}{A_{0_3}}\Delta a_3. \tag{2.97}$$

Conservation of mass and continuity of the total pressure are applied neglecting second order terms. They take the form

$$A_{0_1}\delta u_1 = A_{0_2}\delta u_2 + A_{0_3}\delta u_3, \tag{2.98}$$

$$\delta p_1 = \delta p_2, \tag{2.99}$$

$$\delta p_1 = \delta p_3. \tag{2.100}$$

If the state $(A_{0_1}, 0, 0)$ at the end point of the parent vessel is perturbed with $(\Delta a_1, \Delta p_1, \Delta u_1)$ and $\Delta a_j = \Delta p_j = \Delta u_j = 0$ $(j = 2, 3)$, then Expressions (2.95) to (2.97) reduce to

$$\delta u_1 = \Delta u_1 + \frac{c_{0_1}}{A_{0_1}}\left(\Delta a_1 - \delta a_1\right), \tag{2.101}$$

$$\delta u_2 = \frac{c_{0_2}}{A_{0_2}}\delta a_2, \tag{2.102}$$

$$\delta u_3 = \frac{c_{0_3}}{A_{0_3}}\delta a_3. \tag{2.103}$$

Substituting (2.101) to (2.103) into (2.98) and expressing area variations in terms of pressure variations through (2.40), we obtain

$$A_{0_1}\left(\Delta u_1 + \frac{1}{\rho c_{0_1}}\left(\Delta p_1 - \delta p_1\right)\right) = \frac{A_{0_2}}{\rho c_{0_2}}\delta p_2 + \frac{A_{0_3}}{\rho c_{0_3}}\delta p_3. \tag{2.104}$$

Taking into account (2.99) and (2.100) and rearranging terms, Equation (2.104) yields

$$\delta p_1 = \delta p_2 = \delta p_3 \equiv \delta p = R_1 \left(\Delta p_1 + \rho c_{0_1} \Delta u_1\right), \tag{2.105}$$

where

$$R_1 = \frac{\frac{A_{0_1}}{c_{0_1}}}{\frac{A_{0_1}}{c_{0_1}} + \frac{A_{0_2}}{c_{0_2}} + \frac{A_{0_3}}{c_{0_3}}}.$$

Similarly, if the state $(A_{0_j}, 0, 0)$ at the initial point of either daughter vessel j $(j = 2, 3)$ is perturbed with $(\Delta a_j, \Delta p_j, \Delta u_j)$ and $\Delta a_i = \Delta p_i = \Delta u_i = 0$, for all $i \neq j$, we obtain

$$\delta p_1 = \delta p_2 = \delta p_3 \equiv \delta p = R_j \left(\Delta p_j - \rho c_{0_j} \Delta u_j\right), \tag{2.106}$$

with

$$R_2 = \frac{\frac{A_{0_2}}{c_{0_2}}}{\frac{A_{0_1}}{c_{0_1}} + \frac{A_{0_2}}{c_{0_2}} + \frac{A_{0_3}}{c_{0_3}}}, \qquad R_3 = \frac{\frac{A_{0_3}}{c_{0_3}}}{\frac{A_{0_1}}{c_{0_1}} + \frac{A_{0_2}}{c_{0_2}} + \frac{A_{0_3}}{c_{0_3}}}.$$

Because of the linearity of the problem, when we consider the three perturbations $(\Delta a_i, \Delta p_i, \Delta u_i)$ $(i = 1, 2, 3)$ during the same time step, Equations (2.105) and (2.106) combine to produce

$$\delta p_1 = \delta p_2 = \delta p_3 \equiv \delta p = R_1 \left(\Delta p_1 + \rho c_{0_1} \Delta u_1\right) + R_2 \left(\Delta p_2 - \rho c_{0_2} \Delta u_2\right) + R_3 \left(\Delta p_3 - \rho c_{0_3} \Delta u_3\right). \tag{2.107}$$

The final perturbed areas follow from (2.40). They take the form

$$\delta a_1 = \frac{A_{0_1}}{\rho \left(c_{0_1}\right)^2} \delta p, \qquad \delta a_2 = \frac{A_{0_2}}{\rho \left(c_{0_2}\right)^2} \delta p, \qquad \delta a_3 = \frac{A_{0_3}}{\rho \left(c_{0_3}\right)^2} \delta p, \tag{2.108}$$

and the final perturbed velocities result from (2.95) to (2.97) once δa_1, δa_2 and δa_3 have been determined.

In the case of a merging flow junction perturbed with $(\Delta a_i, \Delta p_i, \Delta u_i)$ $(i = 1, 2, 3)$ (the numbering for the parent and daughter vessels is indicated in Figure 2.5, right) during the same time step, we obtain

$$\delta p_1 = \delta p_2 = \delta p_3 \equiv \delta p = R_1 \left(\Delta p_1 - \rho c_{0_1} \Delta u_1\right) + R_2 \left(\Delta p_2 + \rho c_{0_2} \Delta u_2\right) + R_3 \left(\Delta p_3 + \rho c_{0_3} \Delta u_3\right). \tag{2.109}$$

Expressions (2.108) provide the perturbed areas and the counterparts of Equations (2.95) to (2.97) for a merging flow junction yield the perturbed velocities.

If a perturbation $(\Delta a_1, \Delta p_1, \Delta u_1)$ at the end point of the parent artery of a splitting flow junction consists only of a forward travelling wave, then W_b has the same value as in the initial state $(A_1, p_1, U_1) = (A_{0_1}, 0, 0)$ along the backward characteristic line. Therefore $\Delta W_b = 0$ and, hence, $\Delta u_1 = \frac{c_{0_1}}{A_{0_1}} \Delta a_1 = \frac{1}{\rho c_{0_1}} \Delta p_1$, according to Equations (2.40) and (2.42). Consequently, Equation (2.105) reduces to $\delta p_1 = 2R_1 \Delta p_1$. If we define the reflection coefficient $R_{f_1} \equiv \frac{\delta p_1 - \Delta p_1}{\Delta p_1}$, as suggested by Sherwin *et al* [82] inspired by the linearised acoustics and surface waves problems, we obtain

$$R_{f_1} = \frac{\frac{A_{0_1}}{c_{0_1}} - \frac{A_{0_2}}{c_{0_2}} - \frac{A_{0_3}}{c_{0_3}}}{\frac{A_{0_1}}{c_{0_1}} + \frac{A_{0_2}}{c_{0_2}} + \frac{A_{0_3}}{c_{0_3}}}. \tag{2.110}$$

In the same way, if the state at the point adjacent to the junction of either daughter vessel j $(j = 2, 3)$ of a splitting flow junction is perturbed with $(\Delta a_j, \Delta p_j, \Delta u_j)$, which consists only of a backward travelling wave, then W_f has the same value as in the initial state $(A_j, p_j, U_j) = (A_{0_j}, 0, 0)$ along the forward characteristic line. Therefore $\Delta W_f = 0$ and, hence, $\Delta u_j = -\frac{c_{0_j}}{A_{0_j}} \Delta a_j = -\frac{1}{\rho c_{0_j}} \Delta p_j$, according to Equations (2.40) and (2.41). Consequently, Equation (2.106) reduces to $\delta p_j = 2R_j \Delta p_j$, and defining the reflection coefficient $R_{f_j} \equiv \frac{\delta p_j - \Delta p_j}{\Delta p_j}$ we obtain

$$R_{f_2} = \frac{\frac{-A_{0_1}}{c_{0_1}} + \frac{A_{0_2}}{c_{0_2}} - \frac{A_{0_3}}{c_{0_3}}}{\frac{A_{0_1}}{c_{0_1}} + \frac{A_{0_2}}{c_{0_2}} + \frac{A_{0_3}}{c_{0_3}}}, \qquad R_{f_3} = \frac{\frac{-A_{0_1}}{c_{0_1}} - \frac{A_{0_2}}{c_{0_2}} + \frac{A_{0_3}}{c_{0_3}}}{\frac{A_{0_1}}{c_{0_1}} + \frac{A_{0_2}}{c_{0_2}} + \frac{A_{0_3}}{c_{0_3}}}. \tag{2.111}$$

Combining three perturbations that satisfy $\Delta u_1 = \frac{c_{0_1}}{A_{0_1}} \Delta a_1$, $\Delta u_2 = -\frac{c_{0_2}}{A_{0_2}} \Delta a_2$ and $\Delta u_3 = -\frac{c_{0_3}}{A_{0_3}} \Delta a_3$ in a splitting flow bifurcation, we obtain

$$\delta p_1 = \delta p_2 = \delta p_3 \equiv \delta p = (1 + R_{f_1}) \Delta p_1 + (1 + R_{f_2}) \Delta p_2 + (1 + R_{f_3}) \Delta p_3. \tag{2.112}$$

Equation (2.112) also applies for a merging flow bifurcation with three perturbations that satisfy $\Delta u_1 = -\frac{c_{0_1}}{A_{0_1}} \Delta a_1$, $\Delta u_2 = \frac{c_{0_2}}{A_{0_2}} \Delta a_2$ and $\Delta u_3 = \frac{c_{0_3}}{A_{0_3}} \Delta a_3$.

2.7.3 Terminal boundary conditions

The zero-dimensional (0-D) equations that govern the lumped parameter models used to describe the effect on pulse wave propagation of the wall compliance and the fluid resistance and inertia of the small arteries, arterioles and capillaries are described in Section 2.7.3.1. Next, the 0-D equations are applied to solve the classical two-element windkessel model proposed by Hales and Frank (Section 2.7.3.2).

Sections 2.7.3.3 to 2.7.3.7 detail how to couple the different types of lumped parameter models used in this work to the linear and non-linear 1-D formulations. The coupling is based on the solution of the Riemann problem described in Section 2.6.1, whose layout is depicted in Figure 2.4. The initial state (A_L, U_L) is located at the end point of the 1-D arterial domain and the initial state (A_R, U_R) is selected to produce an upwinded state (A^u, U^u), which satisfies the relation between A^u and U^u dictated by the lumped parameter model used. The values of β and A_0 in (A_R, U_R) are assumed to be equal to their counterparts in (A_L, U_L).

2.7.3.1 Zero-dimensional equations

First, the system of linear 1-D governing equations (2.39) is reduced to

$$\begin{cases} \frac{\partial \Delta a}{\partial t} + A_0 \frac{\partial \Delta u}{\partial x} = 0, \\ \frac{\partial \Delta u}{\partial t} + \frac{1}{\rho} \frac{\partial \Delta p}{\partial x} = -\frac{8\pi\mu\Delta u}{\rho A_0}, \end{cases} \tag{2.113}$$

under the assumptions of constant β and A_0 along the arterial domain and a friction term given by Poiseuille's flow; i.e., $\gamma = 2$ in the generic velocity profile (2.4), which is a better approximation in small arteries than the flatter velocity profile used in large arteries (Olufsen *et al* [63]).

Next, Equation (2.113) is written in terms of the increment in flow rate, $\Delta q \equiv A_0 \Delta u$, and pressure, Δp, as

$$\begin{cases} \frac{A_0}{\rho (c_0)^2} \frac{\partial \Delta p}{\partial t} + \frac{\partial \Delta q}{\partial x} = 0, \\ \frac{\partial \Delta q}{\partial t} + \frac{A_0}{\rho} \frac{\partial \Delta p}{\partial x} = -\frac{8\pi\mu\Delta q}{\rho A_0}, \end{cases} \tag{2.114}$$

making use of (2.40). Integration of (2.114) along the length l of the arterial domain leads to

$$\begin{cases} C \frac{\mathrm{d}\hat{p}}{\mathrm{d}t} + Q_{out} - Q_{in} = 0, \\ L \frac{\mathrm{d}\hat{Q}}{\mathrm{d}t} + R_\mu \hat{Q} + p_{out} - p_{in} = 0, \end{cases} \tag{2.115}$$

where $\hat{p}(t) \equiv \frac{1}{l} \int_0^l \Delta p \, \mathrm{d}x$ and $\hat{Q}(t) \equiv \frac{1}{l} \int_0^l \Delta q \, \mathrm{d}x$ are the mean pressure and flow rate over the whole arterial domain,

$$Q_{in} \equiv \Delta q(0,t), \quad Q_{out} \equiv \Delta q(l,t), \quad p_{in} \equiv \Delta p(0,t), \quad p_{out} \equiv \Delta p(l,t),$$

and

$$R_\mu \equiv \frac{8\pi\mu l}{(A_0)^2}, \tag{2.116}$$

$$L \equiv \frac{\rho l}{A_0}, \tag{2.117}$$

$$C \equiv \frac{A_0 l}{\rho \left(c_0\right)^2}, \tag{2.118}$$

are the resistance to flow, blood inertia and wall compliance, respectively. The value of Q_{in} is given by the 1-D formulation and p_{out} is a constant parameter of the simulation that accounts for the venous pressure. Therefore, System (2.115) has four unknowns ($\hat{p}$, $\hat{Q}$, Q_{out} and p_{in}). To eliminate two of these unknowns it is assumed that $\hat{p} = p_{in}$ and $\hat{Q} = Q_{out}$, which yields

$$\begin{cases} C\dfrac{\mathrm{d}p_{in}}{\mathrm{d}t} + Q_{out} - Q_{in} = 0, \\ L\dfrac{\mathrm{d}Q_{out}}{\mathrm{d}t} + R_\mu Q_{out} + p_{out} - p_{in} = 0. \end{cases} \tag{2.119}$$

Equations (2.119) are analogous to the electric transmission line equations, in which the role of the flow rate is played by the electric current and the blood pressure corresponds to the electric potential. Therefore, System (2.119) can be visualised as the electric circuit showed in Figure 2.6 (Westerhof *et al* [96]), in which R_μ is depicted as an electric resistance, L as an inductance, and C as a capacitance.

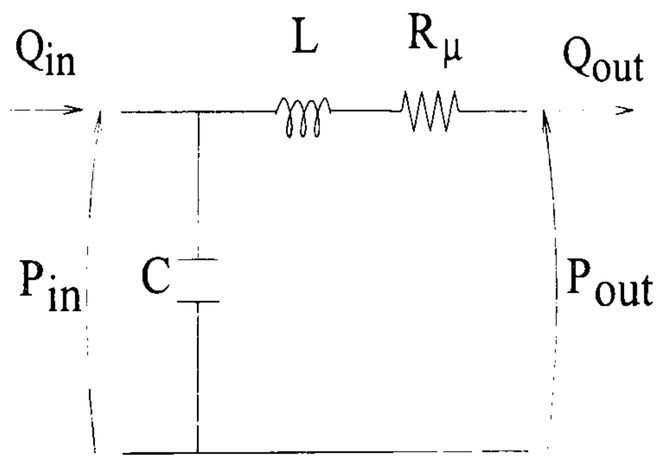


Figure 2.6: Representation of the electric circuit governed by the 0-D governing equations (2.119).

2.7.3.2 The windkessel model

If $L = 0$, System (2.119) reduces to

$$\begin{cases} C\dfrac{\mathrm{d}p_{in}}{\mathrm{d}t} + Q_{out} - Q_{in} = 0, \\ Q_{out} = \dfrac{p_{in} - p_{out}}{R_\mu}, \end{cases} \tag{2.120}$$

which leads to the differential equation

$$\frac{\mathrm{d}p_{in}}{\mathrm{d}t} + \frac{p_{in}}{R_\mu C} = \frac{Q_{in}}{C} + \frac{p_{out}}{R_\mu C} \tag{2.121}$$

that governs the classical windkessel model described by Hales (Figure 1.8). This model can be used to simulate the whole systemic arterial tree if we consider that $C = C_T$ and $R_\mu = R_{\mu_T}$ are the total compliance and resistance of the system, Q_{in} is the outflow from the left ventricle, Q_{out} is the outflow to the venous system, p_{out} is the pressure at which flow from the arteries to the veins ceases, and $p_{in} = p_{wk}$ is an appropriate average of pressure in all the systemic arteries, called the *windkessel pressure*. The general solution of Equation (2.121) with this new notation is

$$p_{wk} - p_{out} = (p_{wk_0} - p_{out})e^{\frac{-t}{R_{\mu_T}C_T}} + \frac{1}{C_T}e^{\frac{-t}{R_{\mu_T}C_T}}\int_0^t Q_{in}(t')e^{\frac{t'}{R_{\mu_T}C_T}}dt', \qquad (2.122)$$

where p_{wk_0} is the pressure at the onset of the ventricular ejection; i.e., the windkessel pressure once the aortic valve is closed. During diastole we have $Q_{in} = 0$ and (2.122) reduces to

$$p_{wk} - p_{out} = (p_{wk_0} - p_{out})e^{\frac{-t}{R_{\mu_T}C_T}}, \qquad (2.123)$$

and Q_{out} becomes

$$Q_{out} = \frac{(p_{wk_0} - p_{out})}{R_{\mu_T}}e^{\frac{-t}{R_{\mu_T}C_T}}. \qquad (2.124)$$

According to Wang *et al* [93], pulse waves are minimal during approximately the last two thirds of diastole. Therefore, pressure in the systemic arteries must approximate p_{wk} during this time. We also notice that the compliance of the system discharges more flow rate during diastole with the increasing pressure p_{wk_0}.

Integration of Equation (2.121) (using the new notation) over a period of time $[t', t' + T]$,

$$\int_{t'}^{t'+T}\frac{\mathrm{d}p_{wk}}{\mathrm{d}t}\mathrm{d}t + \int_{t'}^{t'+T}\frac{p_{wk}}{R_{\mu_T}C_T}\mathrm{d}t = \int_{t'}^{t'+T}\frac{Q_{in}}{C_T}\mathrm{d}t + \int_{t'}^{t'+T}\frac{p_{out}}{R_{\mu_T}C_T}\mathrm{d}t,$$

yields

$$p_{wk}(t'+T) - p_{wk}(t') = \frac{T}{C_T}\left(\overline{Q}_{in} - \frac{\overline{p}_{wk} - p_{out}}{R_{\mu_T}}\right) = \frac{T}{C_T}\left(\overline{Q}_{in} - \overline{Q}_{out}\right), \qquad (2.125)$$

where $\overline{p}_{in} \equiv \frac{1}{T}\int_{t'}^{t'+T} p_{wk}\mathrm{d}t$, $\overline{Q}_{in} \equiv \frac{1}{T}\int_{t'}^{t'+T} Q_{in}\mathrm{d}t$, and $\overline{Q}_{out} \equiv \frac{1}{T}\int_{t'}^{t'+T} Q_{out}\mathrm{d}t$ are the mean pressure and inflow and outflow rates over the period $[t', t' + T]$, respectively. We notice that if p_{wk} is periodic with a period T, then $p_{wk}(t' + T) = p_{wk}(t')$ and Equation (2.125) reduces to

$$\overline{Q} = \frac{\overline{p}_{wk} - p_{out}}{R_{\mu_T}}, \qquad (2.126)$$

with $\overline{Q} \equiv \overline{Q}_{in} = \overline{Q}_{out}$.

2.7.3.3 Terminal reflection coefficient

This terminal boundary condition relates the forward characteristic information, W_f, leaving the outlet of an arterial domain with the backward characteristic information, W_b, reflected by the terminal model through $W_b = -R_t W_f$, where $-1 \leq R_t \leq 1$ is the *terminal reflection coefficient.* Therefore, the solution for velocity of the Riemann problem at the terminal outlet, given by Equation (2.62), can be written as

$$U^u = \frac{W_f\,(A_L, U_L)}{2}(1 - R_t), \tag{2.127}$$

Using Equation (2.71) with $U_{bc} = U^u$ (we need to assume $A_R = A_L$), we obtain the velocity specified at the outlet as

$$U_R = W_f(1 - R_t) - U_L. \tag{2.128}$$

In the linear formulation, this terminal boundary condition is applied through $\Delta u_R = \Delta W_f(1 - R_t) - \Delta u_L$. The linear formulation also provides the following physical interpretation of this boundary condition. If the pulse wave travelling towards the terminal model is a forward travelling wave, with a pressure Δp_L and a velocity Δu_L, then

$$\Delta u_L = \frac{1}{\rho c_{0_L}} \Delta p_L, \tag{2.129}$$

as explained in Section 2.7.2.4 (c_{0_L} is the pulse wave speed at the end point of the artery). If the reflected pressure is δp_L and the reflected velocity is δu_L, then

$$\delta u_L - \frac{1}{\rho c_{0_L}} \delta p_L = \Delta W_b = -R_t \Delta W_f = -R_t(\Delta u_L + \frac{1}{\rho c_{0_L}} \Delta p_L). \tag{2.130}$$

Along the forward characteristic path we have

$$\delta u_L + \frac{1}{\rho c_{0_L}} \delta p_L = \Delta u_L + \frac{1}{\rho c_{0_L}} \Delta p_L. \tag{2.131}$$

Combination of (2.129) to (2.131) leads to

$$\delta p_L = \Delta p_L(1 + R_t), \tag{2.132}$$

$$\delta u_L = \Delta u_L(1 - R_t). \tag{2.133}$$

Equations (2.132) and (2.133) show that $R_t = 1$ represents a blockage or full reflection of the incoming wave ($\delta p_L = 2\Delta p_L$ and $\delta u_L = 0$), $R_t = 0$ represents a non-reflecting or absorbing outflow ($\delta p_L = \Delta p_L$ and $\delta u_L = \Delta u_L$), and $R_t = -1$ represents an outflow with an open end ($\delta p_L = 0$ and $\delta u_L = 2\Delta u_L$).

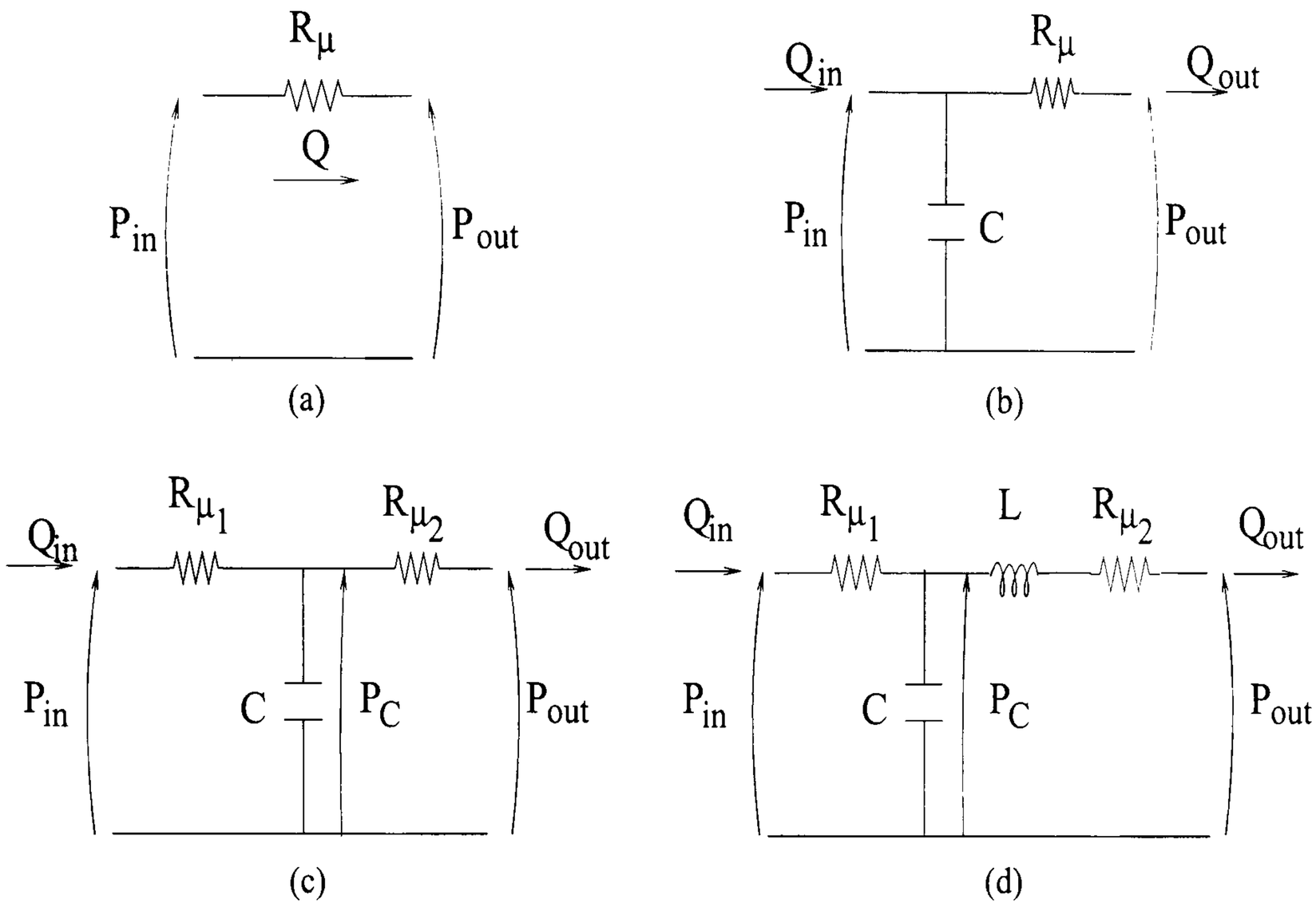


Figure 2.7: Representation of the electric circuits analogous to the terminal lumped parameter models considered: (a) terminal resistance, (b) two-element (CR) windkessel model, (c) three-element (RCR) windkessel model, and (d) four-element (RCLR) windkessel model.

2.7.3.4 Terminal resistance

A terminal reflection coefficient can also be understood as a lumped parameter model made of a resistance R_μ, as depicted in Figure 2.7 (a). Assuming $C = L = 0$, System (2.119) reduces to

$$\begin{cases} Q_{out} = Q_{in} = Q, \\ R_\mu Q_{out} + p_{out} - p_{in} = 0, \end{cases} \tag{2.134}$$

which leads to

$$Q = \frac{p_{in} - p_{out}}{R_\mu}. \tag{2.135}$$

The terminal resistance R_μ is coupled to the 1-D formulation by imposing that (A^u, U^u) satisfies Equation (2.135), so that

$$Q^u = A^u U^u = \frac{p(A^u) - p_{out}}{R_\mu}, \tag{2.136}$$

with $p(A^u)$ expressed through the tube law (2.11). It is also assumed invariance of W_f from the end point of the 1-D terminal artery to the outlet,

$$W_f\left(A_L, U_L\right) = W_f\left(A^u, U^u\right), \tag{2.137}$$

which combines with (2.136) to yield a non-linear equation in A^u given by

$$\mathcal{F}\left(A^u\right) = R_\mu \tilde{W}_f A^u - 4R_\mu \sqrt{\frac{\beta_L}{2\rho A_{0_L}}} \left(A^u\right)^{\frac{5}{4}} - p_0 - \frac{\beta_L}{A_{0_L}} \left(\sqrt{A^u} - \sqrt{A_{0_L}}\right) + p_{out} = 0, \tag{2.138}$$

with $\tilde{W}_f = U_L + 4\sqrt{\frac{\beta_L}{2\rho A_{0_L}}} \left(A_L\right)^{\frac{1}{4}}$. Equation (2.138) is solved for A^u by a Newton's method (with $A^u = A_L$ as the initial guess), and U^u is calculated from (2.136) as

$$U^u = \frac{p\left(A^u\right) - p_{out}}{R_\mu A^u}. \tag{2.139}$$

The terminal boundary condition is prescribed through (2.71) with $U_{bc} = U^u$ and assuming $A_R = A_L$.

In the linear formulation R_μ is related to R_t. Substitution of (2.41) and (2.42) into $R_t = -\Delta W_b / \Delta W_f$, yields

$$R_t = \frac{-\Delta u + \frac{c_{0_L}}{A_{0_L}} \Delta a}{\Delta u + \frac{c_{0_L}}{A_{0_L}} \Delta a}.$$

Expressing Δa in terms of Δp through (2.40) and multiplying numerator and denominator by $\frac{\rho c_{0_L}}{A_{0_L} \Delta u}$, we obtain

$$R_t = \frac{R_\mu - \frac{\rho c_{0_L}}{A_{0_L}}}{R_\mu + \frac{\rho c_{0_L}}{A_{0_L}}}, \tag{2.140}$$

with $R_\mu = \frac{\Delta p}{A_{0_L} \Delta u}$.

2.7.3.5 Two-element (CR) windkessel model

In this model a compliance C is added to the R_μ model shown in Figure 2.7 (a). The electric circuit of the resulting lumped parameter model is shown in Figure 2.7 (b), and its 0-D governing equations follow from (2.119) considering $L = 0$,

$$\begin{cases} C \dfrac{\mathrm{d}p_{in}}{\mathrm{d}t} + Q_{out} - Q_{in} = 0, \\ R_\mu Q_{out} + p_{out} - p_{in} = 0, \end{cases} \tag{2.141}$$

which combine to yield

$$C \frac{\mathrm{d}p_{in}}{\mathrm{d}t} + \frac{p_{in} - p_{out}}{R_\mu} - Q_{in} = 0. \tag{2.142}$$

Equation (2.142) can be written in discrete form using a first-order finite difference approximation in time, so that

$$p\left(A_{in}^n\right) = p\left(A_{in}^{n-1}\right) + \frac{\Delta t}{C} \left(Q_{in}^{n-1} - \frac{p\left(A_{in}^{n-1}\right) - p_{out}}{R_\mu}\right). \tag{2.143}$$

Substitution of the tube law (2.11) into (2.143) yields

$$\sqrt{A_{in}^n} = \sqrt{A_{in}^{n-1}} + \frac{\Delta t A_{0_L}}{C\beta_L}\left[Q_{in}^{n-1} + \frac{1}{R_\mu}\left(p_{out} - p_0 - \frac{\beta_L}{A_{0_L}}\left(\sqrt{A_{in}^{n-1}} - \sqrt{A_{0_L}}\right)\right)\right]. \tag{2.144}$$

Expression (2.144) is coupled to the 1-D formulation by considering $(A^u)^n = A_{in}^n$, $(A^u)^{n-1} = A_{in}^{n-1}$ and $U_R = U_L$. For the first time step ($n = 1$), A_{in}^0 is equal to the reference area at the end point of the 1-D arterial domain. The boundary condition is prescribed through (2.70) with $A_{bc} = (A^u)^n$.

2.7.3.6 Three-element (RCR) windkessel model

The CR model shown in the previous section produces pressure and flow oscillations that disappear when we add a second resistance in front of C, which leads to a model with two resistances, R_{μ_1} and R_{μ_2}, and a compliance C (Figure 2.7, c). This model consists of two coupled compartments. First we have a simple resistance model (R_{μ_1}) coupled to the 1-D terminal branch, followed by a CR_{μ_2} model. The first resistance R_{μ_1} is governed by equation

$$Q_{in} = \frac{p_{in} - p_C}{R_{\mu_1}}, \tag{2.145}$$

and the CR_{μ_2} system by equations

$$\begin{cases} C\dfrac{\mathrm{d}p_C}{\mathrm{d}t} + Q_{out} - Q_{in} = 0, \\ R_{\mu_2}Q_{out} + p_{out} - p_C = 0, \end{cases} \tag{2.146}$$

with p_C the pressure across C. The RCR model is coupled to the 1-D terminal branch by assuming that the state (A^u, U^u) satisfies Equations (2.136) to (2.139), with $R_\mu = R_{\mu_1}$ and $p_{out} = p_C$. The value of A^u is calculated from (2.138) and U^u from (2.139). The boundary condition is prescribed through (2.71) with $U_{bc} = U^u$ and assuming $A_R = A_L$.

At every time step n, p_C is determined by solving a first-order time discretisation of the conservation of mass in (2.146),

$$p_C^n = p_C^{n-1} + \frac{\Delta t}{C}\left(Q_{in}^{n-1} - Q_{out}^{n-1}\right), \tag{2.147}$$

with $Q_{in}^{n-1} = (A^u)^{n-1}(U^u)^{n-1}$ and $Q_{out}^{n-1} = \frac{p_C^{n-1} - p_{out}}{R_{\mu_2}}$. The pressure p_C^{n-1} is assumed to be zero for $n = 1$.

Since R_{μ_1} has been added to eliminate oscillations in the CR_{μ_2} model, the incoming wave from the 1-D terminal branch is allowed to reach C and R_{μ_2} without being reflected in R_{μ_1}. This is achieved by considering $R_t = 0$ in the R_{μ_1} compartment based on (2.140), which leads to

$$R_{\mu_1} = \frac{\rho c_{0_L}}{A_{0_L}}. \tag{2.148}$$

The same algorithm is used to couple the 1-D linear formulation to a RCR windkessel model, though now Equation (2.138) has an analytical solution. According to (2.40), Equation (2.145) becomes

$$Q^u = A^u U^u = \frac{\frac{\rho\left(c_{0_L}\right)^2}{A_{0_L}}\left(A^u - A_{0_L}\right) - p_C}{R_{\mu_1}}, \tag{2.149}$$

and according to (2.41), Equation (2.137) becomes

$$\Delta W_f\left(A_L, U_L\right) = U^u + \frac{c_{0_L}}{A_{0_L}}\left(A^u - A_{0_L}\right), \tag{2.150}$$

with $\Delta W_f\left(A_L, U_L\right) = U_L + \frac{c_{0_L}}{A_{0_L}}\left(A_L - A_{0_L}\right)$. Combination of (2.149) and (2.150) yields

$$R_{\mu_1}\frac{c_{0_L}}{A_{0_L}}\left(A^u\right)^2 + \left(\frac{\rho\left(c_{0_L}\right)^2}{A_{0_L}} - R_{\mu_1}\left(\Delta W_f + c_{0_L}\right)\right)A^u - \left(\rho\left(c_{0_L}\right)^2 + p_C\right) = 0. \tag{2.151}$$

2.7.3.7 Four-element (RCLR) windkessel model

The last model considered includes the wall compliance and fluid resistance and inertia of the vessels beyond the terminal artery (Figure 2.7, d). The initial resistance R_{μ_1} is governed by Equation (2.145) and the CLR_{μ_2} system by equations

$$\begin{cases} C\dfrac{\mathrm{d}p_C}{\mathrm{d}t} + Q_{out} - Q_{in} = 0, \\ L\dfrac{\mathrm{d}Q_{out}}{\mathrm{d}t} + R_{\mu_2}Q_{out} + p_{out} - p_C = 0, \end{cases} \tag{2.152}$$

with p_C the pressure across C. At a time step n, Equation (2.145) takes the form

$$Q_{in}^n = \frac{p_{in}^n - p_C^n}{R_{\mu_1}}. \tag{2.153}$$

The mass conservation equation in (2.152) is expressed in first-order form in time as

$$p_C^n = p_C^{n-1} + \frac{\Delta t}{C}(Q_{in}^n - Q_{out}^n), \tag{2.154}$$

and the momentum equation as

$$Q_{out}^{n} = \left(1 - \frac{\Delta t R_{\mu_2}}{L}\right) Q_{out}^{n-1} + \frac{\Delta t}{L}(p_C^{n-1} - p_{out}). \tag{2.155}$$

Substituting (2.154) into (2.153) with Q_{out}^{n} expressed through (2.155) yields

$$Q_{in}^{n} = \frac{1}{R_{\mu_1} + \frac{\Delta t}{C}} \left[p_{in}^{n} + p_C^{n-1}\left(\frac{\Delta t^2}{LC} - 1\right) + Q_{out}^{n-1}\left(1 - \frac{\Delta t R_{\mu_2}}{L}\right)\frac{\Delta t}{C} - p_{out}\frac{\Delta t^2}{CL}\right]. \tag{2.156}$$

It is considered that the state (A^u, U^u) satisfies (2.156) with $Q_{in}^{n} = (A^u)^n (U^u)^n$ and $p_{in}^{n} = p\left((A^u)^n\right)$, according to (2.11). Combination of (2.137) and (2.156) yields a non-linear equation in A^u that is solved by the Newton's method (with $A^u = A_L$ as the initial guess). Next, $(U^u)^n$ is calculated by means of (2.137). The boundary condition is prescribed through (2.71) with $U_{bc} = U^u$ and assuming $A_R = A_L$. The value of Q_{out}^{n} is updated at every time step using (2.155). Once Q_{out}^{n} is known, p_C^{n} is updated through (2.154), with $Q_{in}^{n} = (A^u)^n (U^u)^n$.

In the linear formulation, Equations (2.150) and (2.156) are combined to obtain an equation in A^u with an analytical solution. The rest of the algorithm follows as in the non-linear formulation.

2.8 Estimation of the peripheral resistance, inertia and compliance

This section proposes a new technique based on scaling laws to estimate the fluid resistance and inertia and the wall compliance of the neglected vessels perfused by the terminal branches of the 1-D model. This technique assumes that the radii and lengths of the neglected vessels are constant, although they vary from bifurcation to bifurcation, and makes the major assumption that the neglected vessels are arranged in a bifurcating tree without the anastomosis present in the network formed by the peripheral vessels (Figure 1.3).

Following Papageorgiou and Jones [66], the radii and lengths of successive generations of bifurcations can be approximated by a geometric series; i.e, if R_0 is the initial radius and l_0 is the length of the terminal artery, then the radius, R_1, and the length, l_1, of its two daughters are

$$R_1 = \varphi\, R_0, \qquad l_1 = \lambda\, l_0,$$

with φ and λ constant scaling factors. Following the same reasoning, the radius, R_2, and the length, l_2, of each of the four vessels originated after the second bifurcation can be expressed as

$$R_2 = \varphi R_1, \qquad l_2 = \lambda l_1.$$

Generalising for the nth bifurcation we can write

$$R_n = \varphi R_{n-1}, \qquad l_n = \lambda l_{n-1}, \tag{2.157}$$

with R_n and l_n the radius and the length of each of the 2^n vessels after the nth bifurcation. We notice that these values are related to R_0 and l_0 through

$$R_n = \varphi^n R_0, \tag{2.158}$$

$$l_n = \lambda^n l_0. \tag{2.159}$$

Therefore, the cross-sectional area of each vessel after the nth bifurcation is

$$A_n = \pi R_n^2 = \varphi^{2n} A_0, \tag{2.160}$$

with A_0 the cross-sectional area of the terminal artery at the reference state $(A, p, U) = (A_0, p_0, U_0)$. The sum of the areas A_n of the 2^n vessels after the nth bifurcation, A_{T_n}, is

$$A_{T_n} = 2^n A_n = (2\varphi^2)^n A_0. \tag{2.161}$$

Similarly, the volume of the 2^n vessels after the nth bifurcation, V_{T_n}, is

$$V_{T_n} = 2^n A_n l_n = (2\lambda\varphi^2)^n V_0, \tag{2.162}$$

with $V_0 = A_0 l_0$. The lateral surface of the 2^n vessels after the nth generation, S_{T_n}, is

$$S_{T_n} = 2^n 2\pi R_n l_n = (2\varphi\lambda)^n S_0, \tag{2.163}$$

with $S_0 = 2\pi R_0 l_0$.

The value of φ and λ can be bounded by assuming:

1. The radius of each vessel decreases after each bifurcation; i.e., $\varphi < 1$.

2. The length of each vessel decreases after each bifurcation; i.e., $\lambda < 1$.

3. The total cross-sectional area increases after each bifurcation up to the capillaries (see Table 1.1); i.e., $2\varphi^2 > 1$.

4. The total volume decreases after each bifurcation; i.e., $2\lambda\varphi^2 < 1$.

5. The total lateral surface increases after each bifurcation; i.e., $2\lambda\varphi > 1$.

The two last conditions aim at providing blood perfusion with a small vessel volume and a large lateral surface. Figure 2.8 shows these conditions plotted in the (φ, λ) space. The shaded area contains the set of all φ and λ values that satisfy all of the constraints. We notice that the choice of a valid pair of φ and λ values is limited to a small region; for a given φ, λ is bounded by

$$\frac{1}{2\varphi} < \lambda < \frac{1}{2\varphi^2}. \tag{2.164}$$

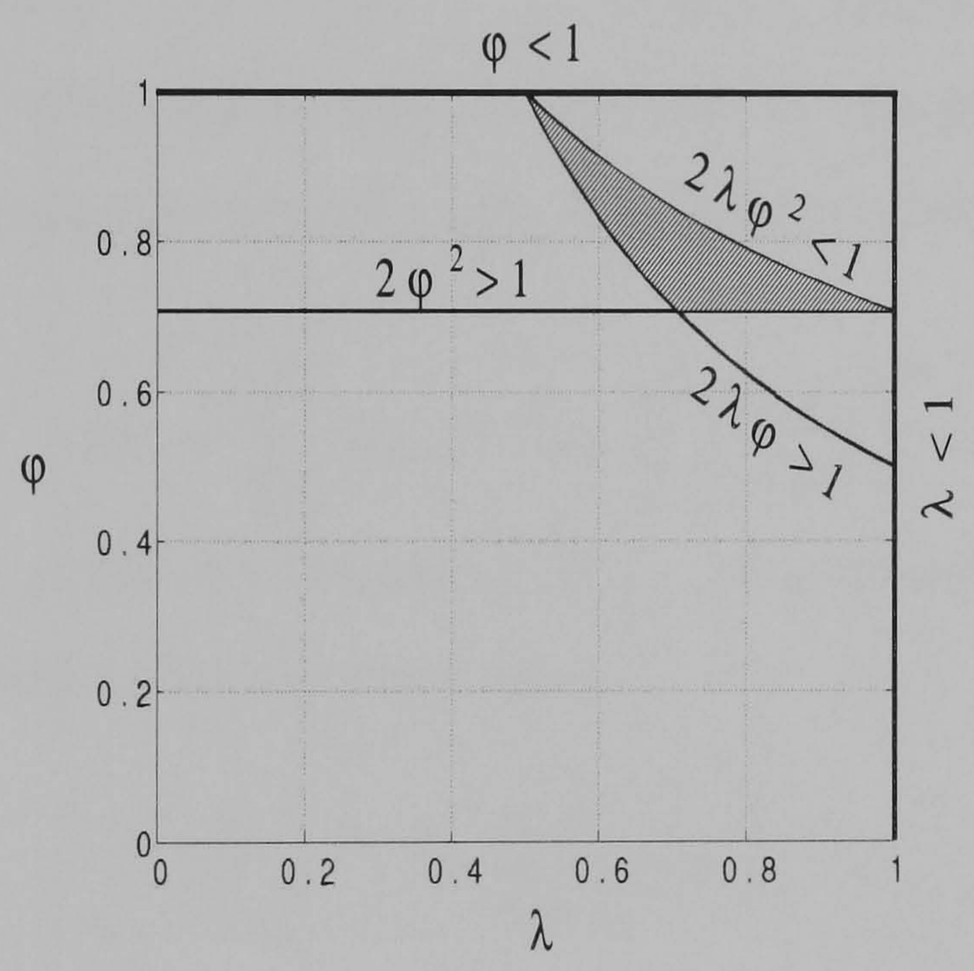


Figure 2.8: The scaling factors φ and λ, used to estimate the radii and lengths of the neglected vessels perfused by the 1-D terminal branches, are limited to the shaded region, according to the constraints explained in the text.

Sections 2.8.1 to 2.8.3 will use the scaling laws proposed in this section to estimate the total resistance, inertia and compliance of the vessels neglected by the 1-D model.

2.8.1 Resistance

Under the assumption of Poiseuille's flow, the pressure gradient in each vessel after the nth bifurcation, Δp_n, is related to the corresponding flow rate, Q_n, through

$$\Delta p_n = \frac{8\mu l_n}{\pi \left(R_n\right)^4} Q_n. \tag{2.165}$$

We notice that Poiseuille's flow is an approximation to the pulsatile flow observed in the small arteries (Figure 1.10) and to the non-Newtonian behaviour of blood in the arterioles and capillaries (Figure 1.6). If we assume that the flow rate is the same in each of the 2^n vessels, then $Q_n = \frac{Q_0}{2^n}$, with Q_0 the mean flow at the outlet of the terminal artery. Therefore, substitution of Expressions (2.158) and (2.159) into (2.165) leads to

$$\Delta p_n = \left(\frac{\lambda}{2\varphi^4}\right)^n \frac{8\mu l_0}{\pi \left(R_0\right)^4} Q_0 = \left(\frac{\lambda}{2\varphi^4}\right)^n \Delta p_0, \tag{2.166}$$

with Δp_0 the mean pressure gradient at the 1-D terminal artery.

According to (2.166), the pressure gradient is the same in all the vessels after the nth bifurcation. Hence, in a network with N generations of bifurcations, the pressure gradient between the outlet of the terminal artery and the outlet of the vessels after the Nth bifurcation, Δp_T, is the sum of the pressure gradients after each bifurcation through the network, Δp_n, starting from the outlet of the terminal artery; i.e.,

$$\Delta p_T = \sum_{n=1}^{N} \Delta p_n = \Delta p_0 \sum_{n=1}^{N} \left(\frac{\lambda}{2\varphi^4}\right)^n. \tag{2.167}$$

Dividing Δp_T by Q_0 yields the resistance, $R_{\mu_{T_N}}$, of a network with N generations of bifurcations attached to the terminal artery

$$R_{\mu_{T_N}} = R_{\mu_0} \sum_{n=1}^{N} \left(\frac{\lambda}{2\varphi^4}\right)^n, \tag{2.168}$$

with $R_{\mu_0} = \frac{\Delta p_0}{Q_0}$. We note that $\frac{\lambda}{2\varphi^4}$ is not always smaller than one. If it is, then $R_{\mu_{T_N}}$ converges to R_{μ_T} as N tends to infinity, with

$$R_{\mu_T} = \left(\frac{1}{1 - \frac{\lambda}{2\varphi^4}} - 1\right) R_{\mu_0} = \left(\frac{\lambda}{2\varphi^4 - \lambda}\right) R_{\mu_0}. \tag{2.169}$$

2.8.2 Inertia

According to (2.117), the inertia, L_n, of the blood flowing in a vessel after the nth bifurcation is

$$L_n = \frac{\rho l_n}{A_n}. \tag{2.170}$$

Substitution of (2.159) and (2.160) into (2.170) yields

$$L_n = \left(\frac{\lambda}{\varphi^2}\right)^n L_0, \tag{2.171}$$

with $L_0 = \rho l_0/A_0$. Since inductances (or inertias) add in the same fashion as resistances, the total inertia of the 2^n vessels after the nth bifurcation, L_{T_n}, is

$$L_{T_n} = \frac{L_n}{2^n} = \left(\frac{\lambda}{2\varphi^2}\right)^n L_0. \tag{2.172}$$

The inertia of the whole network attached to the terminal artery, L_T, is the sum of L_{T_n} after each bifurcation (except for L_0). Since $\lambda < 1$ and $\varphi^2 > \frac{1}{2}$ (see Figure 2.8), then $\frac{\lambda}{2\varphi^2} < 1$ and L_T converges to

$$L_T = \sum_{n=1}^{\infty} L_{T_n} = \left(\frac{1}{1-\frac{\lambda}{2\varphi^2}} - 1\right) L_0 = \left(\frac{\lambda}{2\varphi^2 - \lambda}\right) L_0. \tag{2.173}$$

2.8.3 Compliance

According to (2.25), c_0 is proportional to $A_0^{-1/4}$. If we assume that c_n is proportional to $A_n^{-1/4}$ for any generation of bifurcations n, then from (2.160) we obtain

$$c_n = \varphi^{-n/2} c_0, \tag{2.174}$$

According to (2.118), the compliance of a vessel after the nth bifurcation is

$$C_n = \frac{A_n l_n}{\rho\,(c_n)^2}. \tag{2.175}$$

Substitution of (2.159), (2.160) and (2.174) into (2.175) yields

$$C_n = \left(\lambda\varphi^3\right)^n C_0, \tag{2.176}$$

with $C_0 = \frac{A_0 l_0}{\rho(c_0)^2}$. The total compliance of the vessels after the nth bifurcation, C_{T_n}, is

$$C_{T_n} = 2^n C_n = \left(2\lambda\varphi^3\right)^n C_0. \tag{2.177}$$

The compliance of the whole network attached to the terminal artery, C_T, is obtained by adding the compliances C_{T_n} after each bifurcation (except for C_0). Since $\varphi < 1$ and $2\lambda\varphi^2 < 1$ (see Figure 2.8), then $2\lambda\varphi^3 < 1$, and C_T converges to

$$C_T = \sum_{n=1}^{\infty} C_{T_n} = \left(\frac{1}{1-2\lambda\varphi^3} - 1\right) C_0 = \left(\frac{2\lambda\varphi^3}{1-2\lambda\varphi^3}\right) C_0. \tag{2.178}$$

Section 3.2 will show that C_T converges to the value determined by (2.178) after a few generations, and, hence, the smaller arteries and the arterioles and capillaries have little contribution to the total peripheral compliance, which justifies the assumption of pulsatile flow in the determination of the total peripheral compliance.

2.8.4 Which values of φ and λ?

The value of φ is taken to be $\varphi = \sqrt{0.6}$, which is the value calculated by Papageorgiou and Jones [66] based on data taken from Avolio [6] and Suwa *et al* [89]. Suwa *et al* estimated the diameter of the small arterial branches up to the order of microns. We notice that this value of φ is very similar to the value obtained assuming that the flow rate through each vessel of a branching network, Q_n, is proportional to R_n^3, according to the cube law described by Zamir [101]. With this relation between the radius and the flow rate, conservation of mass at any bifurcation of the network leads to

$$R_{n-1}^3 = 2R_n^3. \tag{2.179}$$

Substitution of (2.157) into (2.179) yields $\varphi = 2^{-1/3} \simeq \sqrt{0.6}$.

We also notice that $R_{f_1} \simeq 0$ in (2.110) if we consider the scaling factor $\varphi = \sqrt{0.6}$ between the radii of the parent and daughter vessels, and the same value of β in each vessel, so that c_0 only depends on A_0 (see Equation (2.25)). Therefore, $\varphi = \sqrt{0.6}$ minimises wave reflections at a bifurcation for forward travelling waves. The cube law assumes Poiseuille's flow and minimises the pumping power required to maintain flow rate through vessels plus the metabolic power to maintain the volume of flow to fill the vessels.

According to (2.164), λ is bounded by two extremes. Closer to the lower extreme, the volume V_{T_n} given by (2.162) is minimum, but so is the lateral surface S_{T_n} given by (2.163) and, hence, blood perfusion. On the other hand, closer to the upper extreme S_{T_n} is maximum but also V_{T_n}. A relation between φ and λ is established by maximising the ratio

$$\frac{S_{T_N}/S_0}{V_T/V_0}, \tag{2.180}$$

where $S_{T_N} = (2\varphi\lambda)^N S_0$ is the lateral surface of the 2^N capillary beds (N is the number of generations to reach the capillary beds from the terminal artery), and V_T is the volume of all the vessels in the network up to the capillaries

$$V_T = \sum_{n=0}^{N} V_{T_n} = \sum_{n=0}^{N} (2\lambda\varphi^2)^n V_0 = \frac{1}{1-2\lambda\varphi^2} V_0, \tag{2.181}$$

since $2\lambda\varphi^2 < 1$ (see Figure 2.8). The surface has been normalised by S_0 and the

volume by V_0, which reduces the ratio (2.180) to

$$\left(1 - 2\lambda\varphi^2\right)\left(2\varphi\lambda\right)^N. \tag{2.182}$$

Expression (2.182) reaches its maximum when

$$\lambda = \frac{N}{N+1}\frac{1}{2\varphi^2}. \tag{2.183}$$

This value guarantees the maximum perfusion at the last bifurcation of capillaries with the minimum space occupied by the whole branching network attached at the outflow of the terminal artery.

2.9 Final remarks

This chapter has detailed the mathematical formulation of the model used in this thesis, both for the linear and non-linear formulations. The model will be validated and applied to study problems of clinical interest in the following chapters. In Chapter 3, the 1-D formulation will be validated by comparison against an experimental model, the algorithm proposed in Section 2.8 to estimate the parameters of the terminal models will be tested with physiological data, and the 1-D formulation will be applied to explain the main *in-vivo* features of pulse wave propagation along the human aorta. Chapters 4 and 5 will use the 1-D formulation to study the effects of anatomic variations and partial or total occlusions of arteries on pulse wave propagation in the human arm and in the cerebral circulation.

Chapter 3

Validation

This chapter starts with a validation of the formulation introduced in Chapter 2 against a well-defined experimental model of the left ventricle, the largest systemic arteries, and the terminal impedances, which has been shown to simulate physiological conditions very well (Section 3.1). Section 3.2 assesses the ability of the algorithm described in Section 2.8 to approximate the wall compliance and the fluid resistance and inertia of the neglected vessels beyond the 1-D terminal branches. Section 3.3 presents a 1-D simulation of the human aorta coupled to a RCR lumped parameter model of the rest of the systemic circulation. This simulation is able to successfully approximate and explain the shapes and values of pressure, velocity, and flow rate pulse waves observed *in-vivo* along the aorta. Finally, Section 3.4 analyses the sensitivity of the results obtained in Section 3.3 to the polynomial and quadrature order of the numerical scheme, the non-linear terms of the governing equations, the geometry and elasticity of the aorta, the density and viscosity of blood, the peripheral resistance, compliance and venous pressure, and the different lumped parameter models described in Section 2.7.3.

3.1 Validation versus a well-defined experimental arterial system

An accurate quantitative validation of the 1-D formulation against *in-vivo* data is very complicated because some of the elastic and geometrical properties of the system are very difficult to measure. In this section, the accuracy of the 1-D numerical scheme is validated against a well-defined laboratory model in which most of the parameters required by the algorithm can be easily measured. The experiment is also a reasonably good approximate representation of the systemic circulation and, hence, it provides a good test of the accuracy of the numerical model. The haemodynamic data registered in the laboratory are clinically relevant because the performance of the heart, the geometrical and elastic properties of the human arteries, and the peripheral impedances are well approximated by the experiment.

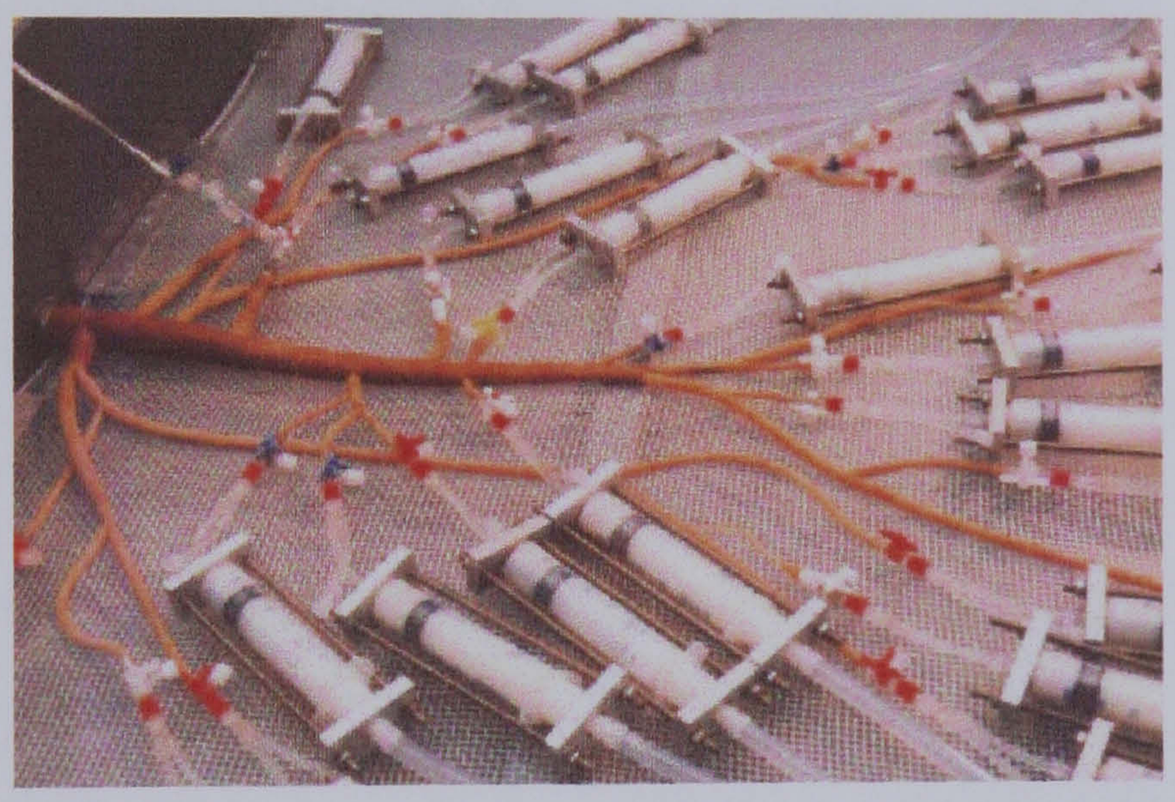


Figure 3.1: Anatomically correct 1:1 replica of the human left heart and the main arteries of the systemic tree made by Segers *et al* [78] at IBITECH (University of Ghent, Belgium) and used in this work to validate the 1-D formulation. The main tapering tube represents the aorta. The syringes simulate the resistance and compliance of the small arteries, arterioles and capillaries. (Taken from Prof. Segers' PhD thesis [77].)

The experimental arterial system, made by Segers *et al* [78] and shown in Figure 3.1, is described in Section 3.1.1. Section 3.1.2 explains how the experiment has been simulated and Section 3.1.3 discusses the results obtained.

3.1.1 Description of the experimental model

The experimental model is an anatomically correct 1:1 replica of the human left heart and the 55 largest human conduit arteries of the systemic circulation (Figure 3.2, left). The arteries are made of natural latex rubber and they reproduce

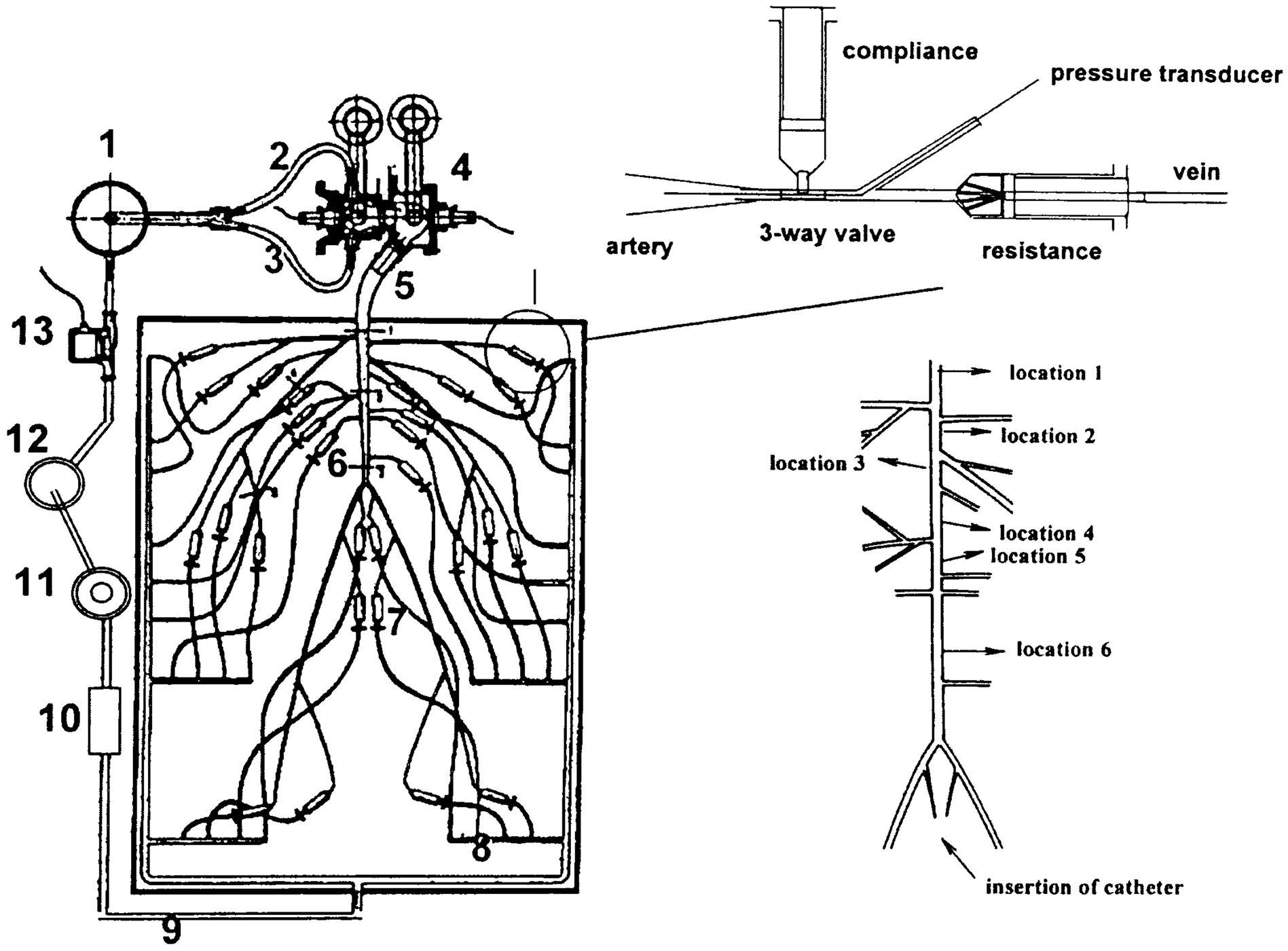


Figure 3.2: (left) Schematic of the experimental model. 1: lung reservoir; 2: pulmonary veins; 3: left atrium; 4: left ventricle; 5: aorta; 6: aorto-iliac bifurcation; 7: peripheral model; 8: veins; 9: venous return conduit; 10: electromagnetic flow meter; 11: venous overflow; 12: buffering reservoir; 13: pump. (top right) Schematic of the peripheral models used to simulate the resistance and compliance of the vessels neglected beyond the terminal branches. (bottom right) Indication of the six measuring locations along the aorta: ascending aorta (1), thoracic I (2) and II (3), and abdominal I (4), II (5) and V (6). (Taken from Segers and Verdonck [80].)

the configuration published by Westerhof *et al* [96] and Stergiopulos *et al* [88] (Figure 3.3), which consists of the aorta, the largest arteries of the upper and lower limbs, the carotid and vertebral arteries, and the major branches to the abdominal organs (mesenterics, kidneys, and splanchnic tree) of a male subject of 1.75 m and 75 Kg.

Tables 3.1 and 3.2 show the length, diameter, thickness, and elastic modulus of each artery in the experiment. The diameters and thicknesses decrease approx-

imately linearly along most of the arteries and the corresponding elastic moduli increase approximately linearly. Along the aorta, wave speed increases from 6 m/s at the inlet of the ascending aorta to 17.5 m/s at the outlet of the abdominal aorta. In general, wave speeds are about 50% higher than the *in-vivo* values in healthy conditions, which indicates that the arteries of the experiment are overly stiff [78].

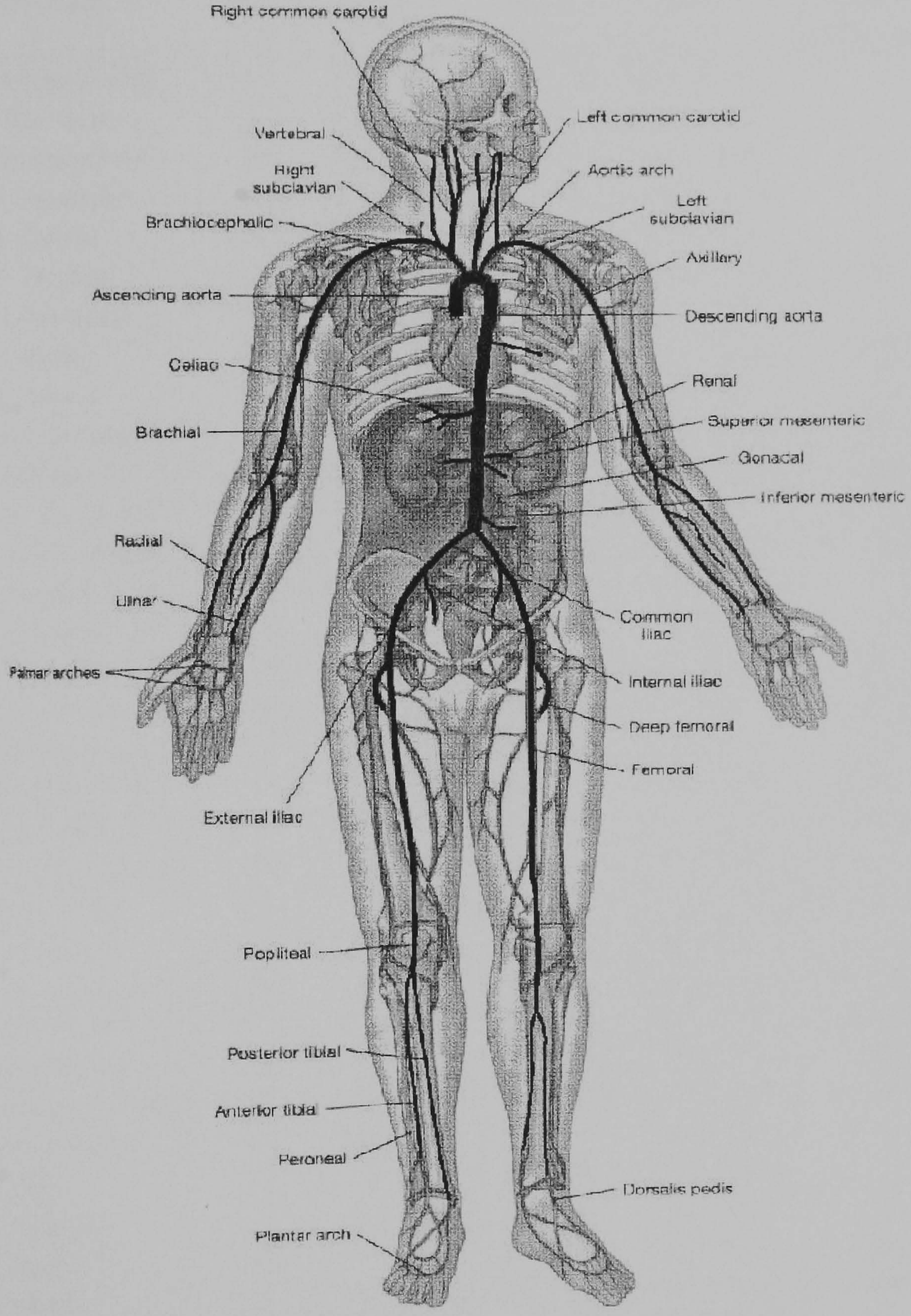


Figure 3.3: The 55 arteries simulated by the experiment. (Modified from Purves *et al* [71].)

Table 3.1: Geometrical and elastic properties of the 55 arterial segments in the hydrodynamic model shown in Figures 3.1 to 3.3. Cross-sectional diameters and wall thicknesses decrease approximately linearly and elastic moduli increase approximately linearly. $D_{in} \rightarrow D_{out}$: diastolic cross-sectional diameters at the inlet and at the outlet of each vessel, $h_{in} \rightarrow h_{out}$: wall thicknesses at the inlet and at the outlet of each vessel, $E_{in} \rightarrow E_{out}$: elastic moduli at the inlet and at the outlet of each vessel. Continued on Table 3.2. (Data from Prof. Segers' PhD thesis [77].)

Arterial segment	Length (mm)	$D_{in} \rightarrow D_{out}$ (mm)	$h_{in} \rightarrow h_{out}$ (mm)	$E_{in} \rightarrow E_{out}$ (kPa)	Peripheral resistance (10^9 Pa s m^{-3})
1. Ascending Aorta	60	29.4 → 28.8	1.43 → 1.44	587 → 819	-
2. Aortic Arch I	20	28.8 → 11.3	1.44 → 1.44	819 → 905	-
3. Brachiocephalic	30	21.5 → 13.7	1.14 → 1.14	741 → 493	-
4. R. Subclavian I	45	8.3 → 8.3	0.7 → 0.7	1434 → 1434	-
5. R. Carotid	160	11.5 → 8.0	0.8 → 0.8	547 → 423	-
6. R. Vertebral	137	3.8 → 3.8	0.4 → 0.4	1073 → 1073	3.08
7. R. Subclavian II	8.3	8.3 → 4.8	0.7 → 0.5	1507 → 1620	-
8. R. Radial	240	3.5 → 3.5	0.4 → 0.4	1317 → 1317	14.66
9. R. Ulnar I	80	3.5 → 3.5	0.3 → 0.3	1745 → 1745	-
10. R. Interosseous	69	2.0 → 2.0	0.3 → 0.3	994 → 994	23.94
11. R. Ulnar II	141	3.5 → 3.5	0.3 → 0.3	1745 → 1745	7.68
12. R. int. Carotid	158	6.0 → 4.2	0.5 → 0.5	573 → 446	134.53
13. R. ext. Carotid	158	6.0 → 4.2	0.5 → 0.5	550 → 428	5.64
14. Aortic Arch II	20	28.8 → 27.1	1.44 → 1.44	905 → 994	-
15. L. Carotid	200	11.3 → 7.8	0.8 → 0.8	599 → 448	-
16. L. int. Carotid	158	6.0 → 4.2	0.6 → 0.6	486 → 378	7.72
17. L. ext. Carotid	158	6.0 → 4.2	0.6 → 0.6	490 → 381	13.26
18. Thoracic Aorta I	30	27.1 → 25.8	1.44 → 1.42	994 → 1133	-
19. L. Subclavian I	40	8.3 → 8.3	0.6 → 0.6	1744 → 1744	-
20. L. Vertebral	137	3.8 → 3.8	0.4 → 0.4	1114 → 1114	7.72
21. L. Subclavian II	392	8.3 → 4.9	0.5 → 0.5	1810 → 1889	-
22. L. Radial	223	3.5 → 3.5	0.3 → 0.3	1725 → 1725	43.55
23. L. Ulnar I	68	3.5 → 3.5	0.4 → 0.4	1291 → 1291	-
24. L. Interosseous	72	2.0 → 2.0	0.3 → 0.3	1183 → 1183	134.90
25. L. Ulnar II	155	3.5 → 3.5	0.4 → 0.4	1291 → 1291	26.75
26. Intercostals	75	12.9 → 9.8	0.9 → 0.9	741 → 546	1.69
27. Thoracic Aorta II	130	25.8 → 20.4	1.42 → 1.27	1133 → 1823	-
28. Abdominal I	60	20.4 → 17.9	1.27 → 1.15	1823 → 2210	-
29. Celiac I	37	8.5 → 5.0	0.5 → 0.5	1649 → 1163	-
30. Celiac II	1	5.0 → 4.9	0.5 → 0.5	1163 → 1145	-
31. Hepatic	62	3.2 → 3.1	0.4 → 0.4	959 → 929	2.92
32. Gastric	54	4.3 → 4.7	0.4 → 0.4	1489 → 1344	2.55
33. Splenic	56	4.3 → 4.0	0.5 → 0.5	879 → 847	2.21
34. Sup. Mesenteric	54	8.1 → 7.3	0.7 → 0.7	1482 → 1405	2.49
35. Abdominal II	40	17.9 → 16.2	1.15 → 1.05	2210 → 2508	-
36. L. Renal	27	5.2 → 5.2	0.9 → 0.9	1001 → 1001	1.93
37. Abdominal III	10	16.2 → 15.8	1.05 → 1.03	2508 → 2590	-
38. R. Renal	27	5.2 → 5.2	0.8 → 0.8	1133 → 1133	1.24
39. Abdominal IV	100	15.8 → 11.6	1.03 → 0.7	2590 → 3684	-

Table 3.2: Continued from Table 3.1.

Arterial segment	Length (mm)	$D_{in} \rightarrow D_{out}$ (mm)	$h_{in} \rightarrow h_{out}$ (mm)	$E_{in} \rightarrow E_{out}$ (kPa)	Peripheral resistance (10^9 Pa s m^{-3})
40. Inf. Mesenteric	44	5.1 → 3.5	0.5 → 0.5	2079 → 1692	4.24
41. Abdominal V	20	11.6 → 10.7	0.7 → 6.4	3684 → 4017	-
42. L. common Iliac	50	8.0 → 7.7	0.5 → 0.5	2591 → 2605	-
43. R. common Iliac	50	8.0 → 7.7	0.5 → 0.5	2833 → 2817	-
44. L. ext. Iliac	140	7.7 → 6.9	0.5 → 0.5	2653 → 2707	-
45. L. int. Iliac	40	4.0 → 4.0	0.4 → 0.4	2075 → 2075	8.40
46. L. Femoral	460	6.9 → 4.4	0.4 → 0.3	2791 → 2989	-
47. L. deep Femoral	112	4.1 → 3.8	0.4 → 0.4	1905 → 1832	19.18
48. L. post. Tibial	358	2.5 → 2.5	0.3 → 0.3	4277 → 4277	7.89
49. L. ant. Tibial	355	2.5 → 2.5	0.4 → 0.4	3465 → 3465	62.61
50. R. ext. Iliac	140	7.7 → 6.9	0.5 → 0.5	2810 → 2740	-
51. R. int. Iliac	40	4.0 → 4.0	0.4 → 0.4	1930 → 1930	6.65
52. R. Femoral	460	6.9 → 4.4	0.5 → 0.4	2708 → 2227	-
53. R. deep Femoral	112	4.1 → 3.8	0.3 → 0.3	2431 → 2338	2.75
54. R. post. Tibial	355	2.5 → 2.5	0.3 → 0.3	3670 → 3670	52.37
55. R. ant. Tibial	350	2.5 → 2.5	0.3 → 0.3	4352 → 4352	5.07

A Newtonian liquid formed by a mixture of 70% water and 30% glycerin with a density of 1 035 Kg m^{-3} and a viscosity of 2.8 mPa s is used to simulate blood. At the peripheral branches, the terminal resistance of the neglected arteries, arterioles and capillaries is modelled with an adjustable resistor made of porous rubber mounted in a syringe, and their terminal compliance is modelled by a syringe with an adjustable air chamber. Resistance and compliance are placed in parallel (Figure 3.2, top right). Downstream of each peripheral model, the resistors are connected to a rigid tube simulating the venous vessels, which are joined together in a venous return conduit that ends in an overflow system to create a constant venous pressure of $p_{out} = 10.4$ mmHg (1.4 kPa) (Figure 3.2, left). The liquid is pumped from the overflow to a lung reservoir connected to a pulse duplicator system that simulates the left heart and is able to produce physiological flow waves. The arterial network is mounted in supine position on a supporting structure and is submersed in water to create an external pressure of 5.8 mmHg (773.1 Pa) and to allow for ultrasound flow measurements.

Figures 3.4 (top) and 3.5 (top) show the pressure and flow rate time histories measured simultaneously along the aorta with high fidelity pressure tip transducers and ultrasonic flow probes. In these measurements, the pulse duplicator system was operating at 60 beats/min and producing a cardiac output of 4.3 l/min. We

observe that the experimental model is able to capture the main physiological features of pulse pressure and flow rate observed *in-vivo* (Figure 1.9) and described in Section 1.2, such as the dicrotic notch, diastolic decay, and peaking and steepening of pulse pressure as we move away from the heart, some backward flow at the end of systole, and a reduction in the amplitude of the flow with the distance from the heart. We also observe that pulse pressures are higher than for a healthy subject. which is a consequence of the latex tubes being stiffer than the arterial walls.

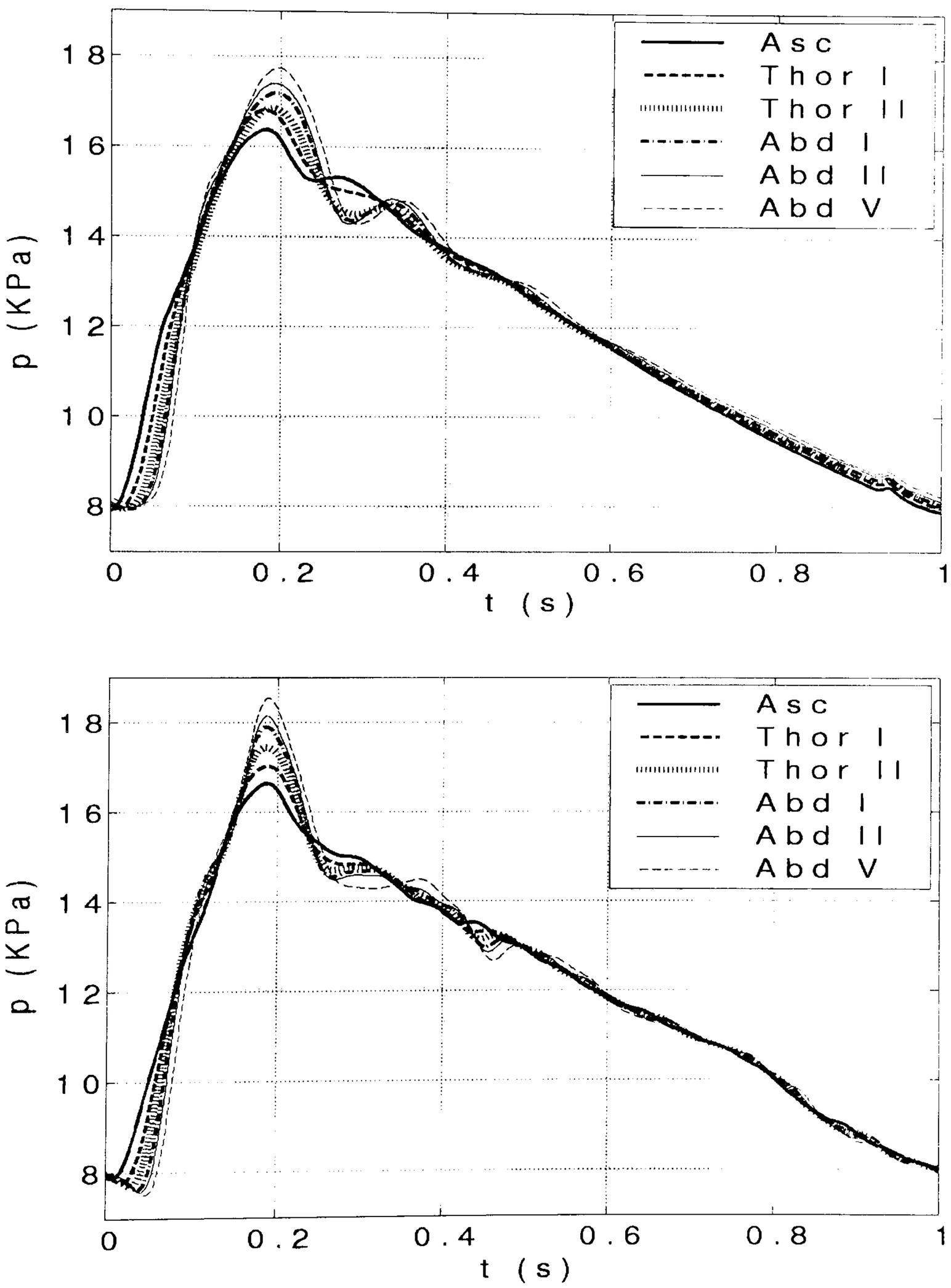


Figure 3.4: Pressure time histories along the aorta measured in the experimental model (top) and simulated by the 1-D numerical model (bottom). The locations of the measurements are the ascending aorta, thoracic I and II, and abdominal I, II and V, as indicated in Figure 3.2 (bottom right). The numerical model has been run until a periodic solution is reached.

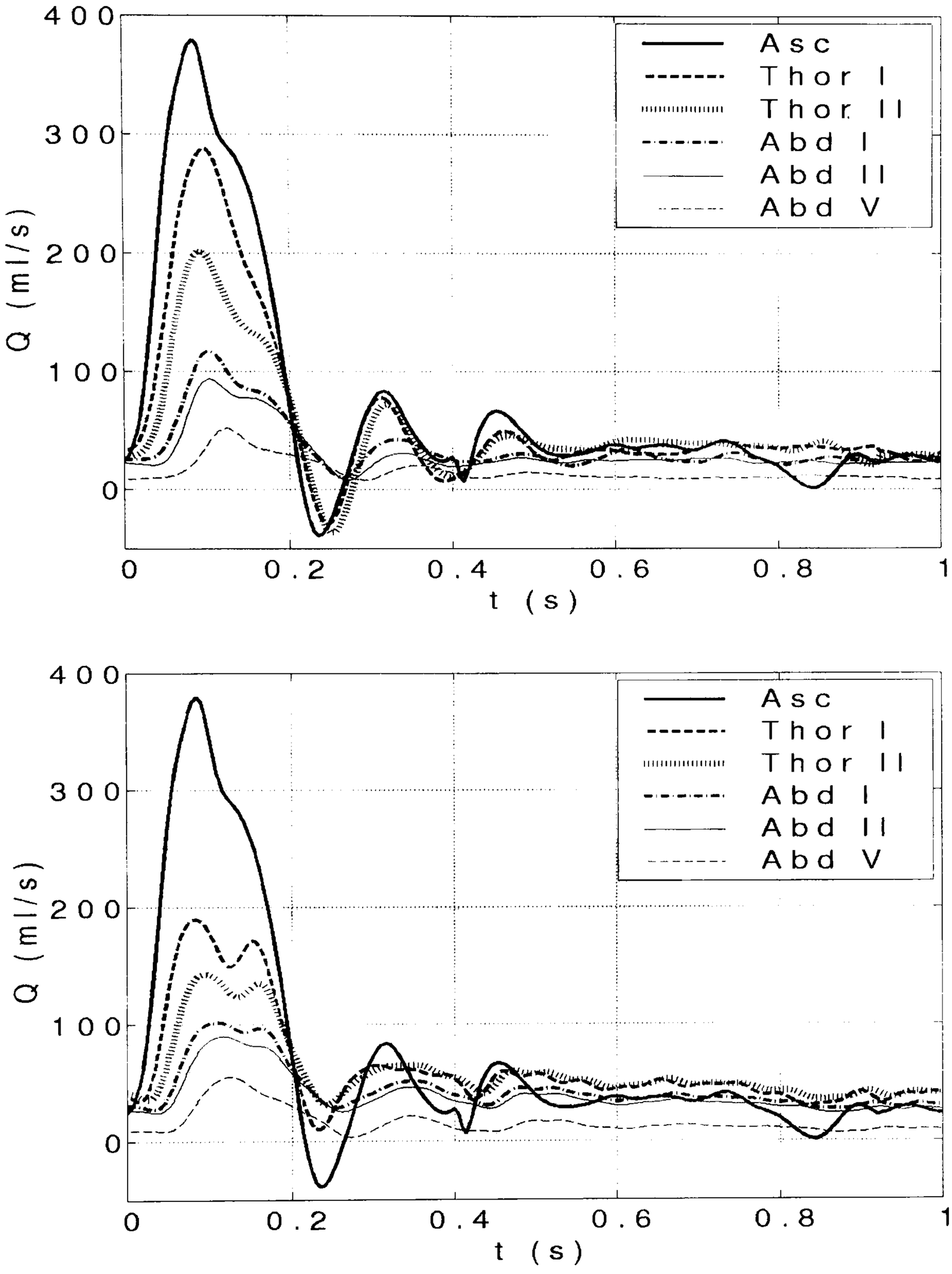


Figure 3.5: Flow rate time histories along the aorta measured in the experimental model (top) and simulated by the 1-D numerical model (bottom). The locations of the measurements are the ascending aorta, thoracic I and II, and abdominal I, II and V, as indicated in Figure 3.2 (bottom right). The numerical model has been run until a periodic solution is reached.

At each terminal branch, Tables 3.1 and 3.2 show the peripheral resistances measured in the experiment as the rate between the mean pressure and the mean flow rate. The total resistance measured at the ascending aorta is 1.26 mmHg s $\text{ml}^{-1}(1.68 \cdot 10^8$ Pa s $\text{m}^{-3})$. The peripheral compliance in each terminal branch is 0.0055 ml mmHg^{-1}, which was calculated by Segers *et al* [78] by means of the gas law $\bar{p}V^{1.2} =$ constant, where $\bar{p}$ is the average mean pressure ($\bar{p} = 90$ mmHg) close

to the outlet of the terminal branch and V is the volume of air at zero reference pressure ($V = 6$ ml) in the syringes that model the terminal compliances. The compliance of the arteries in the experiment (proximal compliance) was obtained experimentally by clamping the ascending aorta and all the terminal branches and plotting the change in pressure with the increase in the volume of all the arteries, as explained by Segers *et al* [78]. The total arterial compliance, C_T, is the sum of the proximal compliance (0.84 ml mmHg^{-1}) and the peripheral compliances in each of the terminal branches, which yields a total compliance of 1.0 ml mmHg^{-1} ($7.5 \cdot 10^{-9}$ m^3 Pa^{-1}).

3.1.2 1-D simulation

The 55 arteries of the experimental model are simulated with the non-linear 1-D formulation. Each arterial domain corresponds to one of the vessels shown in Tables 3.1 and 3.2 and it is divided into elemental regions with different values of the initial area A_0 and elastic constant β to simulate the changes in diameter, wall thickness and elasticity shown in these tables. The number of quadrature points and the polynomial order in each elemental region depend on the length of the region, but they are not larger than four in any region. A time step of $\Delta t = 100$ μs is required to run the simulation. The initial state is (A_0, p_0, U_0), with A_0 obtained from the diameters in Tables 3.1 and 3.2, $p_0 = 773.14$ Pa, which is the external pressure produced by the water that submersed the model, and $U_0 = 0$ in all the arterial domains. Although the latex rubber showed a visco-elastic character [78], the simulation is run with the tube law (2.11) that considers linear elasticity, since elastic non-linearities introduce only secondary effects (Schaaf and Abbrecht [75]).

At the inlet of the ascending aorta, the flow rate measured in the experiment at the location 1 of Figure 3.2 (bottom right) is enforced, which corresponds to the thick solid line shown in Figure 3.5 (top). The first 20 harmonics of this flow (Figure 3.6) are enforced as the inflow boundary condition of the simulation through Equation (2.69).

At the outlet of each terminal branch, the experimental peripheral models (Figure 3.2, top right) are simulated by means of the RCR windkessel model described in Section 2.7.3.6. The total resistance $(R_{\mu_1} + R_{\mu_2})$ in each terminal artery corresponds

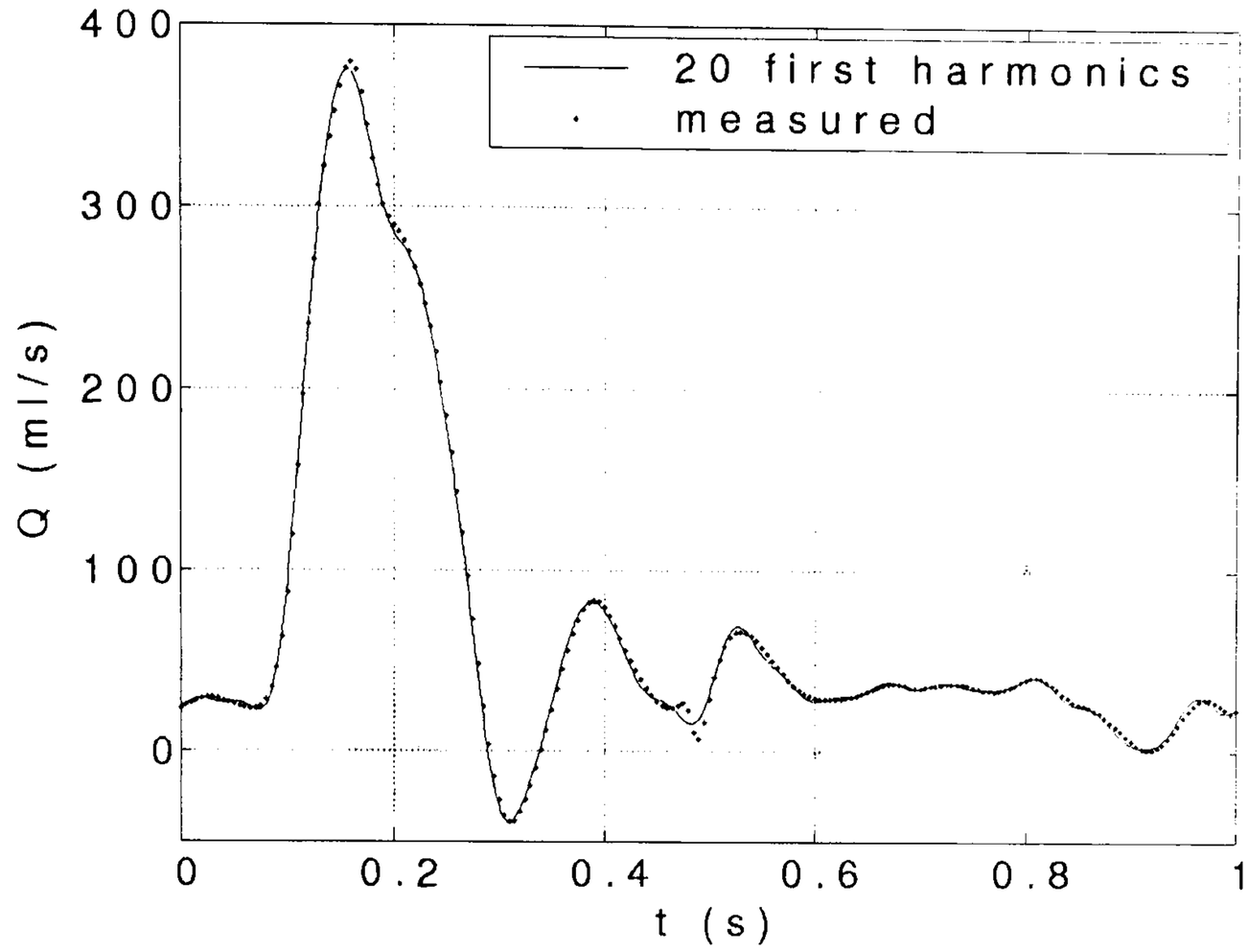


Figure 3.6: Measured flow rate at the ascending aorta (dots) of the experimental model (sampling rate of 200 Hz) and approximation by the first 20 harmonics (solid line), which is enforced as the inflow boundary condition of the 1-D simulation.

to the value shown in the last column of Tables 3.1 and 3.2, and the peripheral compliance is equal to 0.0055 ml mmHg^{-1} ($4.1 \cdot 10^{-11}$ m^3 Pa^{-1}), as explained in Section 3.1.1. We note that the resistances used in the experimental model depend on flow rate [78]. However, since flow is relatively small and nearly constant, the non-linearity of the terminal resistances is assumed to be of minor importance and is not taken into account.

Equation (2.126) is satisfied with the mean pressure ($\overline{p}_{wk} = 90$ mmHg) and flow rate ($\overline{Q} = 71$ ml/s) measured at the ascending aorta (thick solid lines in Figures 3.4 and 3.5, top), $p_{out} = 0$ and R_{μ_T} equal to the total peripheral resistance of the system, $R_{\mu_T} = 1.26$ mmHg s ml^{-1} ($1.68 \cdot 10^8$ Pa s m^{-3}), calculated from the addition in parallel of the terminal resistances shown in Tables 3.1 and 3.2. Therefore, although $p_{out} = 10.4$ mmHg in the venous circuit of the experiment, the simulation is run with $p_{out} = 0$.

3.1.3 Results and discussion

Figures 3.4 and 3.5 compare pressure and flow rate time histories at different locations along the aorta (ascending aorta, thoracic I and II, and abdominal I, II and V) obtained with the experimental and numerical models once a periodic solution has

been achieved, which takes about four cycles and five minutes to run in a normal PC. We observe that the 1-D formulation is able to approximate the dicrotic notch, peaking phenomenon, wave steepening, and diastolic decay of the experimental pressures, and the reduction in amplitude and the increase in width of the experimental flow rate waves as we move away from the heart. Figures 3.7 to 3.9 show in more detail the comparison between the experimental and numerical pulse pressures and flow rates in the ascending aorta (only pressure because the experimental flow rate is enforced as the inflow boundary condition), thoracic aorta II and abdominal aorta V, respectively.

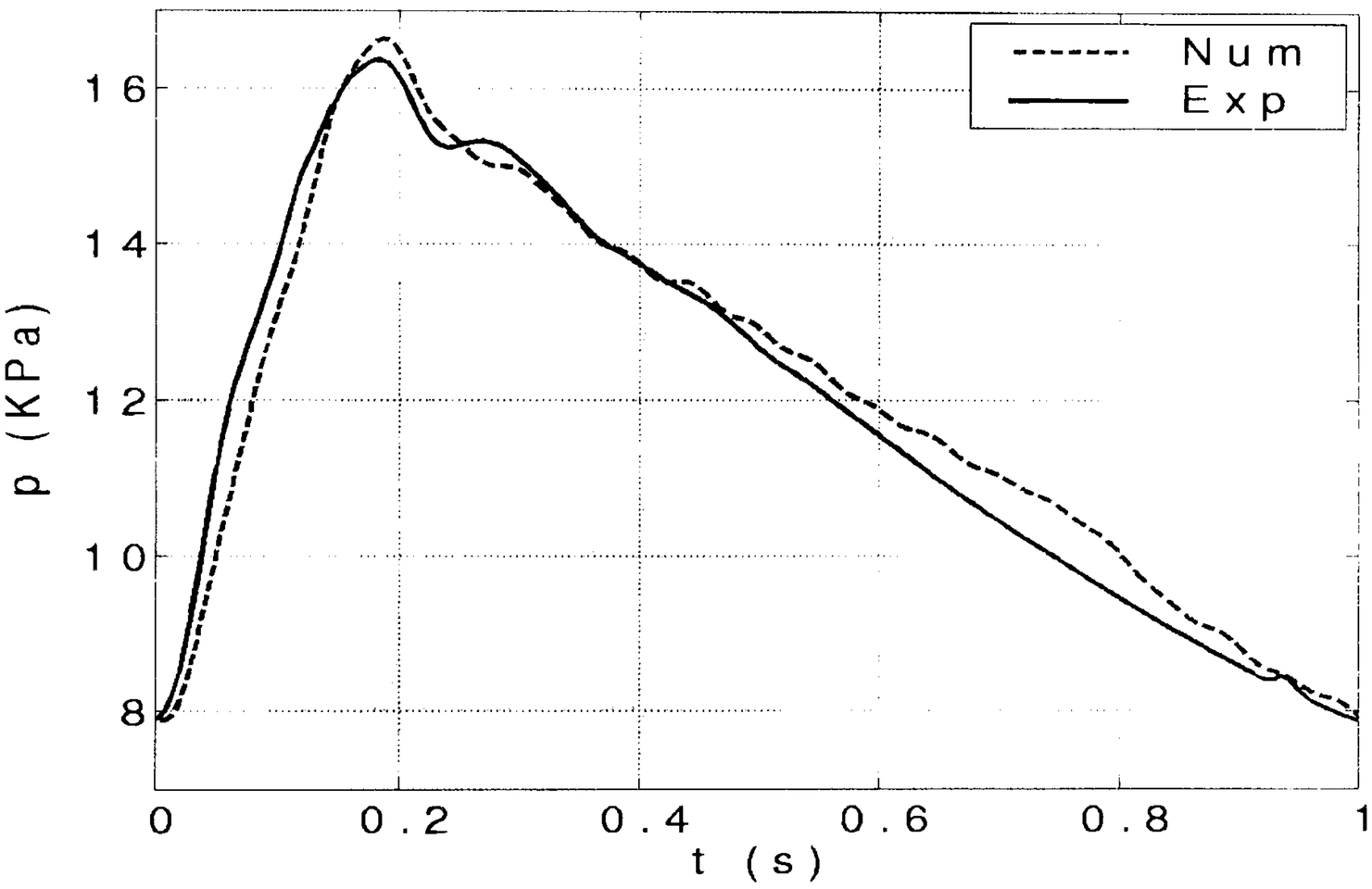


Figure 3.7: Pressure time histories in the ascending aorta of both the hydrodynamic and numerical models.

According to the results shown in Figures 3.4 to 3.9, the non-linear 1-D formulation has proved capable of capturing the main features of pulse pressure and flow rate waveforms along the experimental aorta. Despite the approximations of the 1-D formulation and the error in the experimental measurements, the quantitative agreement is also quite good, as we can see in Table 3.3. The values of the mean pressures along the aorta are well predicted by the 1-D model, with relative errors smaller than 2%. However, the simulated pulse pressures are higher than their experimental counterparts, with relative errors increasing as we move away from the heart and reaching a maximum of about 14% in the abdominal aorta V. Discrepancies in pulse pressures may be caused by the lack of elastic non-linearities and viscoelastic-

ity in the tube law considered, and errors in the measurement of the pulse pressures and elastic moduli (which are directly related to the arterial compliances and the wave speeds through Equations (2.118), (2.25) and (2.11)). Nevertheless, the simulation approximates well the slope of the exponential diastolic decays, which indicates a good approximation of the total compliance and resistance of the experimental network, according to (2.123).

The relative error in the amplitude of the flow rate measurements ($Q_{max} - Q_{min}$) is about 50% in the segments of the thoracic aorta and smaller than 30% in the segments of the abdominal aorta. However, mean flows, which depend on peripheral resistances, are better approximated by the simulation than the amplitudes of the pulse flow waves (see Table 3.3), which depend on the geometry and elasticity of the arterial network (see Section 3.4). The higher disagreement in flow comparisons than in pressure comparisons could be a consequence of the higher error in the flow measurements, although this information is not available.

Although the results of the simulation can only be compared with the experimental results along the aorta, due to the lack of experimental measurements in other locations, and considering the large number of parameters involved in the simulation (each one with an experimental error associated), the 1-D formulation is able to approximate the experimental results with significant accuracy and without tuning any of the parameters measured in the laboratory. This study increases the confidence in the 1-D code and its ability to model clinically relevant problems, such as the applications presented in this thesis.

Table 3.3: Comparison between the experimental (bold numbers) and numerical (normal numbers) systolic (p_s) and diastolic (p_d) pressures, pulse pressures (pp), mean pressures ($\overline{p}$), maximum (Q_{max}) and minimum (Q_{min}) flow rates, maximum minus minimum flow rates ($Q_{max} - Q_{min}$) and mean flow rates ($\overline{Q}$) at the six measuring locations along the aorta indicated in Figure 3.2 (bottom right). Pressures in kPa and flow rates in ml/s.

	asc. aorta	thor. I	thor. II	abd. I	abd. II	abd. V
p_s	**16.37**	**16.80**	**16.84**	**17.18**	**17.38**	**17.73**
	16.63	17.01	17.43	17.89	18.14	18.54
p_d	**7.88**	**7.94**	**7.93**	**7.92**	**7.97**	**8.04**
	7.88	7.79	7.71	7.63	7.57	7.52
pp	**8.49**	**8.86**	**8.91**	**9.25**	**9.41**	**9.69**
	8.75	9.22	9.72	10.26	10.57	11.02
$\overline{p}$	**11.96**	**11.98**	**11.89**	**11.95**	**12.02**	**12.08**
	12.08	12.08	12.07	12.07	12.07	12.07
Q_{max}	**379.30**	**287.90**	**201.00**	**117.40**	**93.77**	**51.94**
	379.30	189.60	142.90	101.70	89.98	55.35
Q_{min}	**-39.33**	**-29.36**	**-36.55**	**9.85**	**7.64**	**8.09**
	-39.33	9.98	31.23	27.08	24.06	3.41
$Q_{max} - Q_{min}$	**418.63**	**317.26**	**237.55**	**107.55**	**86.13**	**43.85**
	418.63	179.62	111.67	74.62	65.92	51.94
$\overline{Q}$	**70.83**	**59.50**	**50.04**	**35.95**	**31.13**	**15.35**
	70.83	62.61	59.29	44.18	38.84	15.91

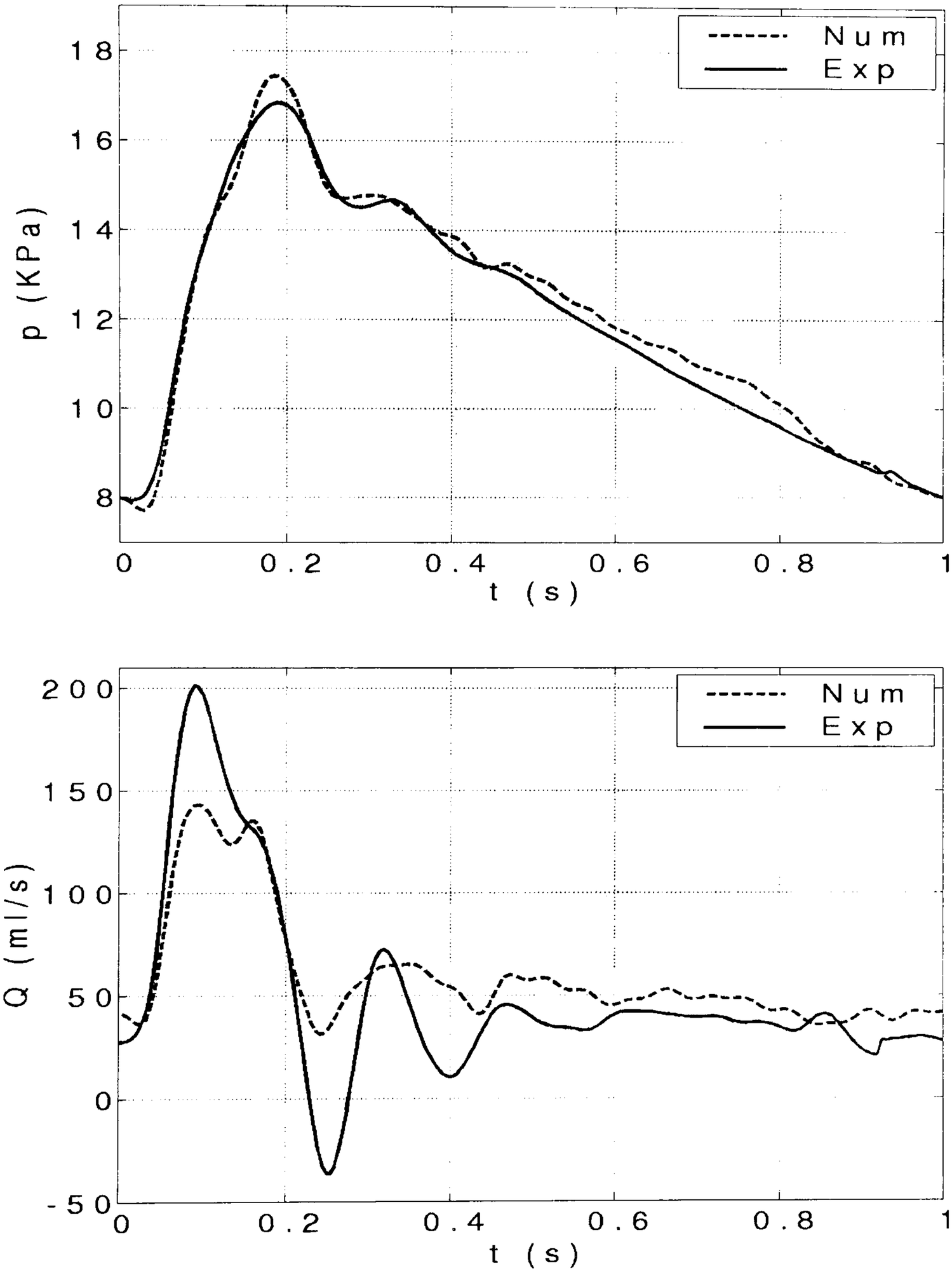


Figure 3.8: Pressure (top) and flow rate (bottom) time histories in the thoracic aorta II of both the experimental and numerical models.

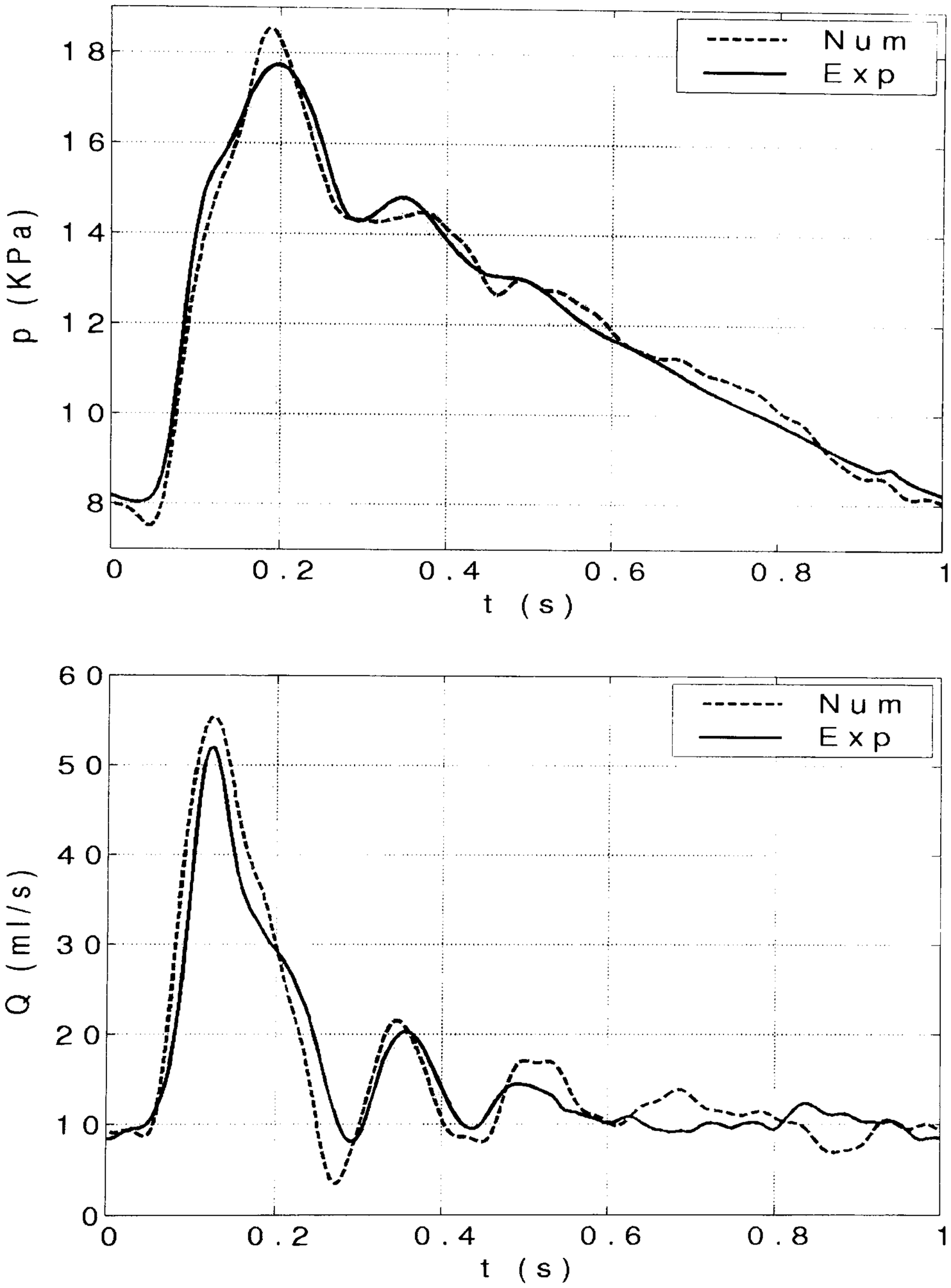


Figure 3.9: Pressure (top) and flow rate (bottom) time histories in the abdominal aorta V of both the experimental and numerical models.

3.2 Implementation of the technique to estimate the peripheral RLC parameters

This section assesses the ability of the technique proposed in Section 2.8 to estimate the fluid resistance and inertia and the wall compliance (RLC) of the vessels beyond the arteries simulated by the 1-D formulation. Physiological data of the value of the peripheral RLC parameters is scarce and, in the case of the peripheral inertias, non-existent to the knowledge of the author. In the absence of detailed knowledge of these parameters, the peripheral resistances and compliances in normal conditions at the outflow of the arteries shown in Table 3.4, which are taken from the model published by Stergiopulos *et al* [88], are compared with the values predicted by the algorithm. The algorithm takes into account the geometry and wave speed of the terminal arteries, which are also shown in Table 3.4.

Table 3.4: Comparison of the peripheral resistance (R_{T_N}) and compliance (C_T) calculated by the algorithm proposed in Section 2.8 (normal numbers) against the corresponding values used by Stergiopulos *et al* [88] (bold numbers). The first columns indicate the name of each terminal artery, its length (l), radius (R), and wave speed (c_0), the number of generations of bifurcations to reach the capillaries (N) and the value of λ.

Terminal artery	l (cm)	R (mm)	c_0 (m/s)	N	λ	R_{T_N} (x 10^9 Pa s m^{-3})	$\mathbf{R_{T_N}}$ **(x 10^9 Pa s m^{-3})**	C_T (x 10^{-11} m^3 Pa^{-1})	$\mathbf{C_T}$ **(x 10^{-11} $m^3 Pa^{-1}$)**
Carotids†	17.7	1.77	13.3	23	0.799	18.4	**13.9**	2.7	**1.3**
Vertebrals	14.8	1.88	9.6	24	0.800	13.9	**6.0**	4.9	**3.1**
Radials	23.5	1.74	10.6	23	0.799	26.1	**5.3**	5.4	**3.5**
Ulnars	17.1	2.03	9.8	24	0.800	11.8	**5.3**	6.4	**3.5**
Interosseous	7.9	0.91	14.7	21	0.795	87.9	**84.3**	0.3	**0.2**
Intercostals	8.0	2.00	5.6	24	0.800	5.9	**1.4**	8.7	**13.4**
Hepatic	6.6	2.20	6.4	24	0.800	3.3	**3.6**	6.7	**5.1**
Gastric	7.1	1.80	6.8	23	0.799	6.9	**5.4**	4.3	**3.4**
Splenic	6.3	2.75	6.2	25	0.801	1.5	**2.3**	10.9	**8.0**
Sup. mesenteric	5.9	4.35	5.7	27	0.804	0.3	**0.9**	30.7	**20.0**
Renals	3.2	2.60	6.2	25	0.801	0.9	**1.1**	4.9	**16.5**
Inf. mesenteric	5.0	1.60	7.0	23	0.799	7.8	**6.9**	2.3	**2.7**
Internal iliacs	5.0	2.00	4.3	24	0.800	3.7	**7.9**	9.6	**2.3**
Deep femorals	12.6	2.55	14.7	25	0.801	4.0	**4.8**	3.3	**3.9**
Posterior tibials	32.1	2.47	16.3	25	0.801	11.7	**4.8**	6.4	**3.9**
Anterior tibials	34.3	1.30	14.4	22	0.797	105.9	**5.6**	2.4	**3.3**

†Both external and internal carotids.

To calculate the number of generations of bifurcations to reach the capillary

beds (N), the radius of any capillary is assumed to be 0.004 mm (see Table 1.1). Equation (2.158) leads to

$$N = \frac{\log \frac{R_n}{R_0}}{\log \varphi}, \tag{3.1}$$

with $R_n = 0.004$ mm, R_0 equal to the radius of the terminal artery, $\varphi = \sqrt{0.6}$, and $n = N$. Once N is known, λ is calculated for every terminal artery through (2.183) and the terminal resistance through (2.168), with a viscosity of $\mu = 4.0$ mPa s. We notice that the scaling factors φ and λ used in each terminal artery belong to the shaded region shown in Figure 2.8, and that $R_{\mu T_N}$ does not converge to $R_{\mu T}$ calculated through (2.169) in any artery, because $\frac{\lambda}{2\varphi^4}$ is always larger than one. Compliances are calculated by means of Equation (2.178).

The results shown in Table 3.4 suggest that the algorithm proposed in this thesis is able to predict the order of magnitude of the peripheral resistances and compliances in most of the terminal arteries considered. The relative error of the peripheral resistances is smaller than 35% in the carotid, interosseous, hepatic, gastric, splenic, renal, inferior mesenteric and deep femoral arteries. The largest error occurs in the anterior tibial arteries. The relative error of the peripheral compliances is smaller than 35% in the interosseous, intercostals, hepatic, gastric, splenic, inferior mesenteric, deep femoral, and anterior tibial arteries. The largest error corresponds to the interior iliac arteries.

The total peripheral resistance in the model by Stergiopulos *et al* [88] is $1.3 \cdot 10^8$ Pa s m^{-3} and the total peripheral compliance is $1.4 \cdot 10^{-9}$ m^3 Pa^{-1}. The corresponding values calculated by the algorithm proposed in this thesis are $1.1 \cdot 10^8$ Pa s m^{-3} and $1.6 \cdot 10^{-9}$ m^3 Pa^{-1}.

Although no data about the values of the peripheral inertias is known to compare them with the values obtained through Equation (2.173), Section 3.4.8.3 will show that they do not have a significant effect on pulse wave propagation when combined with the peripheral resistances and compliances.

To conclude this section, the properties of the network created beyond the carotid arteries (both internal and external) by the algorithm are analysed. Since the results are presented in a non-dimensional form, they are similar to the results obtained in the rest of terminal arteries shown in Table 3.4. Figure 3.10 (left) shows the total cross-sectional area (A_{T_n}), lateral surface (S_{T_n}) and volume (V_{T_n}) of all the vessels

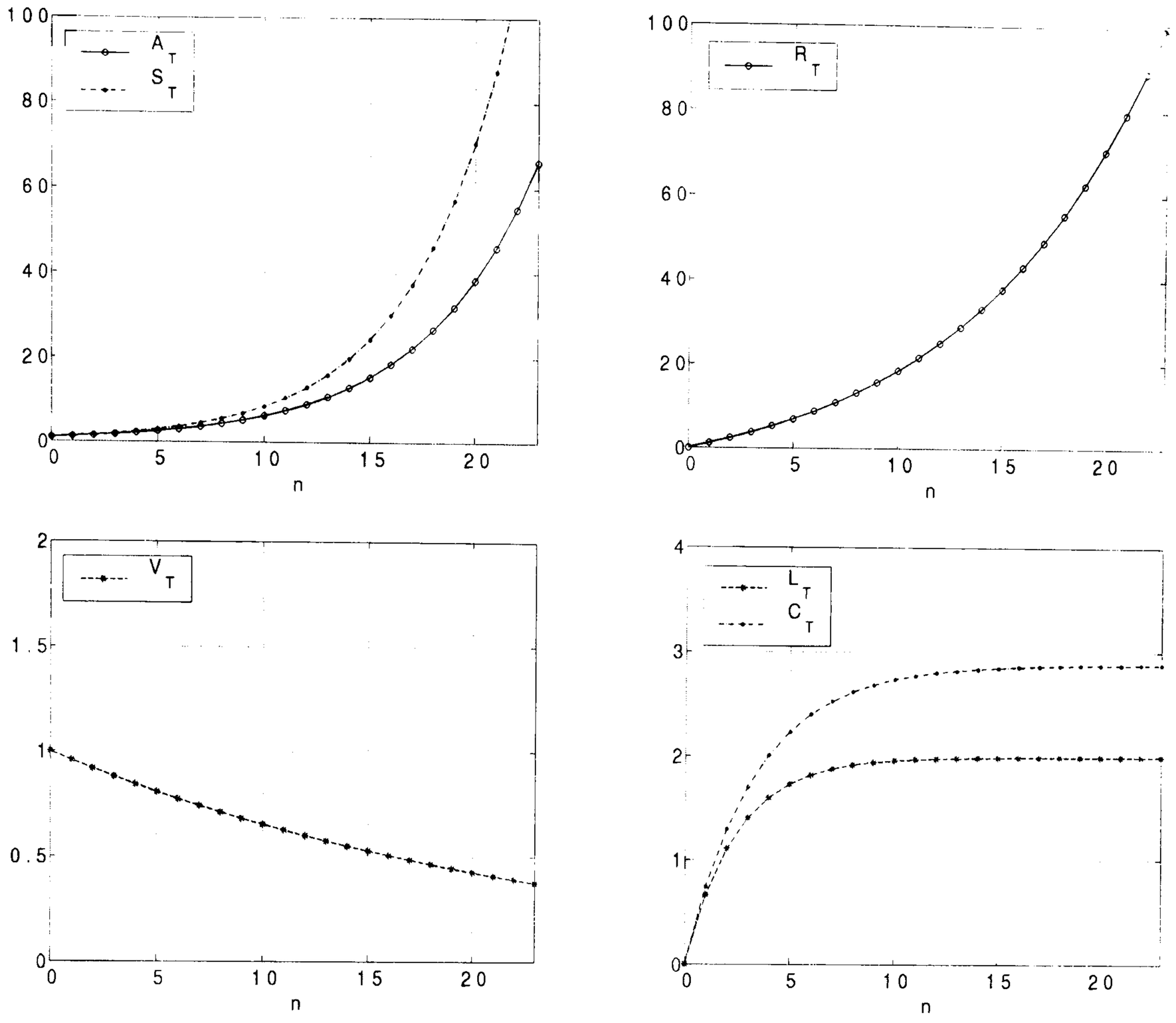


Figure 3.10: (left) Total cross-sectional area (A_{T_n}), lateral surface (S_{T_n}) and volume (V_{T_n}) of all the vessels present in each generation of bifurcations (n) downstream the carotid arteries and up to the capillaries. All the values are non-dimensionalised by their corresponding value at the carotid artery. (right) Evolution of the resistance (R_T), inertia (L_T) and compliance (C_T) at the outflow of the carotid artery with the increasing number of generations of bifurcations (n). All the values are non-dimensionalised by the resistance, inertia and compliance of the carotid artery.

(2^n) present in each generation of bifurcations (n) downstream the carotid arteries and up to the capillaries. The values of (A_{T_n}), (S_{T_n}) and (V_{T_n}) are calculated through (2.161), (2.163) and (2.162), and are non-dimensionalised by A_0, S_0 and V_0, respectively. We observe an exponential increase in both A_{T_n} and S_{T_n} with the increasing number of generations. On the other hand, V_{T_n} decreases with the increasing number of generations, so that perfusion is large and the volume is small at the capillary beds.

Figure 3.10 (right) shows the evolution of the peripheral resistance (R_{μ_T}), inertia (L_T) and compliance (C_T) at the outflow of the carotid artery with the increasing number of generations of bifurcations (n). All the values are non-dimensionalised by the resistance, inertia and compliance of the terminal carotid, respectively. We

observe an exponential increase in R_T with the increasing number of generations. which implies that the total resistance of the systemic circulation is located mainly in the small vessels, which is in agreement with the results depicted in Figure 1.10. On the other hand, both L_T and C_T converge to the value determined by (2.173) and (2.178) after a few generations, and, hence, the smaller arteries and the arterioles and capillaries have little contribution to the total peripheral inertia and compliance.

Although the technique proposed in this thesis is able to approximate some peripheral resistances and compliances with significant accuracy, it still needs further validation with *in-vivo* and experimental data. The method should also be improved by accounting for the anastomosis formed by the peripheral vessels (Figure 1.3), considering different scaling factors for each type of terminal artery, finding a better approximation of fluid resistance in the small arterioles and capillaries than Poiseuille's flow, and taking into account the decrease in viscosity caused by the Fåhraeus-Lindqvist effect, which reduces the fluid resistance in the microcirculation [46].

3.3 Pulse wave propagation along the aorta

This section simulates the human aorta as a 1-D compliant vessel with a length $l = 0.40$ m, an initial radius $R_0 = 1$ cm, a thickness $h = 1.5$ mm, and a Young's modulus $E = 4{\cdot}10^5$ Pa. These parameters are based on data published by Westerhof *et al* [96] for a healthy young adult. According to Section 1.1.3, the model considers $\rho = 1\,050$ Kg/m^3 and $\mu = 4.0$ mPa s.

The rest of vessels of the systemic circulation are represented by an RCR lumped parameter model coupled at the outlet of the aorta (iliac bifurcation), with a total peripheral resistance $R_{\mu_1} + R_{\mu_2} = 1.89 \cdot 10^8$ Pa s m^{-3} and a peripheral compliance $C = 6.31 \cdot 10^{-9}$ m^3/Pa. The peripheral resistance corresponds to the mean value measured by Simon *et al* [83] in 12 male patients without any cardiovascular disease. The peripheral compliance is determined as the mean value of the total compliance ($9.45 \cdot 10^{-9}$ m^3/Pa) evaluated in the same study, minus the compliance of the 1-D aorta ($3.14 \cdot 10^{-9}$ m^3/Pa) calculated through (2.118). At the outlet of the RCR lumped parameter model, a venous pressure $p_{out} = 1\,333$ Pa is considered.

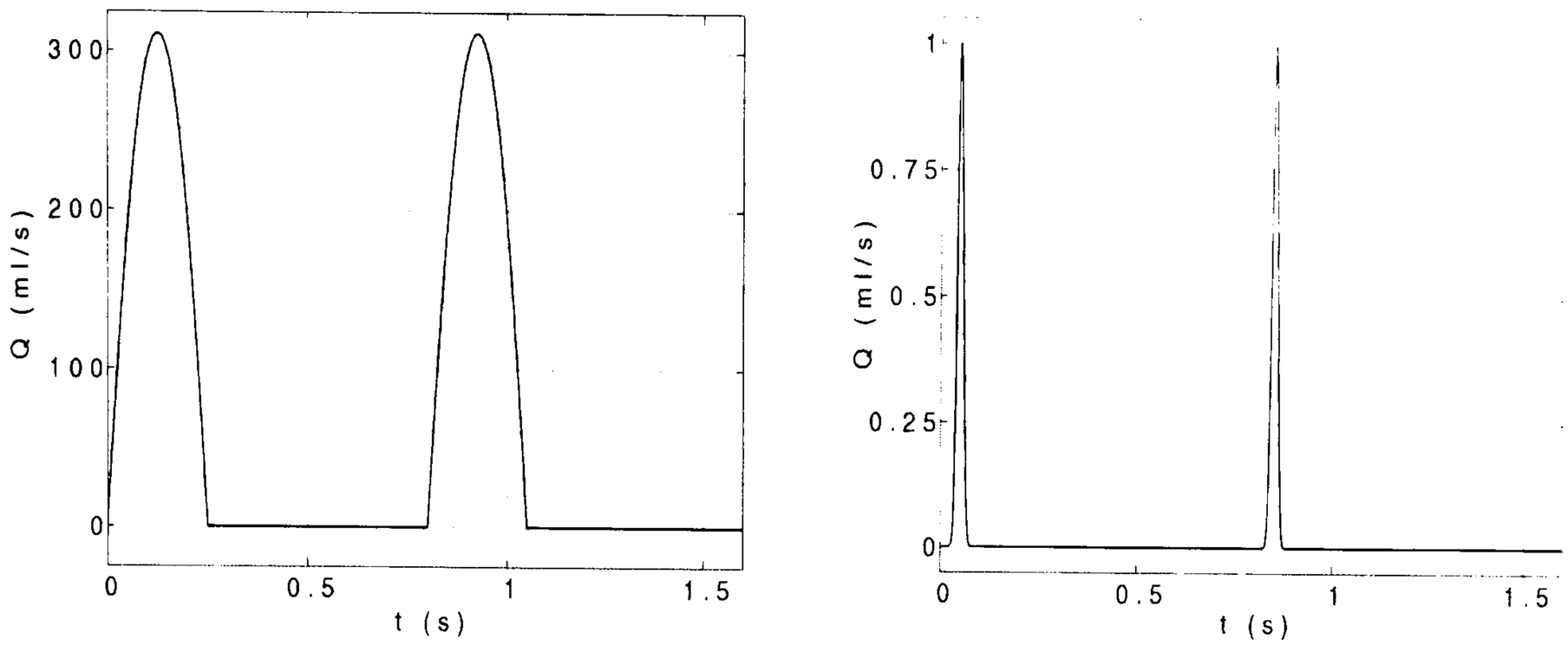


Figure 3.11: Periodic inflow boundary conditions enforced at the inlet of the 1-D aorta: half-sinusoidal flow rate defined by Equation (3.2) (left) and Gaussian delta wave flow rate defined by Equation (3.3) (right).

At the inlet of the 1-D aorta, a flow rate that repeats every 0.8 s (Figure 3.11, left) is enforced through Equation (2.69). The heart rate of this inflow boundary condition is 75 beats/min and similar to the average value measured in [83]. Each period consists of a half-sinusoidal wave defined as

$$Q_{bc}(t) = \begin{cases} \hat{Q} \sin\left(\frac{\pi t}{\tau}\right) & \text{if } t < \tau, \\ 0 & \text{otherwise.} \end{cases}, \tag{3.2}$$

with a peak value $\hat{Q} = 311.5$ ml/s, adjusted to obtain the mean cardiac output of 3.8 l/min measured in [83], and a duration $\tau = 0.25$ s (systole). Velocity is zero in the rest of the period (diastole), which implies that the boundary condition completely reflects any incoming backward wave, and, hence, simulates the closure of the aortic valve.

With the parameters considered in the simulation, Equation (2.25) provides an initial pulse wave speed $c_0 = 6.2$ m/s. Therefore, any wave travels from end to end of the aorta in about 0.06 s and, hence, the first part of the inflow wave gets reflected up to 13 times during each cardiac cycle.

The simulation is run with one elemental region Ω_e containing $q = 21$ quadrature points, a time step $\Delta t = 100$ μs, a polynomial order $P = 20$, and an initial state (A_0, p_0, U_0) with $A_0 = \pi R_0$, $p_0 = 0$ and $U_0 = 0$.

Figure 3.12 shows that pressure, velocity, and flow rate need about 10 heartbeats to build up their periodic waveforms, which takes about one minute to run in a normal PC. The initial transient of the system can be understood by approximating the

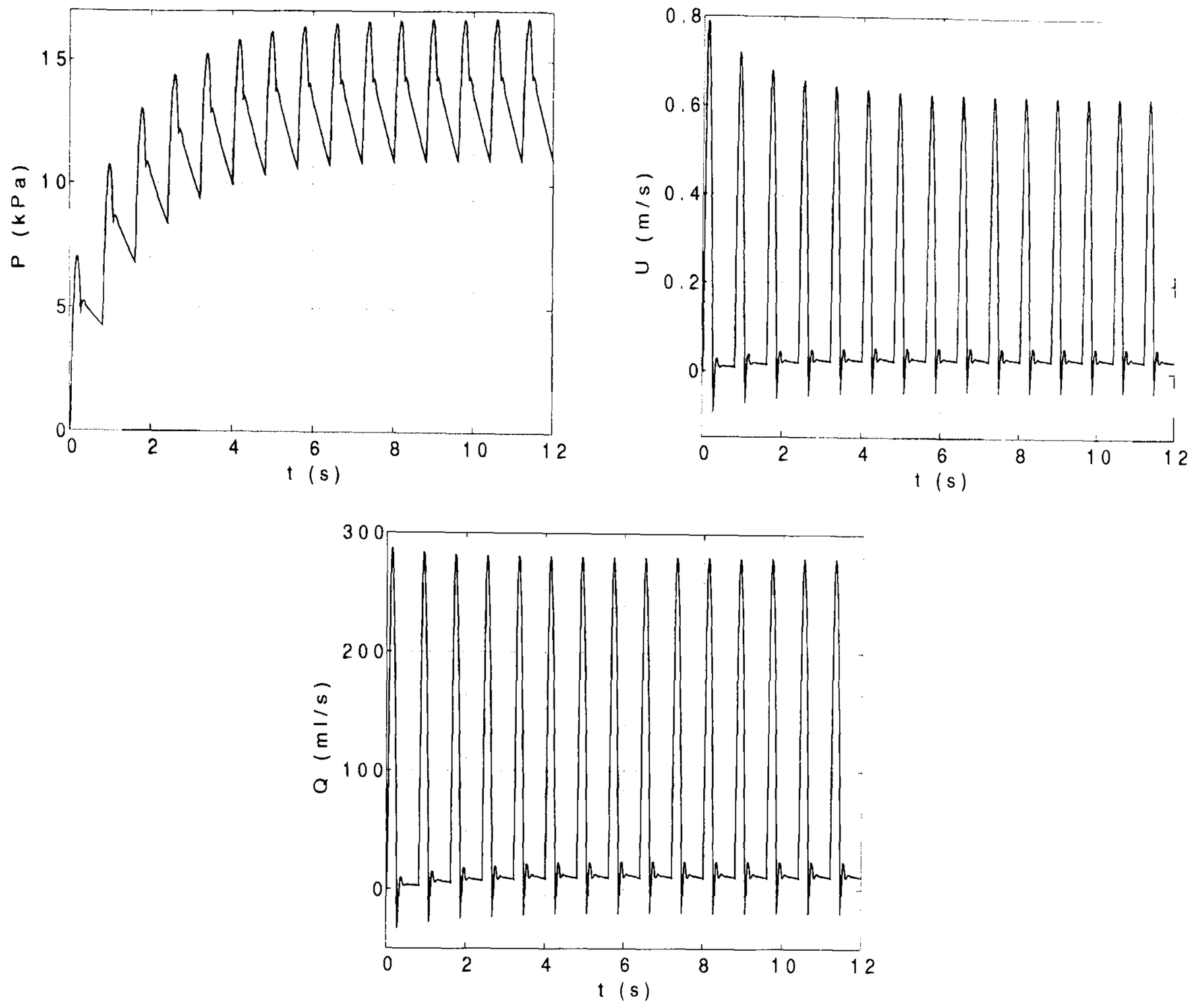


Figure 3.12: Pressure (left), velocity (right), and flow rate (bottom) time histories during the first 15 heartbeats in the middle point of the 1-D aorta coupled to an RCR lumped parameter model to represent the rest of systemic vessels. The inlet is perfused with the periodic velocity shown in Figure 3.11 (left).

1-D aorta and the RCR model by the windkessel model of the whole systemic arterial tree described in Section 2.7.3.2. According to (2.125), the windkessel pressure p_{wk} at the end of the initial heartbeat is $p_{wk}(T) = \frac{T}{C_T}\left(\overline{Q}_{in} - \overline{Q}_{out}\right) > p_{wk}(0) = 0$, since the mean outflow from the left ventricle, $\overline{Q}_{in}$, is higher than the mean outflow to the venous system, $\overline{Q}_{out}$, because the aorta and the RCR lumped parameter model accommodate part of $\overline{Q}_{in}$ by expanding their elastic walls (in the RCR model they are simulated by C). In the next heartbeats of the transient time, $p_{wk}(t' + T)$ gets closer to $p_{wk}(t')$, because the compliance of the system discharges more flow rate during diastole with the increasing pressure, according to Equation (2.124) (see the increase in flow rate with the increasing pressure in the middle of the aorta in Figure 3.12, bottom), and the diastolic decay is steeper (Figure 3.12, left), according to Equation (2.123). Therefore, $p_{wk}(t' + T)$ tends to $p_{wk}(t')$ and $\overline{Q}_{out}$ tends to $\overline{Q}_{in}$ with the increasing number of heartbeats.

The pulse waveforms become periodic when all the volume flow accommodated by the aorta and the RCR model during systole is released during diastole. so that $p_{wk}(t+T) = p_{wk}(t)$ and $\overline{Q}_{out} = \overline{Q}_{in}$, and Equation (2.126) is satisfied with $p_{out} =$ 1 333 Pa and $R_{\mu_T} = R_{\mu_1} + R_{\mu_2}$. As it will be shown in Section 3.4.5, fluid viscosity introduces a resistance to flow along the aorta much smaller than $R_{\mu_1} + R_{\mu_2}$, so that Equation (2.126) is satisfied without accounting for viscous dissipation in R_{μ_T}.

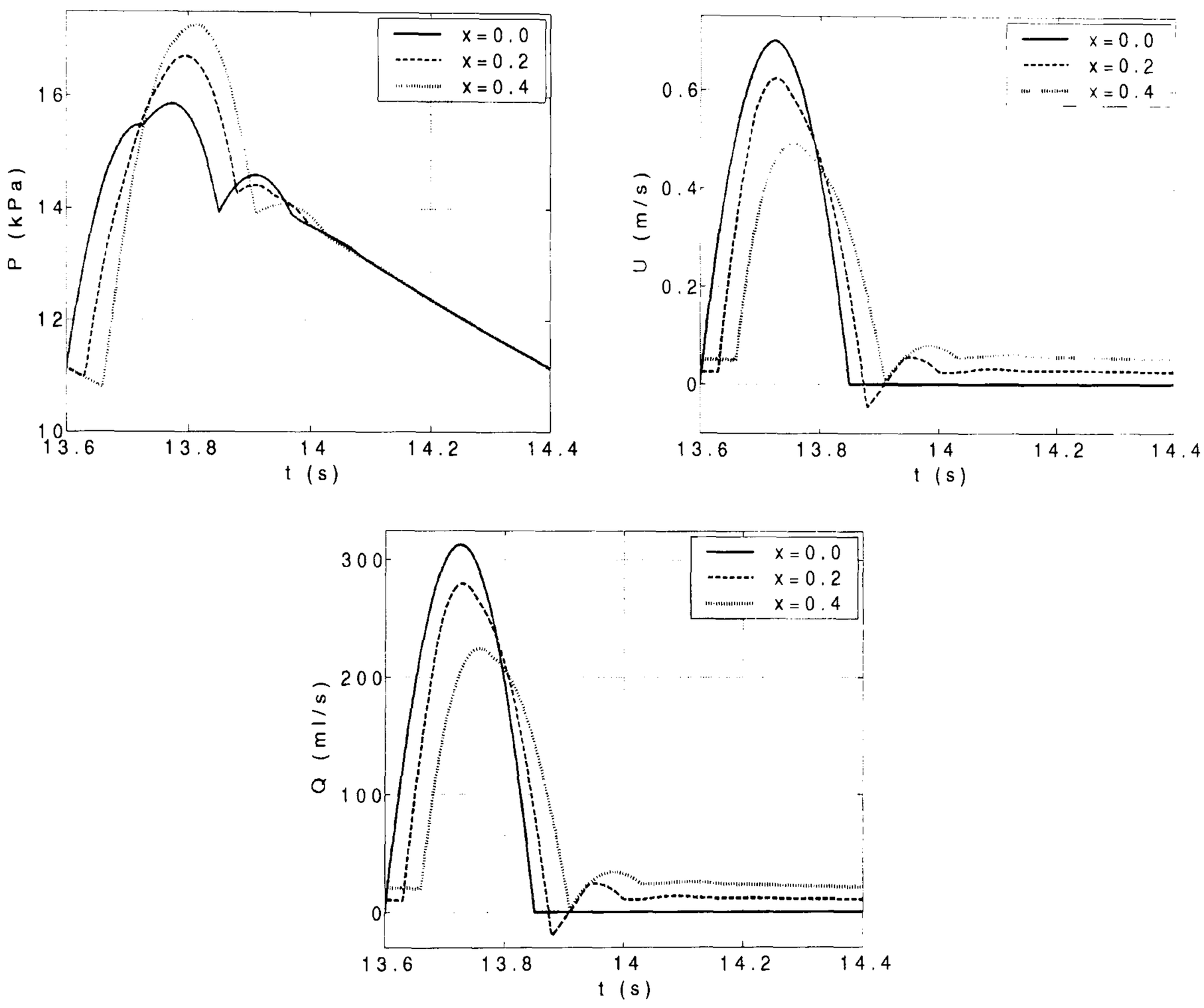


Figure 3.13: Periodic pressure (left), velocity (right), and flow rate (bottom) time histories at three locations ($x = 0.0$, $x = 0.2$ m, and $x = 0.4$ m) along the 1-D aorta coupled to an RCR lumped parameter model. The inlet is perfused with the periodic velocity shown in Figure 3.11 (left).

The periodic waveforms exhibit the main features observed *in-vivo* and described in Section 1.2 (see Figure 1.9). Figure 3.13 (left) shows the periodic pressure at three locations along the aortic vessel ($x = 0.0$, $x = 0.2$ m and $x = 0.4$ m). We observe the presence of the dicrotic notch, diastolic decay, and peaking and steepening of pulse pressure as we move away from the inlet. Moreover, we notice that pressure is very similar everywhere along the aorta during approximately the last two thirds of diastole, since pulse waves are minimal during this period. This result is in

agreement with the observation by Wang *et al* [93] that pressure everywhere in the systemic arteries can be approximated by the windkessel model described in Section 2.7.3.2 during approximately the last two thirds of diastole.

The corresponding velocity waves are characterised by a reduction in their amplitude and an increase in their width with the distance from the heart (Figure 3.13, right). After the closure of the aortic valve, we also observe some backward flow that decreases as we move towards the periphery. Figure 3.13 (bottom) shows that the flow rate waves have a very similar shape as the velocity waves.

Table 3.5 shows that the simulation is able to approximate the main haemodynamic parameters published in the study by Simon *et al* [83]. Furthermore, we observe a gradual decrease in mean pressure towards the periphery, caused by viscous dissipation within the aorta.

Table 3.5: Comparison between the haemodynamic parameters measured by Simon *et al* [83] at a brachial artery of normal patients and the corresponding parameters simulated using the 1-D aorta at $x = 0.0$, $x = 0.2$ m, and $x = 0.4$ m.

	In-vivo	Simulated		
		$x = 0.0$	$x = 0.2$ m	$x = 0.4$ m
Systolic pressure (kPa)	16.8 ± 0.4	15.9	16.7	17.3
Diastolic pressure (kPa)	9.5 ± 0.4	11.1	11.0	10.8
Mean pressure (kPa)	-	13.47	13.46	13.45
Heart rate (beats/min)	72 ± 3		75	
Cardiac output (l/min)	3.8 ± 0.2		3.8	

Figure 3.14 shows the forward and backward pressure and velocity waves simulated at $x = 0.0$, $x = 0.2$ m, and $x = 0.4$ m, separated by means of the technique described in Section 2.4. We observe that the forward waves are very similar in each location along the aorta, except for a temporal shift, and so are the backward waves, because changes in the forward and backward characteristic information ($\mathrm{d}W_f$ and $\mathrm{d}W_b$) produced by the boundary conditions propagate along the characteristic paths C_f and C_b with little alterations, since $\frac{\mathrm{d}\mathbf{W}}{\mathrm{d}t} \approx \mathbf{0}$ in (2.19) (β and A_0 are constant along the simulated aorta and viscous dissipation is very small, as will be shown in Section 3.4.5). We also observe that forward and backward pressure waves are very similar in shape to their corresponding velocity waves (except for the signs), which is in agreement with Equations (2.31) to (2.34).

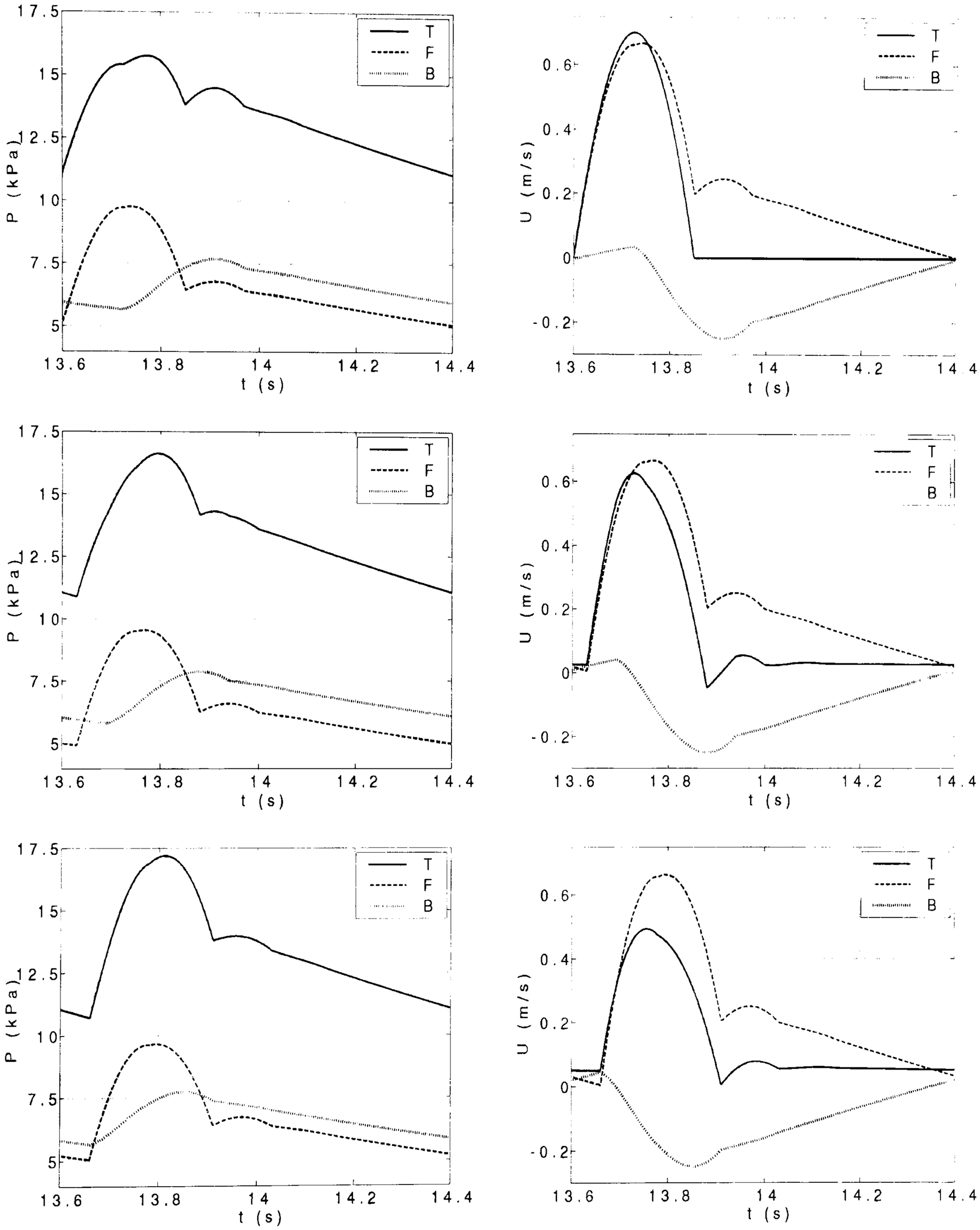


Figure 3.14: Pressure (left) and velocity (right) time histories simulated using the 1-D aorta at $x = 0.0$ (top), $x = 0.2$ m (middle), and $x = 0.4$ m (bottom). The total pulse pressure and velocity waves (T) are shown along with their corresponding forward (F) and backward (B) waves calculated using the wave separation technique described in Section 2.4.

Figure 3.14 also shows that the pulse produced by the left ventricle propagates as a forward wave towards the outlet, where it is smoothed by C and reflected by $R_{\mu 2}$. Consequently, the backward wave generated is smoother and with a smaller amplitude. The foot of this wave arrives at the inlet after about 0.12 s (twice the travelling time between each boundary), where it interacts with the forward waves generated by the inflow boundary condition and produces a point of inflexion just before the systolic pressure peak. Once the aortic valve is closed, the inlet completely reflects any incoming backward wave.

The mechanism of wave propagation along the aorta can be better understood by propagating the Gaussian delta wave flow rate shown in Figure 3.11 (right) and defined by

$$Q_{bc}(t) = \hat{Q}\, e^{-\left(\frac{t-t_0}{\tau}\right)^2}, \tag{3.3}$$

with a peak value $\hat{Q} = 1$ ml/s, $t_0 = 0.05$ s and a small variance $\tau = 0.01$ s. The shape of a Gaussian function approximates the delta function $\delta(t)$ defined as

$$\delta(t) = \begin{cases} 1 & \text{if } t = 0, \\ 0 & \text{otherwise.} \end{cases} \tag{3.4}$$

In the limit $\tau \to 0$ the Gaussian tends to the delta function $\delta(t)$. According to the theory of digital signal processing [48], if the input to a linear system is $\delta(t)$, the output observed after $t = 0$, which is referred to as the *natural response of the system*, must be characteristic of the system itself since the input signal has ceased. Indeed, it is a transfer function that gives the output of any input periodic function by convolution of the transfer and input functions. Although this theory applies only to linear systems, the error introduced when applied to the non-linear 1-D formulation is small, since the effect of non-linearities is not very significant under physiological conditions, as it will be shown in Section 3.4.2. Narrower Gaussian functions would be more desirable, but they present problems of numerical and physical instability, since shock waves are likely to develop.

The pressure and velocity time histories generated at $x = 0.2$ m with the Gaussian delta wave input are shown in Figure 3.15, once they have become periodic, along with their corresponding forward and backward waves. Since Figure 3.24 will show that p_{out} does not affect the shape of the pulse waves, the model has been run

with $p_{out} = 0.0$ to avoid running the simulation for many periods to reach a periodic state. Figure 3.15 shows that when the input Gaussian wave reaches the outlet it is smoothed by C and partially reflected by R_{μ_2}. The amplitude of the resulting wave has been largely reduced compared to the amplitude of the initial Gaussian wave, in accordance with the small reflections produced by the iliac bifurcation for waves arriving from the aorta. The reflected wave appears at $x = 0.2$ m as a backward travelling wave approximately 0.06 s after the first foot of the input Gaussian wave, which is in accordance with the initial pulse wave speed $c_0 = 6.2$ m/s. When it reaches the inlet it is completely reflected, because $Q_{bc} \approx 0$, and it appears as a forward travelling wave at $x = 0.2$ m after approximately 0.06 s.

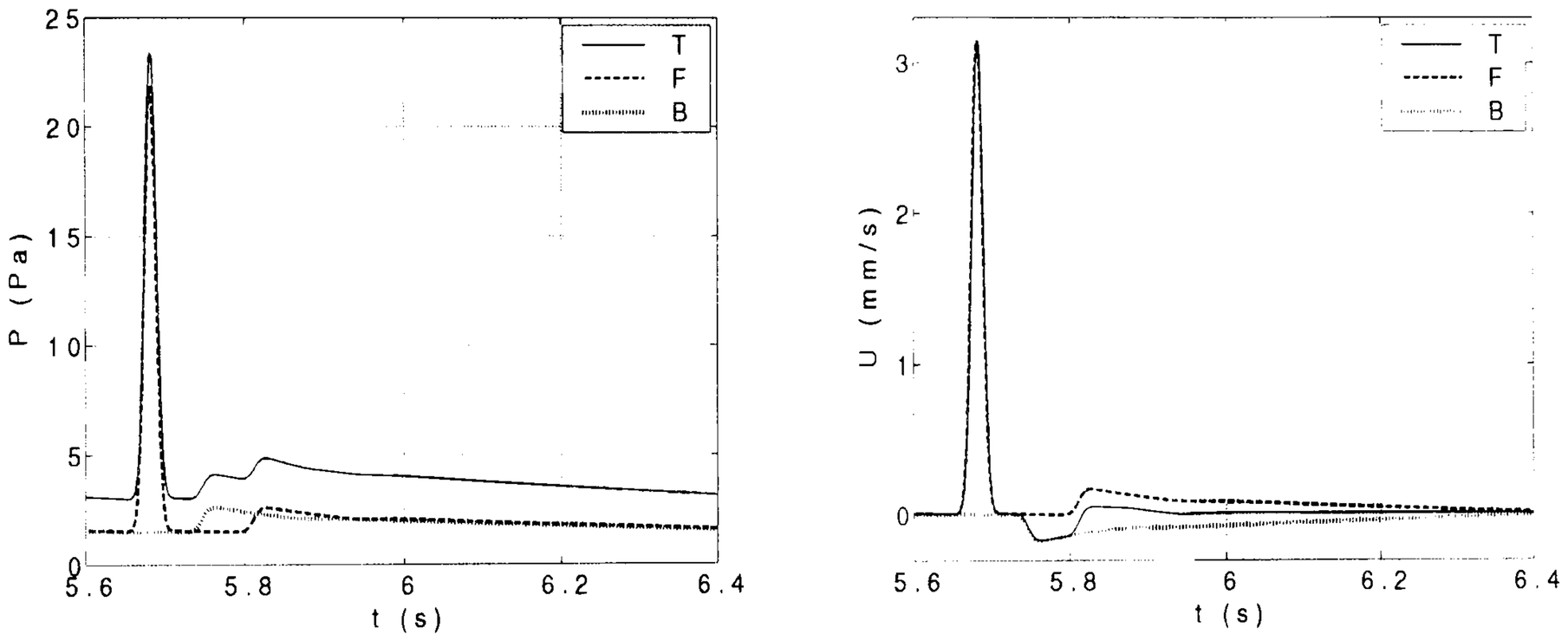


Figure 3.15: Periodic pressure (left) and velocity (right) time histories in the middle point of the aortic vessel (T), along with their forward (F) and backward (B) contributions. The inlet is perfused with the Gaussian flow rate shown in Figure 3.11 (right).

Although single wave reflections at the outlet of the 1-D aorta are small (Figure 3.15), which is in agreement with the close to well-matched iliac bifurcation for forward travelling waves [66, 94], their convolution with the half-sinusoidal wave produced by the heart leads to the pulse waves observed *in-vivo* (Figure 3.13). This explains the smaller reduction in the amplitude of the half-sinusoidal wave at the outlet of the aorta (Figure 3.14) compared to the reduction in the amplitude of the Gaussian wave at the outlet of the aorta (Figure 3.15).

Figure 3.14 (left) shows that the form of the dicrotic notch results from the combination of the half-sinusoidal pressure generated during systole and its corresponding reflection by the outlet. Because these two pressure waveforms are closer in time at locations further away from the heart, the pressure waveform resulting

from their combination has a higher systolic pressure and is steeper towards the periphery. The reduction in amplitude, increase in width and reversal flow of the velocity pulse waves also results from the different combination of the forward and backward velocity waves at each location in space (Figure 3.14, right).

3.4 Sensitivity analysis

This section analyses the sensitivity of the results obtained in Section 3.3, referred to as the control case, to the polynomial and quadrature order of the numerical scheme (Section 3.4.1), the non-linear terms of the governing equations (Section 3.4.2), the geometry and elasticity of the aorta (Sections 3.4.3 and 3.4.4), the density and viscosity of blood (Section 3.4.5), the peripheral resistance, compliance and venous pressure (Section 3.4.6), and the different lumped parameter models described in Chapter 2 (Section 3.4.8). When possible, the study is carried out by analysing the effect of increasing and decreasing the value of the parameters used in the control case by 10%, each time changing only one parameter.

3.4.1 Numerical convergence

This section first studies the effect of reducing the polynomial order on the propagation of pulse waves at $x = 0.2$ m (other locations along the aorta present similar effects). Figure 3.16 shows the pressure and velocity time histories obtained when

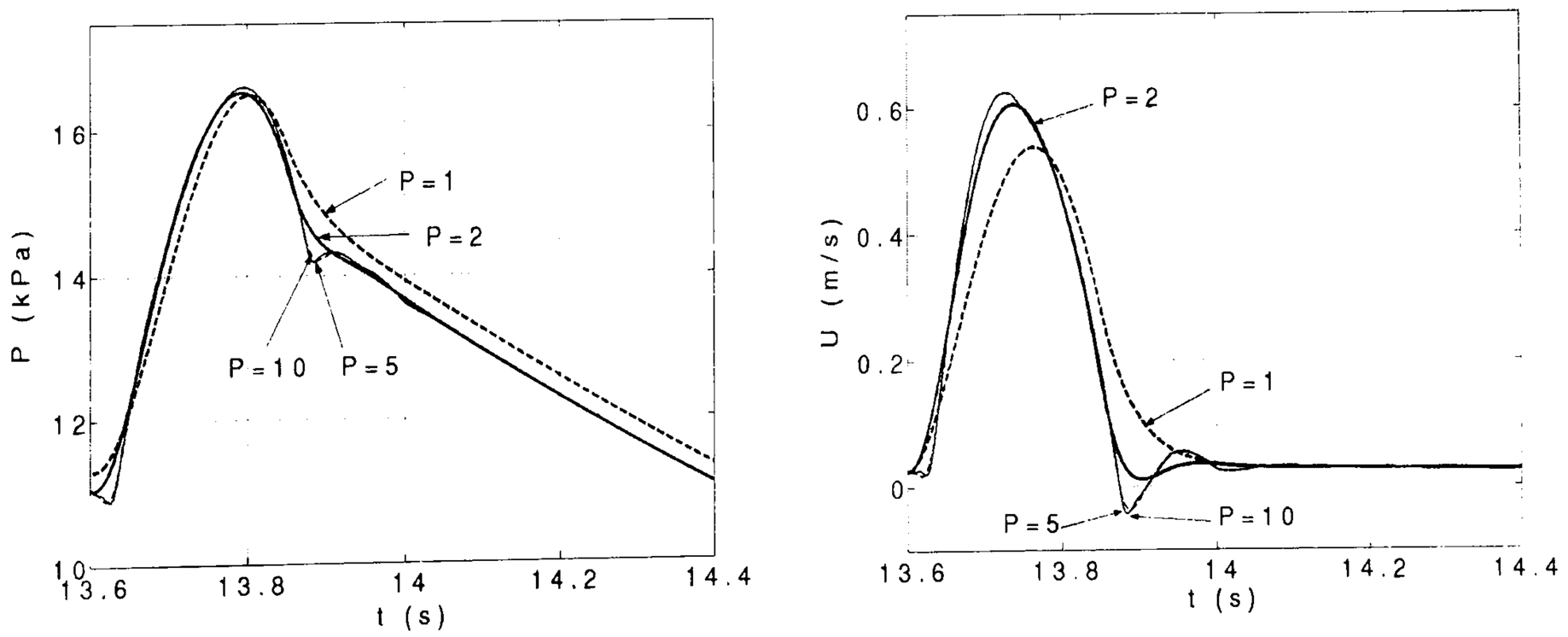


Figure 3.16: Effect of reducing the polynomial order, P, on the pressure (left) and the velocity (right) obtained with the control case at $x = 0.2$ m (Figure 3.13, top).

the polynomial order of the control case ($P = 20$) is reduced to $P = 10$, $P = 5$. $P = 2$, and $P = 1$. The results obtained with $P = 10$ and $P = 5$ only differ from the results obtained with $P = 20$ at the beginning of systole, around the dicrotic notch and when flow reverses, which have in common sudden changes in pressure and velocity. However, when $P < 5$ the waveforms are significantly different over the whole cardiac cycle from the waveforms obtained with $P \geq 5$. The effect on flow rate waveforms is not shown because it is very similar to the effect on velocity waveforms.

The effect of reducing both P and the quadrature order q has also been studied (we can not reduce only q because we require $q \geq P + 1$ to exactly integrate a polynomial of order P). The effect is almost identical, in the scales of Figure 3.16, to the effect of reducing only P, which suggests that P has a higher influence in the results than q, and, hence, we should consider $q = P + 1$.

3.4.2 The effect of non-linearities

The effect of non-linearities is first analysed on the propagation of a half-sinusoidal pulse wave, with a peak pressure of 1 kPa, along a 1 m long compliant artery with a 1 cm cross-sectional radius and an initial wave speed of 5 m/s. This wave propagates from the inlet to the outlet of the artery, where it is completely absorbed. This is achieved by setting the terminal reflection coefficient $R_t = 0.0$. The simulation is run with ten elemental regions Ω_e with 50 quadrature points each, a time step $\Delta t = 10$ μs, a polynomial order $P = 50$, and an initial state (A_0, p_0, U_0) with $A_0 = \pi$ cm^2, $p_0 = 0$ and $U_0 = 0$. Such a small Δt and such a large P and q are required because we are propagating a high-frequency wave.

Figure 3.17 shows the spatial distribution of the pressure and velocity waves obtained at $t = 0.0$, $t = 0.10$ s, $t = 0.15$ s, and $t = 0.20$ s, comparing the non-linear formulation, the linear formulation, and the non-linear formulation without the convective velocity $U\frac{\partial U}{\partial x}$ in the momentum equation (2.6). When non-linearities are included, the pressure and velocity forward waves propagate at a speed $U + c$ (see Section 2.3). Since U increases with the increasing pressure, as well as c (2.24), the peaks of the pressure and velocity inflow waves shown in Figure 3.17 travel at a higher speed than their feet. Consequently, both pressure and velocity waves become

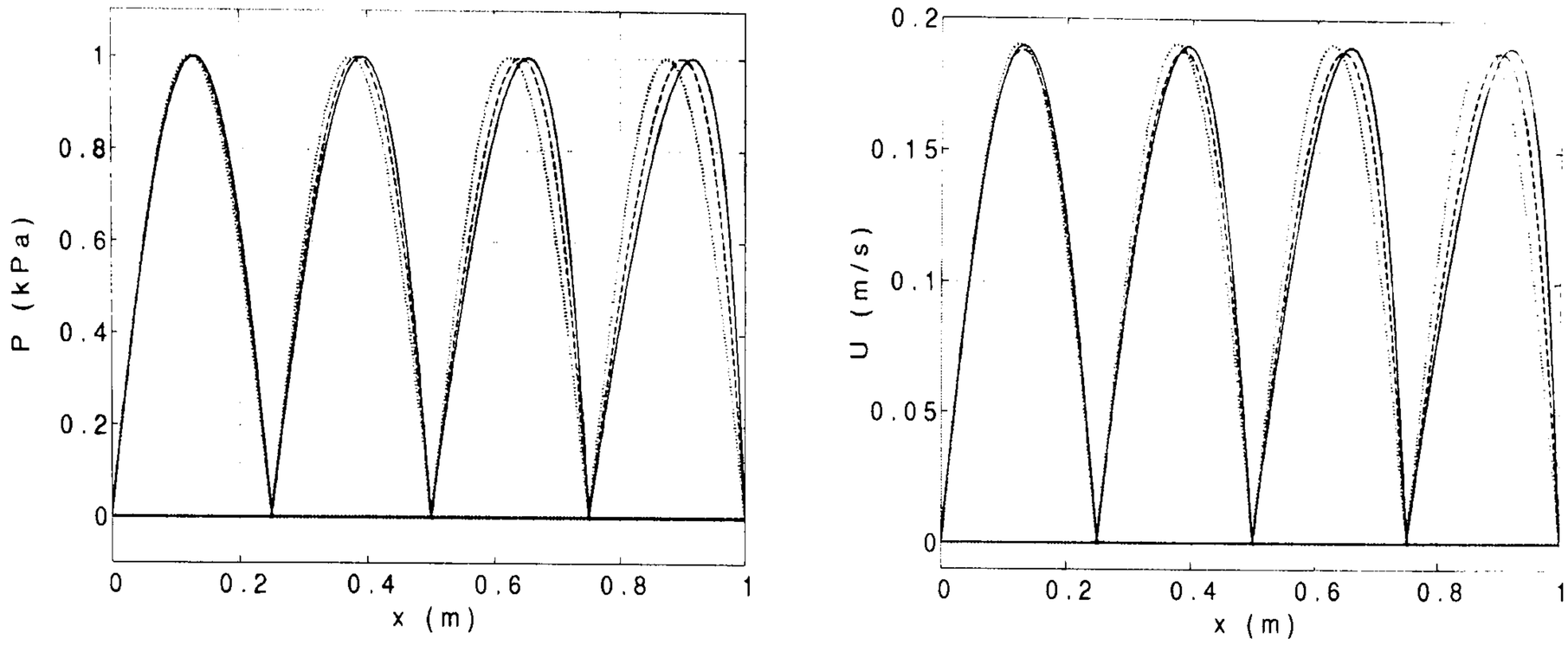


Figure 3.17: Spatial distribution of the pressure (left) and velocity (right) pulse waves along a 1 m long artery at $t = 0.0$, $t = 0.10$ s, $t = 0.15$ s, and $t = 0.20$ s, comparing the non-linear formulation (solid lines), the non-linear formulation without the convective velocity (dashed lines), and the linear formulation (dotted lines).

increasingly skew as they move towards the outlet. Since pulse waves propagate at a constant speed c_0 in the linear formulation (see Section 2.5), the inflow wave passes through the artery without changing its initial shape. When the convective velocity is neglected, the skew of the waves decreases because it is caused only by the non-linear dependence of c on p. We also note that non-linearities do not change the pressure peaks significantly, but they produce small changes in the velocity peaks.

Figure 3.18 shows the effect of non-linearities on pressure, velocity, and flow rate under more physiological conditions. In any case, the propagation of the systolic wave front is delayed and not skew when calculated with the linear formulation. As a result, the linear forward and backward pulse waves are more separated in time than their non-linear counterparts, which yields pulse pressures about 6% smaller and peak velocities about 2% higher in the linear formulation. The effect on flow rate is a decrease in the peaks of the waves towards the periphery, since flow rate at the inlet is enforced by the inflow boundary condition. The change in mean pressures and mean flow rates is smaller than 1% in any location along the aorta. These results show that non-linearities have a small effect on pulse wave propagation under physiological conditions.

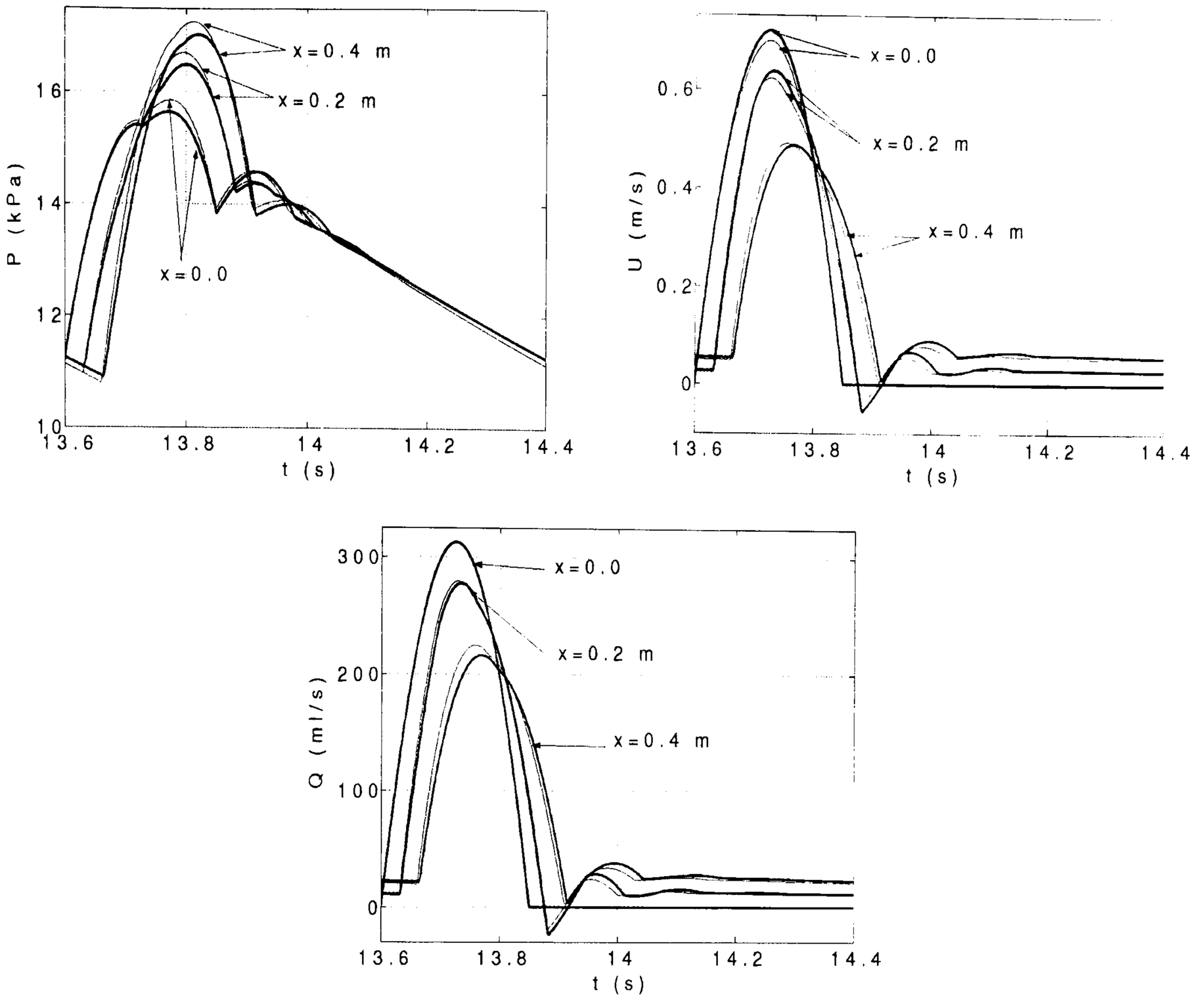


Figure 3.18: Comparison of the periodic pressure (left), velocity (right), and flow rate (bottom) time histories obtained with the non-linear formulation (thin lines) and with the linear formulation (thick lines) at three locations along the 1-D aorta.

3.4.3 Sensitivity to changes in the geometry

This section studies the effect on pulse wave propagation of an increase and a decrease by 10% in the length, diameter, and thickness of the control case. In every study, the total compliance is maintained constant.

The aortic length determines the time it takes a wave to travel along the aorta and the distribution of the total compliance between the aorta and the periphery, according to (2.118). Figure 3.19 shows the effect of changing the length of the control case by $\pm 10\%$ on pressure and velocity wave propagation at $x = 0.2$ (other locations along the aorta present similar effects). We observe that regions around the systolic pressure, the dicrotic notch, the peak velocity, and the reversal of flow are more sensitive to changes in length than the rest of the pressure and velocity time histories. An increase in the length produces systolic pressures about 2% smaller than in the control case, peak velocities about 4% higher, and more significant

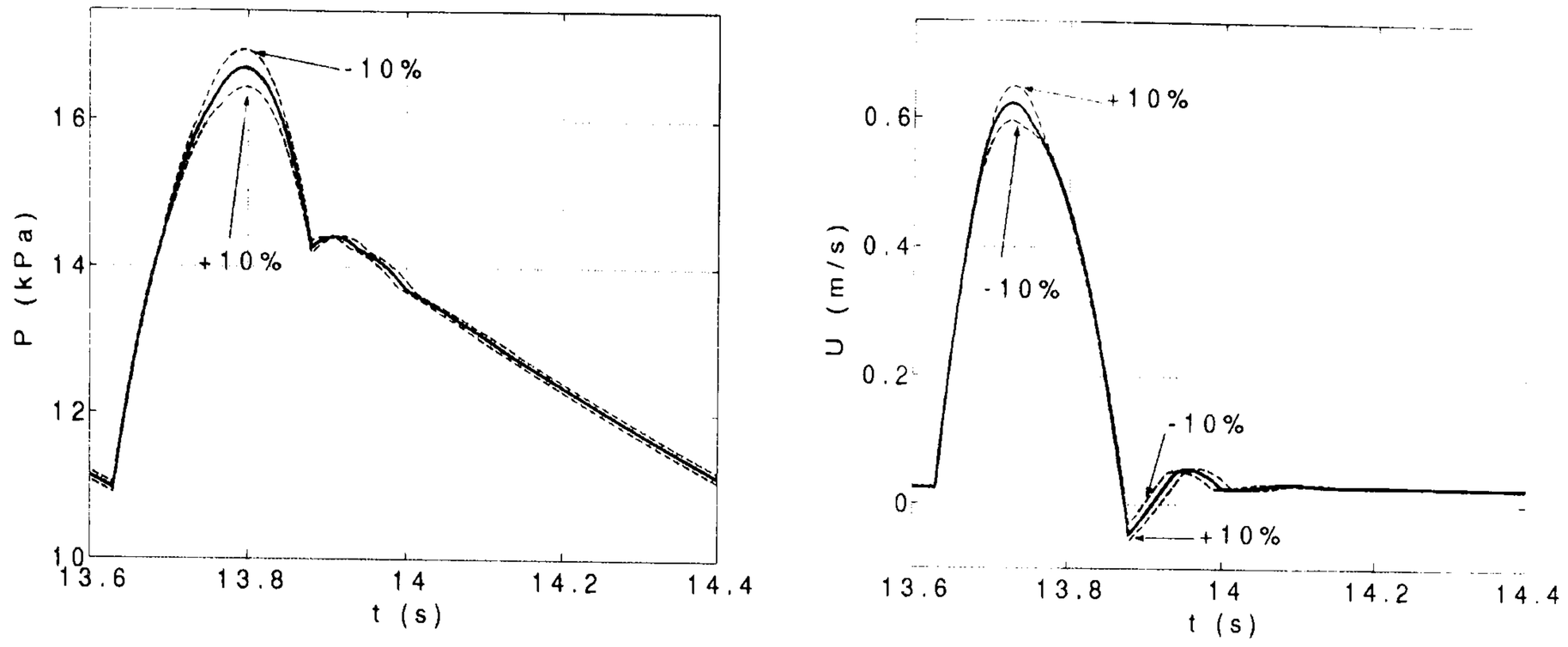


Figure 3.19: Effect of increasing and decreasing by 10% the length of the aorta on the periodic pressure (left) and velocity (right) time histories at $x = 0.2$ m. Solid lines indicate the results obtained with the control case and dashed lines the results obtained with the $\pm 10\%$ changes.

reversal flows, because the temporal shift between forward and backward waves is larger at any location along the aorta compared to the control case (Figure 3.14). The opposite effect is observed when the length is reduced, with approximately the same percentages of change. The qualitative effects on flow rate waveforms are the same as on velocity waveforms, with variations in the peak flow rate of about $\pm 4\%$ the value of the control case. Diastolic pressures and mean pressures and flows change by less than 1% in any case. According to these results, a person with a short aorta should have a higher systolic pressure than a person with a longer aorta and the same cardiac output.

Figure 3.20 (left and right) shows that pressure and velocity waveforms at $x = 0.2$ are more sensitive to variations in the aortic calibre than in the aortic length (Figure 3.19). Again, other locations along the aorta are not shown because they present similar effects. Since the inflow rate is the same in every simulation (it is determined by the inflow boundary condition), an increase in the aortic calibre by 10% produces a decrease in the peak velocity by about 20% the value in the control case. The pulse pressure decreases by about 20% the value in the control case, because the aortic compliance is 33% higher than in the control case, according to (2.118), and leads to a larger windkessel effect, although the total compliance was not changed. With the reduction in the aortic calibre by 10% we observe the opposite effects, with increases in peak velocity of about 25% and in pulse pressure

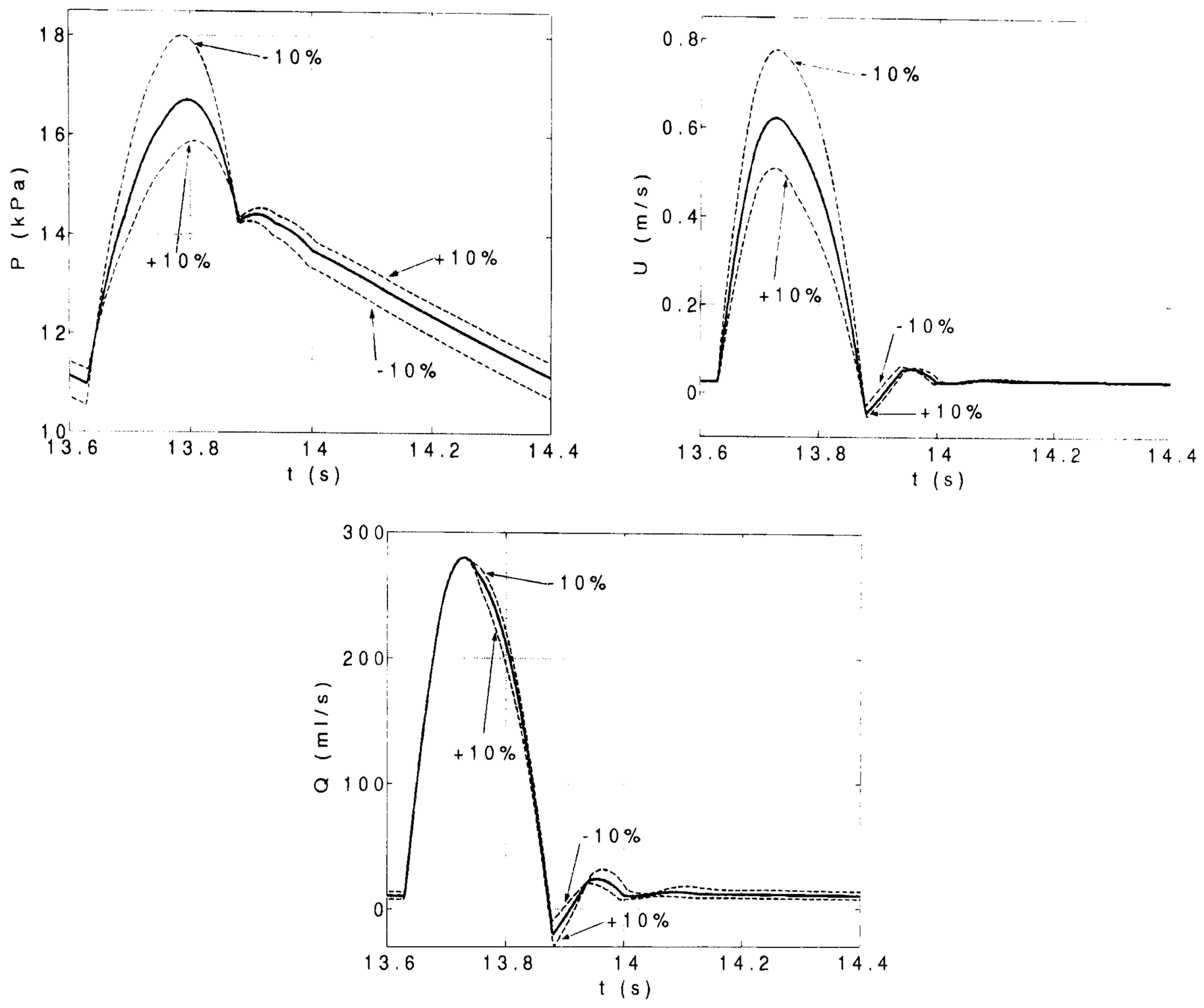


Figure 3.20: Effect of increasing and decreasing by 10% the diameter of the aorta on the periodic pressure (left), velocity (right), and flow rate (bottom) time histories at $x = 0.2$ m. Solid lines indicate the results obtained with the control case and dashed lines the results obtained with the $\pm 10\%$ changes.

of about 30% the corresponding values obtained in the control case. The variations in flow rate waveforms are less significant (Figure 3.20, bottom).

Figure 3.21 shows that an increase in the wall thickness of the control case by 10% produces a pulse pressure about 7% higher and a peak velocity about 2% higher, since the aortic compliance is reduced by about 9%, according to (2.118). A 10% decrease in the wall thickness increases the aortic compliance by about 11%, which decreases by 7% the pulse pressure and by 2% the peak velocity of the control case. These results are obtained at $x = 0.2$ m, but the changes in pressure, velocity, and flow rate are similar at other locations along the aorta. Flow rates are less sensitive to changes in the wall thickness than pressure and velocity.

According to the results shown in this section, pulse wave propagation is more sensitive to changes in the aortic diameter than to changes in the aortic length or wall thickness. We note that the sensitivity of the aortic compliance determined

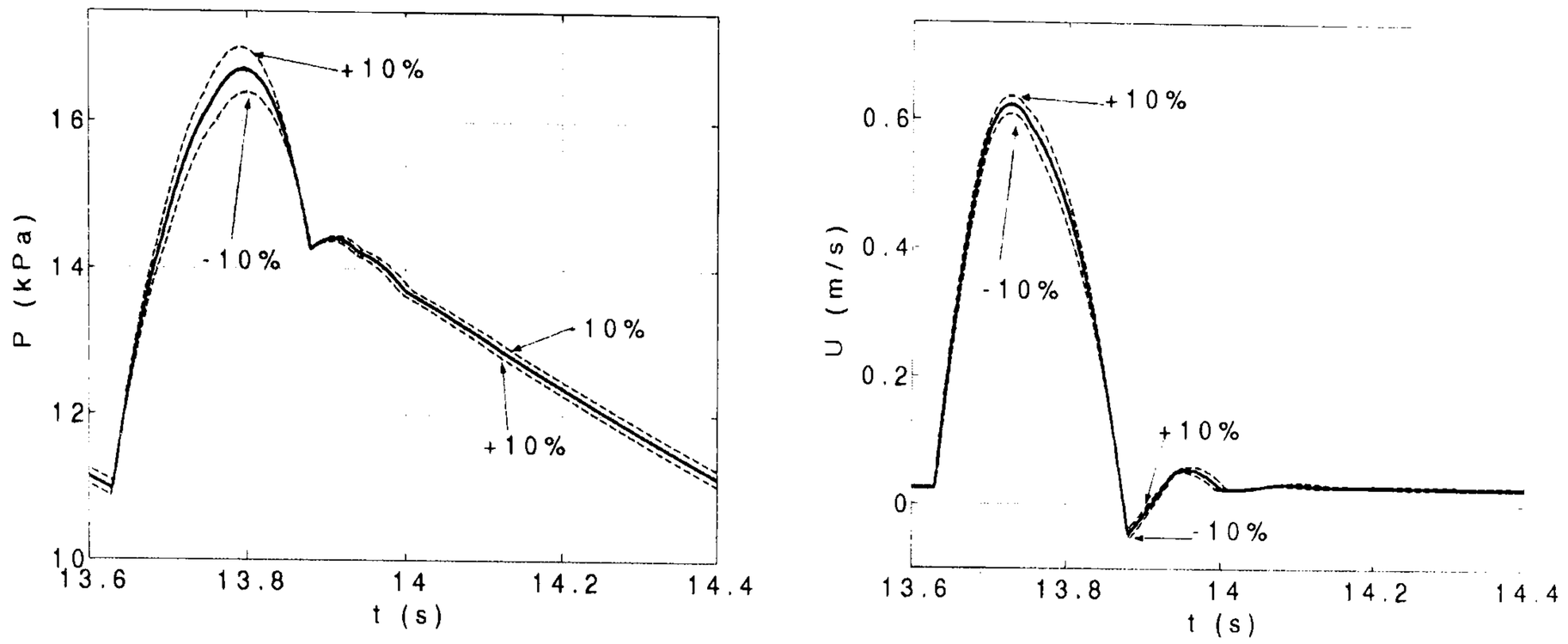


Figure 3.21: Effect of increasing and decreasing by 10% the wall thickness on the periodic pressure (left) and velocity (right) time histories at $x = 0.2$ m. Solid lines indicate the results obtained with the control case and dashed lines the results obtained with the $\pm 10\%$ changes. A change in the elastic modulus of the aortic wall by ± 10 % produces exactly the same effects.

using Equation (2.118) is also higher when the diameter is changed than when the length or wall thickness are changed. Moreover, this study has shown that the windkessel effect increases when a greater part of the total compliance is located in the aorta.

3.4.4 Sensitivity to changes in the elasticity

The sensitivity of pulse wave propagation to changes in the elastic modulus (E) of the aortic wall is exactly the same as the sensitivity to changes in the wall thickness (h) (Figure 3.21), because both E and h have the same weight in the tube law (2.11), and hence in the value of c (2.25) and the aortic compliance determined by (2.118).

3.4.5 Sensitivity to the density and viscosity

Figure 3.22 shows a decrease in the systolic pressures of the control case when the viscous term $\frac{f}{\rho A}$ is neglected in the momentum equation (2.6). The decrease is higher near the inlet and always smaller than 1% the systolic pressure of the control case, which indicates that fluid viscosity does not introduce a significant resistance to flow. This result was indirectly obtained in Section 3.3, since the mean pressure and flow rate produced by the viscous formulation were in good agreement with (2.126) without taking into account the viscous resistance in R_{μ_T}. Changes in the

velocity and flow rate waveforms along the aorta can not be detected in the scales of Figure 3.13 (right and bottom).

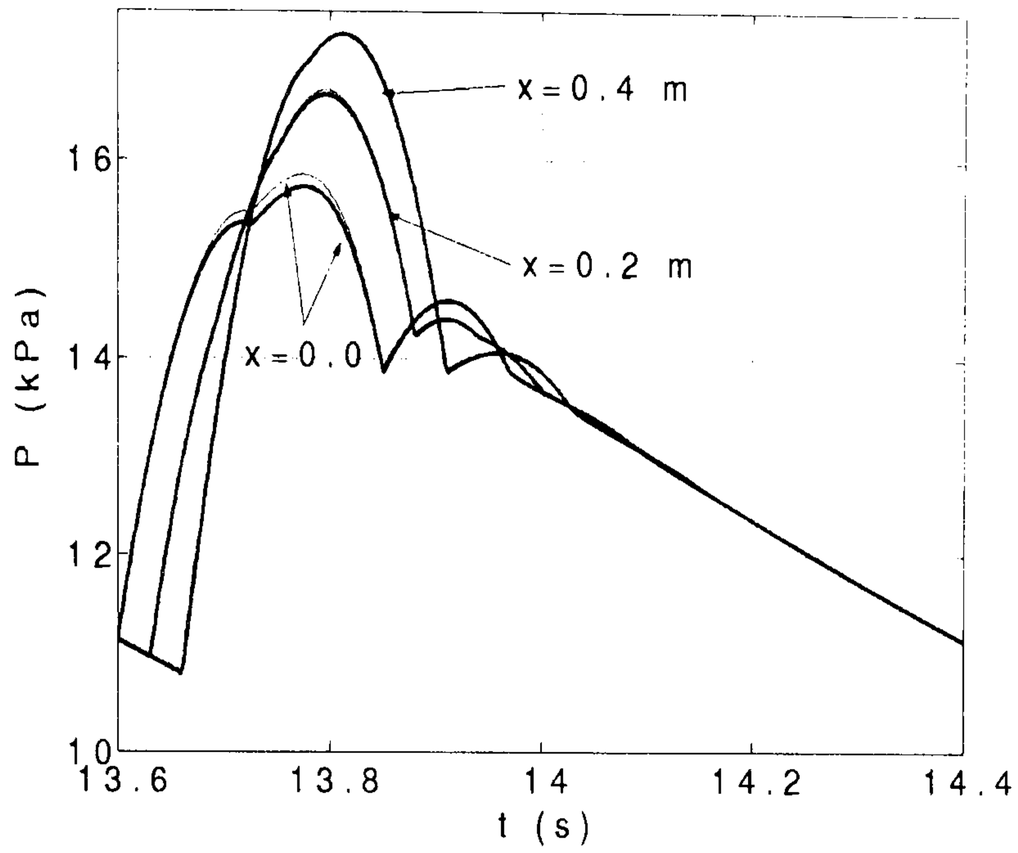


Figure 3.22: Comparison of the periodic pressure time histories at three locations along the 1-D aorta calculated with both the viscous formulation (thin lines) and the inviscid formulation (thick lines).

Pulse waveforms along the aorta are insensitive in the scales of Figure 3.13 to changes by $\pm 10\%$ in the value of the viscosity of the control case. An increase in the density of blood by $\pm 10\%$ of the value of the control case produces a decrease by less than 1% in the pressures simulated by the control case. The opposite effect is observed if the density is decreased by 10%. In any case, velocity and flow rate are insensitive to these changes in density, in the scales of Figure 3.13 (right and bottom).

3.4.6 Sensitivity to the peripheral resistance, compliance and venous pressure

Changes in the peripheral resistance only affect R_{μ_2}, since R_{μ_1} is determined by Equation (2.148). Figure 3.23 (left) shows that an increase by 10% in the peripheral resistance of our control case increases the mean pressure by 9% the value of the control case, without any significant change in the shape of the pressure waveform. The opposite effect is observed with a decrease by 10% in the peripheral resistance. Both results occur everywhere along the aorta and are in good agreement with Equation (2.126). Despite the change in the total pressure R_{μ_T}, we can not observe

any significant change in the diastolic slope. Figure 3.23 (right) shows that the velocity peak decreases by about 3% with the increase in the peripheral resistance, and the opposite occurs with the decrease in the peripheral resistance. Flow rate waveforms remain unchanged in the scale of Figure 3.13 (bottom), since flow rate is enforced by the inflow boundary condition.

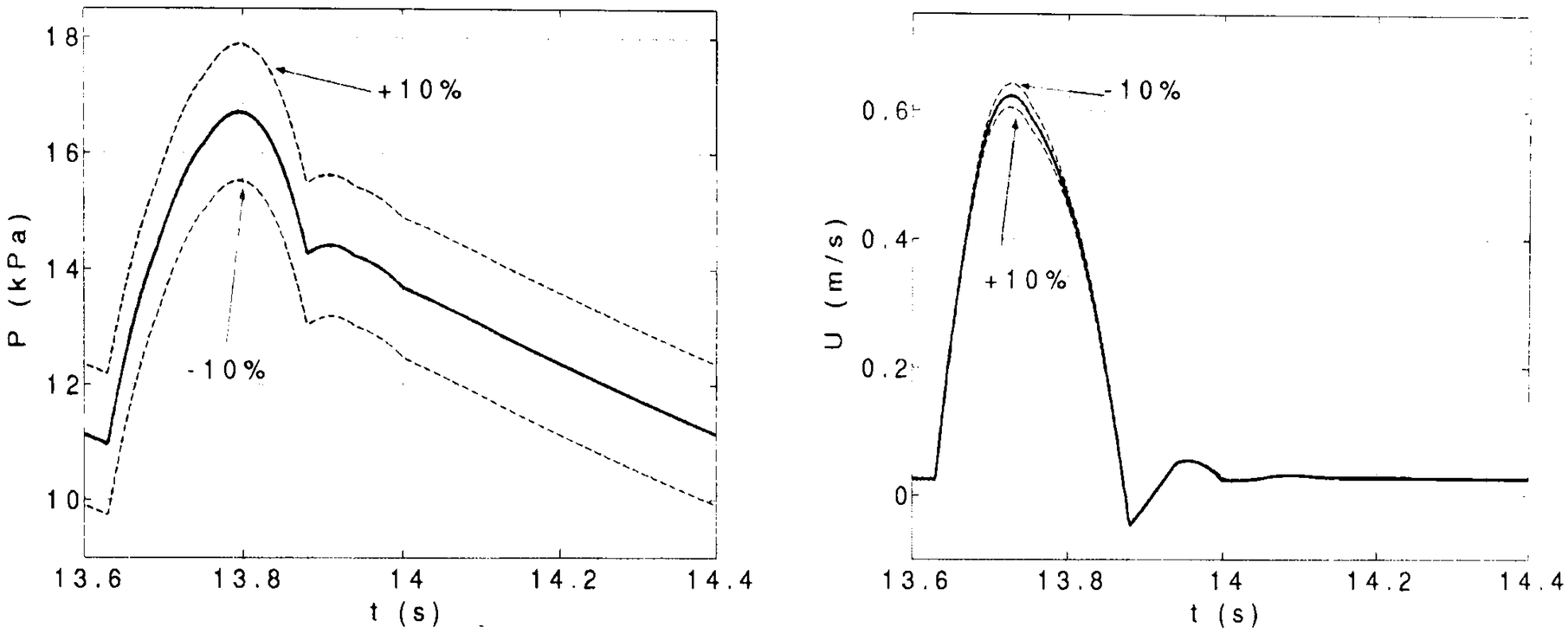


Figure 3.23: Effect of increasing and decreasing by 10% the peripheral resistance on the periodic pressure (left) and velocity (right) time histories at $x = 0.2$ m. Solid lines indicate the results obtained with the control case and dashed lines the results obtained with the $\pm 10\%$ changes.

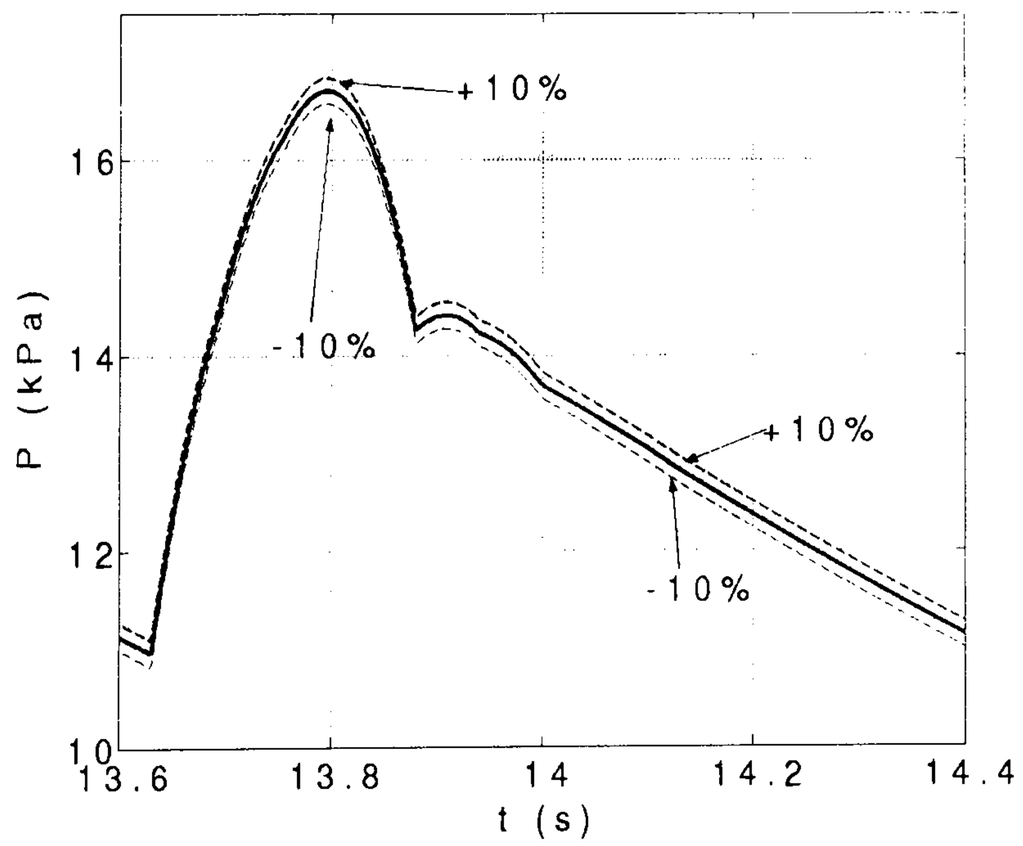


Figure 3.24: Effect of increasing and decreasing by 10% the venous pressure on the periodic pressure time history at $x = 0.2$ m. The solid line indicates the result obtained with the control case and the dashed lines indicate the results obtained with the $\pm 10\%$ changes.

Figure 3.24 shows that an increase by 10% in the venous pressure, p_{out}, produces a translation of the pressure waveform upward by the same value as the increment

in p_{out}, which is in agreement with Equation (2.126), since R_{μ_T} and $\overline{Q}$ remain unchanged. We observe the same effect at other locations along the aorta. Changes in velocity and flow rate are less significant and they can not be detected in the scales of Figure 3.13 (right and bottom).

Sections 3.4.3 and 3.4.4 have assessed the effect of changing the distribution of the total compliance between the aorta and the periphery, by changing the aortic diameter, wall thickness, and elastic modulus, which indicated that the windkessel effect increases when a larger part of the total compliance is located in the aorta.

Table 3.6: Effect on the mean, systolic and diastolic pressures, the mean flow and the peak velocity obtained with the 1-D model of the human aorta at $x = 0.2$ m, of the linear formulation, the non-linear inviscid formulation and changes by $\pm 10\%$ in the length, diameter, wall thickness, elastic modulus, peripheral resistance and venous pressure of the control case. Numbers express the percentage of change relative to the values of the control case.

	Mean pressure	Systolic pressure	Diastolic pressure	Mean flow	Peak velocity
Linear formulation	-0.1	-1.3	1.1	-0.2	2.2
Inviscid formulation	-0.1	-0.3	-0.1	0.0	0.5
+10% length	0.1	-1.6	0.6	0.0	4.2
-10% length	0.0	1.4	-0.6	0.0	-4.5
+10% diameter	-0.1	-5.0	2.6	0.0	-18.3
-10% diameter	0.1	7.7	-3.9	0.0	24.6
+10% wall thickness	0.1	1.7	-0.8	0.0	2.1
-10% wall thickness	0.0	-1.9	1.0	0.0	-2.4
+10% elastic modulus	0.1	1.7	-0.8	0.0	2.1
-10% elastic modulus	0.0	-1.9	1.0	0.0	-2.4
+10% periph. resistance	9.0	7.0	11.1	0.0	-2.9
-10% periph. resistance	-9.0	-7.1	-11.2	0.0	2.9
+10% venous pressure	1.0	0.8	1.3	0.0	-0.4
-10% venous pressure	-1.0	-0.8	-1.2	0.0	0.3

3.4.7 Summary

Table 3.6 summarises the results of the sensitivity analysis carried out with the 1-D model of the human aorta. The percentages shown in the table correspond to the rate of change, relative to the control case, in the mean, systolic and diastolic

pressures, the mean flow and the peak velocity at $x = 0.2$ m, produced by the linear formulation, the non-linear inviscid formulation and changes by $\pm 10\%$ in the length, diameter, wall thickness, elastic modulus, peripheral resistance and venous pressure of the control case.

3.4.8 Role of the terminal lumped parameter models

This section studies the effect of the different lumped parameter models described in Section 2.7.3 on the pulse wave propagation along the 1-D aorta. At the inlet, both the physiological (Figure 3.11, left) and the Gaussian delta wave (Figure 3.11, right) inflow rates are enforced. The study of each lumped parameter model is shown in Sections 3.4.8.1 to 3.4.8.3.

3.4.8.1 Terminal resistance

Figure 3.25 shows the effect on pulse pressure and velocity at three locations along the aorta of coupling the aortic segment to a terminal resistance lumped parameter model with R_μ equal to the total peripheral resistance $R_{\mu_1} + R_{\mu_2}$ used in the control case. The inlet is perfused with the flow rate shown in Figure 3.11 (left). We observe

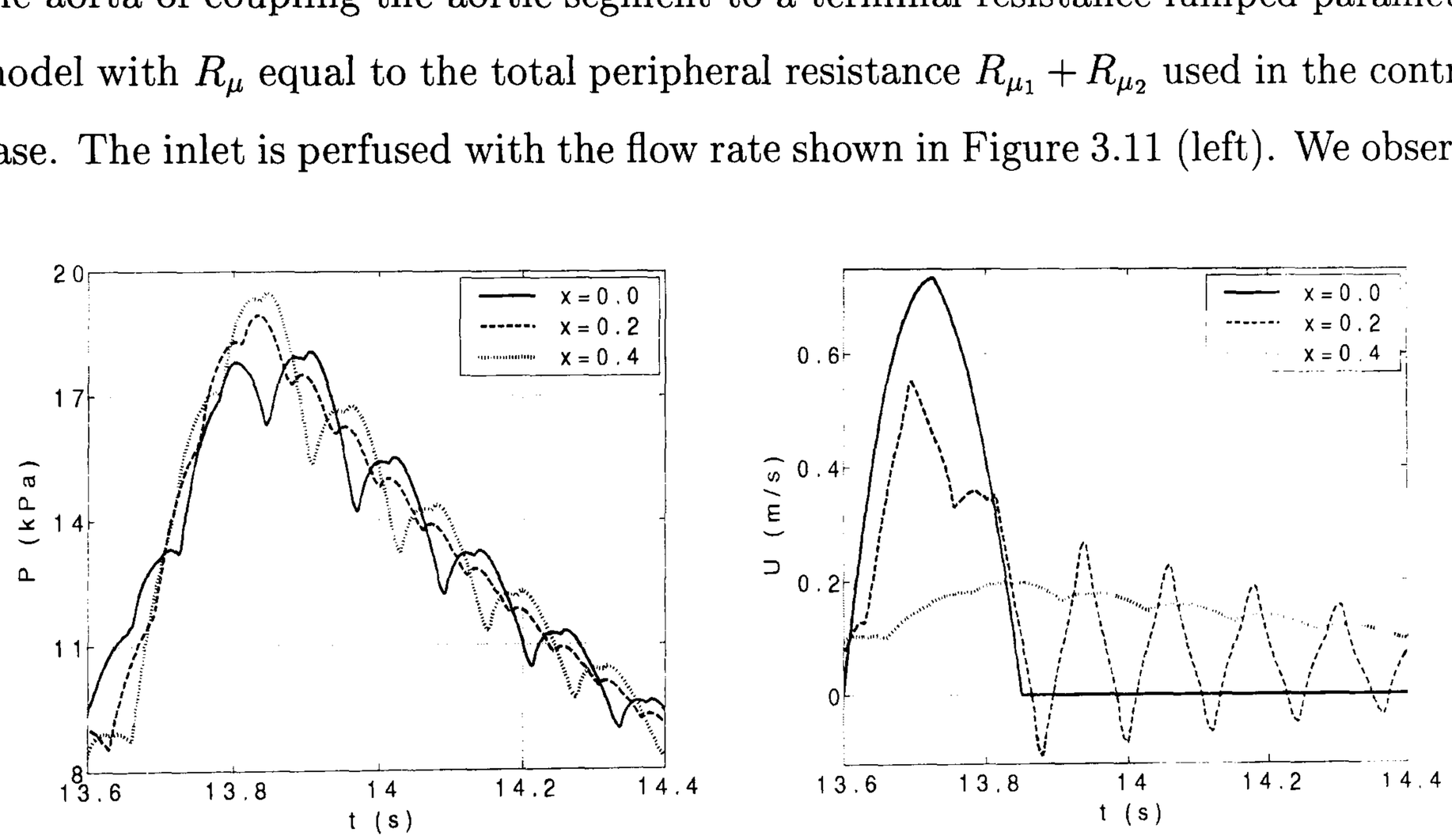


Figure 3.25: Periodic pressure (left) and velocity (right) time histories at $x = 0.0$, $x = 0.2$ m, and $x = 0.4$ m, obtained with the 1-D aorta coupled to a terminal resistance lumped parameter model. The inlet is perfused with the flow rate shown in Figure 3.11 (left).

that the pulse waveforms exhibit many peaks compared to the corresponding waves simulated in the control case (Figure 3.13, top), with a pulse pressure of about twice the value in the control case, since the total compliance has been reduced to the

aortic compliance. We also note that a resistance lumped parameter model yields the same mean pressure as in the control case, since Equation (2.126) also applies. Flow rate waveforms have a very similar shape to velocity flow waveforms.

The shape of the waves obtained with the terminal resistance model can be better understood if we look at the propagation of the Gaussian inflow rate and we separate the forward and backward waves originated (Figure 3.26). We observe that

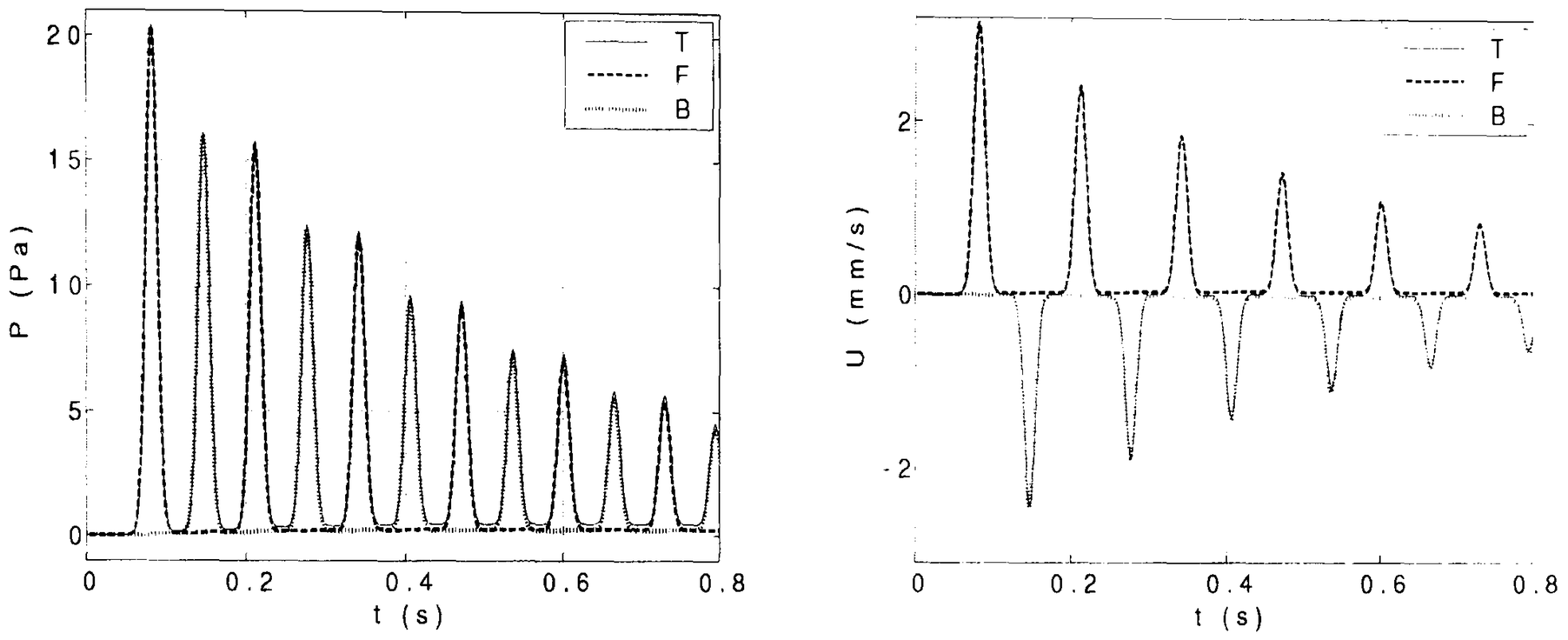


Figure 3.26: Periodic pressure (left) and velocity (right) time histories at $x = 0.2$ m (T), along with their forward (F) and backward (B) contributions. They are obtained with the 1-D aorta coupled to a terminal resistance lumped parameter model. The inlet is perfused with the periodic Gaussian delta wave velocity shown in Figure 3.11 (right).

the outlet only reflects the incoming waves, without smoothing them as does the compliance of the RCR model (Figure 3.15). The amplitude of the reflected waves at the terminal resistance is about 0.78 the amplitude of the incoming wave, which is close to the value of the linear reflection coefficient, $R_t = 0.80$, determined from Equation (2.140). At the inlet, a total reflection ($R_t = 1$) of the incoming waves is obtained, since the inflow velocity is almost zero when the waves arrive. This study has considered $p_{out} = 0.0$ to obtain a nearly periodic solution in the first heartbeat. We also observe that a positive R_t produces a change in the sign of the incoming velocity wave but maintains the sign of the incoming pressure wave, which is in agreement with Expressions (2.132) and (2.133).

3.4.8.2 Three-element (RCR) windkessel model

This section studies the effect on pulse wave propagation of changing the value of R_{μ_1} used in the simulation shown in Figure 3.15 to allow the incoming wave from

the 1-D aorta to reach C and R_{μ_2} without being reflected by R_{μ_1}. Figure 3.27 shows

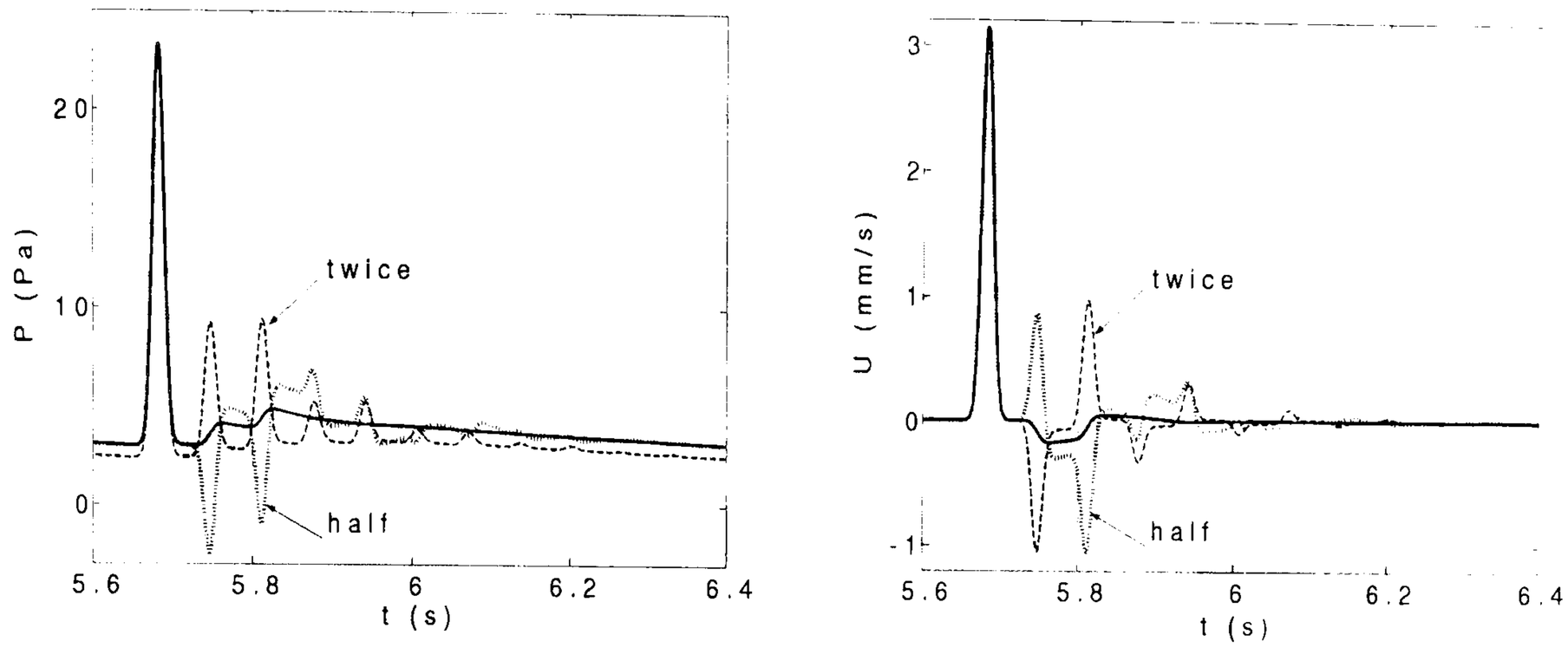


Figure 3.27: Effect of doubling (dashed lines) and halving (dotted lines) the value of R_{μ_1} used in the control case (solid lines) on the periodic pressure (left) and velocity (right) time histories at $x = 0.2$ m of the 1-D aorta coupled to a RCR lumped parameter model. The inlet is perfused with the Gaussian delta wave flow rate shown in Figure 3.11 (right).

that the periodic pressure and velocity time histories at $x = 0.2$ m present more reflections with double (dashed lines) and with half (dotted lines) the value of R_{μ_1} determined by (2.148), since part of the incoming wave is reflected back to the inlet by R_{μ_1} without being smoothed by C. We also observe that the pattern of reflected waves obtained with a higher R_{μ_1} at $x = 0.2$ m is the same as the pattern measured at the same location with the terminal resistance model (Figure 3.26), except for smaller reflections at the outlet, because $R_{\mu_1} < R_{\mu_2}$, and the addition of the waves smoothed by C and reflected by R_{μ_2}. With smaller R_{μ_1}, R_t becomes negative and, hence, the sign of the incoming velocity wave is maintained but not the sign of the incoming pressure wave.

We note that Stergiopulos *et al* [88] considered $R_{\mu_1} = 0.2R_{\mu_2}$ to minimise wave reflections produced by R_{μ_1} in their 55 arteries model. Making use of Equation (2.148) to calculate R_{μ_1} yields $R_{\mu_1} = 0.12R_{\mu_2}$.

3.4.8.3 Four-element (RCLR) windkessel model

This section studies the effect of adding an inductance to the RCR model in order to account for the peripheral blood inertia, which acts as a time-varying resistance that depends on the flow rate. Stergiopulos *et al* [87] determined a total blood inertia of the systemic system of about $7.0 \cdot 10^5$ Kg m^{-4}, by fitting a four-element windkessel

model to *in-vivo* human ascending aortic pressure and flow waves. According to (2.117), the blood inertia of the 1-D aorta (control case) is $13.4 \cdot 10^5$ Kg m^{-4}, and, hence, larger than the total inertia determined by Stergiopulos *et al* [87], which indicates that blood inertia is located mainly in the aorta.

Even if we assume that the total peripheral inertia is 10^6 Kg m^{-4} (the same order of magnitude as the inertia of the total systemic circulation determined by Stergiopulos and co-workers), any change in pressure, velocity, and flow rate is not found in the scales of Figure 3.13, which suggests that the peripheral inertia has a very small effect on pulse waveforms.

3.5 Final remarks

This chapter has first validated the 1-D formulation against a well-defined experimental model, showing that the numerical model is able to capture the main features of pressure and flow pulse wave propagation measured along the aorta of the experimental model, with a good quantitative agreement. This validation increases the confidence in the 1-D code and its ability to model clinically relevant problems, such as the applications presented in this thesis.

Next, the chapter has assessed the ability of the technique proposed in Section 2.8 to estimate the fluid resistance, inertia and compliance (RLC) of the vessels beyond the arteries simulated by the 1-D formulation. Although this technique is able to approximate some peripheral resistances and compliances (data on physiological peripheral inertias is not available) with significant accuracy, it still needs further validation with *in-vivo* and experimental data.

The chapter has used the 1-D formulation to simulate pulse wave propagation in the human aorta. The results of this study suggest that the pulse wave transformation along the aorta is a consequence of the combined effect of wave reflections from the peripheral vessels (simulated as an RCR lumped parameter model) and the aortic valve when shut, the windkessel effect due to the compliance of the system, and the temporal shift between forward and backward travelling waves determined by the pulse wave velocity. Although single wave reflections coming from the peripheral vessels are small for waves arriving from the aorta (Figure 3.15), their convolution

with the half-sinusoidal wave produced by the heart leads to the pulse waves observed *in-vivo* (Figure 3.13).

This chapter has concluded with a sensitivity analysis of the results obtained with the 1-D model of the human aorta. The study has shown that non-linearities and viscous dissipation have small effects on the pulse waveforms along the aorta under physiological conditions. Pulse waveforms are very sensitive to changes in the aortic calibre and the peripheral resistance, but they are less sensitive to changes in the length of the aorta, the thickness and elasticity of the aortic wall, the venous pressure, and especially to changes in the density and viscosity of blood. The study has shown that the mean pressure depends only on the cardiac output, the peripheral resistance (the effect of the viscous resistance along the aorta is secondary) and the venous pressure. The pulse pressure depends mainly on the total compliance. The model studied divides the total compliance into aortic compliance, which depends on the geometry and elasticity of the aorta, and peripheral compliance, which simulates the effect of the geometry and elasticity of the rest of systemic vessels beyond the aorta. The reduction in pulse pressure is higher with the increasing total systemic compliance, which is in agreement with the classical windkessel model described in Section 2.7.3.2, and when a larger part of the total systemic compliance is aortic compliance. The inertia of the vessels beyond the aorta has a neglegible effect on pulse waveforms.

Chapter 4

Pulse wave propagation in the palmar arch

The hand is perfused by the ulnar artery (UA) and the radial artery (RA), both of which branch off of the brachial artery (BA) usually below the elbow (Figure 4.1, left). The UA and RA anastomose across the hand in the form of a superficial palmar arch (SPA) and a deep palmar arch (DPA) that provide collateral flow pathways to the digital arteries, the SPA being the most important route. However, arterial anatomical variations are frequent, with an incomplete SPA reported in approximately 30 to 40% of subjects [47, 56, 61].

It is of clinical interest to determine the presence of sufficient ulnar collateral flow through the SPA or the DPA to decide whether the RA can be harvested to be used as a coronary artery bypass graft without ischemic complications (lack of blood supply) to the hand, particularly the thumb and index finger [10, 70, 81, 85, 98, 102, 103]. Furthermore, the RA is also a favourable access for haemodialysis if ulnar collateral flow is present [41]. A common technique to detect the presence of sufficient collateral flow consists of measuring blood flow in the radial part of the SPA by Doppler ultrasonography (US) before and during RA compression at the wrist. The presence of reversal flow (towards the RA) is considered to be an indicator of adequate collateral flow across the palm. This technique is known as the *modified Allen's test* (MAT).

Some computational studies of pulse wave propagation in the human arm (Balar *et al* [8]) and the human leg (Raines *et al* [73]) have been carried out, but without

including the palmar or plantar arches. This study considers the most prevalent anatomies in the hand, including the SPA and DPA, to investigate if anatomies with a complete palmar arch have a significant effect on pressure and velocity wave propagation in the main conduit arteries of the arm compared to anatomies in which neither palmar arch is complete. Section 4.1 describes the anatomies studied, Section 4.2 investigates if the presence of sufficient collateral flow through the palmar arch can be detected directly from pressure and flow measurements on the arteries of the arm, and Section 4.3 assesses the suitability of the MAT in the anatomies introduced in Section 4.1. The main results obtained in this chapter are summarised in Section 4.4.

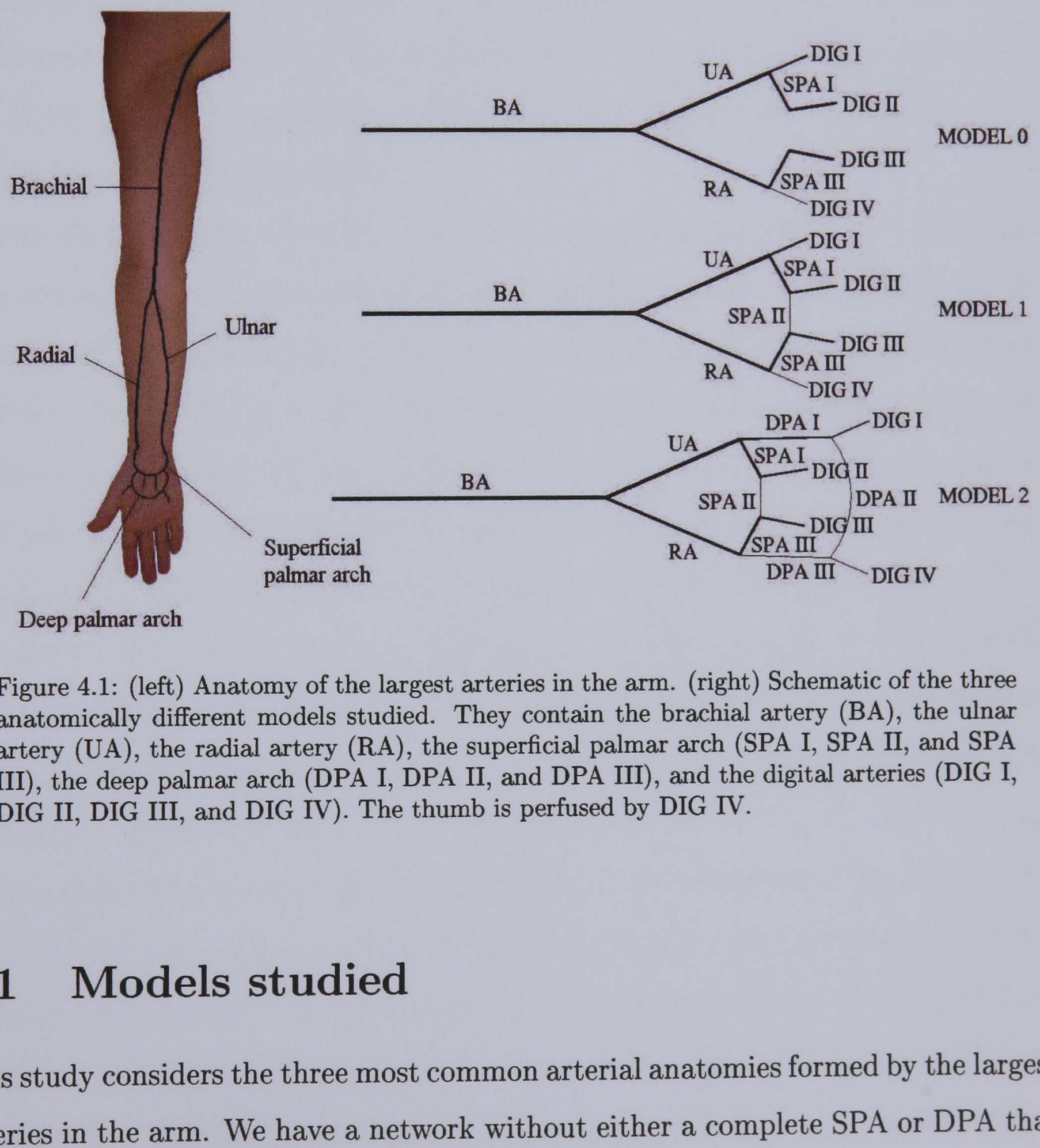


Figure 4.1: (left) Anatomy of the largest arteries in the arm. (right) Schematic of the three anatomically different models studied. They contain the brachial artery (BA), the ulnar artery (UA), the radial artery (RA), the superficial palmar arch (SPA I, SPA II, and SPA III), the deep palmar arch (DPA I, DPA II, and DPA III), and the digital arteries (DIG I, DIG II, DIG III, and DIG IV). The thumb is perfused by DIG IV.

4.1 Models studied

This study considers the three most common arterial anatomies formed by the largest arteries in the arm. We have a network without either a complete SPA or DPA that is called *Model 0* (zero arches), a network with a complete SPA that is called *Model*

1 (one arch) and a network with both a complete SPA and DPA that is called *Model 2* (two arches). Figure 4.1 (right) shows a schematic of these three models.

These three models aim at representing the arterial geometry and elasticity of healthy young adult arms. In the absence of detailed knowledge of these properties, the lengths, l, and initial radii, R_0, of the BA, UA and RA are based on data published by Stergiopulos *et al* [88]. The remaining lengths are estimated from an anatomical atlas [49], whereas the remaining R_0's are assumed to have an area ratio at splitting flow junctions (ratio of the total cross-sectional area of the daughter vessels to that of the parent vessel) close to 1.2. This is the average value calculated by Papageorgiou and Jones [66] at many splitting flow junctions of the systemic circulation, which include vessels whose radii are smaller than those used in the simulations of this chapter. The wall thickness, h, of each artery is assumed to be 10% of R_0, based on the values published by Stergiopulos *et al* [88] for the main conduit human systemic arteries.

According to [66], an area ratio of 1.2 produces minimal wave reflection for forward travelling waves at a splitting flow junction. Based on this result, the elastic modulus, E, of each artery is determined by assuming that the linear reflection coefficient R_{f_1} (2.110) at each splitting flow junction is zero (well-matched junctions for forward travelling waves). Therefore, if A_{0_1} and c_{0_1} are the initial area and wave speed of the parent artery, respectively, and A_{0_2}, c_{0_2}, A_{0_3} and c_{0_3} are the corresponding parameters in the two daughter arteries, then $\frac{A_{0_1}}{c_{0_1}} = \frac{A_{0_2}}{c_{0_2}} + \frac{A_{0_3}}{c_{0_3}}$.

Tables 4.1 to 4.3 show the physiological parameters used in each model and Table 4.4 provides the reflection coefficients R_{f_1}, R_{f_2} and R_{f_3}, and area ratios at the splitting flow junctions of each model. We notice that Model 1 has the same anatomy as Model 0, except for the presence of the middle SPA (SPA II). The anatomy of Model 2 differs from the anatomy of Model 1 in the extension of the digital arteries I and IV and the addition of the DPA. Therefore, the two splitting flow junctions involving the arteries of the DPA and the digital arteries I and IV of Model 2 have $R_{f_1} \neq 0$. Note also that in all the junctions the reflection coefficients for waves approaching the junction through the two daughter vessels are very different from the reflection coefficient for waves coming from the parent vessel.

Table 4.1: Physiological data used in Model 0. The fifth column indicates the time it takes a wave to travel the artery at a speed c_0.

Arterial segment	Length (cm)	R_0 (cm)	c_0 (m/s)	Time (ms)	Periph. resistance (10^{10} Pa s m^{-3})	Periph. compliance (10^{-11} m^3 Pa^{-1})
Brachial	42.2	0.249	9.2	46	-	-
Ulnar	23.8	0.203	10.4	23	-	-
Radial	23.5	0.174	10.8	22	-	-
Digital I	2.5	0.130	12.1	2	5.13	1.63
Digital II	3.0	0.136	11.1	3	4.69	1.79
Digital III	3.0	0.132	13.8	2	5.01	1.67
Digital IV	1.5	0.093	13.6	1	10.00	0.84
SPA I	1.0	0.169	11.1	1	-	-
SPA III	1.0	0.161	12.1	1	-	-

Table 4.2: Physiological data used in Model 1. The fifth column indicates the time it takes a wave to travel the artery at a speed c_0.

Arterial segment	Length (cm)	R_0 (cm)	c_0 (m/s)	Time (ms)	Periph. resistance (10^{10} Pa s m^{-3})	Periph. compliance (10^{-11} m^3 Pa^{-1})
Brachial	42.2	0.249	9.2	46	-	-
Ulnar	23.8	0.203	10.4	23	-	-
Radial	23.5	0.174	10.8	22	-	-
Digital I	2.5	0.130	12.1	2	5.13	1.63
Digital II	3.0	0.136	11.1	3	4.69	1.79
Digital III	3.0	0.132	13.8	2	5.01	1.67
Digital IV	1.5	0.093	13.6	1	10.00	0.84
SPA I	1.0	0.169	11.1	1	-	-
SPA II	1.0	0.114	14.5	1	-	-
SPA III	1.0	0.161	12.1	1	-	-

Table 4.3: Physiological data used in Model 2. The fifth column indicates the time it takes a wave to travel the artery at a speed c_0.

Arterial segment	Length (cm)	R_0 (cm)	c_0 (m/s)	Time (ms)	Periph. resistance (10^{10} Pa s m^{-3})	Periph. compliance (10^{-11} m^3 Pa^{-1})
Brachial	42.2	0.249	9.2	46	-	-
Ulnar	23.8	0.203	10.4	23	-	-
Radial	23.5	0.174	10.8	22	-	-
Digital I	2.5	0.130	12.1	2	5.13	1.59
Digital II	3.0	0.136	11.1	3	4.69	1.74
Digital III	3.0	0.132	13.8	2	5.01	1.63
Digital IV	1.5	0.093	13.6	1	10.00	0.81
SPA I	1.0	0.169	11.1	1	-	-
SPA II	1.0	0.114	14.5	1	-	-
SPA III	1.0	0.161	12.1	1	-	-
DPA I	3.0	0.130	12.1	2	-	-
DPA II	3.0	0.075	14.5	2	-	-
DPA III	3.0	0.093	13.6	2	-	-

Table 4.4: Linear reflection coefficients at the splitting flow junctions of the models shown in Figure 4.1 (right) for a wave coming from the parent vessel (R_{f_1}), the daughter vessel I (R_{f_2}), or the daughter vessel II (R_{f_3}).

Parent—Daughter I—Daughter II	R_{f_1}	R_{f_2}	R_{f_3}	Area ratio	Model
Brachial—Ulnar—Radial	0.00	−0.41	−0.59	1.2	0 1 2
Ulnar—SPA I—Digital I	0.00	−0.35	−0.65	1.1	0 1
Radial—SPA III—Digital IV	0.00	−0.23	−0.77	1.2	0 1
Ulnar—SPA I—DPA I	0.00	−0.35	−0.65	1.1	2
Radial—SPA III—DPA III	0.00	−0.23	−0.77	1.2	2
SPA I—Digital II—SPA II	0.00	−0.35	−0.65	1.1	1 2
SPA III—Digital III—SPA II	0.00	−0.42	−0.58	1.2	1 2
DPA I—Digital I—DPA II	−0.12	−0.12	−0.76	1.3	2
DPA III—Digital IV—DPA II	−0.23	−0.23	−0.53	1.6	2

4.2 Study of pulse wave propagation

First, the wave reflections originated when the SPA and the DPA are complete are analysed by introducing a Gaussian delta pressure wave at the inlet of the BA (Section 4.2.1). They are isolated from the wave reflections originated at the boundaries of each model by considering boundary conditions that completely absorb any incoming wave, and from viscous attenuation by considering inviscid flow. In Section 4.2.2, pulse wave propagation is studied considering more physiological inflow and terminal boundary conditions and viscous flow.

4.2.1 Impulse wave

This section studies the propagation of a Gaussian delta pressure wave introduced at the inlet of the BA, centred at $t_0 = 0.1$ s, with a peak value $\hat{p}$ of 1 kPa and a small variance $\tau = 0.002$ s (Figure 4.2), represented by the equation

$$p_{bc}(t) = \hat{p}\, e^{-\left(\frac{t-t_0}{\tau}\right)^2}. \tag{4.1}$$

This pressure is transformed into an area through the tube law (2.11) and it is

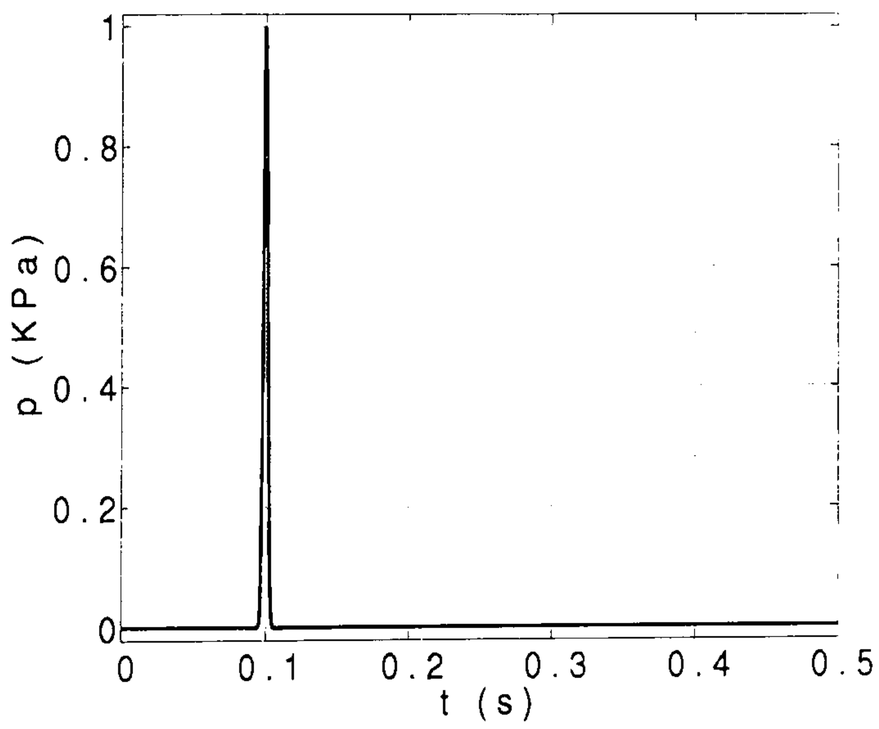


Figure 4.2: Gaussian pressure enforced at the inlet of the brachial artery.

enforced as an inflow boundary condition at the inlet of the BA by means of Equation (2.67). The value of A_R in (2.67) is assumed to be equal to the initial area in the BA, so that any incoming wave is ignored and, hence, completely absorbed by the boundary. The outflow of each digital artery is modelled by the terminal reflection coefficient described in Section 2.7.3.3, with $R_t = 0$ so that any incoming wave is completely absorbed by the outflow boundary.

Each simulation is run with the non-linear formulation, one elemental region Ω_e in each arterial domain, $q = 81$ and $P = 80$ in the BA, UA and RA and $q = 11$ and $P = 10$ in the rest of the arteries (since they are much shorter), a time step $\Delta t = 5$ μs, and an initial state (A_0, p_0, U_0), with A_0 determined from the initial radii, R_0, in Tables 4.1 to 4.3, $p_0 = 0$ and $U_0 = 0$. A normal PC runs the models studied in this section in about five minutes.

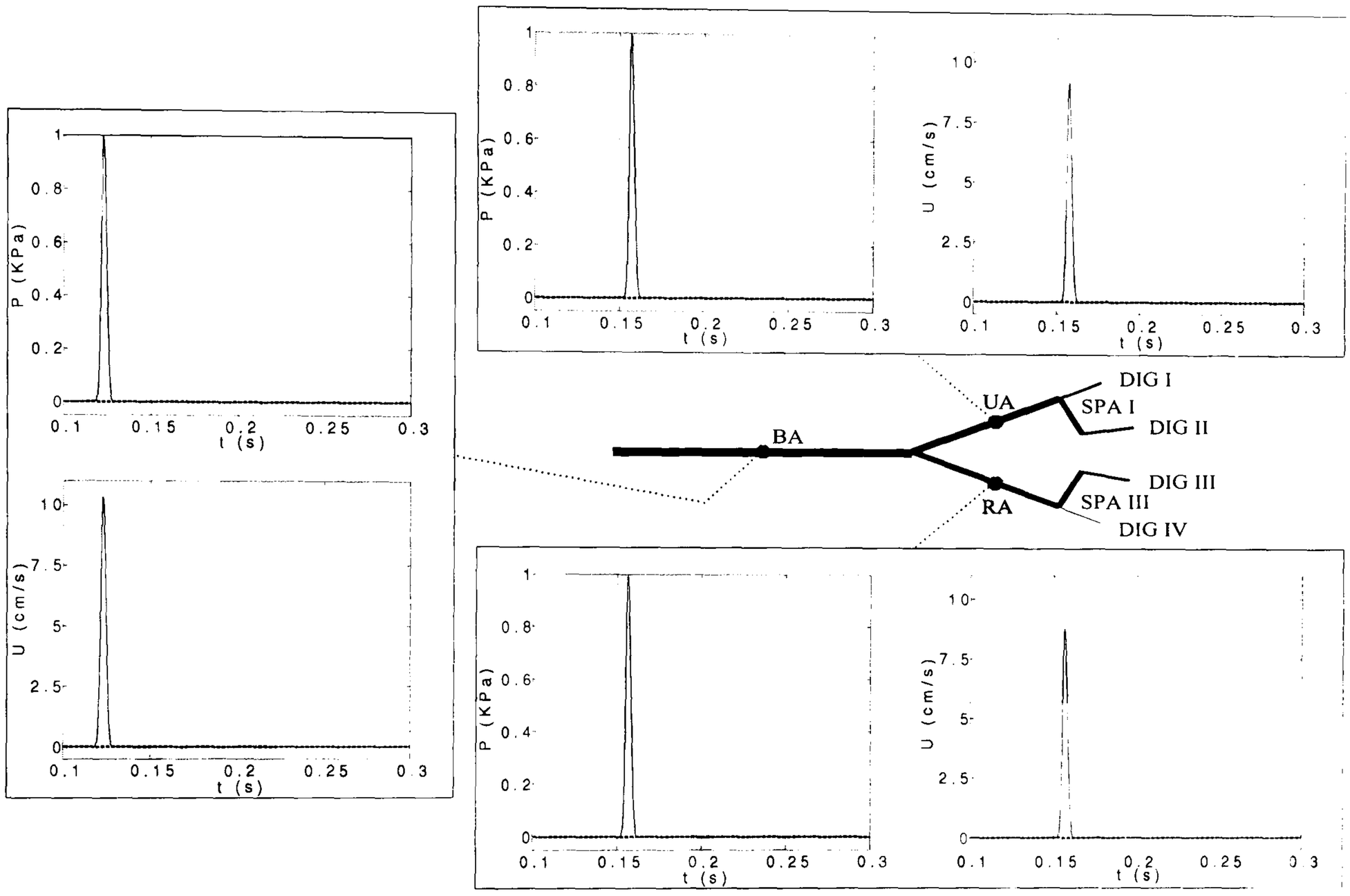
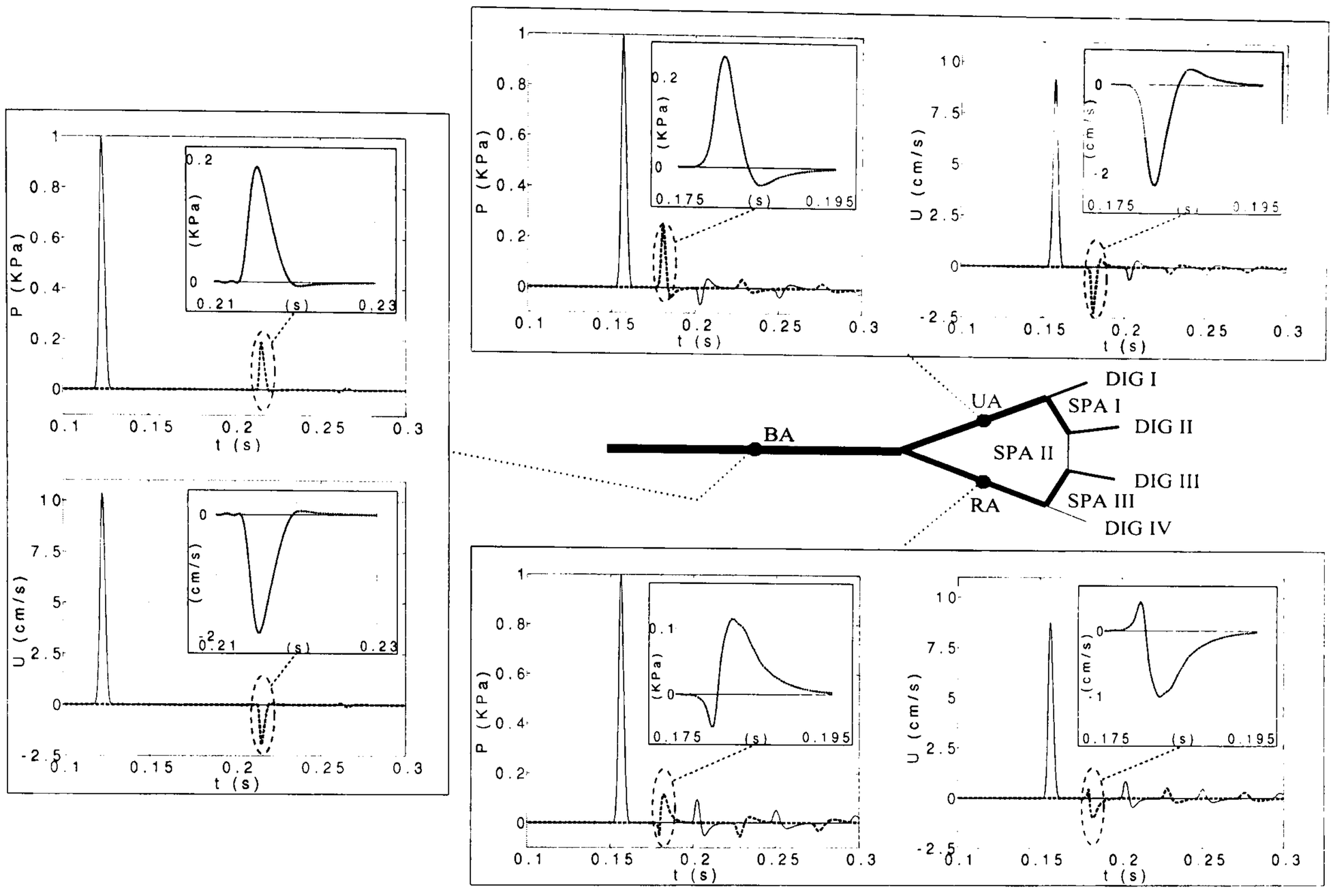


Figure 4.3: Forward (solid lines) and backward (dashed lines) pressure and velocity time histories in the middle points of the brachial (BA), ulnar (UA), and radial (RA) arteries of Model 0, when the Gaussian inflow boundary condition shown in Figure 4.2 is enforced, and $R_t = 0$ is applied at the outlet of each digital artery.

Figure 4.3 shows the forward and backward pressure and velocity time histories in the middle points of the BA, UA and RA of Model 0, obtained with the boundary conditions described above. Since all junctions are well-matched for forward travelling waves, the input pulse wave propagates through the BA, UA and RA with speeds close to the values of c_0 shown in Table 4.1 and without being reflected on its way to the digital arteries. In these three arteries, pressure and velocity waves consist only of forward contributions. The pressure peaks in the UA and RA are almost identical to the pressure peak in the BA, because the kinetic terms $\frac{1}{2}\rho U^2$

in Equations (2.90) and (2.91) are two orders of magnitude smaller than the pressure terms, and because viscous dissipation has been neglected. However, velocity peaks in the UA and RA are smaller than the velocity peak in the BA, which is in agreement with conservation of mass (2.89).

When the same boundary conditions are applied to Models 1 and 2, we initially observe the propagation of the input Gaussian delta wave through the BA, UA and RA exactly as in Model 0, but followed by reflected waves (Figure 4.4). In the BA, the first reflection to arrive is a backward travelling wave with a single peak in Model 1 (Figure 4.4, top) and two very close peaks in Model 2 (Figure 4.4, bottom). In both models, it appears about 0.09 s after the input wave, which is the time it takes a wave to go from the middle point of the BA to the middle SPA (SPA II), and to return, according to the travelling times shown in Tables 4.2 and 4.3. Therefore, this initial reflected wave is the result of the intersection, somewhere in the SPA II, of the input Gaussian delta wave arriving from the UA and RA. The second peak observed in Model 2 corresponds to a reflection in the DPA. Figure 4.5 shows clearly the presence of the second peak in Model 2 when the lengths of the vessels DPA I and DPA III are increased by five times.



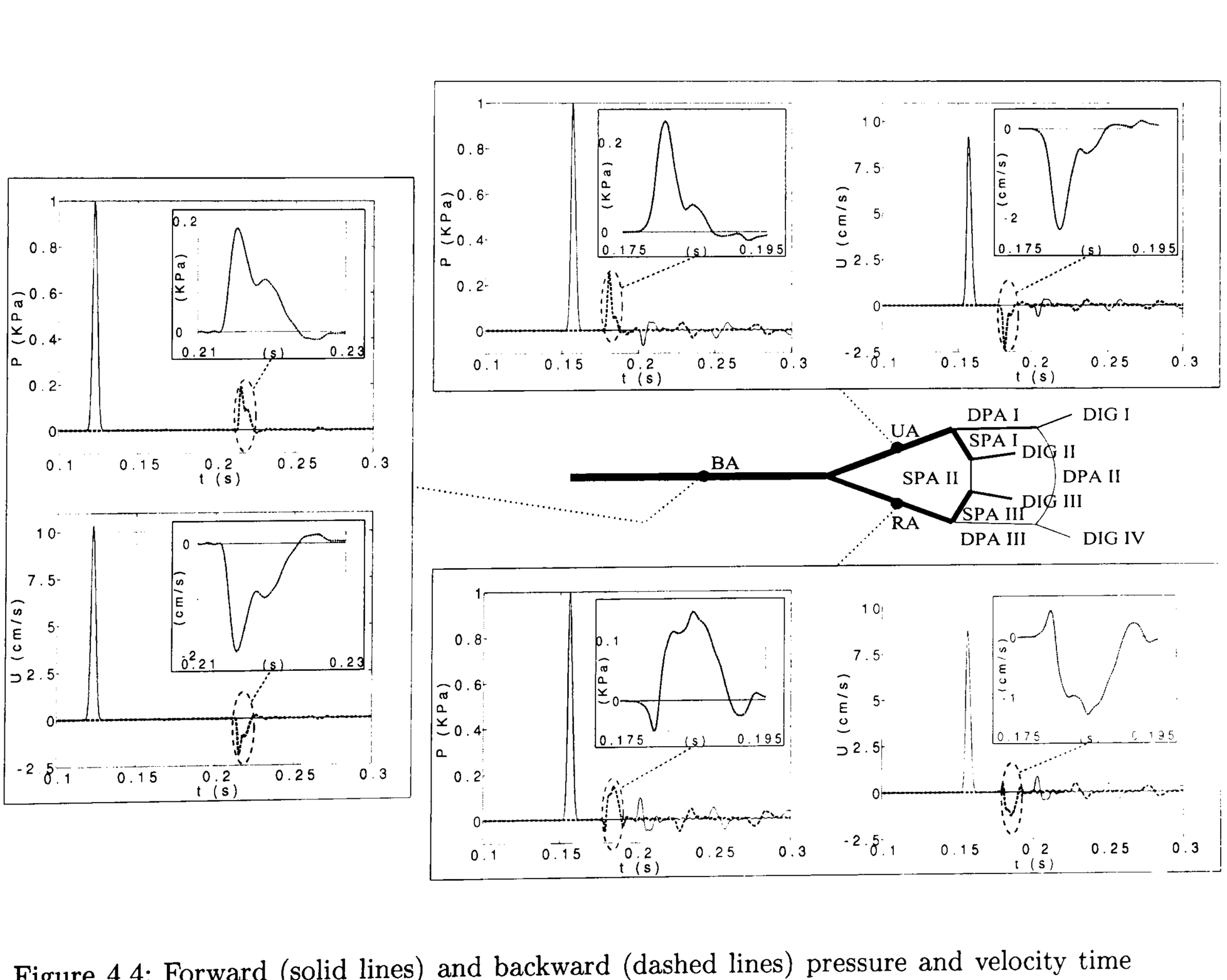


Figure 4.4: Forward (solid lines) and backward (dashed lines) pressure and velocity time histories in the middle points of the brachial (BA), ulnar (UA), and radial (RA) arteries of Model 1 (top) and Model 2 (bottom), when the Gaussian inflow boundary condition shown in Figure 4.2 is enforced, and $R_t = 0$ is applied at the outlet of each digital artery.

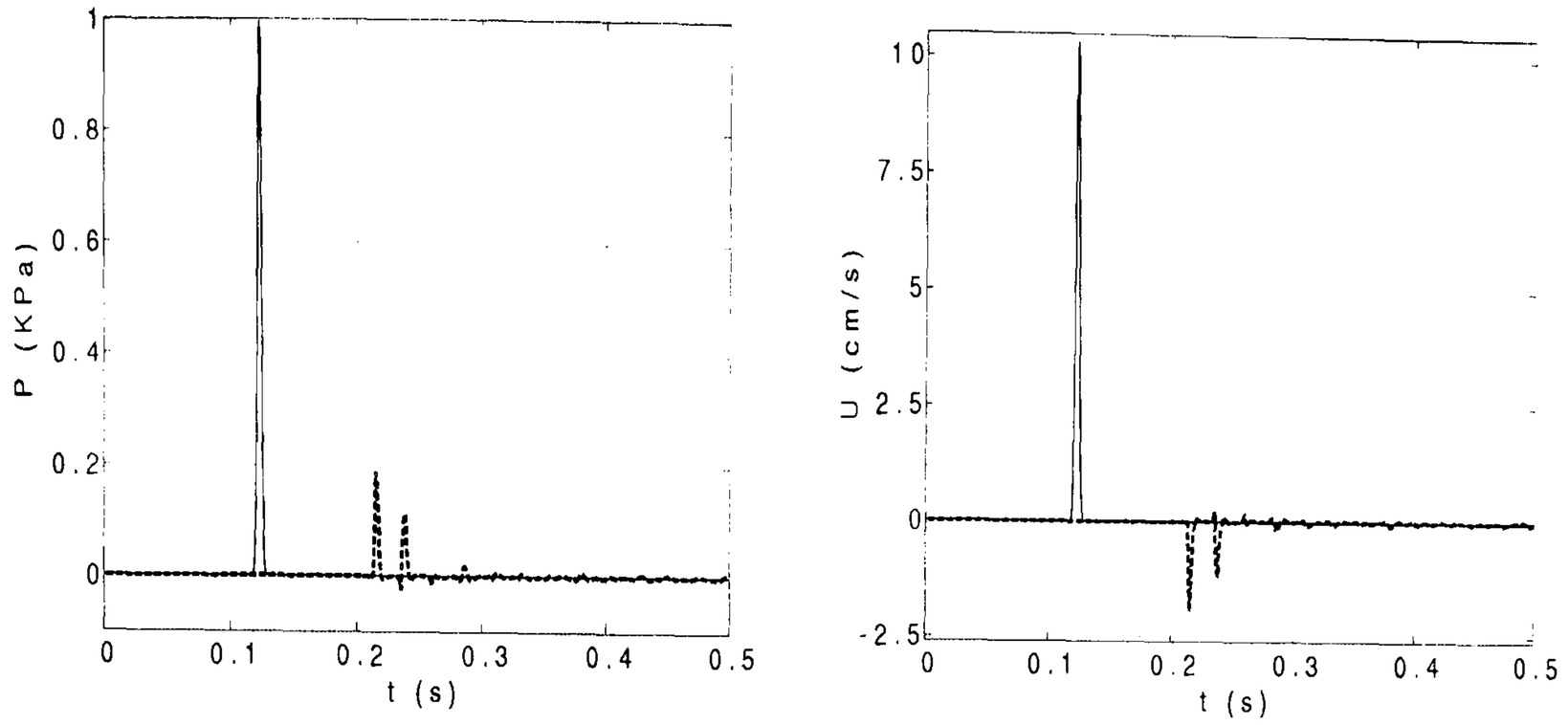


Figure 4.5: Forward (solid lines) and backward (dashed lines) pressure (left) and velocity (right) time histories in the middle point of the BA of Model 2, when the lengths of DPA I and DPA III have been increased by five times. The Gaussian inflow boundary condition shown in Figure 4.2 is enforced, and $R_t = 0$ is applied at the outlet of each digital artery. Two reflected peaks appear, the first one originated in the SPA and the second in the DPA.

The first reflected wave originated in the SPA is also observed in the UA and RA of Models 1 and 2 as a backward travelling wave. When it reaches the junction with the BA, it is partially transmitted to the BA and travels towards its inlet, where it is completely absorbed by the inflow boundary condition. The first backward wave to appear in the UA and RA is also partially reflected at the brachial bifurcation back to the UA and RA, and it travels towards the SPA (and also the DPA in Model 2), where the process of reflections and transmitions starts again to yield the rest of alternating forward and backward waves in the UA and RA, and the rest of backward waves in the BA. The shapes of these waves in Models 1 and 2 are better observed in Figure 4.6, which focuses on the temporal range 0.3 s $< t <$ 0.6 s. The peak values of both pressure and velocity waves present an exponential decay with time, because the peak value of an incident wave is reduced in every reflection and transmission, and the boundaries of each network completely absorb any incoming wave, decreasing the total energy of the system with time. Since R_{f_2} and R_{f_3} are negative in all the splitting flow junctions (see Table 4.4), the signs of both pressure and velocity reflected waves alternate between positive and negative values. We observe that Model 2 contains more pressure and velocity peak values than Model 1, since the former has more bifurcations, and, hence, more reflection sites.

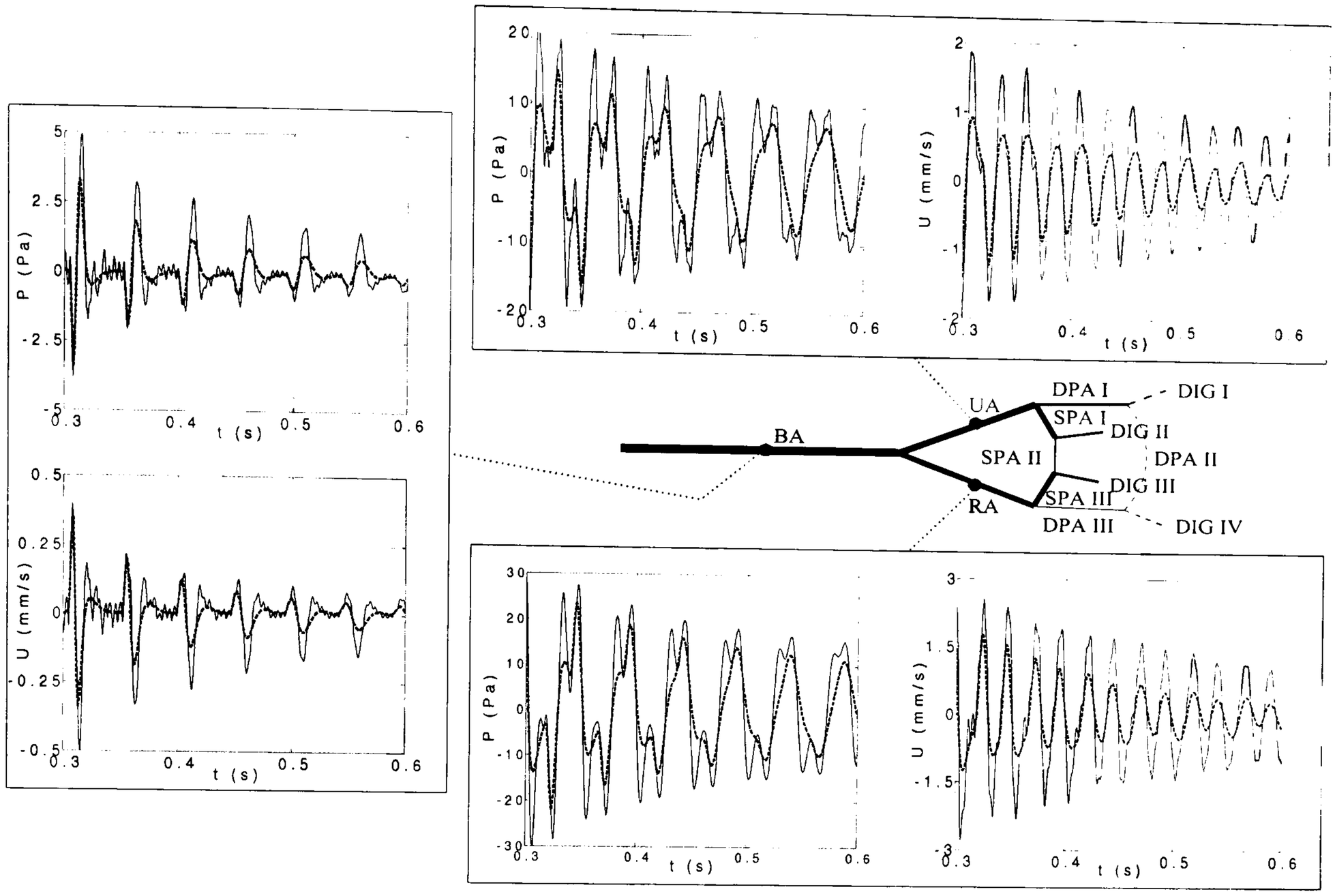


Figure 4.6: Comparison of pressure and velocity time histories in the middle points of the brachial (BA), ulnar (UA), and radial (RA) arteries of Models 1 (dashed lines) and 2 (solid lines), focusing on the temporal range 0.3 s $< t <$ 0.6 s, when the input Gaussian delta wave has travelled up to the digital arteries and only its reflected waves remain.

4.2.2 Physiological conditions

The study in Section 4.2.1 has shown that the topologies of the three models studied produce significant differences in pressure and flow patterns under ideal conditions (Gaussian inflow, absorbent boundary conditions, and inviscid flow) that isolate the waves reflected by each topology. This section analyses if there are also significant differences when more physiological boundary conditions and viscous flow are considered.

At the inlet of the BA, the velocity time history shown in Figure 4.7 (right), measured with Doppler US at the left subclavian artery of a healthy adult patient, is prescribed. At the outlets of each digital artery, an RCR lumped parameter model is coupled as explained in Section 2.7.3.6, with the total peripheral resistances $(R_{\mu_1} + R_{\mu_2})$ and compliances (C) shown in Tables 4.1 to 4.3. Each peripheral resistance is obtained by distributing the total resistance at the inlet of the BA. R_{μ_T}, so that the mean outflow rates in the digital arteries over a heartbeat are

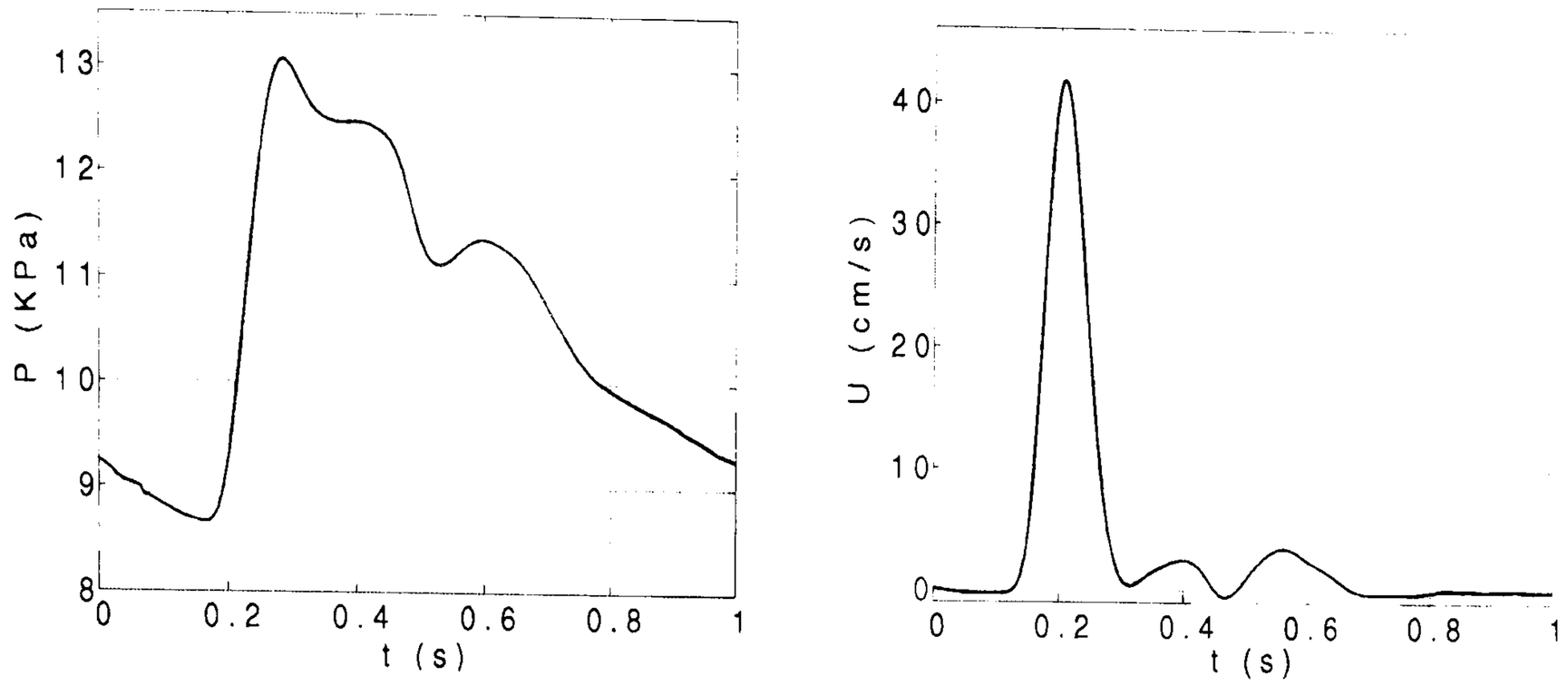


Figure 4.7: *In-vivo* pressure (left), measured with planar tonometry, and velocity (right), measured with Doppler US, over one cardiac cycle at the proximal part of the left subclavian artery.

proportional to the corresponding initial cross-sectional areas. The value of R_{μ_T} is calculated as the ratio between the mean pressure shown in Figure 4.7 (left) and the mean flow rate, according to Equation (2.126) (applying the windkessel model to simulate the systemic arterial tree of the arm). The mean flow rate is determined by multiplying the velocity shown in Figure 4.7 (right) by the cross-sectional area calculated from the pressure shown in Figure 4.7 (left) through the tube law (2.11). The value $R_{\mu_T} = 1.41 \cdot 10^{10}$ Pa s m^{-3} is obtained.

The total compliance of each model, C_T, is determined by fitting an exponential function during the last third of diastole in the *in-vivo* pressure of Figure 4.7 (left). According to (2.123), the time constant of the exponential decay is $R_{\mu_T} C_T$, which leads to $C_T = 2.02 \cdot 10^{-10}$ m^3 Pa^{-1}. The total peripheral compliance is the difference between C_T and the compliance of each artery in the network, calculated through (2.118). The total peripheral compliance is distributed among the digital arteries in proportion to their initial cross-sectional areas.

Each simulation is run with the non-linear formulation, one elemental region Ω_e in each arterial domain, $q = 11$ and $P = 10$ in the BA, UA and RA and $q = 4$ and $P = 3$ in the rest of arteries, a time step $\Delta t = 100$ μs, and an initial state (A_0, p_0, U_0), with A_0 determined from the initial radii, R_0, in Tables 4.1 to 4.3, $p_0 = 0$ and $U_0 = 0$. The waveforms become periodic after about 10 cycles, which takes less than two minutes to run in a normal PC.

Figure 4.8 shows the pressure and velocity time histories in the middle points of

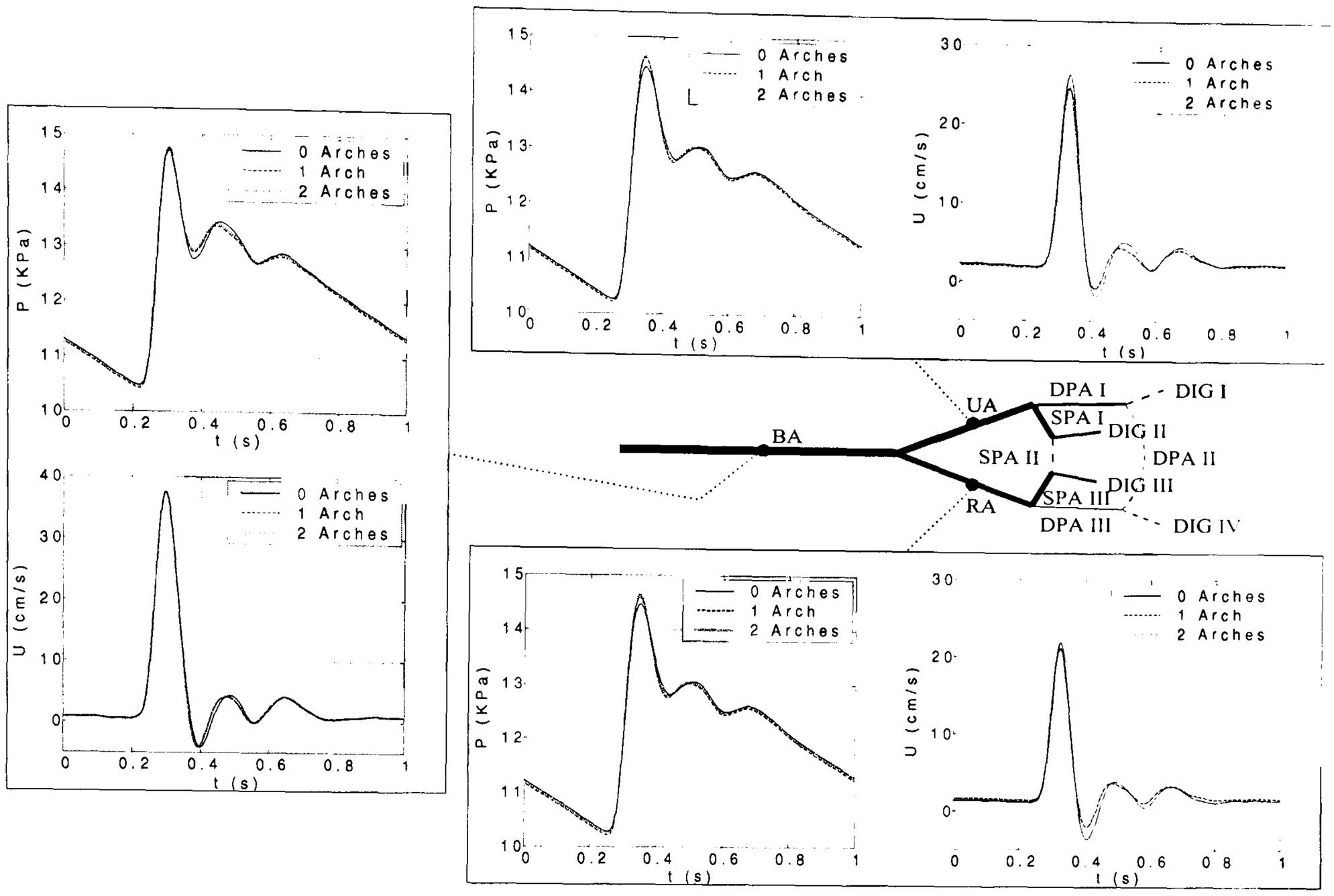


Figure 4.8: Pressure and velocity time histories in the middle points of the brachial (BA), ulnar (UA), and radial (RA) arteries of Models 0, 1, and 2 when the flow measured *in-vivo* in the BA (Figure 4.7, right) is propagated and an RCR model is coupled at the outlet of each digital artery.

the BA, UA and RA of each model. We observe that the different topologies studied do not produce significant changes in pressure and velocity pulse waves in any of the three arteries to be able to detect the presence of a complete SPA or DPA by looking at the pressure and velocity waveforms.

4.3 Assessment of the modified Allen's test (MAT)

As it was explained at the beginning of this chapter, the presence of reversal flow in the radial part of the SPA (SPA III) is considered to be an indicator of adequate collateral flow across the palm, which is referred to as a negative MAT.

Several authors have studied the reliability of the MAT. Studies by Pola *et al* [70], Serricchio *et al* [81] and Zimmerman *et al* [103] showed that all the follow-up patients who underwent harvesting of the RA after a negative MAT did not present signs of hand ischemia (insufficient blood supply). However, a study with 129 patients by Starnes *et al* [85] showed that the test may unnecessarily exclude some patients for

RA graft or RA access for haemodialysis (false-positive) and may also place a number of patients at risk of hand ischemia (false-negative). Kamienski and Barnes [40] reported a 73% false-positive rate of the MAT.

The objective of this section is to simulate the test in the three anatomically different models depicted in Figure 4.1 (right), with the same physiological boundary conditions as used in Section 4.2.2. This study focuses on analysing if small calibres of the middle SPA (SPA II) and insufficient compression of the RA are responsible for false-positive or false-negative results of the MAT. When a false result occurs, the study analyses if the alternative technique proposed by Starnes *et al* [85] can assess the presence of sufficient ulnar collateral flow better. This technique consists of measuring the change in the systolic pressure of the digital arteries III and IV with the compression of the RA. Pressures are measured with a digital pressure cuff placed on the proximal phalanx. A decrease in digital systolic pressure of 40 mmHg (5.3 kPa) or less is considered to be an indicator of sufficient collateral flow.

Section 4.3.1 simulates the MAT in the models of Figure 4.1 (right) and analyses the effect of harvesting the RA on digital outflow rates. It also studies the effect of changing the location of the compression point along the RA on the reversal flow peak measured by the test. Next, the study shows how a reduction in the calibre of the SPA (Section 4.3.2) and an insufficient compression of the RA (Section 4.3.3) affect the result of the MAT.

4.3.1 Simulation of the test

The MAT is simulated in the three models studied in Section 4.2.2. A compression of the RA leading to total occlusion is simulated by enforcing the condition $U = 0$ at the compression point. Again, each simulation is run for sufficient cardiac cycles until the waveforms become periodic. This typically takes around 10 cycles.

Figure 4.9 compares the velocity in the middle point of the SPA III of each model before (left) and during (right) compression of the RA 15 cm proximal to the brachial bifurcation (approximately at the level of the standard pressure point in the wrist). Differences between the three anatomical variations are minimal before compression, with flow coming from the RA and moving towards the central segment of the SPA (SPA II). If a compression leading to total occlusion is simulated, flow becomes

zero in Model 0, since the SPA II is absent, whereas flow reverses remarkably in Models 1 and 2 because it comes from the UA through the SPA. These results are in reasonable agreement with the *in-vivo* Doppler US measurements published by Zimmerman *et al* [103] (Figure 4.10).

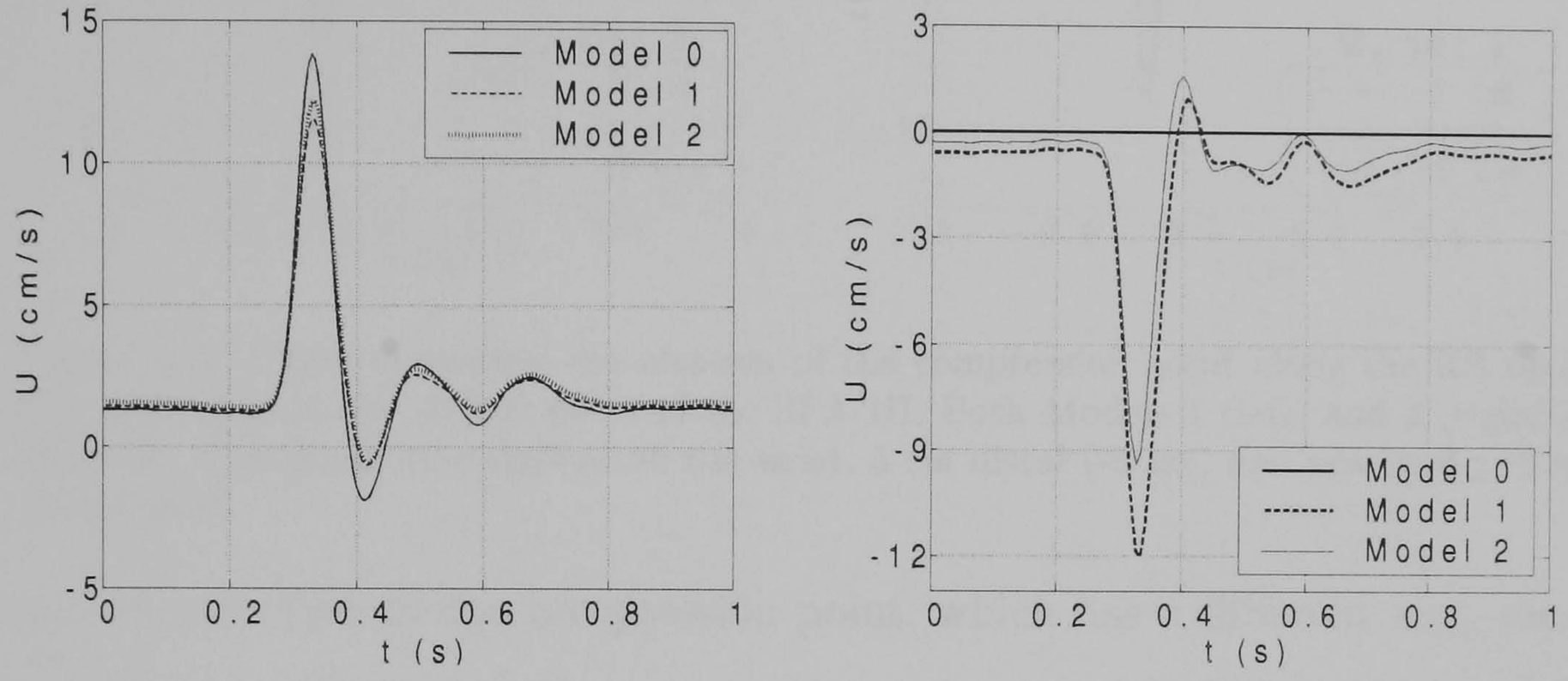


Figure 4.9: Velocity time histories in the middle point of the SPA III of each model before (left) and during (right) compression of the RA at the wrist.

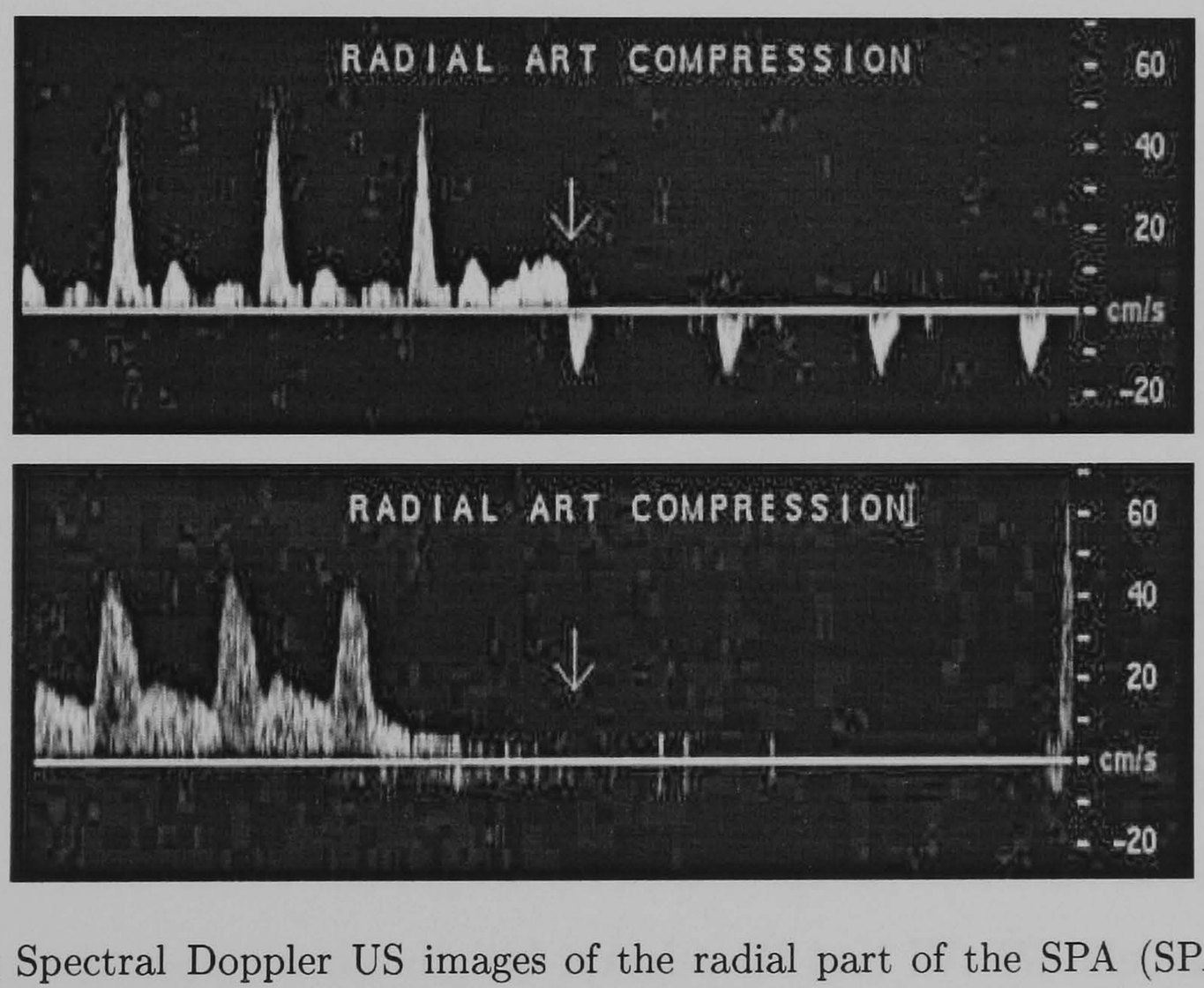


Figure 4.10: Spectral Doppler US images of the radial part of the SPA (SPA III in the models) in a healthy volunteer demonstrate blood flow towards the transducer before compression of the RA (left of arrow). In one hand, flow reverses after the compression (right of arrow), indicating a complete palmar arch (top). In the contralateral hand, flow does not reverse after the compression, indicating an incomplete arch (bottom). (From Zimmerman *et al* [103].)

The 1-D simulations also indicate that the reversal flow peak increases in Models 1 and 2 as the compression point in the RA is moved away from the hand (Figure 4.11), since the temporal shift between the initial wave coming from the SPA

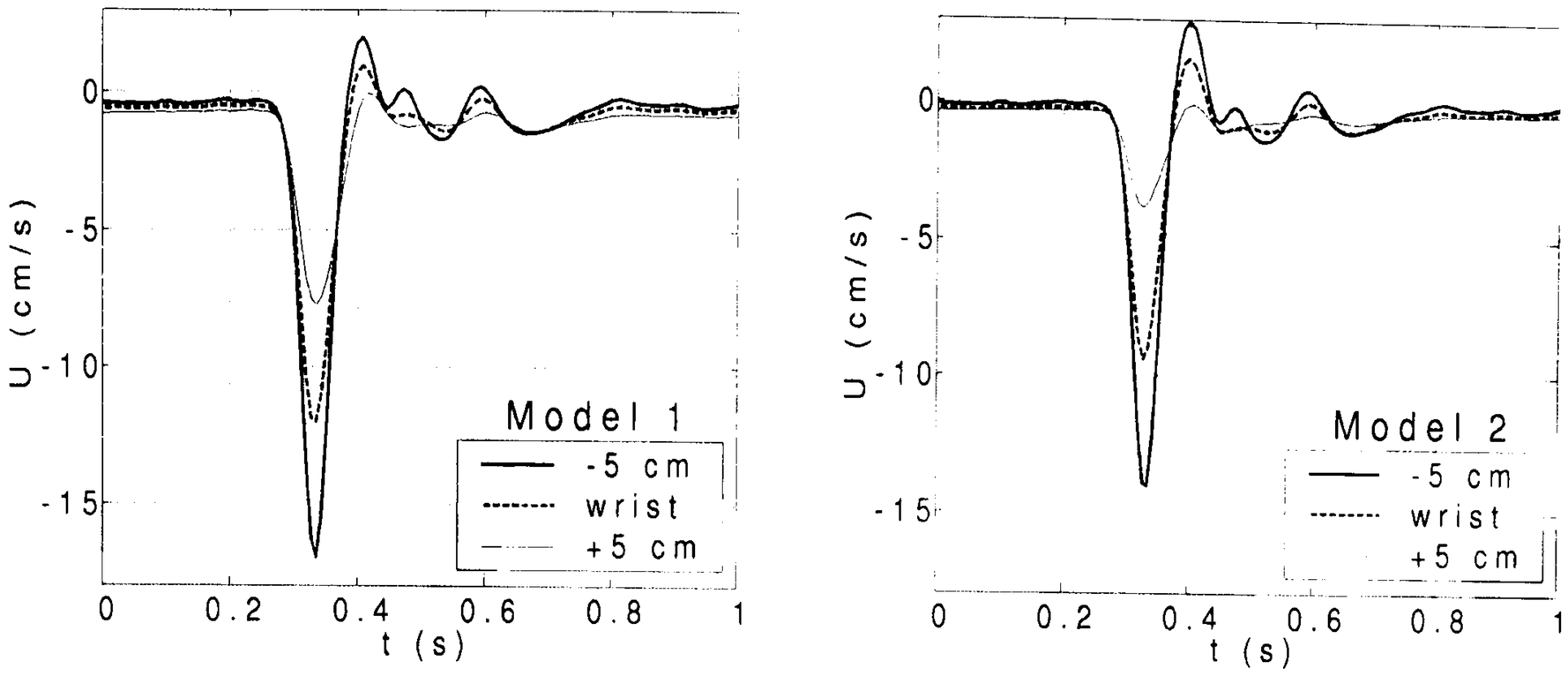
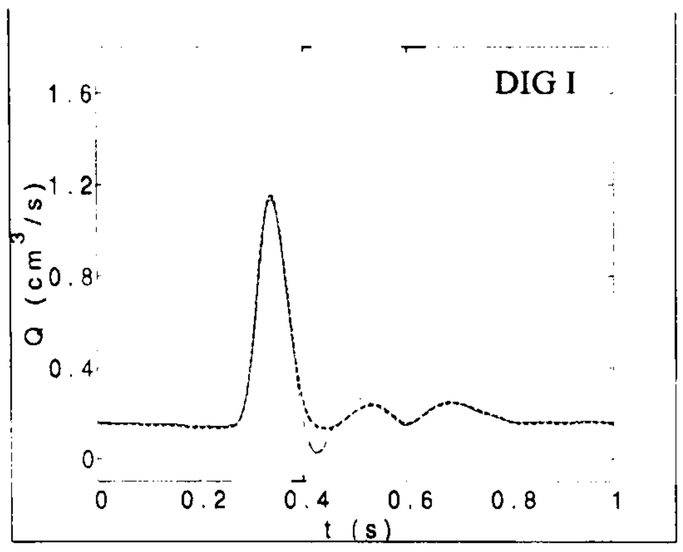
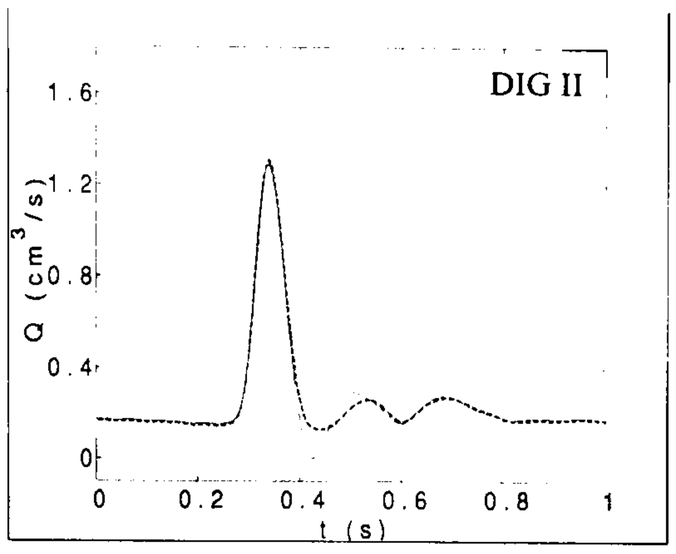


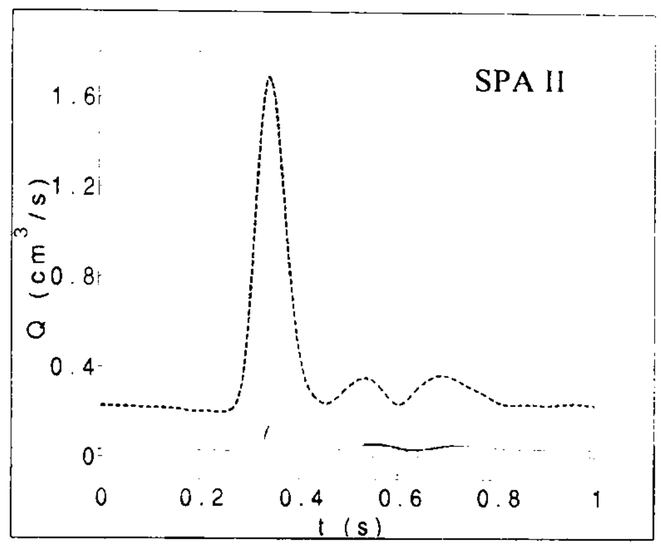
Figure 4.11: Effect of moving the location of the compression point along the RA on the flow measured in the middle point of the SPA III. Both Models 1 (left) and 2 (right) are depicted. Compression is applied on the wrist, 5 cm distal (-5 cm) and proximal (+5 cm) to the hand.

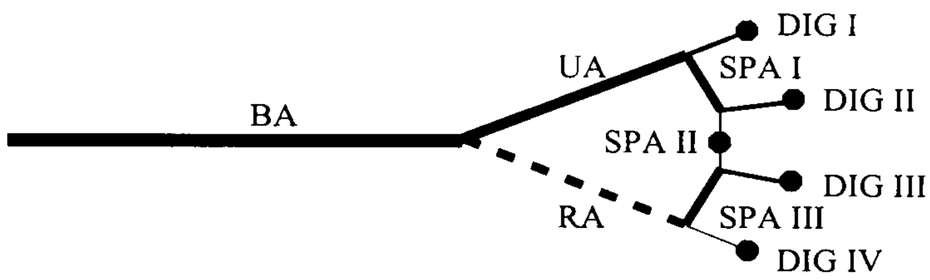
II and its reflection at the compression point, which has a different sign, increases with increasing distance to the compression point from the hand. Hence, the peak of the flow signal can be better detected by the MAT if compression is applied as far as possible from the hand.

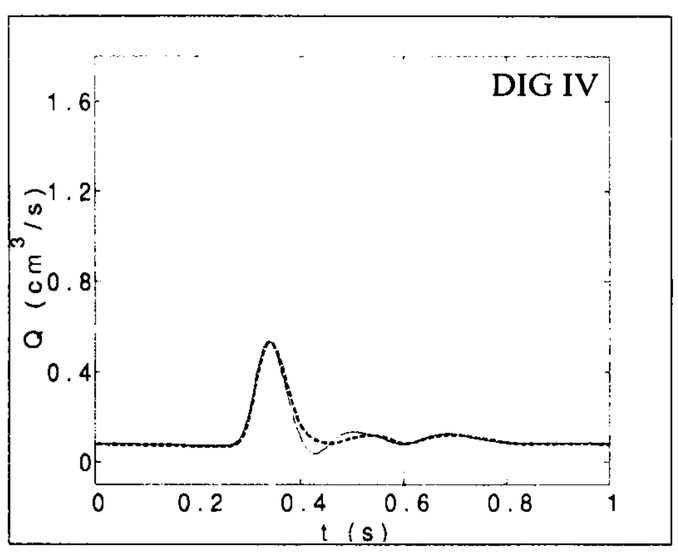
To assess the potential risk of hand ischemia, this section also analyses the effect of removing the RA from Models 1 and 2 on blood supply to the fingers. Figure 4.12 shows flow rate over one cardiac cycle at the outlets of the digital arteries of Models 1 (top) and 2 (bottom), when the RA is present (solid lines) and when it has been harvested (dashed lines). The results in all the digital arteries before and after harvesting do not differ significantly. Mean flow rates change less than 1% in all the digital arteries of Model 1 and less than 7% in all the digital arteries of Model 2, which suggests that changes in digital mean flow rates are small enough for the peripheral arteries to compensate for them with vasoconstriction (increase in peripheral resistance) in the digital arteries I and II, and vasodilation (reduction in peripheral resistance) in the digital arteries III and IV. We also notice that the presence of the DPA in Model 2 does not introduce significant changes in the digital flow pulse waves predicted by Model 1.

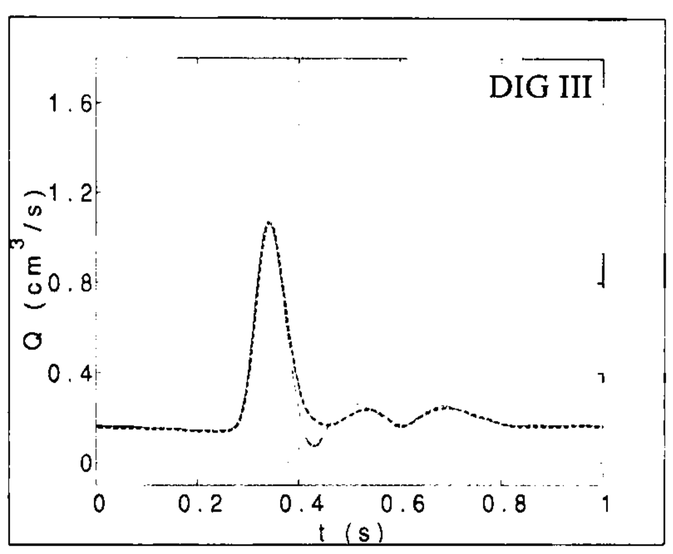


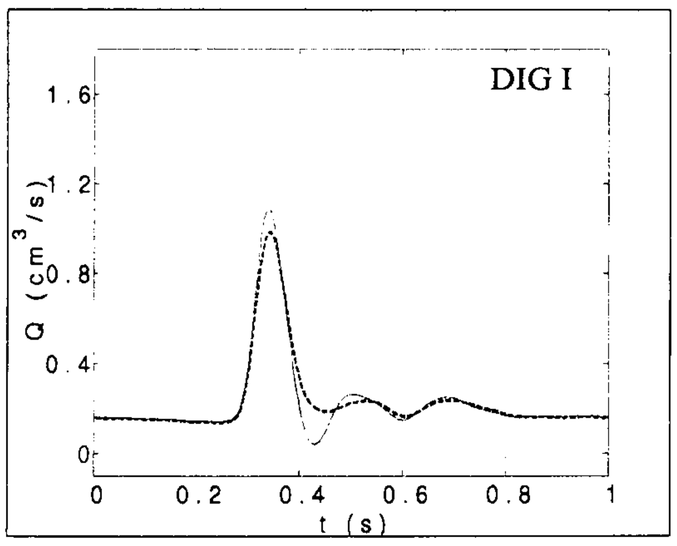


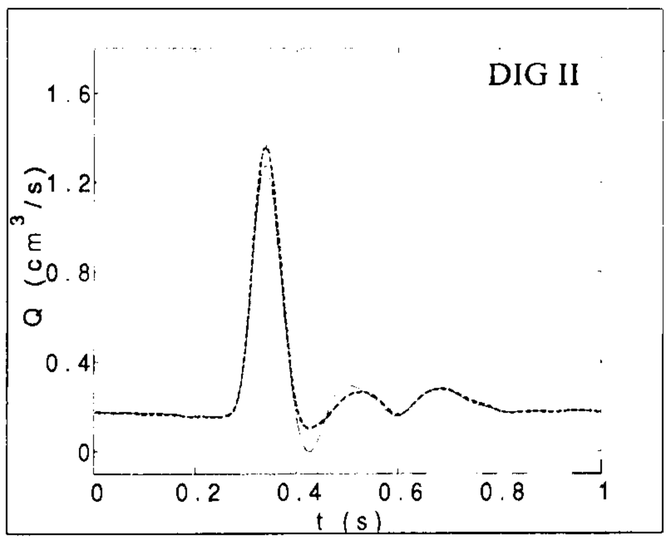


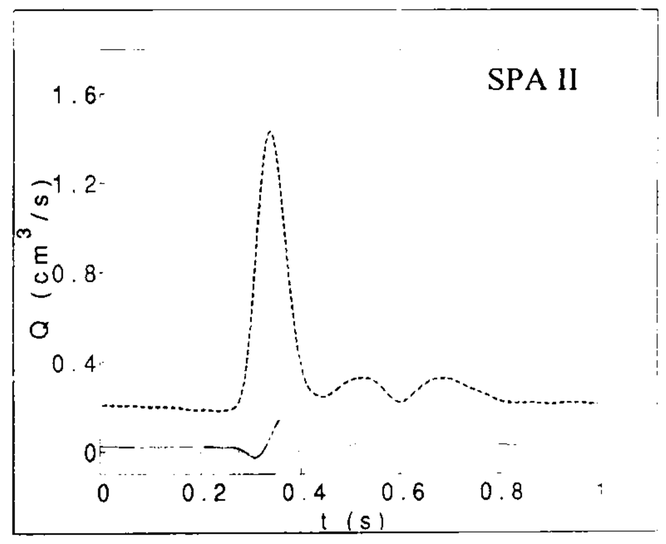


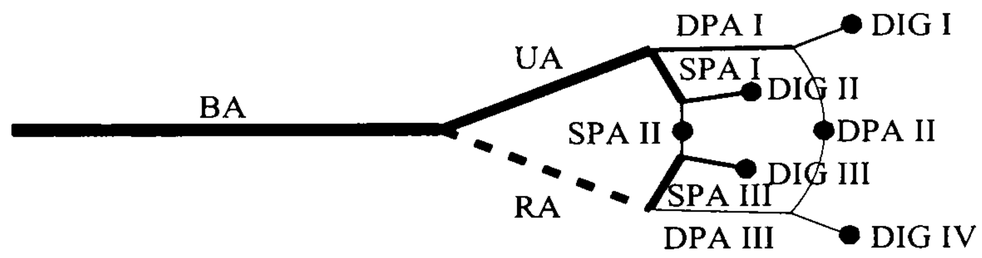


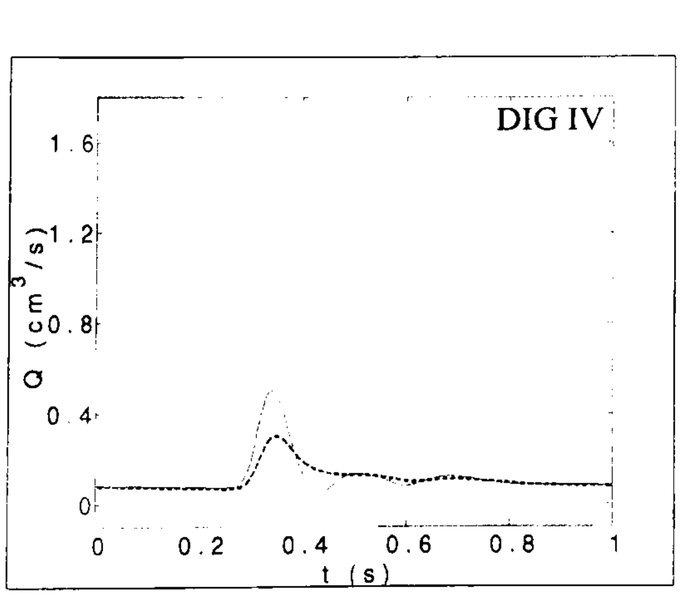


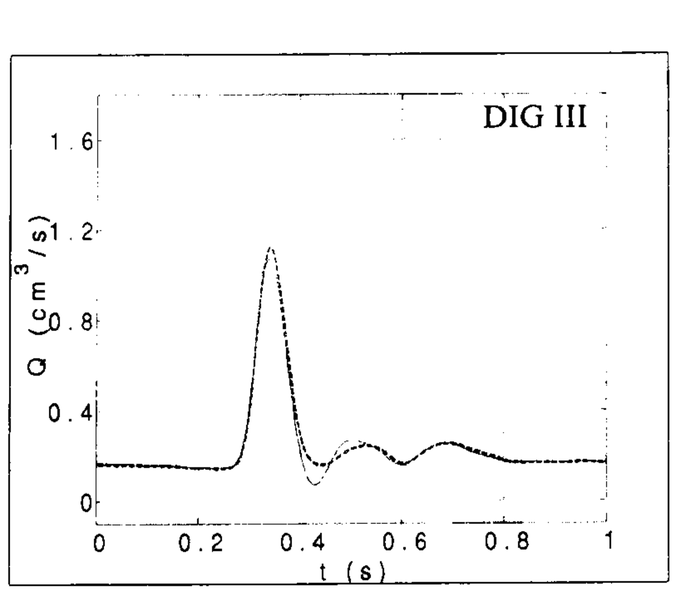












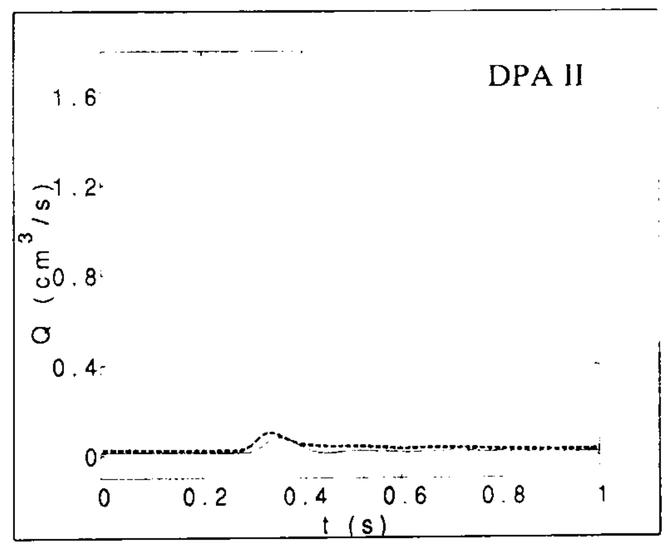


Figure 4.12: Flow rate time histories in the middle point of the SPA II and at the outflows of the digital arteries of Models 1 (top) and 2 (bottom), and in the middle point of the DPA II of Model 2, when the RA is present (solid lines) and when it has been harvested (dashed lines). Flow rates in SPA II and DPA II are positive towards the RA.

Figure 4.12 also compares the collateral flow rates through the SPA II of Models 1 and 2 with and without the RA. If the RA is absent, the mean collateral flow towards the digital arteries III and IV is approximately nine times higher in Model 1, and seven times higher in Model 2. Mean flow through the DPA II of Model 2 does not increase significantly if the RA is removed, which suggests that collateral flow takes place mainly through the SPA. Finally, we note that some ulnar collateral flow towards the digital arteries III and IV is observed in both models when the RA is present.

4.3.2 Effect of reducing the calibre of the SPA

This section studies the effect of reducing the calibre of the central SPA (SPA II) of Models 1 and 2 on the peak of the reversal flow measured at the SPA III during occlusion of the RA, and on the mean outflows in the digital arteries III and IV after harvesting the RA. We reduce the original calibre of the SPA II (100%), referred to as the calibre of the control case, in steps of 10% until it becomes zero.

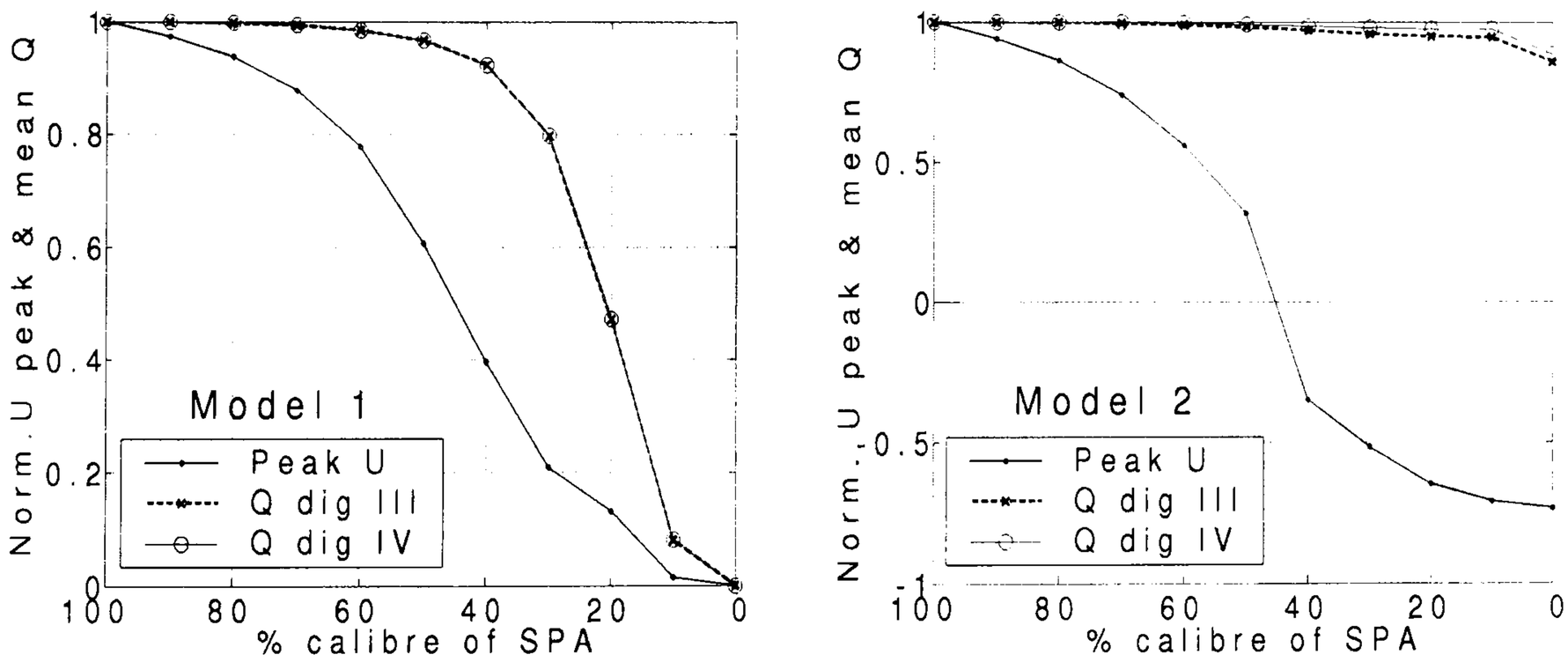


Figure 4.13: Effect of reducing the calibre of the SPA II of Models 1 (left) and 2 (right) on the velocity peak in the middle point of the SPA III during occlusion of the RA at the wrist, and on the mean outflow rates in the digital arteries III and IV after harvesting the RA. Peak velocities and mean digital outflow rates are normalised by their corresponding values obtained with the calibre of the control case (100%). Negative normalised velocity peaks are directed towards the UA.

Figure 4.13 (left) shows that Model 1 presents a higher decrease in the peak of the reversal flow measured by the MAT as we decrease the calibre of the SPA II than the corresponding decreases in the mean digital outflows after harvesting the RA. If the calibre of the SPA II is 30% the value of the control case, the peak reversal

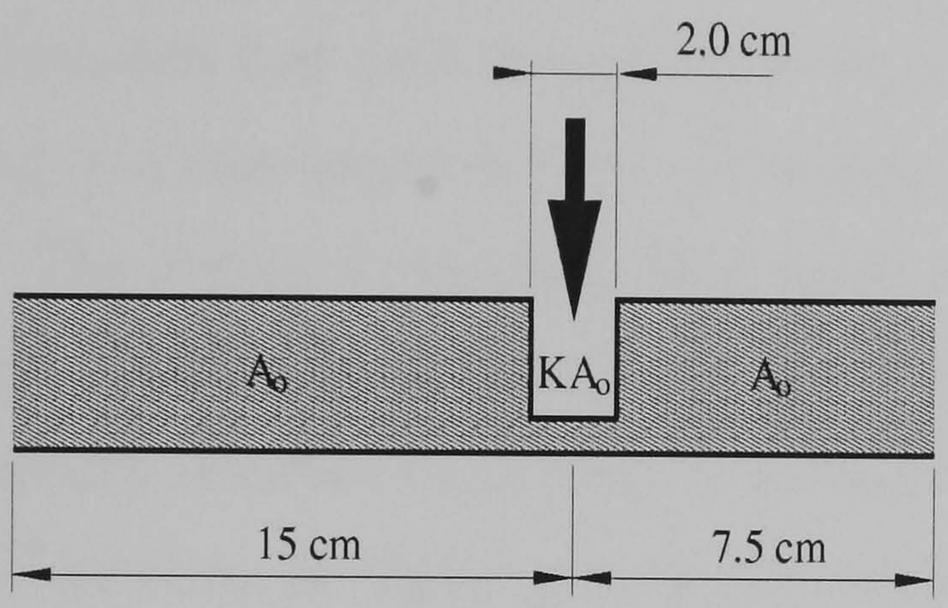
flow is reduced up to 80% and might be too small to be detected by Doppler US. resulting in a positive MAT. However, the mean outflow rates in the digital arteries III and IV are reduced by less than 20% when the RA is absent. Although the MAT predicts insufficient collateral flow, various compensatory mechanisms, such as vasodilatation of the digital arteries III and IV and progressive increase in the calibre of the SPA and the UA once the RA is harvested [10, 102], are likely to increase collateral circulation to avoid hand ischemia. Therefore, the MAT is likely to produce a false-positive result. A calibre of the SPA II of 30% the value of the control case is approximately a third of the calibre of the digital artery IV. For calibres smaller than 30%, the reductions in mean digital outflows are too high and likely to lead to hand ischemia.

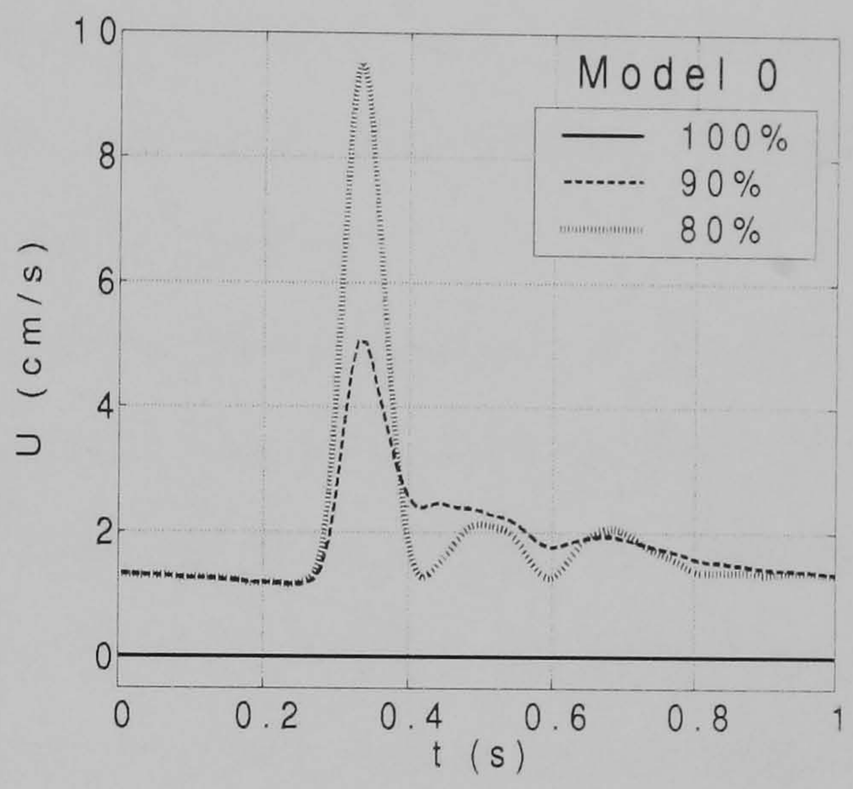
Figure 4.13 (right) shows that the DPA of Model 2 ensures sufficient collateral flow to perfuse the digital arteries even if the SPA II is removed, in which case the mean outflow rates of the digital arteries III and IV decrease by less than 15%. However, the reversal flow peak decreases until it becomes almost zero when the calibre of the SPA II is between 50% and 40% the value of the control case, which is smaller than the calibre of the DPA II. For calibres of the SPA II smaller than 40%, the flow peak changes direction, since blood flows to the digital arteries III and IV mainly through the DPA. According to these results, the MAT clearly leads to a false-positive result for a wide range of calibres of the SPA II in Model 2.

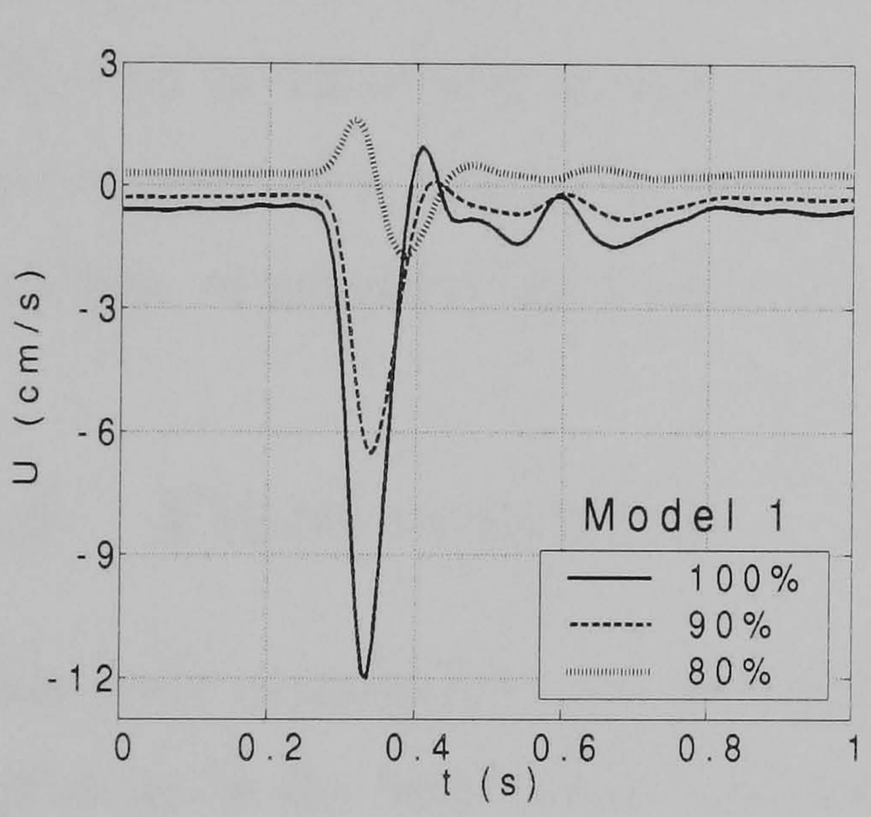
If we measure the decrease in the systolic pressure of the digital arteries III and IV of Model 1 with the compression of the RA (as proposed by Starnes *et al* [85]), we obtain less than 35 mmHg when the calibre of the SPA II is 30% the calibre of the control case. For calibres smaller than 25%, we obtain decreases in digital systolic pressures higher than 40 mmHg. When this test is applied to Model 2, the drop in digital systolic pressure is smaller than 17 mmHg in all the range of calibres of the SPA II studied. Consequently, the change in digital systolic pressure correctly detects sufficient collateral flow to perfuse the hand in all the range of calibres of the SPA II of Models 1 and 2 studied. Zimmerman *et al* [103] noted that the Doppler US evidence of flow reversal in some patients may be subtle and it is prudent to consider the collateral flow inadequate. The 1-D simulations show that the test may unnecessarily exclude some patients in these cases.

4.3.3 Effect of insufficient compression of the RA

A partial occlusion of the RA is simulated by dividing this vessel into three parts, with the centre of the middle part 15 cm proximal to the brachial bifurcation (Figure 4.14, top left). In the middle part, A_0 is considered to be a factor K ($0 < K < 0.2$) of the original value.







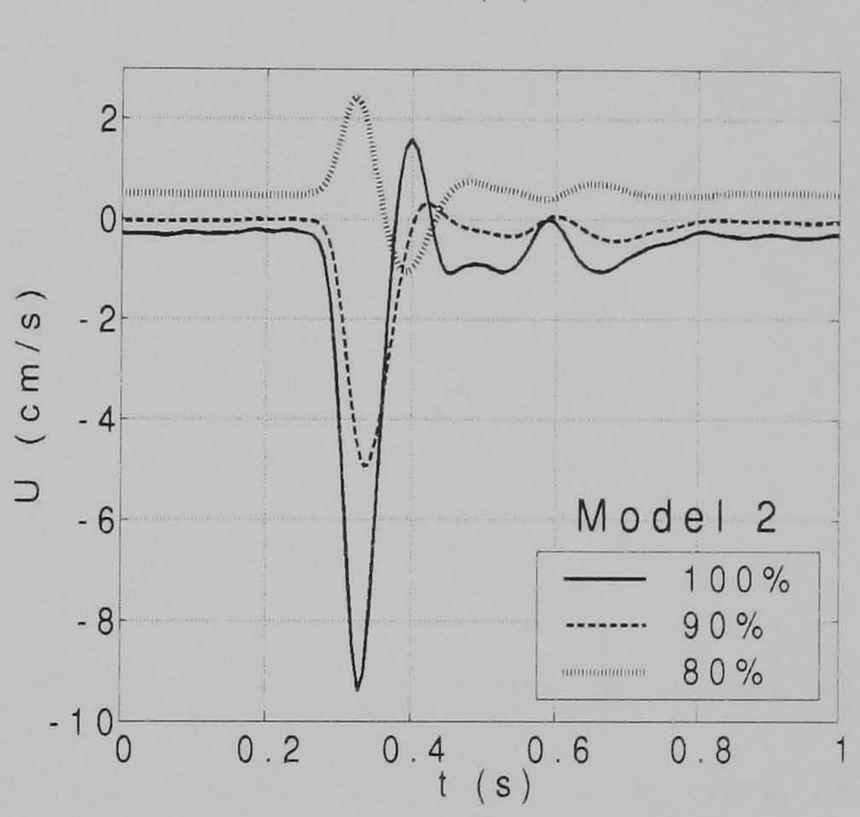


Figure 4.14: Simulation of a partial occlusion of the RA (top left) and velocity time histories in the middle point of the SPA III of Model 0 (top right), Model 1 (bottom left), and Model 2 (bottom right) with a reduction in the cross-sectional area of the compressed part of the RA by 100%, 90% and 80%. Positive velocities are directed towards the SPA II.

The rest of Figure 4.14 shows a comparison of the velocities measured in the middle point of the SPA III of the three models when different degrees of compression of the RA are applied. We observe the appearance of a flow peak directed towards the SPA II when the RA is partially occluded in Model 0 (Figure 4.14, top right). The value of the flow peak increases as the degree of the occlusion is reduced, since more blood flow is allowed through the RA. A partial occlusion of 90% in Models 1 (Figure 4.14, bottom left) and 2 (Figure 4.14, bottom right) yields a decrease

in the corresponding reversal flow peaks of approximately half the value obtained with a total occlusion (100%), because the radial flow combines with the ulnar flow coming from the SPA. With a partial occlusion of 80%, the radial flow increases and produces positive and negative flow peaks in the SPA III that are too small to be detected by Doppler US.

According to these results, insufficient compression of the RA can lead to a false-positive MAT in arterial networks with a complete arch. The presence of a substantial flow peak in topologies without a complete arch (Model 0) should not lead to a false-negative MAT, since flow does not reverse.

The change in digital systolic pressures with the compression of the RA is less than 2 mmHg for the three degrees of occlusion studied in Models 1 and 2, which correctly detects the presence of sufficient collateral flow. However, measurement of the variation in digital systolic pressures in Model 0 yields a false-negative result, since a maximum drop of only 23 mmHg is obtained with a partial occlusion of 90%, and of 12 mmHg with a partial occlusion of 80%. These results indicate the necessity of a second Doppler probe placed over the RA to confirm complete occlusion, as suggested by Starnes *et al* [85].

4.4 Final remarks

Pulse wave propagation has been simulated in the three most prevalent arterial anatomies in the hand. The main limitations of these simulations are the lack of detailed information about the lengths, cross-sectional areas and elasticity of the arteries, together with more precise data on the peripheral resistances and compliances. The results of this study are summarised below.

Topologies with a complete palmar arch produce reflected waves in the palmar arch that propagate throughout the rest of the arteries (Figure 4.4). However, these reflected waves do not introduce significant changes in pressure and velocity waveforms at the BA, UA and RA under physiological conditions (Figure 4.8), which makes it unfeasible to detect their presence from pressure and velocity measurements in the arteries of the arm.

From a haemodynamic point of view, the MAT is too cautious in selecting pa-

tients for RA graft or access for haemodialysis, since the absence of reversal flow in the radial part of the SPA does not always correlate to insufficient perfusion of the hand if the radial flow is interrupted. The MAT is adequate for large calibres of the SPA, as discussed in Figure 4.13, and it has to be performed with a compression of the RA that produces an occlusion of at least 90% of the healthy initial cross-sectional area (Figure 4.14). The peak reversal velocity is higher and, hence, can be better detected by Doppler US, if compression on the wrist is applied as far as possible from the hand (Figure 4.11).

In anatomies with a small calibre of the SPA, measurement of the drop in digital systolic pressures with the compression of the RA can better select patients for harvesting the RA or haemodialysis access through the RA, which is in agreement with the results obtained by Starnes *et al* [85]. However, a second Doppler probe must be placed over the RA to confirm complete occlusion, since digital pressure measurements can fail in detecting sufficient collateral flow and, hence, can lead to hand ischemia in case of an insufficient occlusion.

Chapter 5

Pulse wave propagation in the cerebral circulation

The brain critically depends on the cerebral circulation since it has a high metabolic rate (it receives 15% of the cardiac output in normal conditions, according to Table 1.2) and is very sensitive to ischemia. Sufficient blood supply to the brain is maintained with a network of collateral vessels and a precise system of autoregulation by vasodilatation and vasoconstriction. Blood is delivered to the brain through the two internal carotid arteries (ICAs) and the two vertebral arteries (VAs) (see Figure 5.1, left). Each ICA bifurcates to form a middle cerebral artery (MCA) and an anterior cerebral artery (ACA) to perfuse the temporal, parietal and frontal regions of the brain (anterior circulation). The two VAs anastomose into the basilar artery, which divides into the right and left posterior cerebral arteries (PCAs) to deliver blood to the regions of the brain stem (posterior circulation). The anterior and the posterior circulation are interconnected by the anterior and posterior communicating arteries (ACoA and PCoAs). The resulting ring-like arterial structure, called the *circle of Willis* (CoW), is the main collateral pathway in the cerebral circulation. It provides collateral blood supply to the efferent (outflow) arteries in cases of missing or occluded vessels.

Unfortunately, many anatomical variations of the haemodynamically complete and well-balanced CoW shown in Figure 5.1 (left) are commonly observed. Based on more than 50 radiological and anatomical studies, Lippert and Pabst [47] found that about 50% of the population has a CoW with at least one artery absent or

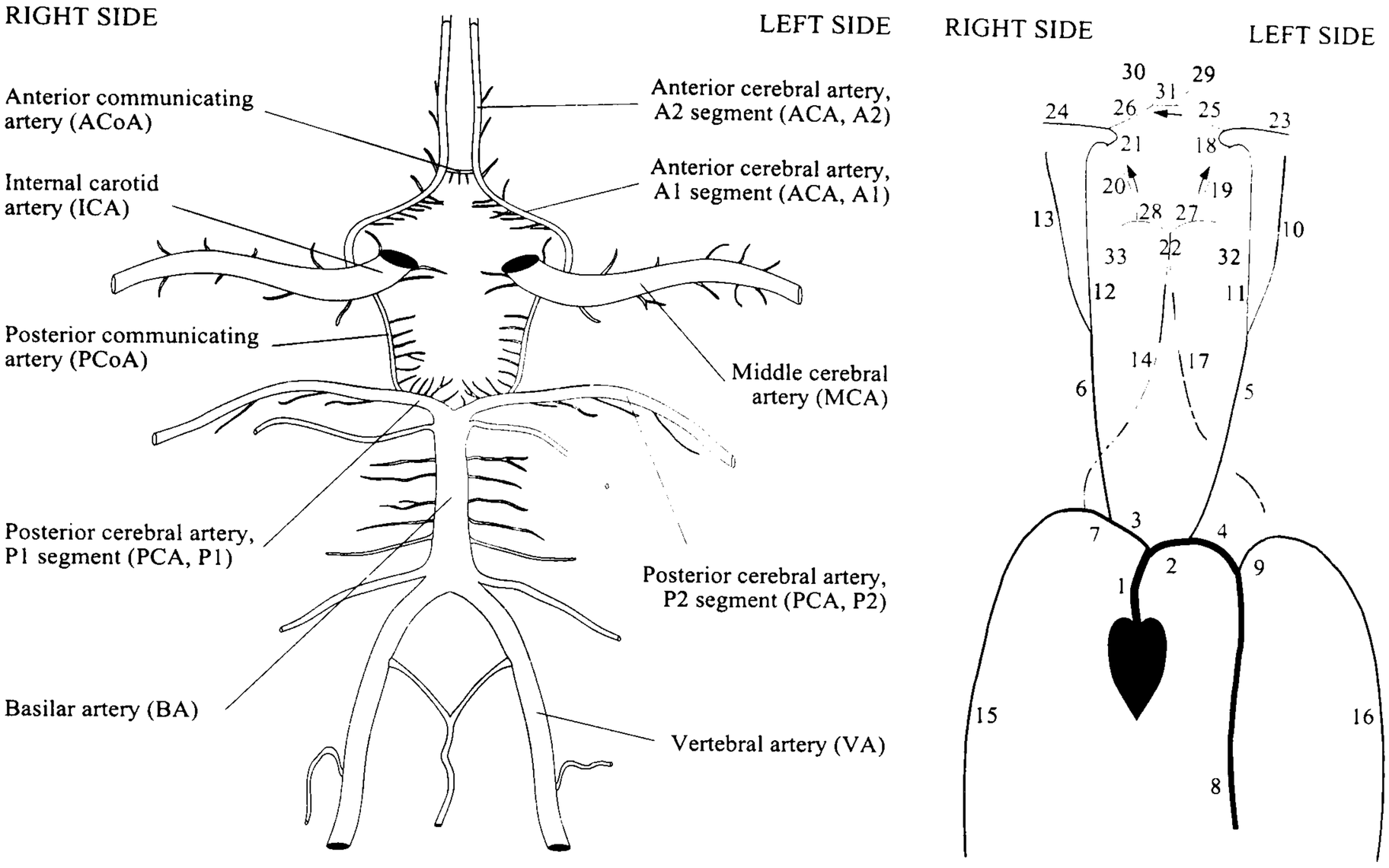


Figure 5.1: Schematic representation of the circle of Willis (left), based on the figure depicted in [54], and of the arterial network simulated (right), which includes the aorta, brachial, carotid, vertebral and the main cerebral arteries. Numbers refer to names in Table 5.1 and the arrows in the communicating arteries indicate the positive direction of flow.

hypoplastic (very small or incompletely developed). These anatomical variations reduce the collateral availability of the system and increase the risk of stroke and transient ischemic attack (TIA) in patients with severe stenosis in an ICA [32]. Knowledge of the compensatory capacity of the CoW is important for neurosurgeons, vascular surgeons, and interventional radiologists when a procedure in the intracranial or extracranial cerebral arteries is to be attempted [37]. Such procedures include carotid endarterectomy (surgical incision in the carotid artery to remove plaque in patients with a severe carotid stenosis), angioplasty (balloon expansion of an artery) and stenting (introduction of a mesh to maintain the lumen open after angioplasty) [16, 32].

In this study, the non-linear 1-D formulation is applied to simulate pulse wave propagation in the cerebral arteries. Section 5.1 reviews previous models found in the literature. Next, Section 5.2 introduces the 1-D model used in this study, which starts at the left ventricle and includes the largest arteries that supply the CoW. Based on published physiological data, this model is able to capture and explain the main features of pulse wave propagation along the aorta, at the brachiocephalic bifurcation and throughout the cerebral arteries (Section 5.3). Section 5.4 studies the

collateral ability of the complete CoW and its most frequent anatomical variations in normal conditions and after total occlusion of a carotid or vertebral artery. This section concludes by studying the effect of partial occlusions of the communicating arteries on the cerebral flows. The chapter ends with a summary of the main results obtained (Section 5.5).

5.1 Previous models of the circle of Willis

Several mathematical studies have been carried out to investigate the capability of the CoW to reduce the effects of haemodynamic pathological alterations. According to Hillen *et al* [34] and based on a non-linear 1-D model of a complete and well-balanced CoW, blood flows in the afferent (inflow) vessels and in the segments of the CoW of healthy subjects are considerably influenced by their diameters, whereas flow in the efferent vessels is dominated by the peripheral resistances.

With a similar model of the CoW, Cassot *et al* [14] claimed that small changes in the diameter of the ACoA (within the range of 0.4 to 1.6 mm) have a strong influence on regulating cerebral haemodynamics in case of ICA stenosis. Viedma *et al* [91] investigated different combinations of the diameters of the communicating arteries that can lead to cerebral ischemia in case of occlusion in an ICA.

Moorhead *et al* [55] used a lumped parameter model with time-varying resistances in the efferent vessels to account for vasodilatation and vasoconstriction. They showed that the omission of a single circulus artery (an artery of the circle of Willis) can be compensated for by the remaining circulus arteries and autoregulation to maintain the required efferent flow rates in case of occlusion in an ICA. Although their model neglects flow pulsatility, it offers the possibility of analytical solutions [15, 33].

The problem has also been approached with a two-dimensional (2-D) model with time-varying resistances, but with rigid arterial walls [23, 19]. Ferrandez *et al* [23] found that the worst configuration of the CoW when the ICA is partially occluded is that of a missing ipsalateral A1 segment of the ACA (see Figure 5.1, left). David *et al* [19] suggested that the PCoA and other small arteries of the CoW, which are often invisible by non-invasive magnetic resonance (MR) techniques, can be better

visualised by performing the scan at the specific point in time when the flux is maximum according to the simulation. They also pointed out that any simulation will be improved if it can take into account the correct time delay between the inflow waves at the ICAs and VAs.

Three-dimensional (3-D) models have been used to simulate the injection of a contrast agent and to study wall-shear stress distributions [16], to investigate the role played by haemodynamics in the formation, development and rupture of cerebral aneurysms [64], and to study cerebral autoregulation [53, 54].

5.2 The model of the circle of Willis

The 1-D model of the CoW used in this study includes the aorta, the subclavian arteries (SCAs), the brachial arteries, the common carotid arteries (CCAs), the external carotid arteries (ECAs) and the VAs (Figure 5.1, right). In this model, the time delay between the inflow waves at the ICAs and VAs is implicitly determined by the pulse wave speeds of the vessels supplying them from the ascending aorta. Only an inflow boundary condition at the ascending aorta is required. Although 3-D models consider a better definition of the geometry and might account for the deformation of the arterial wall, they are computationally too expensive to simulate pulse wave propagation in a model similar to the one depicted in Figure 5.1 (right).

Each simulation is run with the non-linear formulation, one elemental region Ω_e in each arterial domain and a time step $\Delta t = 100$ μs. The number of quadrature points and the polynomial order in each elemental region depends on the length of the region. The simulation is started at the initial state (A_0, p_0, U_0), with A_0 determined from the initial radii in Table 5.1, $p_0 = 0$ and $U_0 = 0$. The waveforms become periodic after about six cycles, which takes less than 5 minutes to run in a normal PC.

At the proximal end of the ascending aorta, a periodic inflow rate $Q_{bc}(t)$ with a period of 1 s (Figure 5.2) is enforced using Equation (2.69). Each period consists of a half-sinusoidal flow rate wave with a peak value $\hat{Q}$ of 485 ml s^{-1} (adjusted to produce a physiological cardiac output and aortic mean pressure with the peripheral resistances shown in Table 5.1) and a duration $\tau = 0.3$ s (systole). The flow rate is

zero in the rest of the period (diastole). The inflow rate is thus given by

$$Q_{bc}(t) = \begin{cases} \hat{Q} \sin\left(\frac{\pi t}{\tau}\right) & \text{if } t < \tau, \\ 0 & \text{otherwise.} \end{cases} \tag{5.1}$$

This boundary condition acts as a total reflector ($R_t = 1.0$) when flow is zero, simulating the closure of the aortic valve during diastole.

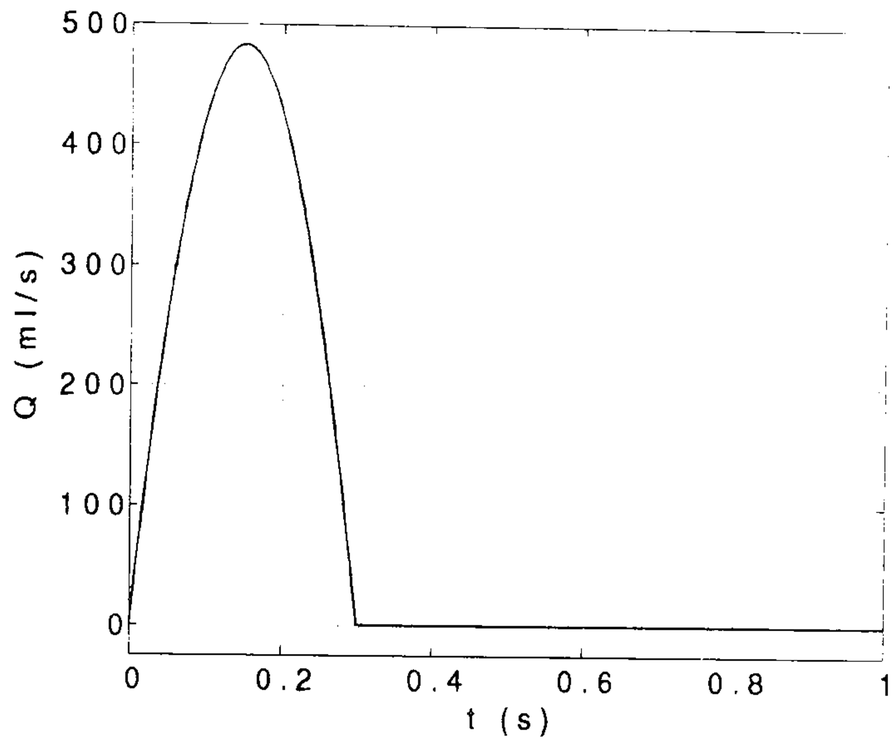


Figure 5.2: Periodical inflow rate enforced at the ascending aorta.

The distal end of each terminal branch is coupled to a three-element (RCR) windkessel model, as described in Section 2.7.3.6, which accounts for both the resistive and the compliant effects of the vessels supplied by the terminal arteries. The pressure at the entrance of the venous system (p_{out}) is taken to be 5 mmHg. At any point in the network, a total occlusion can be simulated by enforcing the condition $U = 0$ at the desired point, or a partial occlusion by decreasing locally the calibre of the artery, as applied in the models of the arm in Chapter 4.

The physiological parameters used in each arterial segment are given in Table 5.1. The model of this study aims at representing the arterial geometry and elasticity of a healthy young adult. In the absence of detailed knowledge of these properties. the geometry and wall elasticity of the arteries up to the carotids and vertebrals are based on data published by Stergiopulos *et al* [88]. In the cerebral arteries, the lengths published by Fahrig *et al* [22], obtained from average values from several published sources, are considered. The lumen radii at the reference state (p_0, U_0) correspond to an average of 13 magnetic-resonance angiographies (MRAs) of complete CoWs by Moore *et al* [53]. In all the cerebral vessels, it is assumed that the wall thickness (h) is 25% of the radius at the reference state. In the carotids and

vertebral arteries, the value of E is considered to be E=8·10^5 Pa, and in the remaining vessels E=16·10^5 Pa, since they are stiffer than extracranial vessels with similar calibres, according to Hayashi [31].

The total resistance of the arterial system in normal conditions is considered to be $R_{\mu_T} = 1.34{\cdot}10^8$ Pa s m^{-3}, according to Stergiopulos *et al* [88]. The value of each peripheral resistance ($R_\mu = R_{\mu_1} + R_{\mu_2}$) is determined by assuming the following flow distribution in normal conditions: 15% of the cardiac output perfuses the head (see Table 1.2), 5% supplies each arm, and 75% flows to the rest of the body through the thoracic aorta. In the terminal vessels of the head, mean outflows are assumed to be proportional to the initial cross-sectional areas of the perfusing terminal arteries.

The total volume compliance of the arterial system in normal conditions is taken to be 9.45·10^{-9} m^3 Pa^{-1}, according to Simon *et al* [83]. This value corresponds to the compliance of each arterial segment, calculated through (2.118), plus the total peripheral compliance. In the absence of any data, the total peripheral compliance is distributed among the terminal branches in the same proportion as the mean flow distribution determined by the peripheral resistances.

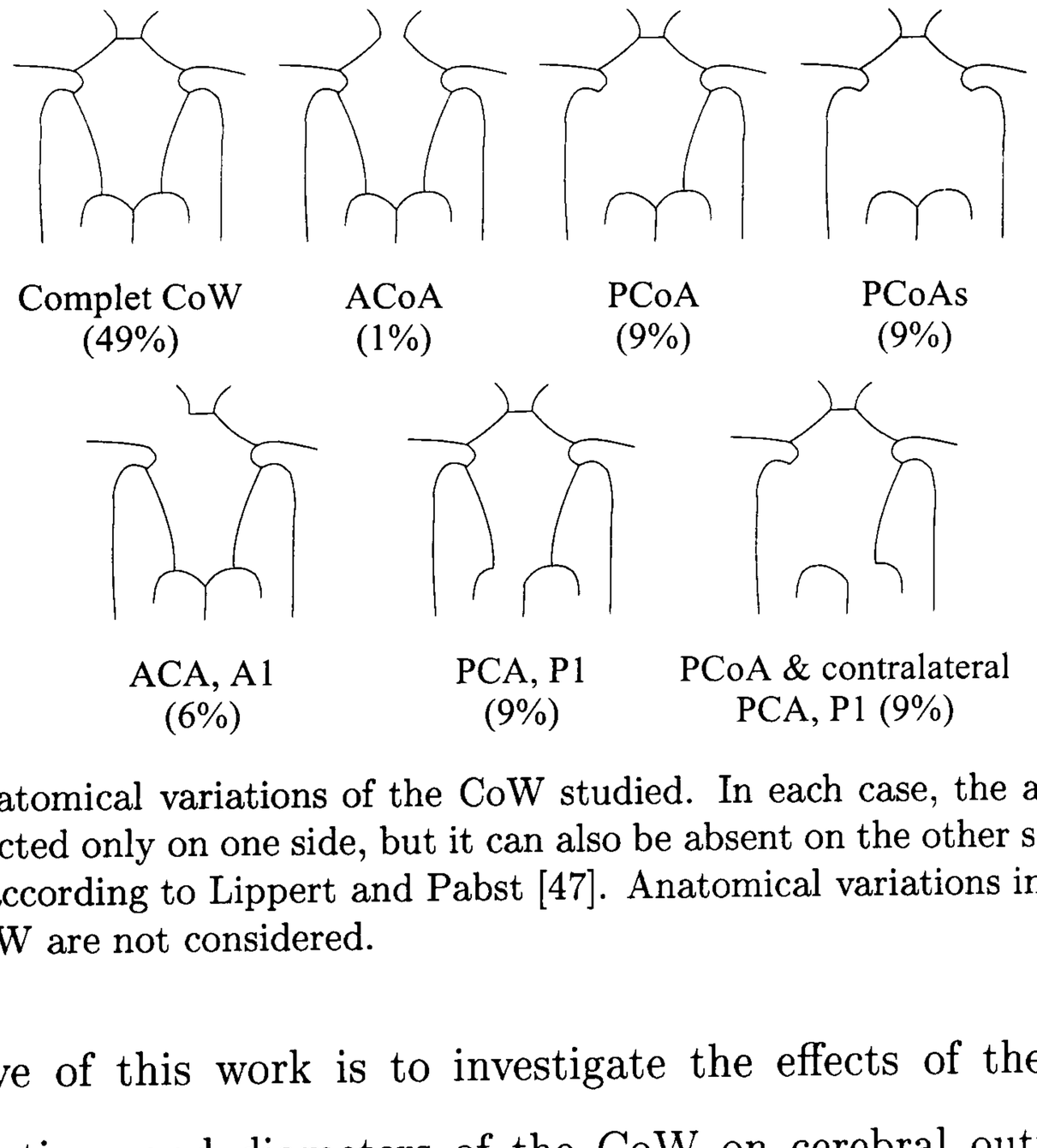


Figure 5.3: Anatomical variations of the CoW studied. In each case, the artery absent is indicated (depicted only on one side, but it can also be absent on the other side) along with its frequency, according to Lippert and Pabst [47]. Anatomical variations involving vessels outside the CoW are not considered.

The objective of this work is to investigate the effects of the most frequent anatomical variations and diameters of the CoW on cerebral outflows and pulse wave propagation, in healthy conditions and after complete occlusion of an ICA or a VA. This study is limited to the most frequent anatomical variations reported

Table 5.1: Physiological data used in the model shown in Figure 5.1 (right) based upon the data collected by Stergiopulos *et al* [88], Fahrig *et al* [22] and Moore *et al* [53].

Arterial segment	Length (cm)	Initial radius (cm)	Thickness (cm)	Elastic modulus (10^6 Pa)	Peripheral resistance (10^9 Pa s m^{-3})	Peripheral compliance (10^{-10} m^3 Pa^{-1})
1. Ascending aorta	4.0	1.200	0.163	0.4	-	-
2. Aortic arch I	2.0	1.120	0.126	0.4	-	-
3. Brachiocephalic	3.4	0.620	0.080	0.4	-	-
4. Aortic arch II	3.9	1.070	0.115	0.4	-	-
5. L. common carotid	20.8	0.250	0.063	0.4	-	-
6. R. common carotid	17.7	0.250	0.063	0.4	-	-
7. R. subclavian	3.4	0.423	0.067	0.4	-	-
8. Thoracic aorta	15.6	0.999	0.110	0.4	0.18	38.70
9. L. subclavian	3.4	0.423	0.067	0.4	-	-
10. L. ext. carotid	17.7	0.150	0.038	0.8	5.43	1.27
11. L. int. carotid I	17.7	0.200	0.050	0.8	-	-
12. R. int. carotid I	17.7	0.200	0.050	0.8	-	-
13. R. ext. carotid	17.7	0.150	0.038	0.8	5.43	1.27
14. R. vertebral	14.8	0.136	0.034	0.8	-	-
15. R. brachial	42.2	0.403	0.067	0.4	2.68	2.58
16. L. brachial	42.2	0.403	0.067	0.4	2.68	2.58
17. L. vertebral	14.8	0.136	0.034	0.8	-	-
18. L. int. carotid II	0.5	0.200	0.050	1.6	-	-
19. L. PCoA	1.5	0.073	0.018	1.6	-	-
20. R. PCoA	1.5	0.073	0.018	1.6	-	-
21. R. int. carotid II	0.5	0.200	0.050	1.6	-	-
22. Basilar	2.9	0.162	0.040	1.6	-	-
23. L. MCA	11.9	0.143	0.036	1.6	5.97	1.16
24. R. MCA	11.9	0.143	0.036	1.6	5.97	1.16
25. L. ACA, A1	1.2	0.117	0.029	1.6	-	-
26. R. ACA, A1	1.2	0.117	0.029	1.6	-	-
27. L. PCA, P1	0.5	0.107	0.027	1.6	-	-
28. R. PCA, P1	0.5	0.107	0.027	1.6	-	-
29. L. ACA, A2	10.3	0.120	0.030	1.6	8.48	0.82
30. R. ACA, A2	10.3	0.120	0.030	1.6	8.48	0.82
31. ACoA	0.3	0.074	0.019	1.6	-	-
32. L. PCA, P2	8.6	0.105	0.026	1.6	11.08	0.62
33. R. PCA, P2	8.6	0.105	0.026	1.6	11.08	0.62

by Lippert and Pabst [47] with one or two circulus arteries absent or hypoplastic (simulated as absent). Figure 5.3 shows the cases studied and their estimated frequency. Although the ACoA is missing in less than 1% of the cases, this anatomical variation is included because the ACoA is commonly recognised as the functionally most important collateral route in case of severe occlusion of an ICA [14, 33, 36].

5.3 Pulse wave propagation along the aorta and in the arteries supplying the circle of Willis

The 1-D model is able to capture the main wave propagation features observed in *in-vivo* measurements along the aorta (shown in Figure 1.9 and described in Section 3.3), such as the increase in pulse pressure as we move away from the heart, the dicrotic notch at the end of systole and the diastolic decay due to the windkessel effect (Figure 5.4, left). Moreover, the peak flow decreases as we move down the thoracic aorta, though the characteristic backward flow after the closure of the aortic valve is almost absent (Figure 5.4, right). At the inlet of the ascending aorta, the systolic pressure is 17.3 kPa (130 mmHg) and the diastolic pressure is 10.1 kPa (76 mmHg). The cardiac output is 5.7 l min^{-1}. All of these values are in good agreement with *in-vivo* measurements in healthy young adults [57, 83].

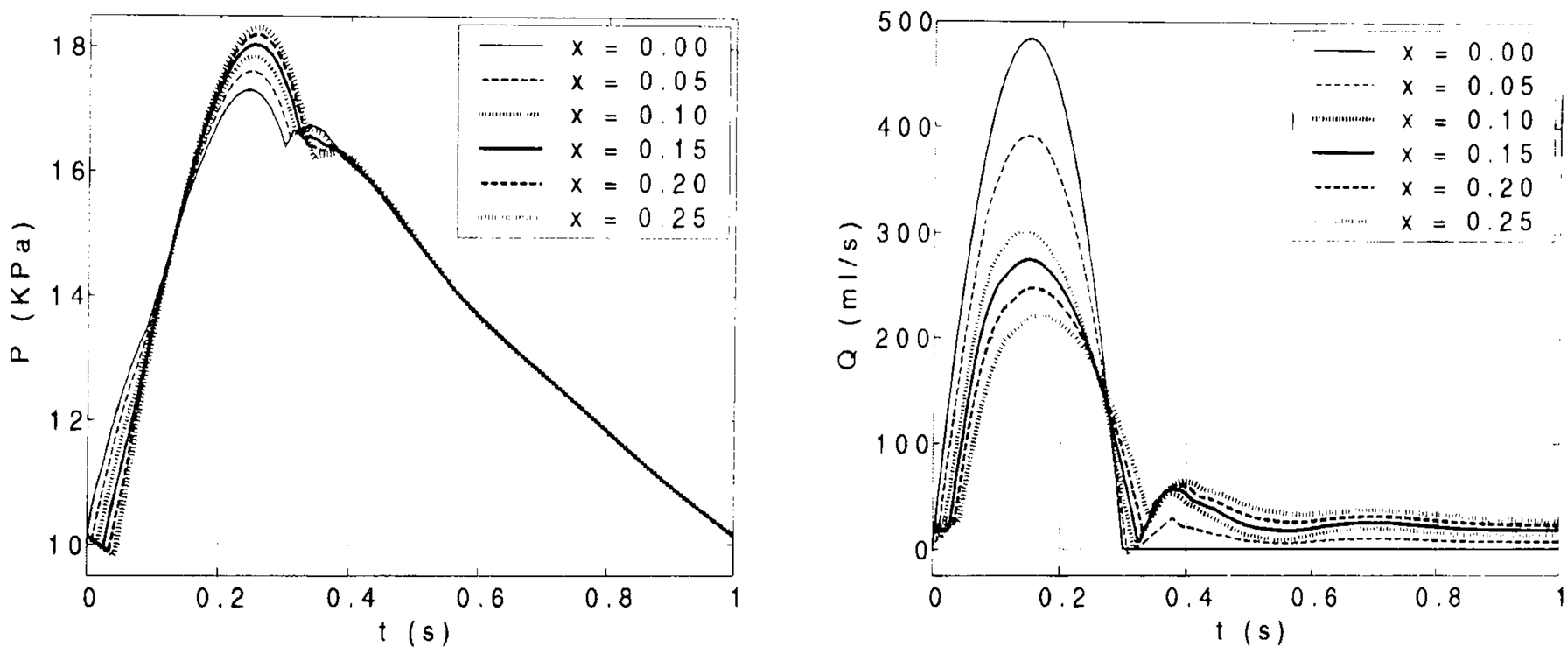


Figure 5.4: Pressure (left) and flow rate (right) over one cardiac cycle along the aorta. The legend indicates the distance of the measurement from the left ventricle.

This model is also able to predict the *in-vivo* observed pressure and flow patterns at the brachicephalic bifurcation. *In-vivo* Doppler measurements of velocity in the brachiocephalic artery, BrA, (parent) and the right SCA and CCA (daughters) of a healthy young adult (all taken approximately 1 cm from the bifurcation) show a significant difference between velocity waveforms (Figure 5.5, top). Flow is always directed towards the head (antegrade) in the CCA, ensuring cerebral blood supply at any instant during the cardiac cycle, whereas, in the BrA and right SCA, flow is biphasic, with a period of backward flow at the end of systole. These measurements are in agreement with the velocity waveforms from a young normal subject published

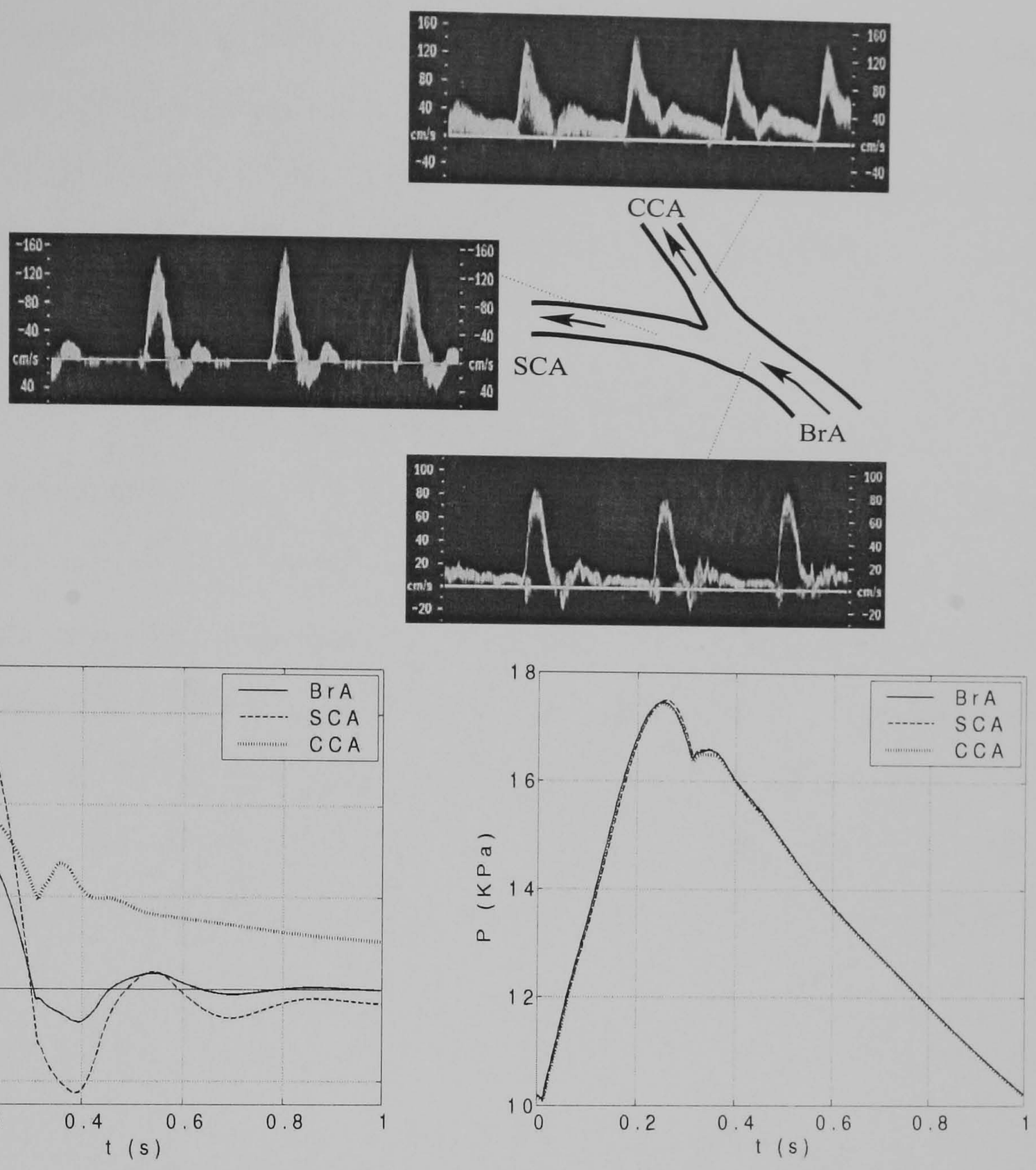


Figure 5.5: Flow velocity at the brachiocephalic (BrA), right subclavian (SCA) and right common carotid (CCA) arteries measured *in-vivo* with Doppler ultrasound in a healthy young adult (top) and predicted by our model 1 cm proximal to the bifurcating point (bottom left). We also show the predicted pressures (bottom right).

by Oates [60]. The results predicted by the 1-D simulation in the BrA and the right SCA and CCA are in good qualitatively agreement with the *in-vivo* measurements (Figure 5.5, bottom left). However, a quantitative comparison can not be achieved because of the lack of information about the inflow at the ascending aorta and the arterial geometry and elasticity of the subject. The simulated flow patterns where the left CCA branches off the aortic arch and the two VAs branch off the corresponding SCA present the same pattern as in the brachiocephalic bifurcation, so that flow is always antegrade during the cardiac cycle in the four arteries perfusing the head. These results are also in agreement with the Doppler measurements published by Oates [60].

According to the 1-D model, flow is antegrade in the CCAs and the VAs of all the anatomical variations depicted in Figure 5.3, even though the predicted

pressure waveforms in these vessels are very similar to the corresponding pressures in their adjacent arteries (Figure 5.5, bottom right). Therefore, antegrade flow is a consequence of the length, diameter, elasticity and mean flow (determined by the terminal resistances) of the CCAs, VAs and their adjacent arteries.

5.4 Flow in the cerebral arteries

This section investigates how cerebral flows are affected by anatomical variations (Section 5.4.1), by the total occlusion of an ICA or a VA (Section 5.4.2), and by several degrees of partial occlusions in the communicating arteries (Section 5.4.3). This study focuses on flow rates, because they are clinically important in brain perfusion and they can be measured non-invasively with phase-contrast MR (PC-MR) [16], and on flow velocity patterns, which can be measured non-invasively with transcranial colour-coded duplex ultrasonography (TCCD) [37] and PC-MR [16].

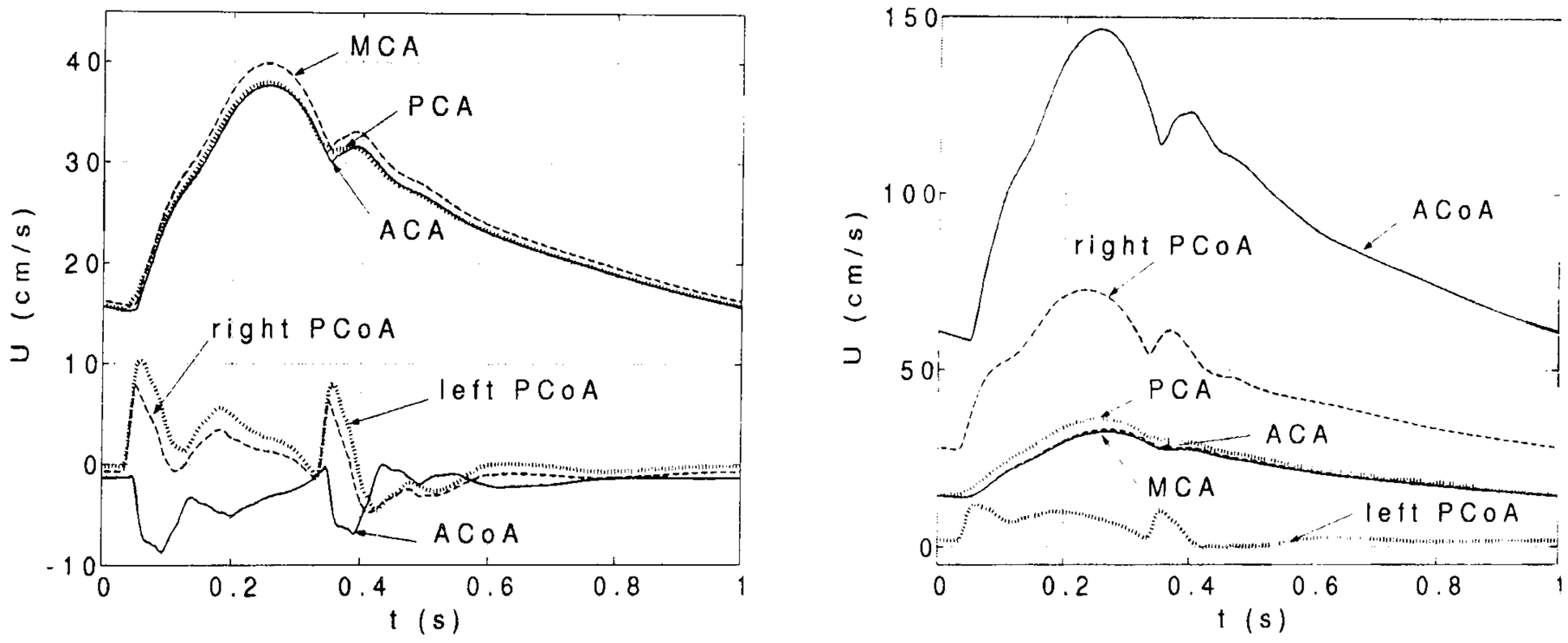


Figure 5.6: Velocity over one cardiac cycle in the middle point of the efferent and communicating arteries of the complete CoW, in normal conditions (left) and after occlusion of the right ICA (right). In normal conditions, the results in the same cerebral vessel at both sides of the CoW can not be distinguished in the scale of the figure. The results with the right ICA occluded correspond to the right side. On the left side, they present similar patterns but with slightly higher values. Positive values in the communicating arteries follow the direction of the arrows in Figure 5.1 (right).

5.4.1 Normal conditions

The 1-D simulation predicts very similar flow patterns in all the efferent arteries of the complete CoW (Figure 5.6, left), with flows always directed towards the brain. Differences between the same cerebral artery at both sides of the CoW can not be

appreciated in the scale of the figure, which indicates that flows in the cerebral arteries are not affected by the asymmetry introduced by the BrA. The predicted flow pattern in the MCA is in good qualitative agreement with the typical *in-vivo* velocity waveforms measured with a ultrasound duplex machine (Figure 5.7).

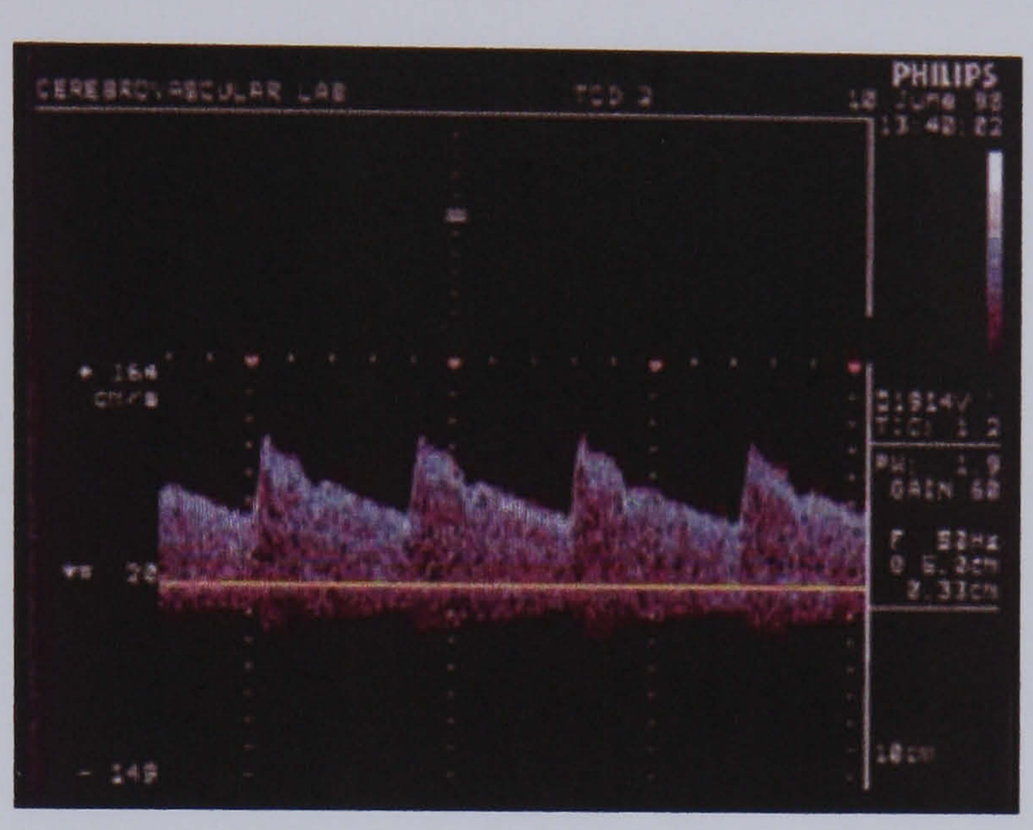


Figure 5.7: Typical MCA velocity waveform recorded on a Philips ultrasound duplex machine. (Taken from [17].)

Table 5.2 (first study case) shows the mean outflow rates in the cerebral arteries. We observe that the MCAs receive the highest blood supply, followed by the ACAs. The values and distribution of these outflows are within acceptable physiological ranges compared to averaged *in-vivo* measurements calculated by Fahrig *et al* [22] based on several published sources (last row of Table 5.2).

Table 5.2: Mean outflow rates (in ml/s) at the outlet of the efferent arteries and in the middle of the communicating arteries for different study cases. The last row shows an average of published *in-vivo* measurements at the efferent arteries calculated by Fahrig *et al* [22]. Positive values of flow in the communicating arteries follow the direction of the arrows in Figure 5.1 (right). R stands for right and L for left.

Study case	RACA	LACA	RMCA	LMCA	RPCA	LPCA	RPCoA	LPCoA	ACoA
Complete circle	1.16	1.16	1.73	1.72	0.90	0.89	-0.01	0.01	-0.05
ACoA absent	1.16	1.16	1.73	1.72	0.90	0.89	-0.01	0.02	-
RPCoA absent	1.16	1.16	1.73	1.72	0.89	0.89	-	0.01	-0.05
LPCoA absent	1.16	1.16	1.73	1.72	0.90	0.90	0.00	-	-0.05
PCoAs absent	1.16	1.16	1.73	1.72	0.90	0.90	-	-	-0.05
RACA (A1) absent	1.07	1.11	1.78	1.68	0.90	0.90	-0.22	0.22	1.07
LACA (A1) absent	1.12	1.08	1.69	1.78	0.90	0.90	0.18	-0.19	-1.08
RPCA (P1) absent	1.15	1.16	1.70	1.72	0.79	0.93	-0.79	0.27	0.21
LPCA (P1) absent	1.16	1.15	1.73	1.70	0.93	0.79	0.25	-0.79	-0.32
RPCA (P1) & LPCoA absent	1.15	1.15	1.70	1.71	0.79	0.94	-0.79	-	0.14
LPCA (P1) & RPCoA absent	1.15	1.14	1.72	1.69	0.94	0.79	-	-0.79	-0.25
Fahrig *et al* (1999)	1.10	1.10	2.00	2.00	0.80	0.80	-	-	-

Figure 5.6 (left) shows that the flows in the communicating arteries are small

but sufficiently significant to maintain these vessels active. They arise from pressure phase delays between both sides of the CoW, as a consequence of the asymmetry introduced by the BrA. Table 5.2 shows that the volume flow rates along these arteries are about two orders of magnitude smaller than the volume outflow rates in the efferent arteries, which suggests that the system does not require the collateral flow pathways through the communicating arteries to adequately perfuse the brain of healthy subjects with a complete CoW. Their MCAs and ACAs are supplied with flow coming mainly from the ipsalateral ICA, and their PCAs with flow through the basilar artery.

Anatomical variations with missing communicating arteries present mean outflow rates in the efferent arteries and the remaining communicating arteries that differ in less than 1% the results obtained for the complete CoW (Table 5.2). The flow patterns in their efferent arteries also differ in less than 1% the results shown in Figure 5.6 (left) for the complete CoW.

When one of the ACAs (A1) or PCAs (P1) is absent or hypoplastic, high collateral flow rates through the communicating arteries are observed, since they are the only possible pathway to an efferent vessel (Table 5.2). Flows in the cerebral arteries present the same patterns as shown in Figure 5.6 (left) for the complete CoW, though with differences of less than 15% in the value of flow velocities. In terms of mean outflow rates, the differences between these anatomies and a complete CoW are also less than 15% (Table 5.2), which suggests that collateral flows through the communicating arteries are sufficient to perfuse all the areas of the brain in subjects with a hypoplastic ACA (A1) or PCA (P1). Although fluxes are reduced in some efferent vessels, the vasoconstriction and vasodilatation of the cerebral vessels and the wall remodelling in the active collateral vessels to increase the calibre of their lumen, are likely to compensate for any reduction in blood flows. However, these autoregulation mechanisms have not been considered in the 1-D simulations.

Therefore, when velocity or flow rate in any communicating artery is high enough to be measured in a patient without a significant stenosis in any afferent artery, at least one of the ACAs (A1) or PCAs (P1) is hypoplastic. Figure 5.8 (left) shows that the direction of the flow in the ACoA indicates the side where there is a hypoplastic ACA (A1) or PCA (P1). Furthermore, flow waveforms in the ACoA are

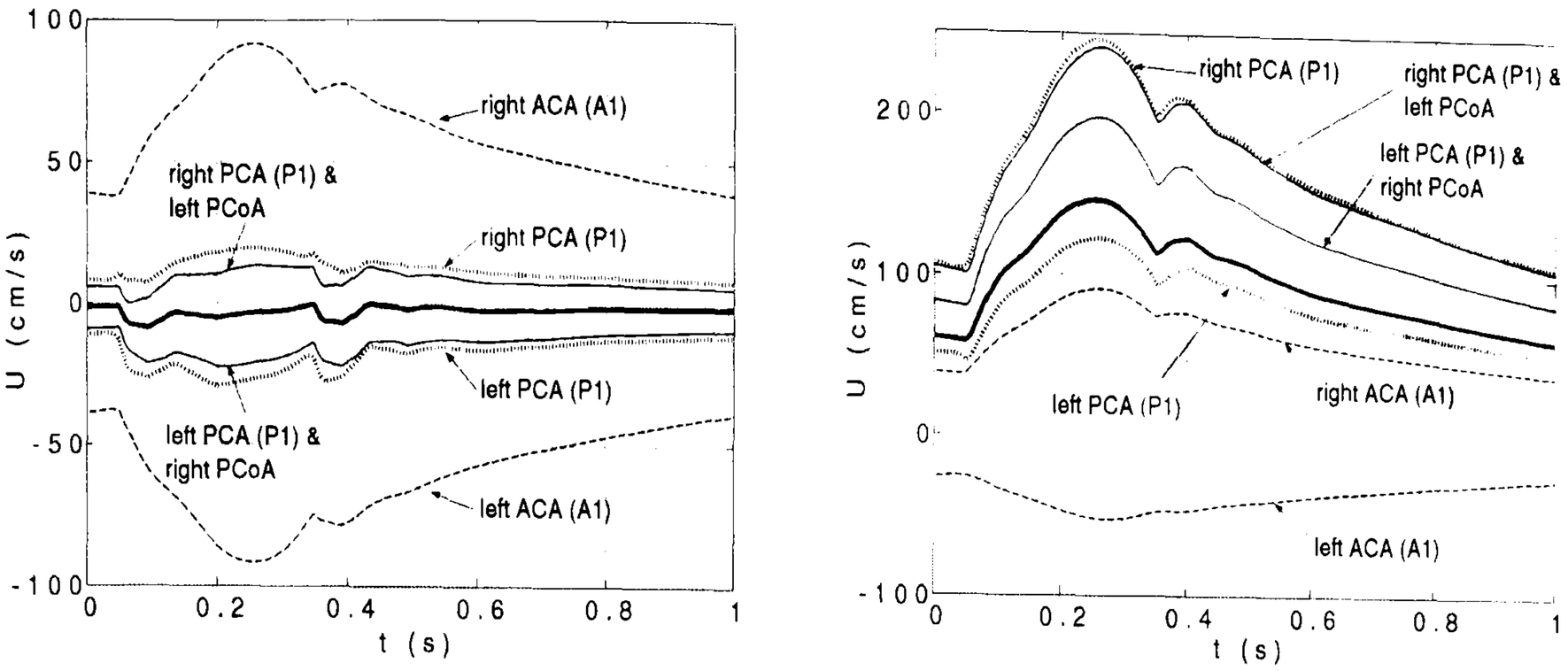


Figure 5.8: Velocity over one cardiac cycle in the middle point of the ACoA of the complete CoW (thick solid line) and the anatomical variations with missing vessels as indicated in the figures, in normal conditions (left) and after occlusion of the right ICA (right). Positive values follow the direction of the arrows in Figure 5.1 (right). In normal conditions, we notice that the direction of the flow in the ACoA depends upon the side where there is the missing ACA (A1) or PCA (P1).

similar to flow waveforms in the ACAs (A2) in anatomies with a hypoplastic ACA (A1), which suggests that TCCD measurements in the ACoA should allow us to detect the presence of a hypoplastic ACA (A1). The direction of the flow in the

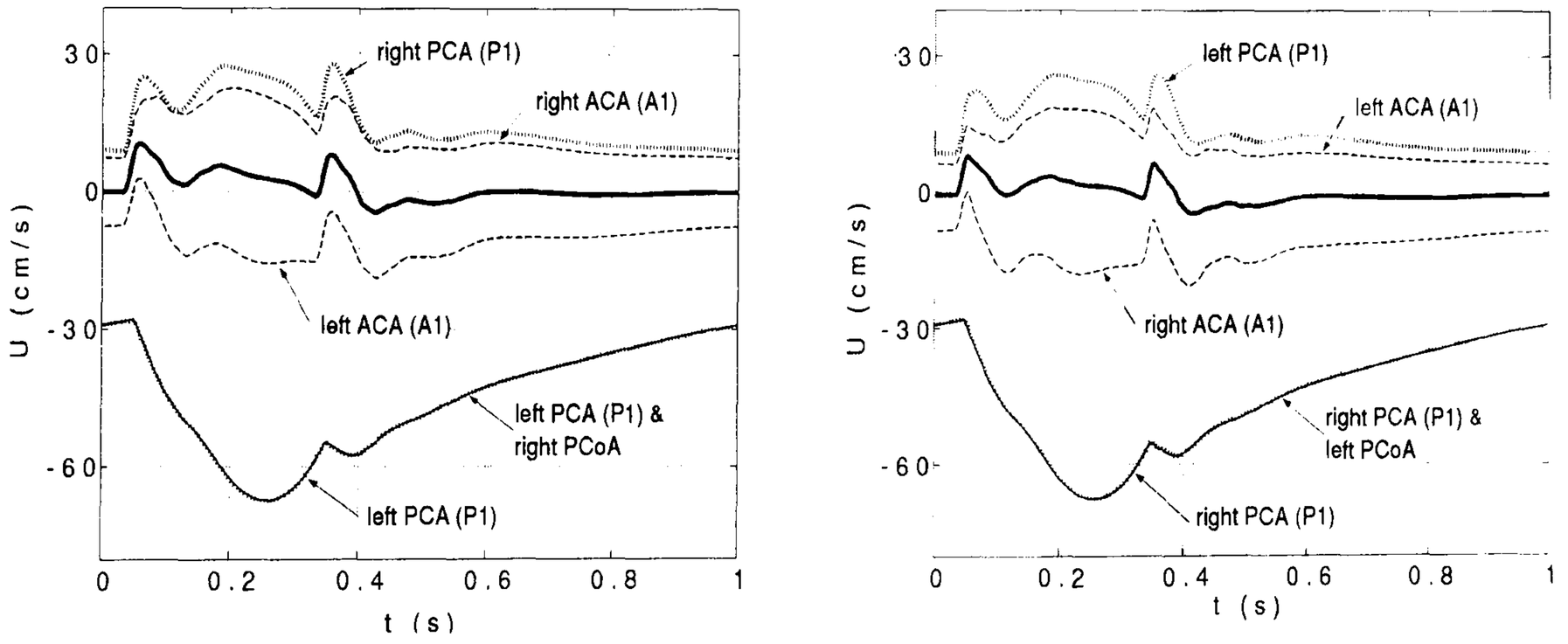


Figure 5.9: Velocity over one cardiac cycle in the middle point of the left PCoA (left) and right PCoA (right) of the complete CoW (thick solid lines) and the anatomical variations with missing vessels as indicated in the figures. Positive values follow the direction of the arrows in Figure 5.1 (right). We notice that the direction of the flow in the PCoAs depends upon the side where there is the missing or hypoplastic ACA (A1) or PCA (P1).

PCoAs also indicates the side where there is a hypoplastic ACA (A1) or PCA (P1) (Figure 5.9). In this case, flow waveforms in a PCoA are similar to flow waveforms in the ipsalateral PCA (P2) if the ipsalateral PCA (P1) is hypoplastic.

The mean flow rates given in Table 5.2 depend on the input flow rate enforced at the ascending aorta and the peripheral resistances. For the cases with an absent

ACA (A1) or PCA (P1) they also depend on the resistance of the communicating arteries. Consequently, cerebral mean flow rates are very sensitive to changes in the geometry and elasticity of the communicating arteries when an ACA (A1) or PCA (P1) is absent. Changes in the the rest of the arteries simulated (within physiological ranges) affect pulse waveforms but not mean flows.

Finally, it is important to notice that MRA techniques may not be able to detect the presence of the communicating arteries in subjects with a complete CoW or with anatomical variations involving these arteries, since flow velocities in the communicating arteries of these anatomies are about two orders of magnitude smaller than in the rest of the cerebral vessels, according to our model.

5.4.2 The effects of occlusions in the afferent arteries

The occlusion of an ICA considerably increases the flow in the communicating arteries of the complete CoW (Figure 5.6, right) and in all the anatomical variations studied.

Figure 5.10 investigates the ability of each anatomical variation in Figure 5.3 to maintain sufficient efferent outflow rates after an occlusion of either the right ICA (dark numbers) or the right VA (light numbers). The number at the outlet of each efferent artery indicates the percentage of reduction in mean outflow rate calculated as $\frac{Q_{NC}-Q_{OC}}{Q_{NC}} \cdot 100$, where Q_{NC} is the mean outflow rate in normal conditions shown in Table 5.2 and Q_{OC} is the mean outflow rate with the occlusion.

In all the cases studied the occlusion of the VA has relative little effect compared to the occlusion of the ICA. If the right ICA is occluded, the right MCA is the efferent artery with the highest reduction in outflow rate in all the anatomies, followed by the right ACA (A2) in most of the anatomies. In anatomical variations involving the communicating arteries, the absence of the ACoA is the case with the highest decrease in efferent mean outflows in the right MCA and ACA (A2), because collateral flow from the left ICA to these two arteries has less viscous dissipation through the ACoA than through the PCoAs, since the former route is shorter. Hence, the ACoA is a more critical collateral pathway than both PCoAs if an ICA is occluded. This is in agreement with the results obtained in [36, 33, 14]. If the right VA is occluded, the PCAs (P2) are the efferent arteries with the highest reduction in out-

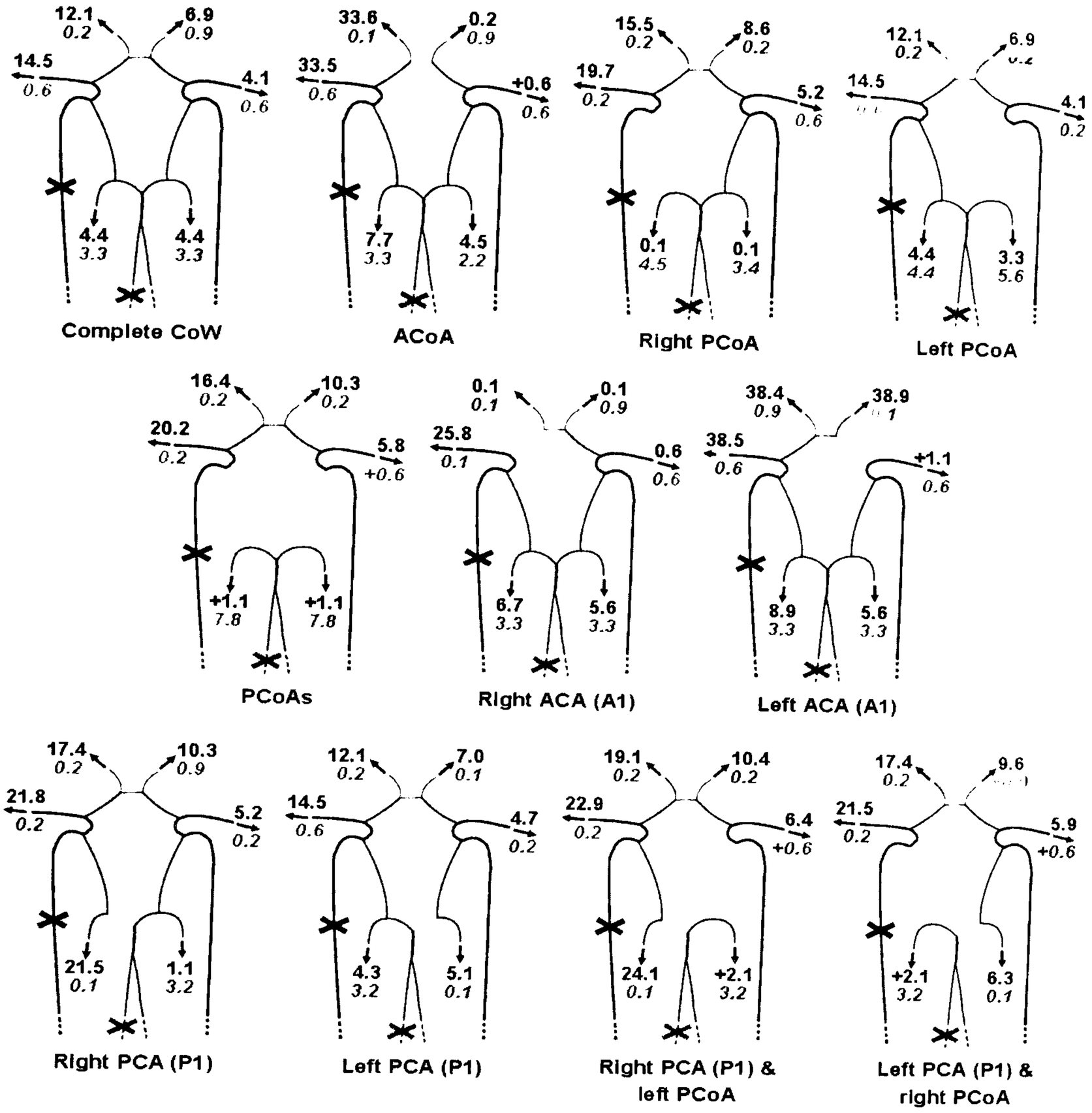


Figure 5.10: Reduction in mean outflow rate at the outlet of the efferent arteries of each anatomical variation (the arteries absent are indicated at the bottom of each case), when the right ICA (black numbers) or the right VA (light numbers) are occluded. Numbers express the percentage of reduction in mean outflow rate between normal conditions and with the occlusion, as explained in the text. Numbers with "+" indicate an increase in mean outflow rates with the occlusion.

flow rates and the PCoAs become the collateral routes that play a more important role in the compensatory mechanism of the CoW.

Among all the cases studied, the anatomical variation without an ACA (A1) and with a complete occlusion of the contralateral ICA presents the highest reduction in mean outflow rates in three efferent arteries (the ipsalateral MCA and both ACAs, A2). Therefore, this is the anatomy at the highest risk of TIA and cerebral stroke according to the 1-D model.

Finally, Figures 5.8 (right) and 5.11 show that the direction of flow velocity over one cardiac cycle in the middle point of the communicating arteries does not indicate the side where there is a missing circulus artery, as was the case in normal conditions.

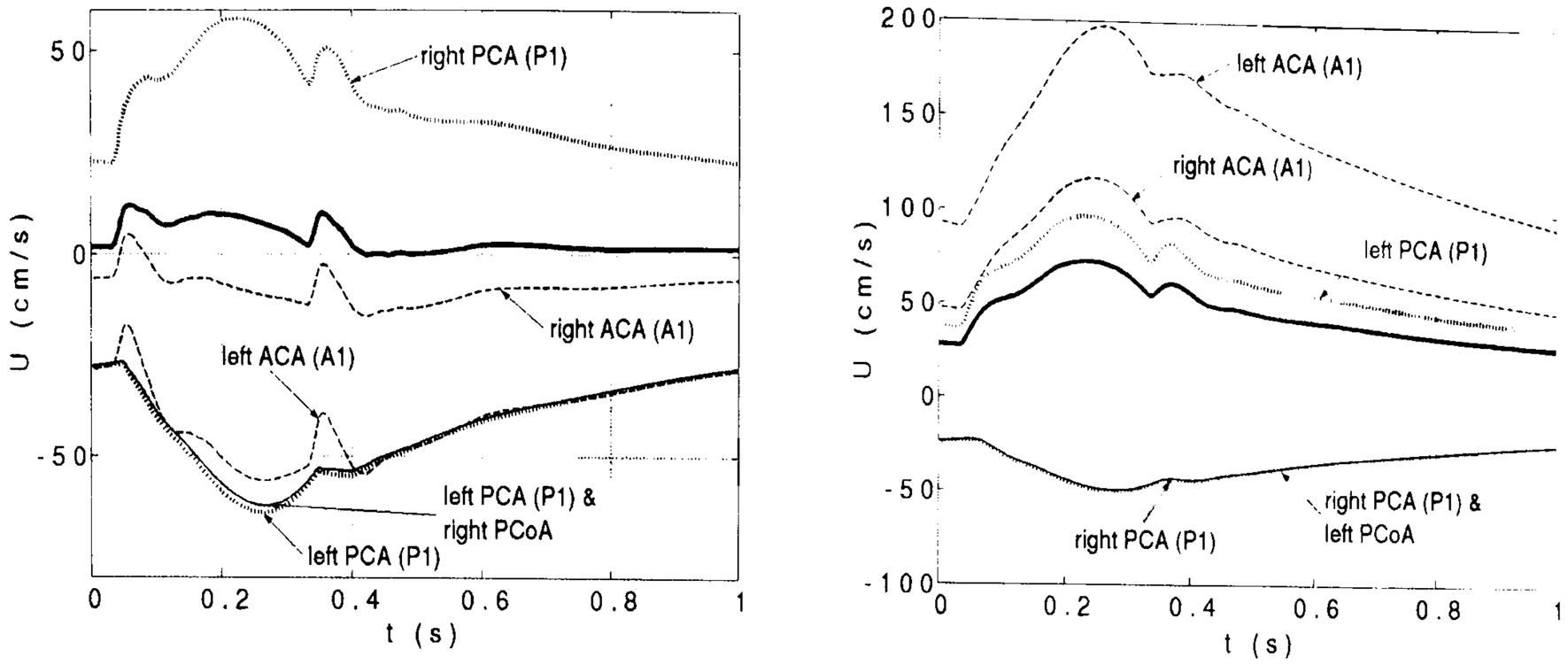


Figure 5.11: Velocity over one cardiac cycle in the middle point of the left PCoA (left) and right PCoA (right) of the complete CoW (thick solid lines) and the anatomical variations with missing vessels as indicated in the figures. The right ICA is completely occluded. Positive values follow the direction of the arrows in Figure 5.1 (right). We notice that the direction of flow in the PCoAs does not indicate the side where there is the missing or hypoplastic ACA (A1) or PCA (P1).

5.4.3 The effect of partial occlusions in the communicating arteries

This section studies the effect of partial occlusions of the communicating arteries combined with the occlusion of the right ICA. Figure 5.12 shows the effect of the calibre of the ACoA (left) and the right PCoA (right) on the mean outflow rates in the three right efferent arteries, when the right ICA is completely occluded in its middle point. We observe that the outflows of the ACA (A2) and the MCA depend strongly on the calibre of the ACoA in the range of calibres from 0.4 mm to 1.6 mm, approximately, whereas the outflow rate at the PCA (P2) remains almost constant in all the range of calibres studied. On the other hand, the calibre of the right PCoA affects the outflows at the three efferent arteries, specially in the range of calibres from 0.8 mm to 2.2 mm. For a given calibre, collateral flow through the ACoA is higher than through the right PCoA. Furthermore, a reduction in the calibre of the ACoA produces a higher reduction in the mean flow rates of the ACA (A2) and MCA than a reduction in the calibre of the right PCoA. These observations confirm the previous results showing that the ACoA is a more important collateral pathway than the PCoAs if an ICA is occluded.

We also observe that the mean flow rate of the right PCA (P2) decreases with increasing calibre of the right PCoA, since more blood from the posterior circulation

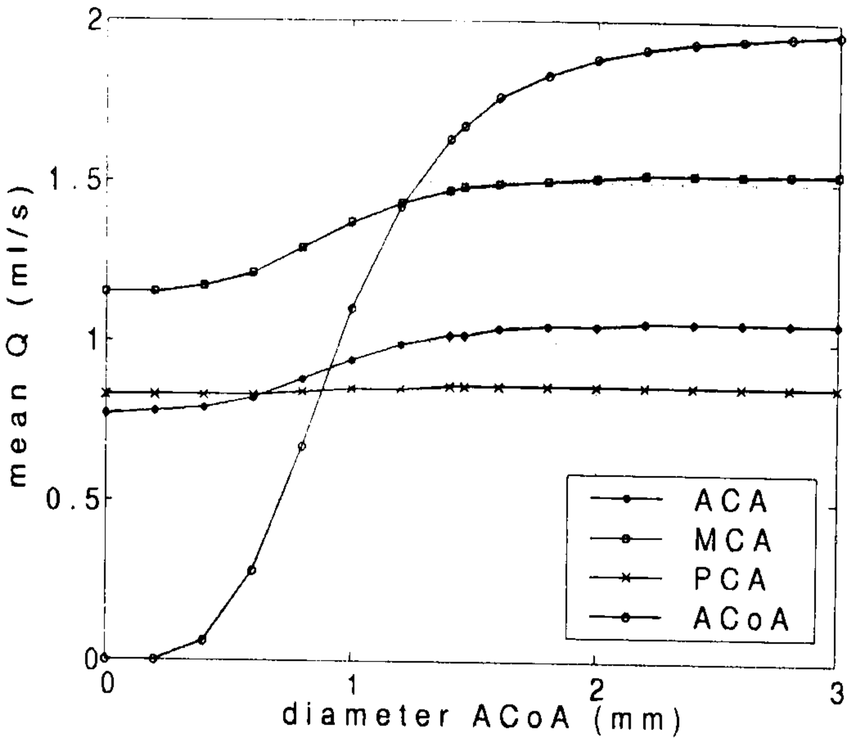


Figure 5.12: Mean outflows in the right efferent arteries and in the ACoA and right PCoA as a function of the diameter of the ACoA (left) and the right PCoA (right). The right ICA is completely occluded in its middle point.

is transported to the anterior circulation through the PCoA.

Using TCCD measurements and postmortem anatomy, Hoksbergen *et al* [35] determined that the threshold diameter allowing for collateral flow through the communicating arteries is between 0.4 mm and 0.6 mm. Cassot *et al* [14] and Dickey *et al* [20] computationally obtained a threshold calibre of 0.4 mm for the ACoA. Moreover, Dickey *et al* found that the threshold diameter for the PCoA in patients with a well-functioning ACoA and with an occlusion of an ICA is between 0.5 mm and 0.6 mm. According to the results shown in Figure 5.12, collateral flow in the ACoA starts for smaller calibres than in the PCoA (0.2 mm versus 0.4 mm). The efferent outflows significantly change for calibres higher than 0.4 mm in the ACoA and 0.8 in the PCoA, approximately. The minimum diameter allowing for collateral flow through the PCoA is larger than through the ACoA because the longer length of the PCoAs compared to the length of the ACoA produces a higher resistance to flow.

5.5 Final remarks

The non-linear 1-D model of the cerebral circulation described in this chapter is able to capture the main pulse wave propagation features observed *in-vivo* along the aorta (Figure 5.4), at the brachiocephalic bifurcation (Figure 5.5), and throughout the cerebral arteries (Figure 5.6, left and Figure 5.7), without tuning the value of any published physiological data and with a simple input waveform. From the

origin of the carotid and vertebral arteries and up to the efferent vessels of the CoW, a continuous blood flow towards the brain has been observed during all the cardiac cycle, which is in agreement with *in-vivo* measurements (Figure 5.5 and reference [60]).

The effects of the most frequent anatomical variations of the CoW on cerebral outflow rates and pulse waveforms in the communicating and efferent arteries have also been studied. The results suggest that the system does not require collateral pathways through the communicating arteries to adequately perfuse the brain of healthy subjects (Table 5.2). The communicating arteries become important to maintain sufficient brain perfusion in anatomical variations with a missing ACA (A1) or PCA (P1), or when an ICA or a VA is occluded. Moreover, the ACoA is a more critical collateral pathway than the PCoAs if an ICA is occluded (Figure 5.10). which is in agreement with other clinical and numerical studies [36, 33, 14]. If a VA is occluded, the reductions in mean outflow rates are significantly smaller than if an ICA is occluded, and the PCoAs are the collateral routes that play a more important role in the compensatory mechanism of the CoW. The worst scenario among all the anatomies studied, in terms of reduction in the mean cerebral outflows, is a CoW without the ACA (A1) and with a complete occlusion of the contralateral ICA (Figure 5.10).

This study has also shown that a hypoplastic or missing ACA (A1) can be detected with flow measurements at the ACoA (Figure 5.8, left), and a hypoplastic PCA (P1) with flow measurements at the PCoAs (Figure 5.9). Moreover, the direction of the flow in any communicating artery indicates the side of the CoW with such a hypoplastic artery. It is also important to notice that in subjects with a complete CoW or with anatomical variations involving the communicating arteries, velocities within these arteries may be too small for MRA techniques to detect their presence.

The simulation of partial occlusions in the communicating arteries have confirmed that the ACoA is a more important collateral pathway than the PCoAs if the ICA is occluded (Figure 5.12). Collateral flow through the ACoA increases the efferent outflows for calibres higher than about 0.4 mm in the ACoA and 0.8 in the PCoA, which is agreement with other computational and clinical studies [14, 20, 35].

An obvious drawback of this study is the lack of experimental confirmation, because of the lack of detailed information on the geometry and elasticity of the arterial network and on the boundary conditions. The results presented depend on the physiological data used, which is based on published measurements in healthy young adults.

All the simulations have always been carried out with the same peripheral impedances and, hence, this work has analysed the compensatory ability of the CoW itself to reduce the effects of pathological alterations. This is the first mechanism of autoregulation that takes place. Other mechanisms such as vasodilatation, vasoconstriction and wall remodelling have been ignored. As mentioned previously, autoregulation by vasodilatation and vasoconstriction can be simulated with time-varying resistances (David *et al* [19], Ferrandez *et al* [23] and Moorhead *et al* [55]).

The 1-D model presented in this work is a fast and powerful research tool to enhance the understanding of blood flow patterns and distributions throughout the brain within a prescribed geometry. If used in conjunction with patient-specific geometry, it can predict the haemodynamic effect of clinical interventions such as carotid endarterectomy, angioplasty and stenting. It can be also applied to study the effect on cerebral outflows of time dependent changes within the cardiac output, since it allows for a non-periodic inflow boundary condition at the ascending aorta. Furthermore, it has the potential to simulate local flows in detail if coupled to a 3-D simulation of a local area of the cerebral circulation, which, in turn, can be used to investigate, for instance, the flow patterns that lead to increased probability of formation of atherosclerosis or intracraneal aneurysms (local dilatations of the arterial wall).

Chapter 6

Conclusions

This thesis concludes with a summary of the achievements described in the previous chapters (Section 6.1) and with some directions for future research (Section 6.2).

6.1 Summary of the thesis achievements

This thesis has successfully accomplished the objectives set out in Section 1.4. The modelling capabilities of the existing non-linear, 1-D model of pulse wave propagation in arterial networks have been enhanced by including more physiological boundary conditions and viscous dissipation. With these improvements, the new model is able to simulate physiological pressure and flow waveforms in the largest human conduit arteries.

The accuracy of the new code has been assessed by simulating a 1:1 scale hydrodynamic replica of the 55 largest human conduit arteries (Section 3.1). This has shown the ability of the 1-D model to capture the main features of pulse wave propagation measured along the experimental aorta (Figures 3.4 to 3.9). Although the numerical results could only be compared with the experimental results along the aorta, due to the lack of experimental measurements in other locations, and considering the large number of parameters involved in this simulation, the 1-D model developed in this thesis has been able to approximate the experimental results with good accuracy. This study has increased the confidence in the 1-D formulation and its ability to model clinically relevant problems, such as the applications presented in this work.

The validated 1-D model has been used to understand the haemodynamics of

the pressure and flow waveforms observed along the human aorta (Sections 3.3 and 3.4), and to investigate the effect of anastomoses and partial or total occlusions of arteries in two arterial networks: the arm (Chapter 4) and the cerebral circulation (Chapter 5). These applications have shown that the 1-D model is a powerful tool to understand the effect on pulse wave propagation of changes in the geometry and elasticity of the arterial system, which can be caused by cardiovascular diseases (e.g., atherosclerosis), clinical procedures (e.g., stenting, angioplasty, surgical interventions, haemodialysis, harvesting of arteries) or anatomical variations.

The single vessel model of the human aorta has shown that the pressure and flow waveforms along the aorta are a consequence of the combined effect of wave reflections from the peripheral vessels and the aortic valve when shut, the velocity of propagation of these waves and the windkessel effect due to the compliance of the arterial walls. Although single wave reflections coming from the peripheral vessels are small (Figure 3.15), their convolution with the half-sinusoidal wave produced by the heart leads to the pulse waves observed *in-vivo* (Figure 3.13). This thesis has also shown that non-linearities and viscous dissipation have a small effect on the pulse waveforms along the aorta under physiological conditions (Figures 3.18 and 3.22). Pulse waveforms are very sensitive to changes in the aortic calibre (Figure 3.20) and the peripheral resistance (Figure 3.23), but they are less sensitive to changes in the length of the aorta, the thickness and elasticity of the aortic wall, the venous pressure, and especially to changes in the density and viscosity of the blood. The mean aortic pressure depends only on the cardiac output, the peripheral resistance (the effect of the viscous resistance along the aorta is secondary) and the venous pressure. The pulse pressure depends mainly on the total compliance: it decreases with increasing total systemic compliance (which is in agreement with the classical windkessel model described in Section 2.7.3.2) and when a larger part of the total systemic compliance is associated with the aortic compliance. The inertia of the blood in the vessels beyond the aorta has a neglegible effect on aortic pulse waveforms.

The study of the three most prevalent arterial anatomies in the arm (Chapter 4) has shown that when a Gaussian wave (an approximation of a delta wave) is propagated from the brachial artery, the waves reflected in an anatomy with a complete

palmar arch introduce significant changes in pulse waveforms along the main conduit arteries of the arm, compared to anatomies with an incomplete palmar arch (Figures 4.3 and 4.4). However, differences in waveforms between the anatomies studied are insignificant under physiological conditions (Figure 4.8), which makes it unfeasible to detect their presence from pressure and velocity measurements. This study has also shown that small calibres of the superficial palmar arch and insufficient compression of the radial artery can lead to false-positive results of the modified Allen's test (Figures 4.13 and 4.14). Measurement of the drop in digital systolic pressures with radial artery compression has proved to be a more sensitive test to predict the presence of sufficient ulnar collateral flow if the calibre of the superficial palmar arch is small. However, this study has also shown that digital pressure measurements can fail in detecting sufficient collateral flow (false-negative result) if the radial artery is insufficiently compressed.

The last application of the 1-D model presented in this thesis is the study of blood flow in the cerebral circulation, including the circle of Willis (CoW) (Chapter 5). It has been shown that the system does not require collateral pathways through the communicating arteries to adequately perfuse the brain of normal subjects (Table 5.2). The communicating arteries become important in cases of hypoplastic or occluded vessels, the anterior communicating artery (ACoA) being a more critical collateral pathway than both posterior communicating arteries (PCoAs) if the internal carotid artery (ICA) is occluded (Figure 5.10). Occlusions of the vertebral arteries have proved to be far less critical than occlusions of the ICAs. The worst scenario among all the anatomies studied, in terms of reduction in the mean cerebral outflows, is a CoW without the first segment of an anterior cerebral artery combined with an occlusion of the contralateral ICA. Furthermore, in patients without any severe occlusion of a carotid or vertebral artery, the direction of the flow measured at the communicating arteries indicates to the side of the CoW with a disfunctional artery (Figures 5.8, left, and 5.9).

This thesis has also described the main anatomical and physiological features of the cardiovascular system needed to understand the 1-D formulation and its results (Chapter 1). Both the linear and non-linear 1-D formulations have been detailed, starting from the general non-linear governing equations, and analysed using the

method of characteristics (Chapter 2). A linear formulation has also been included because it leads to analytical solutions that are very useful in providing insight into the interpretation of the results. It has been shown that the 1-D formulation can be interpreted in terms of forward and backward travelling waves moving at a speed that depends on the elasticity of the arterial wall. If this speed is known, forward and backward waves can be determined at any location in the arterial system using the wave separation technique described in Section 2.4, which has been used to assist in the interpretation of the results obtained in this thesis.

Another contribution of this thesis is the technique proposed in Section 2.8 to estimate the fluid resistance, inertia and compliance of the neglected vessels perfused by the terminal branches of the 1-D model. This technique assumes that the neglected vessels are arranged in a bifurcating tree and the radii and lengths of successive generations of bifurcations can be approximated by a geometric series. The scaling factor of the radii has been obtained from a published statistical study [66] and the scaling factor of the lengths is based on the maximisation of the lateral surface of the capillaries (and hence, perfusion) and the minimisation of the volume occupied by the whole branching network up to the capillaries. Although this method has been able to approximate some peripheral resistances and compliances with significant accuracy (Table 3.4), it still needs further validation with *in-vivo* and experimental data that are not available to the knowledge of the author.

In conclusion, the main contribution of this thesis has been the development and validation of a reliable 1-D model that produces clinically relevant results with a reasonable computational cost. This model offers an important insight into the performance of the arterial system, in healthy conditions and after total or partial occlusions of arteries, and it has the potential to assist in the diagnosis and treatment of cardiovascular diseases if applied with patient-specific data.

6.2 Future Work

This section describes the further applications of the 1-D model developed in this thesis (Section 6.2.1) and its further developments (Section 6.2.2).

6.2.1 Further applications of the model

The 1-D code developed in this thesis can be applied to understand the haemodynamics of other parts of the arterial system that have not been studied in this work (except for the coronary arteries because the movement of the heart can not be simulated with the current model). The current 1-D formulation can also assist in determing the effects on the shape of pulse waves of drugs that change the haemodynamic properties of the arterial system, such as nitrovasodilators [95]. These studies can be carried out by making a hypothesis of the changes that these drugs produce in the compliance, geometry and/or peripheral resistance of the arterial system, and validating this hypothesis by comparing the pulse waveforms predicted by the 1-D simulation with the waveforms measured *in-vivo*.

The current model can also be used to study the effect on arterial blood flow of other cardiovascular pathologies not studied in this thesis. For instance, the effects of arterial hemorrhages on pulse wave propagation can be studied by considering a 1-D model of the largest conduit arteries and simulating a hemorrhage as a 1-D artery branching off the point of the hemorrhage and ending with a negative terminal reflection coefficient. With such a model, it should be feasible to explain the early return of pressure wave reflection from the abdominal vasculature induced by a hemorrhage in the brachial artery, as measured in pigs by Dark *et al* [18].

The 1-D model can also assist in verifying the validity of methods for estimating pulse wave speed [51, 43], and the effect of nearby reflections at the measuring site.

6.2.2 Further developments of the methodology

It would be interesting to enhance the modelling capabilities of the 1-D formulation presented in this thesis by including the effect of arterial curvature on pulse waves, to investigate its significance in arteries with high curvature, such as the circle of Willis and the palmar arch. To model a curved artery, the system of 1-D governing equations (2.1), (2.6) and (2.11) used in this thesis needs to be modified to include conservation of mass and momentum in the radial dimension [9]. The code could also be modified to deal with prescribed wall motions by solving the 1-D governing equations for pressure and flow with a prescribed area. A 1-D code that includes

the effect of curvature and can predict pressure and flow for a prescribed area would allow us to simulate pulse wave propagation in the coronary arteries taking into account the contraction of the ventricles.

Other developments of the current code are the inclusion of pressure-area relationships that better describe the non-linear physiological behaviour of the arterial wall observed in Figure 1.5. It would be interesting to find out if the 1-D model can be applied to simulate venous flows, perhaps with a tube law that accounts for the collapse of the vessel as it is observed in veins. Energy losses at junctions can be modelled by adding a loss coefficient into the Bernoulli's law expressed by Equations (2.90) and (2.91), which should depend on the branching angles, according to the experiments by Gardel [28, 29]. Gardel proposed empirical expressions to calculate the value of energy losses, which have already been used to simulate blood flow in an arterial bypass (Steele *et al* [86]).

The outflow boundary conditions of the current model could be improved by using time-varying resistances to account for autoregulation by vasodilatation and vasoconstriction of the peripheral vessels, as in the models of the circle of Willis by David *et al* [19], Ferrandez *et al* [23] and Moorhead *et al* [55].

The large range of scales within the cardiovascular system suggests the use of a multiscale modelling involving 3-D, 1-D and 0-D models, as advocated by Formaggia *et al* [24]. It would be very interesting to couple the 1-D model of the largest conduit arteries developed in this thesis with a complete lumped parameter description of the resistance, compliance and inertia of the rest of the human circulation, by means of 0-D models similar to the terminal models used in this work. This new model would include the systemic vessels neglected by the 1-D model along with the systemic venous system, the pulmonary circulation, and the left and right chambers of the heart with their valves. A lumped parameter model including all the main compartments of the cardiovascular system has been proposed by Ottensen *et al* [65]. The current 1-D model could provide better boundary conditions for detailed 3-D simulations to accurately describe local blood flow fields in regions where we want to investigate the effect of wall shear stresses on endothelial cells and its relation to degenerative pathologies of the vascular tissue, such as artherosclerosis or aneurysms. For instance, in the model of the cerebral circulation described in Chap-

ter 5, such a multiscale approach could be used to study the formation, development and posterior rupture of cerebral aneurysms.

All the developments enumerated in this section should always be validated by comparison against *in-vivo* or *in-vitro* data and they should be used with patient-specific data, when available. This is of fundamental importance to confidently apply numerical modelling to improve the diagnoses and treatment of cardiovascular diseases, since haemodynamics in the systemic circulation strongly depends on the geometry, elasticity and anatomy of the arteries, as we have seen in this work.

Bibliography

[1] J. Alastruey, K.H. Parker, J. Peiró, and S.J. Sherwin. A one-dimensional simulation of the human conduit arteries compared to experimental data. *Proc. of the ASME Summer Biongineering Conf., abstract 0328683, Vail, CO. 22–26 June*, 2005.

[2] J. Alastruey, K.H. Parker, J. Peiró, and S.J. Sherwin. Can the modified Allen's test always detect sufficient collateral flow in the hand? A computational study. *Accepted by Comp. Meths. Biomech. Biomed. Engng.*, 2006.

[3] J. Alastruey, K.H. Parker, J. Peiró, and S.J. Sherwin. Modelling the circle of Willis to assess the effects of anatomical variations and occlusions on cerebral flows. *Accepted by J. Biomech.*, 2006.

[4] M. Anliker, R.L. Rockwell, and E. Odgen. Nonlinear analysis of flow pulses and shock waves in arteries. *ZAMP*, 22:217–246, 1971.

[5] H.B. Atabek. Wave propagation through a viscous fluid contained in a tethered, initially stressed, orthotropic elastic tube. *Biophysical J.*, 8:626–649, 1968.

[6] A.P. Avolio. Multi-branched model of the human arterial system. *Med. and Biol. Engng. and Comput.*, 18:709–718, 1980.

[7] A.P. Avolio, S. Chen, R. Wang, C. Zhang, M. Li, and M.F. O'Rourke. Effects of aging on changing arterial compliance and left ventricular load in a northern chinese urban community. *Circulation*, 68:50–58, 1983.

[8] S.D. Balar, T.R. Rogge, and D.F. Young. Computer simulation of blood flow in the human arm. *J. Biomech.*, 22:691–697, 1989.

[9] S. Balbis, L. Formaggia, G. Pontrelli, and C. Guiot. Reduced models for blood flow in curved vessels. *ESAIM*, 14:14–24, 2005.

[10] R.F. Brodman, L.E. Hirsh, and R. Frame. Effect of radial artery harvest on collateral forearm blood flow and digital perfusion. *J. Thorac. Cardiovasc. Surg.*, 123:512–516, 2002.

[11] B.S. Brook, S.A.E.G. Falle, and T.J. Pedley. Numerical solutions for unsteady gravity-driven flows in collapsible tubes: evolution and roll-wave instability of a steady state. *J. Fluid Mech.*, 396:223–256, 1999.

[12] A.C. Burton. *Physiology and biophysics of the circulation.* Year book medical publishers, Inc., 1965.

[13] C.G. Caro, T.J. Pedley, R.C. Schroter, and W.A. Seed. *The mechanics of the circulation.* Oxford University Press, 1978.

[14] F. Cassot, V. Vergeur, P. Bossuet, B. Hillen, M. Zagzoule, and J.P. Marc-Vergnes. Effects of anterior communicating artery diameter on cerebral hemodynamics in internal carotid artery disease. *Circulation*, 92:3122–3131, 1995.

[15] F. Cassot, M. Zagzoule, and J.P. Marc-Vergnes. Hemodynamic role of the circle of Willis in stenoses of internal carotid arteries. An analytical solution of a linear model. *J. Biomech.*, 33:395–405, 2000.

[16] J.R. Cebral, M.A. Castro, O. Soto, R. Löhner, and N. Alperin. Blood-flow models of the circle of Willis from magnetic resonance data. *J. Engng. Maths.*, 47:369–386, 2003.

[17] Cerebrovascular laboratory, Department of Neurological Surgery, University of Washington, Seattle. *http://depts.washington.edu/uwtcdlab/tcd.html.*

[18] P. Dark, R. Little, M. Nirmalan, and J. Purdy. Systemic arterial pressure wave reflections during accute hemorrhage. *Crit. Care Med.*, 34:1–9, 2006.

[19] T. David, M. Brown, and A. Ferrandez. Auto-regulation and blood flow in the cerebral circulation. *Int. J. Numer. Meth. Fluids*, 43:701–713, 2003.

[20] P.S. Dickey, P. Kailasnath, G. Bloomgarden, I. Goodrich, and J. Chaloupa. Computer modeling of cerebral blood flow following internal carotid occlusion. *Neurol. Res.*, 18:259–266, 1996.

[21] L. Euler. Principia pro motu sanguinis per arterias determinando. *Opera posthuma mathematica et physica anno 1844 detecta*, 2:814–823, 1775. Ediderunt P.H. Fuss et N. Fuss Petropoli; Apund Eggers et Socios.

[22] R. Fahrig, H. Nikolov, A.J. Fox, and D.W. Holdsworth. A three-dimensional cerebrovascular flow phantom. *Med. Phys.*, 26:1589–1599, 1999.

[23] A. Ferrandez, T. David, and M.D. Brown. Numerical models of auto-regulation and blood flow in the cerebral circulation. *Comp. Meth. Biomech. Biomed. Engng.*, 5:7–20, 2002.

[24] L. Formaggia, J.-F. Gerbeau, F. Nobile, and A. Quarteroni. On the coupling of 3D and 1D Navier-Stokes equations for flow problems in compliant vessels. *Comp. Meth. App. Mech. Engng.*, 191:561–582, 2001.

[25] L. Formaggia, D. Lamponi, and A. Quarteroni. One-dimensional models for blood flow in arteries. *J. Engng. Math.*, 47:251–276, 2003.

[26] L. Formaggia and A. Veneziani. One dimensional models for blood flow in the human vascular system. VKI Lecture Series 07-2003, MOX. Dipartamento di Matematica, Politecnico di Milano, 2003.

[27] O. Frank. Die Grundform des arteriellen Pulses. *Z. Biol.*, 37:483–526, 1899.

[28] A. Gardel. Les pertes de charge dans les écoulements au travers de branchements en té. *Bull. Technique de la Suisse Romande*, 9:123–130, 1957.

[29] A. Gardel. Les pertes de charge dans les écoulements au travers de branchements en té. *Bull. Technique de la Suisse Romande*, 10:143–148, 1957.

[30] D. Gregg. *The physiological basis of medical practice*, chapter Dynamics of blood and lymph flow. Williams and Wilkins, New York, 8th edition, 1966.

[31] K. Hayashi, H. Handa, S. Nagasawa, A. Okumura, and K. Moritake. Stiffness and elastic behavior of human intracraneal and extracraneal arteries. *J. Biomech.*, 13:175–184, 1980.

[32] R.D. Henderson, M. Eliasziw, A.J Fox, P.M. Rothwell, and H.J.M. Barnett. Angiographycally defined collateral circulation and risk of stroke in patients with severe carotid artery stenosis. *Stroke*, 31:128–132, 2000.

[33] B. Hillen, B.A.H. Drinkenburg, H.W. Hoogstraten, and L. Post. Analysis of flow and vascular resistance in a model of the circle of Willis. *J. Biomech.*, 21:807–814, 1988.

[34] B. Hillen, H.W. Hoogstraten, and L. Post. A mathematical model of the flow in the circle of Willis. *J. Biomech.*, 19:187–194, 1986.

[35] A.W.J. Hoksbergen, B. Fülesdi, D.A. Legemate, and L. Csiba. Collateral configuration of the circle of Willis. Transcranial color-coded duplex ultrasonography and comparison with postmortem anatomy. *Stroke*, 31:1346–1351, 2000.

[36] A.W.J. Hoksbergen, D.A. Legemate, D.T. Ubbink, and M.J.H.M. Jacobs. Collateral variations in circle of Willis in atherosclerotic population assessed by means of transcranial color-coded duplex ultrasonography. *Stroke*, 31:1656–1660, 2000.

[37] A.W.J. Hoksbergen, C.B.L. Majoie, F.J.H. Hulsmans, and D.A. Legemate. Assessment of the collateral function of the circle of Willis: three-dimensional time-of-flight MR angiography compared with transcranial color-coded duplex sonography. *Am. J. Neuroradiol.*, 24:456–462, 2003.

[38] T.J.R. Hughes. *A study of the one-dimensional theory of arterial pulse propagation.* Report 74-13, Dept. of Civil Engng. University of California, 1974.

[39] C.V. Ioannou, N. Stergiopulos, A.N. Katsamouris, I. Startchik, A. Kalangos, M.J. Licker, N. Westerhof, and D.R. Morel. Hemodynamics induced after acute reduction of proximal thoracic aorta compliance. *Eur. J. Vasc. Endovasc. Surg.*, 26:195–204, 2003.

[40] R.W. Kamienski and R.W. Barnes. Critique of the Allen test for continuity of the palmar arch assessed by Doppler ultrasound. *Surg. Gynecol. Obstet.*, 142:861–864, 1976.

[41] T. Kapoian, J.L. Kaufman, J. Nosher, and R.A. Sherman. *Atlas of diseases of the kidney*, volume 5, chapter Dialysis access and recirculation. Current medicine, Inc, 1999.

[42] G.E. Karniadakis and S.J. Sherwin. *Spectral/hp element methods for CFD.* Oxford University Press, 2003.

[43] A.W. Khir, A. O'Brien, J.S.R Gibbs, and K.H. Parker. Determination of wave speed and wave separation in the arteries. *J. Biomech.*, 34:1145–1155, 2001.

[44] D.J. Korteweg. Uber die Fortpflanzungsgeschwindigkeit des Schalles in elastischen Röhern. *Ann. Phys. Chem. (NS)*, 5:525–527, 1878.

[45] G. Landes. Physikalische Probleme bei der Untersuchung des menschlichen Kreislaufs. *Z. Tech. Physik*, 8:192, 1941.

[46] J.R. Levick. *An introduction to cardiovascular physiology.* Arnold, London, 4th edition, 2003.

[47] H. Lippert and R. Pabst. *Arterial variations in man: classification and frequency.* J.F. Bergmann, Munich, 1985.

[48] P.A. Lynn and W. Fuerst. *Introductory digital signal processing with computer aplications.* John Wiley & Sons, 1989.

[49] F.H. Martini. *Fundamentals of Anatomy and Physiology.* Prentice Hall, Inc, 3rd edition, 1995.

[50] D.A. McDonald. *Blood flow in arteries.* Edward Arnold, London, 1974.

[51] W.R. Milnor. *Hemodynamics.* Williams and Wilkins, Baltimore, 1989. Appendix D.

[52] A.I. Moens. Over de voortplantingssnelheid von den pols (on the speed of propagation of the pulse). *Technical report, Leiden*, pages 814–823, 1877.

[53] S. Moore, T. David, J.G. Chase, J. Arnold, and J. Fink. 3D models of blood flow in the cerebral vasculature. *J. Biomech.*, 39:1454–1463, 2006.

[54] S.M. Moore, K.T. Moorhead, J.G. Chase, T. David, and J. Fink. One-dimensional and three-dimensional models of cerebrovascular flow. *J. Biomech. Engng.*, 127:440–449, 2005.

[55] K.T. Moorhead, C.V. Doran, J.G. Chase, and T. David. Lumped parameter and feedback control models of the auto-regulatory response in the circle of Willis. *Comp. Meth. Biomech. Biomed. Engng.*, 7:121–130, 2004.

[56] S.R.A. Moraes, T.N. Araújo, A.R. Silva, A.R. Paula, and J.L. Salgado. Morphologic variations of the superficial palmar arc. *Acta Cirúrgica Brasileira*, 18:183–188, 2003.

[57] J.P. Murgo, N. Westerhof, J.P. Giolma, and S.A. Altobelli. Aortic input impedance in normal man: relationship to pressure wave forms. *Circulation*, 62:105–116, 1980.

[58] A. Noordergraaf, H.B.K. Boom, and P.D. Verdouw. A human systemic analog computer. *Proc. 1st Congr. Soc. for Ballistocardiographic Res.*, page 23. 1960.

[59] A. Noordergraaf, P.D. Verdouw, and H.B.K. Boom. The use of an analog computer in a circulation model. *Prog. Cardiovasc. Dis.*, 5:419–439, 1963.

[60] C. Oates. *Cardiovascular haemodynamics and Doppler waveforms explained.* Greenwich Medical Media LTD, 2001.

[61] E. Olave, J.C. Prates, E. Mandiola, M. del Sol Calderón, and C. Gabrielli. Formaciones arteriales superficiales de la palma de la mano. *Revista Chilena de Anatomía*, 11:35–40, 1993.

[62] M.S. Olufsen. Structured tree outflow condition for blood flow in larger systemic arteries. *Am. J. Physiol.*, 276:H257–H268, 1999.

[63] M.S. Olufsen, C.S. Peskin, W.Y. Kim, E.M. Pedersen, A. Nadim, and J. Larsen. Numerical simulation and experimental validation of blood flow in arteries with structured-tree outflow conditions. *Annals Biomed. Engng.*, 28:1281–1299, 2000.

[64] M. Oshima. A new approach to cerebral hemodynamics. Patient-specific modeling and numerical simulation of blood and arterial wall interaction. *IACM Expressions*, 16:4–9, 2004.

[65] J.T. Ottesen, M.S. Olufsen, and J.K. Larsen. *Applied mathematical models in human physiology.* SIAM, Philadelphia, 2004.

[66] G.L. Papageorgiou and N.B. Jones. Arterial system configuration and wave reflection. *J. Biomed. Engng.*, 9:299–301, 1987.

[67] K.H. Parker and C.J.H. Jones. Forward and backward running waves in the arteries: analysis using the method of characteristics. *J. Biomech. Engng.*, 112:322–326, 1990.

[68] T.J. Pedley. *The fluid mechanics of large blood vessels.* Cambridge University Press, 1980.

[69] S. Peterson, V. Peto, and M. Rayner. *Coronary heart disease statistics.* British Heart Foundation Health Promotion Reasearch Group. Dept. of Public Health, University of Oxford, 2004.

[70] P. Pola, M. Serricchio, R. Flore, E. Manasse, A. Favuzzi, and G.F. Possati. Safe removal of the radial artery for myocardial revascularization: a doppler study to prevent ischemic complication to the hand. *J. Thorac. Cardiovasc. Surg.*, 112:737–744, 1996.

[71] W.K. Purves, D. Sadava, H. Orians, and H.C. Heller. *Life: the science of biology.* Sinauer associates and W.H. Freeman, 4th edition, 2003.

[72] J.K. Raines, M.Y. Jaffrin, and A.H. Shapiro. A computer simulation of the human arterial system. *Proc. of the Summer Computer Simulation Conf. (SCSC), Boston*, 1971.

[73] J.K. Raines, M.Y. Jaffrin, and A.H. Shapiro. A computer simulation of arterial dynamics in the human leg. *J. Biomech.*, 7:77–91, 1974.

[74] B. Riemann. Gesammelte mathematische Werke und wissenschaftlicher Nachlass. *Liepzig, B.G. Teubner (ed.)*, pages 145–164, 1876. (originally published as *Über die Fortpflanzung ebener Luftwellen von endlicher Schwingungsweite. Technical report, Göttingen 8 (1860) 43*).

[75] B.W. Schaaf and P.H. Abbrecht. Digital computer simulation of human systemic arterial pulse wave transmission: a nonlinear model. *J. Biomech.*, 5:345–364, 1972.

[76] D.L. Schultz, D.S. Tunstall-Pedoe, G.J. Lee, A.J. Gunning, and B.J. Belhouse. *Velocity distributions and transition in the arterial system. In Ciba Symposium on Circulatory and Respiratory and Mass Transport.* GEW Wolstenholme and J. Knight, London, 1969.

[77] P. Segers. *Biomedical modelling of the arterial system for the non-invasive assessment of arterial compliance (Biomechanische modellering van het arterieel systeem voor de niet-invasieve bepaling van de arteriële compliantie).* PhD thesis, Ghent University, 1997.

[78] P. Segers, F. Dubois, D. De Wachter, and P. Verdonck. Role and relevancy of a cardiovascular simulator. *Cardiov. Engng.*, 3:48–56, 1998.

[79] P. Segers and P. Verdonck. Arterial mechanics. Notes published by IBITECH, University of Ghent, Belgium.

[80] P. Segers and P. Verdonck. Role of tapering in aortic wave reflection: hydraulic and mathematical model study. *J. Biomech.*, 33:299–306, 2000.

[81] M. Serricchio, M. Gaudino, P. Tondi, A. Gasbarrini, L. Gerardino, A. Santoliquido, P. Pola, and G. Possati. Hemodynamic and functional consequences of radial artery removal for coronary artery bypass grafting. *Am. J. Cardiol.*, 84:1353–1356, 1999.

[82] S.J. Sherwin, V.E. Franke, J. Peiró, and K.H. Parker. One-dimensional modelling of a vascular network in space-time variables. *J. Engng. Maths.*, 47:217–250, 2003.

[83] A.C. Simon, M.E. Safar, J.A. Levenson, G.M. London, B.I. Levy, and N.P. Chau. An evaluation of large arteries compliance in man. *Am. J. Physiol.*, 237:H550–H554, 1979.

[84] N.P. Smith, A.J. Pullan, and P.J. Hunter. An anatomically based model of transient coronary blood flow in the heart. *SIAM J. Appl. Math.*, 62:990–1018, 2001.

[85] S.L. Starnes, S.W. Wolk, R.M. Lampman, C.J. Shanley, R.L. Prager, B.K. Kong, J.J. Fowler, J.M. Page, S.L. Babcock, L.A. Lange, E.E. Erlandson, and W.M. Jr. Whitehouse. Noninvasive evaluation of hand circulation before radial artery harvest for coronary artery bypass grafting. *J. Thorac. Cardiovasc. Surg.*, 117:261–266, 1999.

[86] B.N. Steele, J. Wan, J.P. Ku, T.J.R. Hughes, and C.A. Taylor. *In Vivo* validation of a one-dimensional finite-element method for predicting blood flow in cardiovascular bypass grafts. *IEEE Trans. Biomed. Engng.*, 50:649–656, 2003.

[87] N. Stergiopulos, B.E. Westerhof, and N. Westerhof. Total arterial inertance as the fourth element of the windkessel model. *Am. J. Physiol.*, 45:H81–H88, 1999.

[88] N. Stergiopulos, D.F. Young, and T.R. Rogge. Computer simulation of arterial flow with applications to arterial and aortic stenoses. *J. Biomech.*, 25:1477–1488, 1992.

[89] N. Suwa, T. Niwa, H. Fukasawa, and Y. Sasaki. Estimation of intravascular blood pressure gradient by mathematical analysis of arterial casts. *Tohoku J. Exper. Med.*, 79:168–198, 1963.

[90] Y. Tardy, J.J. Meister, F. Perret, H.R. Brunner, and M. Arditi. Non-invasive estimate of the mechanical properties of peripheral arteries from ultrasonic and photoplethysmographic measurements. *Clin. Phys. Physiol. Meas.*, 12:39–54, 1991.

[91] A. Viedma, C. Jiménez-Ortiz, and V. Marco. Extended Willis circle model to explain clinical observations in periorbital arterial flow. *J. Biomech.*, 30:265–272, 1997.

[92] S. Vogel. *Vital Circuits. On pumps, pipes, and the working of the circulatory system.* Oxford University Press, New York, 1993.

[93] J.J. Wang, A.B. O'Brien, N.G. Shrive, K.H. Parker, and J.V. Tyberg. Time-domain representation of ventricular-arterial coupling as a windkessel and wave system. *Am. J. Heart Circ. Physiol.*, 284:H1358–H1368, 2003.

[94] J.J. Wang and K.H. Parker. Wave propagation in a model of the arterial circulation. *J. Biomech.*, 37:457–470, 2004.

[95] P.D. Weinberg, F. Habens, M. Kengatharan, S.E. Barnes, J. Matz, E.E. Änggård, and M.J. Carrier. Characteristics of the pulse waveform during altered nitric oxide synthesis in the rabbit. *British J. Pharmacology*, 133:361–370, 2001.

[96] N. Westerhof, F. Bosman, C.J. de Vries, and A. Noordergraaf. Analog studies of the human systemic arterial tree. *J. Biomech.*, 2:121–143, 1969.

[97] R.L. Whitmore. *Rheology of the circulation.* Pergamon Press, Oxford, 1968.

[98] J.T. Winterer, J. Ennker, K. Scheffler, U. Rosendahl, O. Schäfer, M. Wanner, J. Laubenberger, and M. Langer. Gadolinium-enhanced elliptically reordered three-dimensional MR angiography in the assessment of hand vascularization before radial artery harvest for coronary artery bypass grafting: first experience. *Investigat. Radiol.*, 36:501–508, 2001.

[99] J.R. Womersley. *An elastic tube theory of pulse transmission and oscillatory flow in mammalian arteries.* Wright Air Development Centre, Technical Report WADC-TR, 1957.

[100] T. Young. Hydraulic investigations, subservient to an intended Croonian lecture on the motion of the blood. *Phil. Trans. Roy. Soc., London*, 98:164–186, 1808.

[101] M. Zamir. *The physics of pulsatile flow.* Biological and Medical Physics Series. Springer-Verlag (New York), 2000.

[102] W. Zhen, H. Tong, Y. Wang, Y. Sun, W. Huan, Y. Ma, J. Tian, and L. Wu. Coronary bypass revascularization with radial artery and internal mammary artery grafts. *Chinese Med. J.*, 115:55–57, 2002.

[103] P. Zimmerman, E. Chin, S. Laifer-Narin, N. Ragavendra, and E.G. Grant. Radial artery mapping for coronary artery bypass graft placement. *Radiology*, 220:299–302, 2001.